Modélisation physique et numérique de la micro-mécanique des milieux granulaires saturés. Application à la stabilité de substrats sédimentaires en génie cotier.

Emanuele Catalano

UNIVERSITÉ DE GRENOBLE

THÈSE

Pour obtenir le grade de

DOCTEUR DE L'UNIVERSITÉ DE GRENOBLE

Spécialité : **Sciences de la Terre et Univers, Environnement**

Arrêté ministérial : xxx

Présentée par

Emanuele CATALANO

Thèse dirigée par **Eric Barthélémy**
et codirigée par **Bruno Chareyre**

préparée au sein **du Laboratoire 3SR - Grenoble**
et de **l'École Doctorale TUE - Terre Univers Environnement - Grenoble**

A pore-scale coupled hydromechanical model for biphasic granular media.

Application to granular sediment hydrodynamics

Thèse soutenue publiquement le **18/06/2012**,
devant le jury composé de :

M Félix Darve
Professeur à l'INP Grenoble, Président
Stéphane Bonelli
Directeur de Recherche à IRSTEA, Rapporteur
Farhang Radjai
Directeur de Recherche au CNRS, Rapporteur
Giovanni Barla
Professeur au Politecnico di Torino, Examinateur
Eric Barthélémy
Professeur à l'INP Grenoble, Directeur de thèse
Bruno Chareyre
Matre de confrences à l'INP Grenoble, Co-Directeur de thèse

Inevitabilmente a te.

Contents

List of Figures

List of symbols

A	wave amplitude, [Pa]
A_{ij}^{f}	area of the fluid part $S_{ij} \cap \Theta$ of facet ij, [m^2]
A_k	generic particle surface, [m^2]
a	k_n/k_t ratio, , [-]
A_{ij}^{k}	area of the intersection $S_{ij} \cap \Gamma_i$ of facet ij and sphere k, [m^2]
α_B	Biot's coefficient, [-]
B	Skempton coefficent, [-]
$\mathbf{C}$	Stiffness tensor
$\mathbf{C^s}$	Global stiffness matrix
C_v	consolidation coefficent, [-]
c	speed of sound, [m/s]
Δt_{cr}	critical time step, [s]
Δt_{M-K}	critical time step relative to the elastic problem, [s]
Δt_{M-V}	critical time step relative to the viscous problem, [s]
Δt	time step, [s]
D_{TV}	polygonal domain for microstress derivation, [m^3]
δ_c	normal particle displacement, [m]
Δu_s	incremental tangential relative displacement, [m]
d_{50}	mass median diameter, [m]
d_{max}	maximum diameter, [m]
d_{min}	minimum diameter, [m]
d	generic particle diameter, [m]
$\mathbf{e}$	deviatoric component of $\underline{\underline{\varepsilon}}$, [Pa]
$\mathbf{E}$	Global volume change matrix
E_{oed}	oedometric modulus, [Pa]
E_{global}	global stiffness modulus, [N/m]
E	solid particle elastic modulus, [Pa]
$\underline{\underline{\varepsilon}}$	small strain tensor, [Pa]
$\mathbf{F}^c$	generic contact force, [N]
$\mathbf{F}_i$	generic force applied on particle i, [N]
F_n	normal component of contact force, [N]
F_t	tangential component of contact force, [N]
$\mathbf{F}^f$	fluid force vector, [N]
$\mathbf{F}^{b,k}$	buoyancy force, [N]
$\mathbf{F}^{p,k}$	fluid pressure force, [N]
$\mathbf{F}^{v,k}$	fluid shear force, [N]
$\mathbf{F}^{sv}$	fluid shear viscous force, [N]
$\mathbf{F}^{ext}$	resultant of all forces on a particle, [N]
f	fluid body force per unit volume, [N]
F	bulk material body force per unit volume, [N]
f_V	fluid body forces, [N/kg]
G	shear modulus of the drained elastic solid, [Pa]
g_{ij}	hydraulic conductance of facet (throat) ij, $[m^4\,Pa^{-1}\,s^{-1}]$

$\mathbf{G}$	Global conductance matrix
g	gravity acceleration, [m/s^2]
γ_f	fluid unit weigth, [N/m^3]
H	piezometric or total hydraulic head, [m]
γ_{ij}^k	area of the part of $\partial\Theta_{ij}$ in contact with sphere k, [m^2]
γ'	apparent unit weight, [kg/m^3]
γ_{sat}	saturated soil unit weight, [kg/m^3]
γ_s	solid unit weight, [kg/m^3]
Γ	Part of Ω occupied by the solid phase, [m^3]
Γ_i	Domain occupied by solid particle i, [m^3]
$\mathbf{I}$	Generalized inertia matrix
i_c	critical gradient of liquefaction, [-]
i	hydraulic gradient, [-]
J_i	particle moment of inertia
K	bulk modulus of the drained elastic solid, [Pa]
K_u	bulk modulus of the undrained elastic solid, [Pa]
K_s	compressibility modulus of the solid constituent, [Pa]
K_f	compressibility modulus of the fluid constituent, [Pa]
K_d	hydraulic conductivity, [m/s]
κ	intrinsic permeability, [m^2]
KE	kinetic energy, [J]
$\mathbf{K}$	Global stiffness matrix
k_n	normal secant stiffness, [N/m]
k_t	shear tangential stiffness, [N/m]
κ_b	bulk volume viscosity (fluid), [Pa·s]
l_{ij}	distance between pores i and j Voronoi vertices, [m]
λ	quasi-staticity indicator, [-]
L_{TV}	boundary of D_{TV}, [m]
M_i	generic moment applied on particle i, [N·m]
$\mathbf{M}$	Global mass matrix
m_i	particle mass, $[kg]$
μ	fluid shear viscosity, [Pa·s]
M	Mach number, [-]
M_k	generic particle mass, [kg]
N	number of particles, [-]
N_i	number of interactions, [-]
ν	fluid kinematic viscosity, [m^2/s]
ν_d	Poisson's ratio of the drained elastic solid, [-]
n	porosity, [-]
Ω	Full domain of the two-phase problem, [m^3]
Ω_i	Domain defined by tetrahedron i, [m^3]
Ω_{ij}	union of tetrahedra (S_{ij}, P_i) and (S_{ij}, P_j), [m^3]
ω_i	particle rotational velocity, [m/s]
$\dot{\omega}_i$	particle rotational acceleration, [m/s^2]
ϕ_c	intergranular friction angle

p^a	absolute fluid pressure, [Pa]
p_i	fluid pressure in tetrahedra i, [Pa]
P_i	Voronoi weighted center of tetrahedra i
P	mean stress, [Pa]
p	piezometric fluid pressure, [Pa]
q	specific discharge vector, [m/s]
q_{ij}	flux through facet ij, [m^3/s]
Q	volumetric flow rate, [m^3/s]
$\mathbf{Q_q}$	vector of source terms
$\mathbf{Q_p}$	vector of imposed pressures
R^h_{ij}	hydraulic radius of a throat, [m]
$R^{[k]}$	radius of particle k, [m]
ρ	bulk mass density, [kg/m^3]
ρ_s	solid mass density, [kg/m^3]
ρ_f	fluid mass density, [kg/m^3]
ρ^f	fluid mass density, [kg/m^3]
Re	Reynolds number, [-]
R_i	particle radius, [m]
$\underline{\underline{\sigma}}$	total stress tensor, [Pa]
$\underline{\underline{\sigma}}'$	effective stress tensor, [Pa]
$\mathbf{s}$	deviatoric component of $\underline{\underline{\sigma}}$, [Pa]
$\mathbf{S}$	Global matrix of local geometries
S_{TV}	surface of D_{TV}, [m^2]
S_{ij}	surface of the facet ij, separating tetrahedra i and j, [m^2]
S_t	Stokes number, [-]
Σ	fluid stress, [Pa]
τ_V	particle relaxation time, [s]
τ_F	flow field characteristic time, [s]
t_l	tortuosity, [-]
t	time, [s]
T	total time costfor DEM-PFV calculation, [s]
T_{DEM}	total time cost for DEM calculation, [s]
T_{PFV}	total time cost for PFV calculation, [s]
t_c	characteristic time of consolidation, [s]
$\mathbf{T_N}$	Natural period , [s]
T_v	dimensionless consolidation time
Θ	Part of Ω occupied by the fluid phase (pore space), [m^3]
Θ_i	Part of Ω_i occupied by the fluid phase (pore), [m^3]
Θ_{ij}	part of Ω_{ij} occupied by the fluid phase (throat), [m^3]
$\mathbf{T}$	deviatoric component of fluid stress, [Pa]
U^n	intergranular distance, [m]
$\mathbf{u}$	fluid velocity, [m/s]
V_k	generic particle volume, [m^3]
V	velocity head (fluid), [m]
V_i	particle volume, [m^3]

V_i^f	fluid volume in pore i, [m^3]
V_p	poral fluid velocity, [m/s]
V_R	relative source/medium velocity, [m/s]
$\mathbf{v}$	pore contour velocity, [m/s]
$\mathbf{V}$	Global viscosity matrix
V_v	total void volume, [m^3]
V	total volume, [m^3]
$\mathbf{W}$	vector of particles weigths
$\mathbf{dX}$	solid generic displacement vector, [m]
∂X	contour of domain X, [m]
$\partial^s X$	part of contour of X intersecting (or in contact with) the solid phase, [m]
$x_i^{[w]}$	cartesian coordinates of the center of wall w, [m]
$x_i^{[k]}$	cartesian coordinates of the center of mass of particle k, [m]
$x_i^{[C]}$	cartesian coordinates of the contact point, [m]
x_i	particle position, [m]
$\dot{x}_i$	particle velocity, [m/s]
$\ddot{x}_i$	particle acceleration, [m/s^2]
ζ	fluid mass content, [-]
z	elevation head (fluid), [m]

Abstract

The behaviour of multiphase materials covers a wide range of phenomena of interest to both scientists and engineers. The mechanical properties of these materials originate from all component phases, their distribution and interaction. A new coupled hydromechanical model is presented in this work, to be applied to the analysis of the hydrodynamics of saturated granular media. The model associates the discrete element method (DEM) for the solid phase, and a pore-scale finite volume (PFV) formulation of the flow problem. The emphasis of this model is, on one hand, the microscopic description of the interaction between phases, with the determination of the forces applied on solid particles by the fluid; on the other hand, the model involves affordable computational costs, that allow the simulation of thousands of particles in three dimensional models. The medium is assumed to be saturated of an incompressible fluid. Pore bodies and their connections are defined locally through a regular triangulation of the packings. The analogy of the DEM-PFV model and the classic Biot's theory of poroelasticity is discussed. The model is validated through comparison of the numerical result of a soil consolidation problem with the Terzaghi's analytical solution. An approach to analyze the hydrodynamic of a granular sediment is finally presented. The reproduction of the phenomenon of soil liquefaction is analysed and discussed.

Key words: saturated granular materials, discrete element method, finite volume, hydromechanical coupling, soil consolidation, soil liquefaction, sediment hydrodynamics

Résumé

Le comportement des matériaux multiphasiques couvre une multitude de phénomènes qui suscitent un grand intérêt dans le domaine scientifique et professionnel. Les propriétés mécaniques de ces types de matériau trouvent leur origine dans les phases dont ils sont composés, leur distribution et interaction. Un nouveau modèle hydrodynamique couplé est présenté dans ce travail de thèse, à appliquer à l'analyse de l'hydrodynamique des milieux granulaires saturés. Le modèle associe la méthode des éléments discrets (DEM) pour la modélisation de la phase solide, avec une formulation en volumes finis, à l'échelle des pores (PFV), du problème de l'écoulement. Une importance particulière est donné à la description de l'interaction entre les phases, avec la détermination des forces fluides à appliquer sur chacune des particule, tout en assurant un coût de calcul abordable, qui permet la modélisation de plusieurs milliers des particules en trois dimensions. Le milieux est considéré saturé par un fluide incompressible. Les pores et leur connectivité est basée sur une triangulation régulière des assemblages. L'analogie de cette formulation avec la théorie classique de Biot est présenté. Le modèle est validé par la comparaison des résultats numériques obtenus pour un problème de consolidation d'un sol granulaire avec la solution analytique de Terzaghi. Une approche pour analyser l'hydrodynamique d'un sédiment granulaire est finalement présenté. La reproduction du phénomène de liquéfaction d'un sol est également présentée.

Mots clés: matériaux granulaires saturés, méthode des éléments discrets, volumes finis, couplage hydromécanique, consolidation, liquéfaction, hydrodynamique sédimentaire

General Introduction

The behaviour of multiphase materials covers a wide range of phenomena of interest to both scientists and engineers. The mechanical properties of these materials originate from all component phases, their distribution and interaction. Ideally, to test each single phase would be of significative importance for understanding and controlling the mechanical behaviour of the bulk multiphase material. However, although modern technologies allow the observation of these materials at a very small scale and the identification of each phase distribution and texture, it is generally difficult to characterize the relation between microscopical and macroscopical experimental evidences.

Among the existing multiphase materials, of various nature, the study of the behaviour of pulverulent materials is central in sciences like solid mechanics, soil mechanics, and branches of physical and chemical engineering. Topics as the geometry of the packing of particles, size measurement, sieving and grading, as well as electrical, optical, sonic, surface properties of particles, etc. constitute the basis of those disciplines. A solid, a liquid and a gaseous phase are usually recognized in multiphase pulverulent materials. They may reduce to the first two as long as the gaseous phase may be seen as a liquid phase of specified properties. In the survey which follows, we consider the applications which relate to the hydromechanical interaction between the solid and the liquid phases, with a special regard to soil mechanics applications. Within this framework, fluid-solid interactions characterize in fact many important phenomena and influence heavily humans living and activities. Processes like internal or external erosion, earth works or foundations instability, swelling/shrinkage of porous materials associated to a variation of the water content, etc. are few examples of classical hydromechanical problems, which involve complex issues to be addressed on the basis of fluid and granular solid mechanics theories.

Parallely to the evolution of optical and tomographic technologies, upon the last decades, which have been giving access to detailed informations about the structure and the behaviour of complex systems, new powerful and efficient numerical tools have been developed to interprete, analyse and predict their behaviour. In such context it become clearer how the scale at which scientists observe and try to describe the physics of such systems gets smaller down to the microscopic scale, at the interfaces where phases interact between each other, to later recover by upscaling processes the macroscopic behaviour.

The discrete element method (DEM) is one of those numerical tools which is experiencing a widespread success among the scientific communities. The DEM provides a relevant framework in modelling the behaviour of granular materials. Based on the modelling of particles interaction, it allows the reproduction of the behaviour of either purely frictional materials [22] and multiphase materials [90] [38] [81] by defining small microscopical laws.

In this work, we will propose the coupling of the DEM with a flow model, in which the viscous flow equations will be upscaled at the pore level, then approximated with a finite volume numerical scheme. The discrete nature of the DEM is preserved by such modelling. The exceptional advantage of such coupling strategy comes from the possibility of handling each single phase and access a high number of informations that would be unaccessible experimentally, and as such are often neglected in phenomenological macroscopic hydromechnical models.

Modelling the pore flow at the scale of pores and particles allows the definition of the interaction of each single particle with the fluid surrounding it. This is generally the case for all flow models based on a fine discretization of the pore space, providing a solution in terms of fluid pressure at the particles contour. The aim of the model we are proposing is to provide a per-particle definition of the fluid forces that result from pore flow, by reducing the number of degrees of freedom related to the flow problem to a minimum, by doing the hypothesis of pore-wise constant pressure, finally ensuring good performances for a detailed description of fluid-particles interactions.

The existing numerical models for the study of fluid-structure interaction (FSI) problems, are based on a coupling strategy that uses to be defined *monolithic* or *partitioned*, depending on how the numerical problem is formulated and resolved. In the monolithic approach, the flow equations and structural equations are solved simultaneously such that their mutual influence can be taken into account directly. On the other hand, the partitioned approach is based on separately solving of the flow equations and the structural equations which means that the flow does not change while the solution of the structural equations is calculated and viceversa. The partitioned approach thus requires a coupling algorithm to allow for the interaction and to determine the solution of the coupled problem, but software modularity is preserved and different, possibly more efficient, solution techniques can be used for the flow equations and structural equations [32].

The DEM-PFV ("Pore-scale Finite Volume") coupled model follows a partitioned approach. The resolution of the elastic-plastic problem at particle interactions and of the flow problem are indeed independent and will be treated separately. The PFV-DEM model will be applied to the analysis of the interaction between fluid flow and internal deformation in coastal sediments.

This thesis is organized in six chapters grouped in three parts.

The **part 1** introduces primarly the reader to the physics and mechanics of porous media. The governing equations for the description of pore flow are presented, focusing on those aspects that consitute the basis of the PFV model. A second chapter concerns the numerical modelling in the framework of saturated porous media. The discrete element method, the main hypothesis and the resolution scheme, are presented. A third and last chapter briefly present the existing families of coupled DEM-flow model, to give an insight into this subject, and properly introduce the following part.

The **part 2** concerns the description of the DEM-PFV coupled model, organized in three chapters. A first one (chapter 3) presents the details of the PFV model, and its validation by some comparison with small scale FEM simulations. A second one (chapter

4) is related to the coupling with the DEM, and the validation by the simulation of an oedometer test. The last chapter (chapter 5) focuses on some numerical aspects, on model performances and possible optimizations.

The **part 3** presents the application of the model to the analysis of a granular sediment hydrodynamics. The consequences of the action of sea waves on the stability of the seafloor, the influence of initial state conditions such as porosity and the relation existing between the period of wave loading and the characteristic time of consolidation of the packing will be presented and discussed.

This study is part of the Hydro-Fond[1] project ("Hydromécanique des Géomatériaux de Fondation Immergés").

[1]Realised with the support of the Department of Ecology, of the sustainable development, transports and housing, general direction of substructures, transports, and the sea,within the C2D2 program of RGCU.

Part I

Literature Review

Chapter 1

Physics and mechanics of porous media

The study of the physics of flow through porous media is at the base of many disciplines as soil mechanics, ground water hydrology, petroleum engineering, industrial filtration, powder metallurgy, etc. Although practical hydraulics has its origins in antiquity, scientific attention to flow relative to particulate media began one hundred years ago. Among the numerous contributions to this field, particular consideration should be given to the work of C.-L. Navier (1785-1836) who, together with sir G.G. Stokes (1819-1903), is credited with the formulation of the equations of motion used in hydrodynamics (see section 1.2.1); J.L.M. Poiseuille (1799-1869), whose careful experiments on laminar flow established the law which bears his name (presented in section 1.2.1) [77]; J.W.S. Rayleigh (1842-1919), who investigated many aspects of hydrodynamics, including energy dissipation [80]; J.V. Boussinesq (1842-1929), who made comprehensive mathematical treatment of laminar flow in pipes and channels.

Studies of flow through porous media first engaged the attention of several engineers of the famous *Corps des Ponts et Chaussées* during the second half of the nineteenth century. The contribution by Henry P.G. Darcy (1803-1858), as the director of public works of the city of Dijon, in charge of the design and execution of a municipal water supply system, encountered a great success and gave rise to a series of researches which he conducted on the flow of water through sand bed filters [31]. The law which Darcy discovered, namely, that the rate of flow is proportional to pressure drop through a bed of fine particles, bears his name (section 1.2.2). It is widely employed for investigating the behaviour of all types of water flow through porous media, such as underground flow to wells, flow in soils and permeability of dam foundations. The flow of oil in underground structures has been found to follow Darcy's law as well, and a unit of permeability designated as *darcy* is quite generally used in the oil industry today. A.J.E.J. Dupuit (1804-1866) and H.E. Bazin (1829-1917) continued Darcy's work after his death, and published his researches on the movement of running water in open canals, and on transportation and distribution of water [34]. In particular, Dupuit made the first comments on the capacity of a flow stream to transport sedimentary particles in suspension, inspiring the successive works regarding the transport of sediment by rivers.

One of the main contributions to the formulation of a permeability equation is attributed to C.S. Slichter, who was led to a study of sphere arrangements in order to reduce the hydraulics of a complex soil to an idealized system [93]. One of the main assumptions of his treatment was that the average cross-sectional area for flow would be triangular,

across which the flow could be considered as laminar and be described by Poiseuille's law. Although his oversimplified assumptions, his work inspired many subsequent studies. F.C. Blake suggested the use of the empirical hydraulic radius concept for the prediction of resistance to flow through porous media [14]. His intuition was that flow in a packed bed can be seen as a collection of various noncircular conduits which can be brought into agreement with that of circular pipes by dividing the interstitial fluid volume by the wetted packing area. J. Kozeny (1927) and P.C. Carman (1937) extended his treatment, finally defining a semiempirical equation now widely used to correlate date for flow through packed beds [54] [55].

The interest in understanding the microscopical origin of experimental evidences constitutes an objective that evolves rapidly as technologic breakthroughs allow to access new informations. At the same time, engineering technical practices evolves by adopting the new tools which integrate new knowledge and are usually more efficient thanks to the monotonically increasing power of calculators. The choice of following a discrete approach in modelling granular materials becomes, within such context, more and more popular in the engineering academic and industrial frameworks. On one side, analyzing the behaviour of granular materials through the description of the material discontinuities that characterize such media at the phases interface demands very few parameters, compared to constitutive models which are at the base of continuum-based modelling. Furthermore, following a purely micromechanical approach, the physics and the mechanics at such scale have to interpreted and important phenomena, whose nature is in fact micromechanical, may be observed. Parameters that for practical reasons are unaccessible experimentally, become accessible through discrete modelling.

Various approaches have been attempted in order to model the hydromechanical coupled behaviour of porous media. At the microscopic (sub-pore) scale, the solid and fluid phases occupy different portions of the spatial domain and interact at their common interface. Thus, the microscopic fields which describe the properties of constituents may be considered as continua within a single phase, while exhibit discontinuities at the interfaces between phases. In saturated porous media, the state of stress in a material point of the partial solid consists of two parts, the weighted liquid pressure and the so-called *effective stress* for which a constitutive equation must be formulated as a function of the respective state of the solid deformation. Only the effective stress is assumed to describe the strength of the partial solid. In the theory of porous media, the separation of the total stress into the effective stress and the weighted liquid pressure is founded on the basic assumption of the incompressibility of both constituents, i.e. liquid and solid materials. This is a reasonable assumption since liquids are in general incompressible and since the compressibility of the solid material can be neglected in comparison with the compressibility of the whole porous body.

Skempton,[1] in a paper titled *"Significance of Terzaghi's Concept of Effective Stress"* [92], stated:

[1] A Skempton's paper extract is reported, as De Boer did [15], while observing how the effective stress concept, generally attributed to Karl von Terzaghi, finds in fact its origin in a former study on the theory of water-filled porous media by Paul Fillunger (1883-1937), in which the austrian scientist states that the porewater pressure has no influence on the strength of the solid skeleton.

> *"The principle of effective stress has been stated by Terzaghi in the following terms: the stresses in any point of a section through a mass of soil can be computed from the total principal stresses σ_1, σ_2, σ_3 which act in this point. If the voids of the soil are filled with water under a stress u, the total principal stresses consist of two parts. One part, u, acts in the water and in the solid in every direction with equal intensity. It is called the neutral stress (or the porewater pressure). The balance $\sigma_1' = \sigma_1 - u$, $\sigma_2' = \sigma_2 - u$, $\sigma_3' = \sigma_3 - u$ represents an excess over the neutral stress u and it has its seat exclusively in the solid phase of the soil. This fraction of the total principal stresses will be called effective principal stresses [..] A change in the neutral stress u produces practically no volume change and has practically no influence on the stress conditions for failure. [..] Porous materials (such as sand, clay and concrete) react to a change of u as if they were incompressible and as if their internal friction were equal to zero. All the measurable effects of a change of stress, such as compression, distortion and a change of shearing resistance are exclusively due to changes in the effective stresses σ_1', σ_2', σ_3'. Hence every investigation of the stability of a saturated body of soil requires the knowledge of both the total and the neutral stresses."*

Karl von Terzaghi (1883-1963) was the first author to treat a deformable porous solid with an inviscid liquid, namely water-saturated clay. After a long period of experimental and theoretical investigations he succeeded in describing this problem and in 1923 he published his partial differential equation for the description of the consolidation problem [95], well-known in soil mechanics. Internationally well-known is the work of Maurice Biot (1905-1985), who continued Karl von Terzaghi's concept, namely the treatment of the fluid-saturated porous solid as one body, whereby the coupling terms were introduced separately. In 1935, Maurice Biot started his enormous work on porous media. He adopted Karl von Terzaghi's ideas and extended the one-dimensional consolidation theory to the three-dimensional case for linear elastic porous solids and inviscid liquids. In the mid 1950s, Biot [12] returned to his research on porous media and extended his previous considerations to the more general cases of viscoelastic anisotropic porous solids. In a final paper [13] he summarized all his basic findings on saturated porous media. Obviously, he was of the opinion that the development of the basic equations of the porous media theory had been brought to an end.

1.1 Physics of porous media

Studying the hydrodynamics of a porous media, one should primarly focus on the physical and mechanical properties of each component. These are on one hand the solid skeleton, which characterizes the intrinsic structure of the porous media, and on the other hand the fluids which are flowing within it. The analysis of the interaction between the solid and the fluid phases, in static and dynamic conditions, is one step further to a complete description of such complex material.

Porous media can be assumed as solid bodies having pores (see fig.1.1). Pores are void spaces frequently distributed through the material, whose size is somewhere intermediate between extremely small voids, present in solid at the scale of its molecules, and

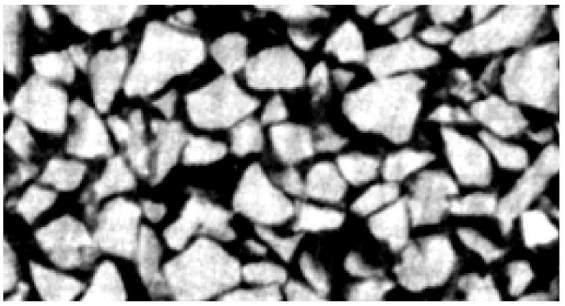

Figure 1.1: Internal structure of sand [4]

very large ones, which may be called "caverns" [85]. Pores in a porous system may be interconnected or non-interconnected. The interconnected part of the pore space, where flow of interstitial fluid is possible, is the *effective pore space* of the porous medium.

By these definitions, it's deducible how the term "porous media" includes a wide variety of natural and artificial materials, of geological (soils and rocks), composite (concrete) or biological (bones, tissues) nature. Generally a porous medium is characterized by a variety of geometrical properties. A classification would be possible by considering the size of the pores that characterize the medium, and how they influence the local hydrodynamic phenomena. Pore spaces may also be classified according to whether they are ordered or disordered, dispersed or connected [85].

1.1.1 Geometrical properties of porous media

The character of porous media is disorder rather than order, and one ought to take this into account in attempting any model representation. The *porosity*, defined as the fraction of void to total volume, is of primary importance in the characterization and classification of a porous medium.

$$n = \frac{V_v}{V} \quad [-] \tag{1.1}$$

Another geometrical quantity of a porous medium is its *specific internal area*, defined as the ratio of internal area to bulk volume and expressed as a reciprocal length. Its value is greater for a fine-graded than for a coarse-graded medium, the behaviour of the former being governed by body forces whereas surface forces govern the behaviour of the latter. It is often expressed in [m^2/g] units. For a generic solid particle, named A_k its surface, V_k its volume and M_k its mass, it can be defined as follows:

$$S = \frac{A_k}{V_k} \quad [\mathrm{m}^{-1}] \quad or \quad S = \frac{A_k}{M_k} \quad [\mathrm{m}^2/\mathrm{g}] \tag{1.2}$$

A third geometrical property which is often employed is *tortuosity*, defined as a geometrical property equal to the relative average length of the flow path l_c of a fluide particle from one side of the porous medium to the other. It is a dimensionless quantity.

$$t_l = \frac{l_c}{l} \quad [-] \tag{1.3}$$

Being generally impracticable to measure the size of the pores inside the medium, correlations can be established between the particles and pores size distribution. In order to do that, one has to know something about the packing of the particles as well as about their shape. By the way, for even if the particle size is known, the shape is still not determined. Thus, to be able to construct proper models, according to Scheidegger [85], one may investigates the modes of packing of spheres assemblies, which allows a qualitative visualization of the conditions involved. Obviously, natural materials deviate appreciably from that of spheres. Then, correlations between particle sizes and pore sizes are based on experimental investigations rather on the theory, and still, a true understanding of such aspect cannot be obtained in this manner either. A proper characterization of geometrical properties of porous media can be achieved only by the use of statistical methods.

1.1.2 Scale of observation

Numerical modelling in engineering is generally based on governing equations which are *locally* derived, over the so-called *Representative Elementary Volume* (REV), and then integrated over a domain of finite dimensions. From a mathematical point of view, the REV is represented by an infinitesimal volume $d\Omega$, whereas from a physical point of view, such volume element has a finite dimension h, such that it can be considered as a homogenous continuum [20]. The length of such dimension h depends on the scale of observation which characterizes the problem one wants to study.

According to a *macroscopic* approach, any quantity that appears in the mechanical description of a complex, structured materials is taken to be averaged over the above stated length scale, which is assumed to be large with respect to the microstructure heterogeneities (i.e. the typical dimension of the pores or solid particles), yet small enough to allow the introduction of genuine macroscopic scale material heteorgeneity. Otherwise, the modelling approach may be based at a *mesoscopic* scale, then at the scale of soil strata, or fracture spacing in rocks, in case of geomaterials modelling, or at a *microscopic* scale, which would be represented by the dimension of clay patricles or sand grains, clasts or schists.

1.2 The description of pore flow

1.2.1 Governing Equations

Navier-Stokes equations

The Navier-Stokes equations, named after Claude-Louis Navier (1785-1836) and George Gabriel Stokes (1819-1903), describe the generic motion of fluids. These equations were obtained by application of the Newton's second law, together with the assumption that the fluid stress is the sum of a diffusing viscous term (proportional to the gradient of velocity) and an isotropic pressure term.

The equation of continuity is obtained by applying the law of conservation of mass to a small stationary volume element within a flowing fluid. In vector form it may be written as:

$$\frac{\partial \rho_f}{\partial t} = -\nabla \cdot (\rho_f \mathbf{u}) \tag{1.4}$$

where ρ_f is the local density of the fluid, $\mathbf{u}$ is the local fluid velocity, and $\frac{\partial}{\partial t}$ refers to the time rate of change at a fixed point in the fluid. The vector $\rho_f \mathbf{u}$ is the mass flux density, its divergence expressing the net rate of mass flux per unit volume. Thus, eq.(1.4) states that the rate of increase of density in a differential volume element fixed in space is equal to the net rate of mass influx into the element divided by its volume. In case of incompressible fluids (constant ρ_f), the continuity equation reduces to:

$$\nabla \cdot \mathbf{u} = 0 \tag{1.5}$$

We consider next the equation of linear momentum, that can be obtained by application of the Newton's law of motion to a differential volume of fluid, according to which the external forces exerted by the surroundings on a stationary domain are equal to time rate at which momentum is being created within the domain. Thus, we have:

$$\frac{\partial(\rho_f \mathbf{u})}{\partial t} + \nabla(\rho_f \mathbf{u} \otimes \mathbf{u}) = \nabla \cdot \Pi + \rho_f \mathbf{f}^{\mathbf{V}} \tag{1.6}$$

where the first term represents the rate of increase of momentum per unit volume, the second term the rate of momentum loss by convection through the surface, per unit volume; the right-hand terms represent the external forces, exterted by the fluid stresses (stress tensor Π) over the surface of the element (third element), and volume or body forces exerted on the element (fourth term). The stress tensor Π can be decomposed in its isotropic and deviatoric components, as follows:

$$\Pi = -p\mathbf{I} + \mathbf{T} \tag{1.7}$$

and can be rewritten, using the theory of newtonian fluids, as follows:

$$\Pi = -p\mathbf{I} + \kappa_b(\nabla \cdot \mathbf{u})\mathbf{I} + 2\mu D^d \tag{1.8}$$

where p is the hydrostatic pressure, $\mathbf{I}$ the identity tensor, κ_b is the bulk or volume viscosity, μ the shear viscosity and $D^d = \frac{1}{2}[\nabla\mathbf{u} + (\nabla\mathbf{u})^T] - \frac{1}{3}\mathbf{I}(\nabla \cdot \mathbf{u})$, the deviatoric strain rate tensor. The bulk viscosity coefficient relates the stress to volumetric strain rate. The bulk viscosity is important in the case of fluids subjected to rapidly varying forces such as those caused by ultrasonic vibrations. This term will be henceforth neglected.

For constant density ρ_f, thus in case of incompressible fluids ($\nabla \cdot \mathbf{u} = 0$) and constant viscosity μ, we end up with one form of the Navier-Stokes equation, derived by Navier in 1827:

$$\rho_f \left(\frac{\partial \mathbf{u}}{\partial t} + grad\mathbf{u} \cdot \mathbf{u} \right) = -\nabla p + \mu \nabla^2 \mathbf{u} + \rho_f \mathbf{f}^{\mathbf{V}} \tag{1.9}$$

Flow regimes

The solution of the complete Navier-Stokes equations is highly tricky. In order to formulate a tractable mathematical model for a flow system, a number of simplifications are generally introduced. The flow motion can be *turbulent* or *laminar*. In the turbulent regime, dependent variables such as velocity and pressure are not unique functions of space and time coordinates, but must be described by stochastic laws. Although the time-independent forms of the equations of continuity (1.4) and motion (1.9) presumably

apply, their solution for instantaneous velocities and pressures are not possible. Then, various approximation schemes must be invoked. Generally, the hypothesis of *laminar* flow is adopted when the velocity of the fluid is sufficiently slow and viscous effects are dominant over the inertial effects. In this case, each fluid particle follows a path without interfering with other particles and their trajectories.

The mathematical treatment is greatly simplified by this assumption. A dimensionless parameter which determines the relative importance of viscous and inertial effects for a fluid flow is the Reynolds number:

$$Re = \frac{\rho_f \mathbf{u} \cdot \nabla \mathbf{u}}{\mu \nabla^2 \mathbf{u}} \simeq \frac{U L}{\nu} \tag{1.10}$$

where ρ_f is the fluid density, $\mathbf{u}$ its velocity, L a characteristic lenght describing the problem, often equal to the diameter d_T of the throat, U a characteristic fluid velocity, μ and ν are the fluid absolute and kinematic viscosity, respectively ($\nu = \mu/\rho_f$). Situations in which the Reynolds number is small are called *slow viscous flows*, because viscous forces arising from shearing motions of the fluid predominate over inertial forces associated with acceleration or deceleration of fluid particles.

For the cases of interest in our work, the Reynolds number is low enough to assume the flow as laminar. As an example, we could quantify some representative parameter to assess its order of magnitude. In the last chapter we will describe the analysis of the hydrodynamics of a granular seabed, reproducing numerically some laboratory experiment performed in LEGI laboratory [2]. A relatively high permeable medium ($K_d \simeq 10^{-3}$ m/s) is subjected to the action of a stationary wave of specified amplitude of oscillation and wavelength, ensuring a gradient of hydraulic charge $\nabla H \simeq 10^{-2}$. Then, the velocity of the fluid is of the order of magnitude of 10^{-5} m/s. Assuming $L = d_{av} \simeq 0.001$ m in eq.(1.10), with d_{av} the average diameter of the particles employed in the laboratory experiments, and the kinematic viscosity of water, $\nu = 10^{-6}$ m^2/s, the Reynolds number is of the order of magnitude of 10^{-8}, thus justifying the hypothesis of laminar flow which will be assumed in our model.

Stokes flow

In multiphase systems, a dimensionless number that describes the behaviour of particles suspended in a fluid flow is the Stokes number, defined as follows:

$$S_t = \frac{\tau_V}{\tau_F} \tag{1.11}$$

where τ_V is the relaxation time of the particle and τ_F is some time characteristic of the flow field, the characteristic time d_T/U of the flow through a venturi for example, where d_T is the throat diameter, and U a chracteristic fluid velocity. The Stokes number then becomes:

$$S_t = \frac{\tau_V U}{d} \tag{1.12}$$

[2]The Laboratory of Geophysical and Industrial Flows (LEGI) is a public research laboratory of the University of Grenoble. It is a joint research unit common to the National Center for Scientific Research (CNRS), Université Joseph Fourier (UJF) and Institut National Polytechnique de Grenoble (Grenoble INP)s.

If $S_t << 1$, the response time of the particles is much less than the characteristic time associated with the flow field. The particle will have ample time to respond to changes in flow velocity, thus the particle and fluid velocities will be nearly equal (velocity equilibrium). On the other hand, if $S_t >> 1$, then the particle will have essentially no time to respond to the fluid velocity change and the particle velocity will be little affected during its passage through the venturi.

In case of steady motion of an incompressible fluid, which is the case of interest in our study, the inertial term $\rho_f \mathbf{u} \cdot \nabla \mathbf{u}$ can be neglected if compared to the viscous term $\mu \nabla^2 \mathbf{u}$ (low Reynolds number and high Stokes number, according to eq.s (1.10), (1.12)). Navier-Stokes equations (1.9), reduce to the so-called creeping motion or Stokes equations:

$$\nabla p = \mu \nabla^2 \mathbf{u} \quad (Re << 1) \tag{1.13}$$

$$\nabla \cdot \mathbf{u} = 0 \quad (S_t >> 1) \tag{1.14}$$

When applicable, the neglect of the quadratic inertial terms constitutes a very substantial simplification, since the equations are now linear.

In presence of a potential field Φ (i.e. gravitational field), the piezometric pressure p is related to the absolute pressure p^a by the following relation:

$$p = p^a - \rho_f \Phi \tag{1.15}$$

Stokes equation becomes:

$$\nabla p = \mu \nabla^2 \mathbf{u} - \rho_f \nabla \Phi \tag{1.16}$$

Mach number

The Mach number is named after Austrian physicist and philosopher Ernst Mach (1838-1916). In fluid mechanics, Mach number (Ma or M) is the speed of an object moving through air, or any other fluid substance, divided by the speed of sound as it is in that substance for its particular physical conditions (temperature and pressure). It is commonly used to represent the speed of an object when it is travelling close to or above the speed of sound.

$$M = \frac{V_R}{c} \tag{1.17}$$

where V_R is the velocity of the source relative to the medium and c the speed of sound in the medium. Another application of this dimensionless ratio is to determine if a flow can be treated as an incompressible flow. If $M < 0.2 - 0.3$ and the flow is (quasi) steady and isothermal, the flow can be assumed as incompressible and a simplified incompressible flow model can be used.

As already done for the Reynolds number, we can give an assessment of the Mach number characterizing the experiences we will present in this work. Taking a velocity (estimated above) $V_R \simeq 10^{-5}$ m/s, the speed of sound in the water being $c_w = 1480$ m/s, the Mach number is of the order of magnitude of 10^{-8}, thus justifying the hypothesis of incompressible flow which is at the base of our modelling.

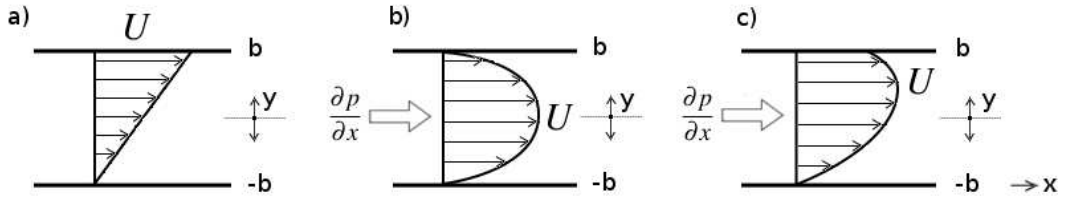

Figure 1.2: a) Couette flow. b) Poiseuille flow. c) Combined flow.

Parallel shear flows

Let's consider a simple class of flows of a viscous fluid having only x component u of velocity $\mathbf{u}$:

$$\mathbf{u} = (u(y,z,t),0,0) \tag{1.18}$$

This is called *parallel shear flow*, or *unidirectional flow* [50]. In this type of flow, the convection term vanishes identically since $(\mathbf{u}\cdot\nabla\mathbf{u} = u\,\partial_x u = 0$. Without external forces, the x, y, z components of Navier-Stokes equations (1.9) reduce to:

$$\frac{\partial u}{\partial t} - \mu\frac{\partial^2 u}{\partial y^2} = -\frac{1}{\rho_f}\frac{\partial p}{\partial x} \tag{1.19}$$

$$\frac{\partial p}{\partial y} = 0 \tag{1.20}$$

The pressure is then function of x and t, $p = p(x,t)$. The left-hand side of eq.(1.19) depends on y,z,t, while the right-hand side depends on x,t. Therefore, the equality states that both sides should be a function of t only for the consistency of the equation.
In steady flows, we have $\partial_t u = 0$ and $\partial_x p = cst$. Eq.(1.19) reduces to:

$$\frac{\partial^2 u}{\partial y^2} = \frac{1}{\mu}\frac{\partial p}{\partial x} \tag{1.21}$$

The acceleration of a fluid particle vanishes identically in steady unidirectional flows, hence the density does not make its appearance explicitely. A solution $u = u(y,z)$ satisfying eq.(1.21) is in fact an exact solution of the incompressible Navier-Stokes equation. Some of such solutions are as follows (see fig.1.2 for the meaning of parameters):

$$u_C(y) = \frac{U}{2b}(y+b), \quad \frac{\partial p}{\partial x} = 0, (\mid y \mid < b) \text{ : Couette flow} \tag{1.22}$$

$$u_P(y) = \frac{1}{2\mu}\frac{dp}{dx}(b^2 - y^2), \quad \frac{\partial p}{\partial x} \neq 0, (\mid y \mid < b) \text{ : Poiseuille flow} \tag{1.23}$$

Eq.(1.22) represents the flow between a fixed plate at $y = -b$ and a plate at $y = b$ moving with velocity U in the x direction where there is no pressure gradient, known as Couette flow (fig.1.2).

Hagen-Poiseuille flow Eq.(1.23) describes a flow between two parallel walls at $y \pm b$ under a constant pressure gradient, known as *plane Poiseuille flow*. As we've just seen in last paragraph, dp/dx is a constant along the pipe length for steady state conditions. It may be written as $\Delta p/L$ where $\Delta p > 0$ is the difference of piezometric pressure between the ends of the pipe and L is its length. End effects are neglected. The maximum velocity U is attained at the center $y = 0$, given by:

$$U = \frac{\Delta p}{2\mu L} b^2 \tag{1.24}$$

Eq. (1.24) describes a flow with a parabolic distribution. The volumetric flow rate per unit width of gap in a lateral direction is obtained by integration, giving:

$$Q = \frac{2\Delta p}{3\mu L} b^3 \tag{1.25}$$

For a pipe of circular section (radius R_1), eq.s (1.24) and (1.25) are replaced by the so-called *Hagen-Poiseuille* flow:

$$u(r) = \frac{\Delta p}{4\mu L}(R_1^2 - r^2) \tag{1.26}$$

$$Q = 2\pi \int_0^{R_1} r\,u\,dr = \frac{\pi R_1^4 \Delta p}{8\mu L} \tag{1.27}$$

Eq.(1.27) is known as Poiseuille's law for laminar flows.

Poiseuille's law can be generalized to polygonal-shaped pores, by using the hydraulic radius concept [88], [14]. This aspect will be resumed and discussed in the part devoted to the description of the model (section 3).

1.2.2 Flow in porous media - Macroscopical approach

Bernoulli's principle

Seepage takes place from a point, to which a certain energy can be associated, to another point of lower energy. This energy can be expressed as the sum between the kinetic energy KE, linked to the velocity of the fluid at one point, and the potential energy P, linked to the position of such point and the fluid pressure.

Considering a fluid *sample* of unitary weight, we generally refer to the hydraulic or piezometric head H to express its energy:

$$H = z + \frac{p}{\gamma_f} + \frac{V^2}{2g} \tag{1.28}$$

where:

- (z), the *elevation head*, that is, potential energy per unit weight of the water;
- (p/γ_f), the *pressure head*, representing the pressure energy per unit weight of a fluid of specific weight γ_f at that point.

- $(V^2/2g)$, the *velocity head* ($V^2 = u^2 + v^2 + w^2$) expressing the energy of a fluid linked to its velocity V (g = gravity acceleration).

In the case of an incompressible and inviscid fluid in a steady irrotational motion (or a compressible flow at low Mach numbers), only subjected to the gravitational acceleration, the Bernoulli's principle states that the total hydraulic head H is constant along a given fluid particle trajectory:

$$z_A + \frac{p_A}{\gamma_f} + \frac{V_A^2}{2g} = z_B + \frac{p_B}{\gamma_f} + \frac{V_B^2}{2g} \tag{1.29}$$

Equation (1.29) is known as Bernoulli's principle.

The difference ΔH between two points represents a measure of the energy that is dissipated as an effect of the flow in the porous medium. The ratio between the hydraulic head difference ΔH and the length L of the consequent flow path defines the *hydraulic gradient i*:

$$i = \frac{\Delta H}{L} \quad [-] \tag{1.30}$$

Darcy's law

In 1856, Henry Darcy investigated the flow of water in vertical homogeneous sand filters in connection with the fountains of the city of Dijon (France). From his experiments, Darcy concluded that the rate of flow, Q, is proportional to the cross sectional area A and the gradient of hydraulic charge, defined in eq.(1.30). When combined, these conditions give the famous Darcy's law:

$$\mathbf{q} = \frac{\kappa}{\mu} \nabla H \tag{1.31}$$

where $\mathbf{q}$ is the specific discharge, expressed in m/s, ∇H is the hydraulic gradient and κ is the permeability expressed in m^2. The loss of piezometric head is due to friction in the flow through the narrow tortuous paths of the porous medium. Actually, in Darcy's law, the kinetic energy of the water is neglected as, in general, changes in the piezometric head along the flow path are much larger than changes in the kinetic energy.

It is worth noticing that the intrinsic permeability of a porous medium, that we call κ, expresses the capacity of a medium to trasmit a fluid, and is generally expressed in surface units [m^2]. Being an intrinsic property of the medium, it's a fluid-independent characteristic. The hydraulic conductivity as it appears in Darcy's law, is linked to κ by the following relation:

$$\kappa = K_d \frac{\mu}{\gamma_f} \tag{1.32}$$

where μ is the viscosity of the fluid.

Considering the high heterogeneity of cross sections shape within a porous media, Darcy's law can be seen a statistical representation of flow conditions within such medium. The velocity that can be computed using eq.(1.31), is an *apparent* velocity of the fluid, lower than the effective velocity of interstitial fluid inside the pores V_p ($V_p \simeq V/n$). Furthermore, eq.(1.31) includes implicitly the effect of viscosity and internal friction, as such it allows the analysis of filtration motion without explicitely taking into account of such effects. In this sense, Darcy's law can be seen as a statistical representation equivalent to Navier-Stokes equations.

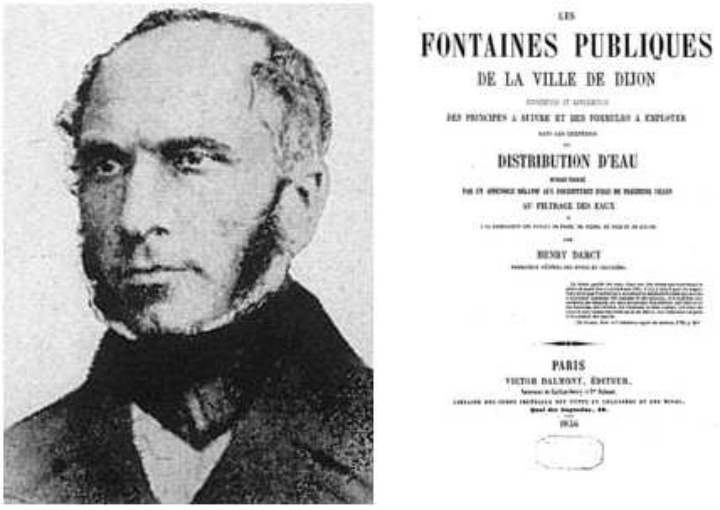

Figure 1.3: Henry P.G. Darcy (1803-1858) and the cover of his famous book.

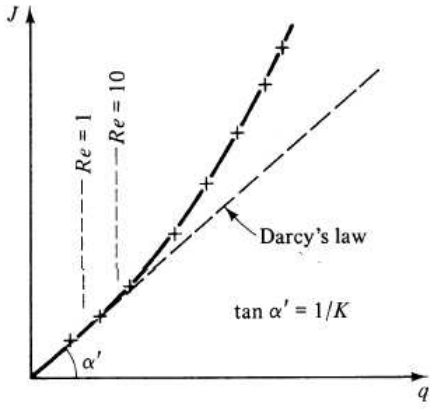

Figure 1.4: Relation specific discharge q - hydraulic gradient $J = \nabla H$ [10].

As the specific discharge increases, the relation with the hydraulic gradient deviates from the linear relationship expressed by Darcy's law (see fig.1.4), whose range of validity must therefore be discussed. By analogy with the definition of eq.(1.10), a Reynolds number may be defined also for flow through porous media:

$$Re = \frac{qd}{\nu} \tag{1.33}$$

where d is a representative length of the porous matrix, usually related to the average particle size, ν is the kinematic viscosity of the fluid. All evidence indicates that Darcy's law is valid as long as the Reynolds number does not exceed some value between 1 and 10 [10].

1.3 Hydromechanical coupling

1.3.1 Biot's theory of poroelasticity

In practical applications, the hypothesis of dry or saturated media generally holds. In the first case, pores are entirely filled by the air phase, whose influence in terms of mechanical response of the medium is completely neglected. The solid skeleton is assumed to equilibrate alone the external actions applied to the medium. In the second case, the pore space is occupied by the liquid phase. In classical continuum-based mechanics of porous media, the saturated medium is modelled as the overlap of two continua representing the solid skeleton and the liquid phase, respectively. Such operation leads to the decomposition of the stress tensor in two parts: the *effective stress* tensor σ', responsible of solid skeleton deformations, and a tensor which will be proportional to the fluid pressure, $p\mathbf{I}$.

$$\sigma = \sigma' + p\mathbf{I} \tag{1.34}$$

It follows a reciprocal influence between the fluid motion within the medium, governed by the fluid pressure field, and the mechanical response of the medium, which entails the existence of an hydro-mechanical coupled behaviour of such systems.

Such considerations inspired Terzaghi, whose one-dimensional theory of consolidation, formulated in 1923, was based on the definition of the well-known *effective stress principle* [95]. He modelled the progress of strains of a saturated clay as an effect of the gradual transfer of the load from the liquid to the solid phase, and the dissipation of the excess pore pressure as a consequence of the motion of the fluid inside the medium. Some decades later, Biot extended such theory to the three dimensional case, without the hypothesis of incompressibility of the fluid and solid phases, as in Terzaghi's theory.

The Biot model of a fluid-filled porous material is constructed on the conceptual model of fully connected solid skeleton and fluid phase. The kinematic quantities are the solid displacement vector $\mathbf{dX}$ which tracks the movement of the porous solid with respect to a reference configuration, and a specific discharge vector $\mathbf{q}$ which describes the motion of the fluid relative to the solid and can be defined as the rate of fluid volume crossing a unit area of porous solid. In the Biot model, the description of stress and strain in the fluid is limited to their isotropic component. The shear stress at the contact between fluid and solid, associated with a local velocity gradient in the fluid is not considered in his formulation.

Governing equations To construct a well-posed mathematical system for the description of the stress, pore pressure, flux and displacement in the medium, equations based on mass and momentum conservation principles need to be introduced.

Linear isotropic poroelastic processes are finally described by:

- a **constitutive equations** for the **porous solid**:

$$f(G,K,K_u,\alpha_B) : \underline{\underline{\varepsilon}} \rightarrow (\underline{\underline{\sigma}}, p) \tag{1.35}$$

  where K_u and K are the bulk moduli relative to the undrained and the drained elastic solid, G the shear modulus of the drained elastic solid, and α_B is defined as:

$$\alpha_B = 1 - K/K_s \tag{1.36}$$

where K_s is the modulus of compressibility of the solid constitutent. α_B represents the ratio of the fluid volume gained (or lost) in a material element to the volume change of that element (then $\alpha_B \leq 1$), and is known as Biot's coefficient. The small strain tensor $\underline{\underline{\varepsilon}}$ is defined as:

$$\underline{\underline{\varepsilon}} = \frac{1}{2}(\nabla \mathbf{dX} + \nabla^T \mathbf{dX}) \tag{1.37}$$

- a **constitutive equations** for the **fluid**:

$$f(G, K, K_u, \alpha_B) : \zeta \rightarrow (\underline{\underline{\sigma}}, p) \tag{1.38}$$

- Darcy's law, to describe the **fluid transport** in the interstitial space (see section 1.2.2),

$$\mathbf{q} = -K_d(\nabla p^a - \mathbf{f}) = -K_d \nabla p \tag{1.39}$$

where $\mathbf{f} = \rho_f \mathbf{g}$ is the body force per unit volume of fluid, K_d the coefficient of hydraulic conductivity, ∇p^a and ∇p the absolute and piezometric pressure gradients, respectively (see eq.(1.15));

- the **equilibrium equation**, obtained from standard considerations of static equilibrium,

$$\nabla \cdot \underline{\underline{\sigma}} = -\mathbf{F} \tag{1.40}$$

where $\mathbf{F} = \rho \mathbf{g}$ is the body force per unit volume of the bulk material, $\rho = (1 - n)\rho_s + n\rho_f$ is the bulk density, ρ_s and ρ_f are the densities of the solid and the fluid phase, respectively.

- the **continuity equation**, obtained by imposing mass conservation of a compressible fluid,

$$\frac{\partial \zeta}{\partial t} + \nabla \cdot \mathbf{q} = \gamma \tag{1.41}$$

where γ is the source density (the rate of injected fluid volume per unit volume of the porous solid).

Coupling equations

These governing equations are finally combined into field equations to give:

- a Navier-type equation for **dX**, obtained by combining the constituive equation expressed in eq.(1.35) and the continuity equation (1.40):

$$G\nabla^2 \mathbf{dX} + \frac{G}{1 - 2\nu_d} \nabla \cdot (\nabla \mathbf{dX}) = \alpha_B \nabla p - \mathbf{F} \tag{1.42}$$

where ν_d is the Poisson's ratio of the drained elastic solid and ε denotes the volumetric component of $\underline{\underline{\varepsilon}}$, defined below;

- a diffusion equation for p, obtained by combining Darcy's law (1.39), the continuity equation (1.41) and the constituive relation (1.38):

$$\frac{\partial p}{\partial t} - K_d M \nabla^2 p = -\alpha_B M \frac{\partial \varepsilon}{\partial t} \tag{1.43}$$

  where M is a fundamental constant:

$$M = \frac{K_u - K}{\alpha_B^2} \tag{1.44}$$

Constitutive equations The Biot formulation of the constitutive equations for a fluid-filled porous material is based on the assumption of linearity between the stress $(\underline{\underline{\sigma}}, p)$ and the strain $(\underline{\underline{\varepsilon}}, \zeta)$ and reversibility of the deformation process:

$$\Lambda : (\underline{\underline{\sigma}}, p) \rightarrow (\underline{\underline{\varepsilon}}, \zeta) \tag{1.45}$$

The constitutive relation for an isotropic poroelastic material can be separated into a deviatoric and a volumetric response. The deviatoric component reads:

$$\underline{\underline{e}} = \frac{1}{2G} \underline{\underline{s}} \tag{1.46}$$

where $\underline{\underline{s}}$ and $\underline{\underline{e}}$ denote the deviatoric component of $\underline{\underline{\sigma}}$ and $\underline{\underline{\varepsilon}}$. The volumetric components, defined for both the strain quantities ε and ζ, read:

$$\varepsilon = -\frac{1}{K}(P - \alpha_B p) \tag{1.47}$$

$$\zeta = -\frac{\alpha_B}{K}(P - \frac{p}{B}) \tag{1.48}$$

where:

- P is the mean stress, $P = \underline{\underline{\sigma}}_{ii}/3$;
- B is known as the Skempton pore pressure coefficient and defined as follows:

$$B = \frac{K_u - K}{\alpha_B K_u} \tag{1.49}$$

  The undrained modulus K_u can be defined from the fundamental constitutive constants of constituents:

$$K_u = K + \frac{\alpha_B K_s}{1 - \frac{n}{\alpha_B}\left(1 - \frac{K_s}{K_f}\right)} \tag{1.50}$$

  where K_f is the modul of compressibility of the fluid.

The dependence of the bulk continuum constants α_B, B, K and K_u on the porosity and compressibility of the fluid, solid and pores entails the following possible cases:

- *Highly compressible fluid constituent*: in this case the porous material behaves like an elastic material without fluid;

- *Compressible fluid constituent*: the component associated to the compression or dilation of the interstitial fluid has to be taken into account in evaluating the volumetric deformation of the porous material;
- *Incompressible solid constituent*: the compressibility of the solid phase is negligible compared to that of the drained bulk material;
- *Incompressible solid and fluid constituents* ($\alpha_B = 1$, $M \to \infty$, $B \to 1$): for this limiting situation all the poroelastic parameters assume their upper bound values.

The last case is therefore characterized by the strongest poroelastic effects. It is worth noticing that at these conditions the first term of eq.(1.43) $\partial p/\partial t$ becomes negligible. This leads to instantaneous changes of pore pressure as a response to the deformation, and long range effects of any perturbation. The solution of eq.(1.43), at such conditions, can be obtained only by implicit methods.

Chapter 2

Numerical models of saturated granular materials

2.1 The discrete element method

One possibility to obtain informations about the behaviour of granular media is to perform experiments. An alternative are simulations with the discrete element method (DEM) [29]. In this section this method will be presented in detail, trying to focus on the key aspects that contribute to make it win great success among scientists in the academic and industrial frameworks.

Among the existing discrete numerical approaches that have been developed to simulate the behaviour of granular materials, we can distinguish two families of models:

- the classical Discrete Element Method as it has been initiated by Cundall and Strack [29], in which the mechanical action between the particles are expressed explicitely as function of the increment or the rate of deformation of the contact, according to simplified contact laws;
- the non-smooth Contact Dynamics (NSCD) method [48] [78] [79], in which particles are non-deformable bodies whose interactions are governed by shock laws. The resolution of the problem, for the computation of particles motion and interaction forces, is based on an implicit scheme for the equation of dynamics and intergranular relations.

The common denominator is that the particles are considered as independent entities and thus the material behaviour is attributed to contact zones, with local kinematic variables derived from rigid-body degrees of freedom (translations and rotations) of the particles. In fact, what is attractive in discrete methods is the possibility to describe the physics and mechanics of the discontinuities that characterize natural materials, using a relatively low number of parameters. Linked to this aspect is the possibility to measure mechnical quantities at the scale of such discontinuities that would be inaccessible experimentally. The computational cost for the resolution of the problem is proportional to the number of particles which are employed for one simulation. The number of particles that can be used for the simulation of structures at the real scale comes therefore from a compromise between the available CPU and RAM resources and the representativity of the sample for the problem one wants to study, or the mechanism to reproduce.

Classic DEM and CD models essentially differ in the treatment of small length and time scales involved in the dynamics of granular media. The time-stepping schemes used for the numerical integration of the equations of motions implies for the former a fine resolution of the small time and length scales involved in contact interactions. In the CD method, these small scales are neglected and their effects absorbed into contact laws together with a non-smooth formulation of particle dynamics described at a larger scale than small elastic response times and displacements [78].

2.1.1 Computation cycle

The computational cycle of a classical DEM computation is presented, as it is schematically represented on fig.2.1. The problem being solved at small length and time scales, particle motions are smooth, then twice differentiable, and the equations of dynamics are integrated with the help of force laws governing particle interactions. Let's consider the case of spherical-shaped particles, which will be also the case of our simulations. In an oriented space of dimensions i (i=*1,2,3* in 3D), the motion of a particle will be characterized by its position x_i, its translational - $\dot{x}_i$ - and rotational - $\dot{\omega}_i$ - velocities. Let's name its mass m and its moment of inertia as J_i. The translational and rotational accelerations are obtained by applying the Newton's second law of motion:

$$\begin{aligned} \ddot{x}_i &= F_i/m \\ \dot{\omega}_i &= M_i/J_i \end{aligned} \tag{2.1}$$

where F_i and M_i are the forces and moments applied to each particle. To follow the evolution of the system in time, particles position are updated at each time step Δt by integration of the accelerations $\ddot{x}_i$ and $\dot{\omega}_i$ according to a first-order centered finite difference scheme. We have:

$$\begin{aligned} \dot{x}_i^{[t+\Delta t/2]} &= \dot{x}_i^{[t-\Delta t/2]} + (\ddot{x}_i^{[t]} + g) \cdot \Delta t \\ \omega_i^{[t+\Delta t/2]} &= \omega_i^{[t-\Delta t/2]} + \dot{\omega}_i^{[t]} \cdot \Delta t \end{aligned} \tag{2.2}$$

where particles translational and rotational velocities $\dot{x}_i$ and $\dot{\omega}_i$ are evaluated at time $t + \Delta t/2$. Then, particles position are computed at time $t + \Delta t$:

$$x_i^{[t+\Delta t]} = x_i^{[t]} + \dot{x}_i^{[t+\Delta t/2]} \cdot \Delta t \tag{2.3}$$

Once the new position for each particle is computed, the list of interactions is updated and new interaction forces are computed. Dealing with spherical-shaped particles a great advantage comes from a relative simple geometry treatments, then two particles will be considered as interacting bodies if the distance between their centres is lower than the sum of their radii. Such operation would be less trivial in the case of polyhedric-shaped particles.

2.1.2 Interaction Law

The definition of a law to characterize the interaction between two bodies is a key aspect of DEM models, since such choice determines the microscopic and macroscopic behaviour

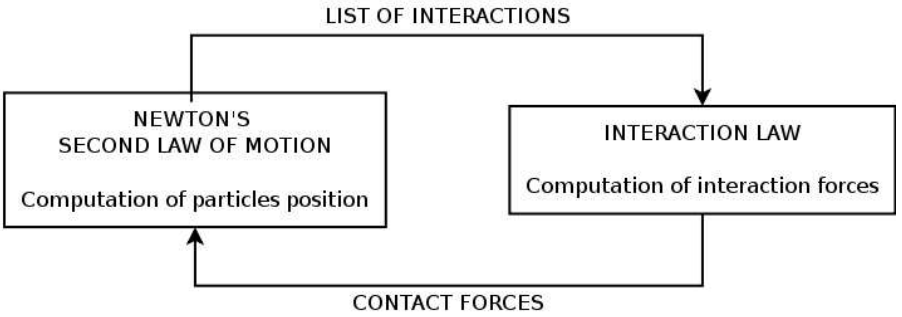

Figure 2.1: Computation cycle of a DEM model.

of particles assemblies. In addition to spherical particles, classical DEM models include also "walls". Walls allow one to apply velocity boundary conditions to assemblies of balls for purposes of compaction and/or confinement. Spherical particles and walls interact with one another via the forces that arise at contacts. The equations of motion are satisfied for each sphere; however, the equations of motion are not satisfied for each wall — i.e., forces acting on a wall do not influence its motion. Instead, its motion is specified by the user and remains constant regardless of the contact forces acting upon it. Also, contacts may not form between two walls; thus, contacts are either ball-ball or ball-wall.

Local geometry

In the global cartesian reference system $OXYZ$, a centre $x_i^{[k]}$ and a radius $R^{[k]}$ can be associated to each particle k, and a center $x_i^{[w]}$ to each wall w. Let's consider the interaction between two particles A and B (fig.2.2a), and between a sphere b and a wall w (fig.2.2b). For both types of interaction, forces arise from contact occurring at a point. A local reference system $(\mathrm{C}, \mathbf{n}, \mathbf{t})$ is defined for the interaction (see fig.2.2c). The contact point $x_i^{[C]}$ is within the interpenetration volume of the two entities and represents the application point of the resultant interaction force $\mathbf{F^c}$. It lies on a contact plane, defined by a unit normal vector $\mathbf{n}$, defined for sphere-sphere contacts as the normal vector directed along the line between spheres centers, whereas for sphere-wall contact as the normal vector directed along the line defining the shortest distance between the sphere center and the wall. For the sphere-sphere contact, we have:

$$\mathbf{n} = \frac{\{\mathbf{x}^{[A]} - \mathbf{x}^{[B]}\}}{\| \mathbf{x}^{[A]}\mathbf{x}^{[B]} \|} \quad \text{(sphere-sphere contact)} \tag{2.4}$$

The $\mathbf{t}$ unit vector is defined such that:

$$\mathbf{t} \cdot \mathbf{n} = 0 \tag{2.5}$$

The contact force is then decomposed into a normal component acting in the direction of the normal vector and a shear component acting in the contact plane. The intergranular distance is finally defined as:

$$U^n = \| \{x_i^{[A]} - x_i^{[B]}\} \| - (R^{[A]} + R^{[B]}) \quad \text{(sphere-sphere)} \tag{2.6}$$

The counterpart expressions for a sphere-wall contact, are represented on fig.2.2b.

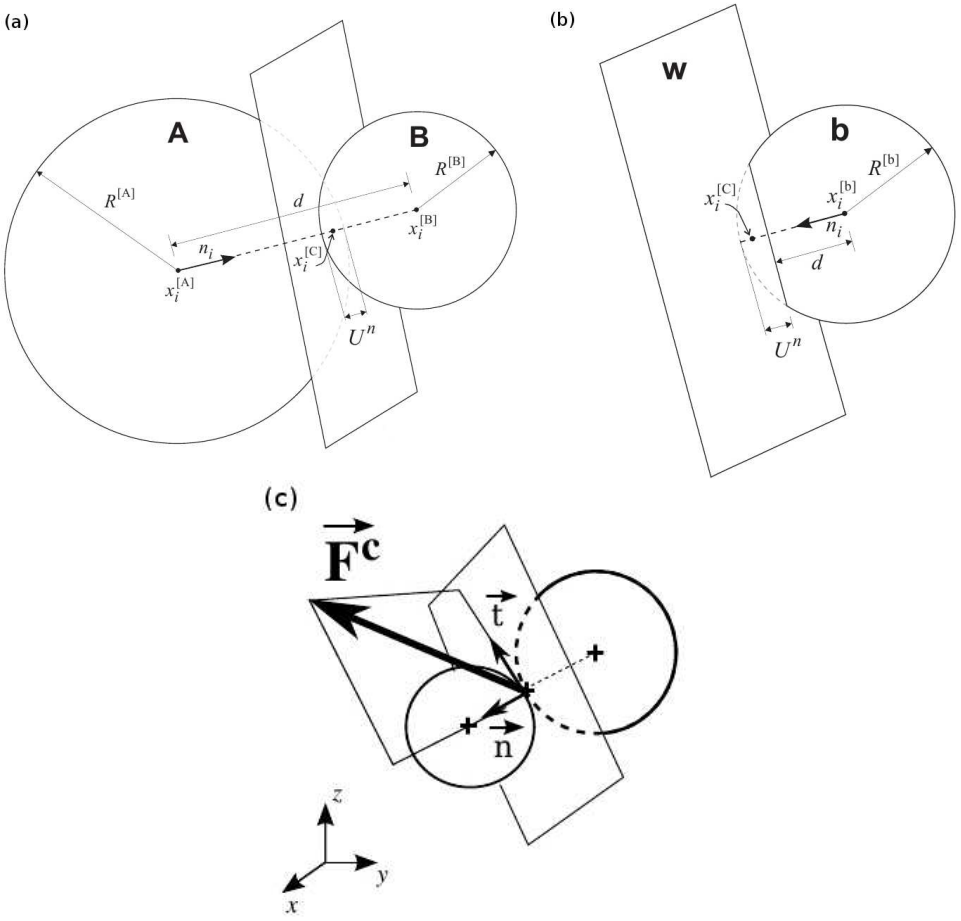

Figure 2.2: Local geometry of bodies interaction (after [46], [89]).

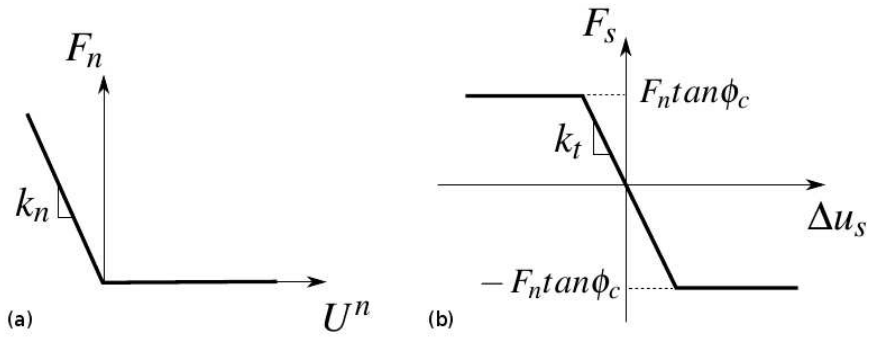

Figure 2.3: Elastic-plastic contact model. Normal (a) and tangential (b) interaction law [89]

Contact stiffnesses

A contact constitutive model have to be defined for the computation of those forces and moments that appears in eq.s (2.1), as a function of the local geometry that characterizes bodies interactions, as it has been described in the previous paragraph. Considering deformable bodies, a component of the resultant contact force would be computed as a function of the distance to each other. During the evolution of the system, such distance may become negative. Although this negative distance is often called overlap, it is clear that it corresponds to a deformation of the solid material near the contact zone, whose details are ignored, according to a "soft contact" approach.

We define δ_c (see fig.2.2), according to eq.(2.6) and the following condition:

$$\delta_c = \begin{cases} U^n & U^n < 0 \\ 0 & U^n \geq 0 \end{cases} \tag{2.7}$$

In presence of friction at the interaction, the contact force will have also a tangential component, that is computed at each time step as function of the increment of tangential relative displacement Δu_s.

The adoption of constant normal secant stiffness k_n and shear tangential stiffness k_t is the simplest but very popular choice (see fig.2.3) [29], [24], [91]. The normal component $\mathbf{F_n}$ is defined as follows:

$$\mathbf{F_n} = F_n \mathbf{n} = k_n \delta_c \mathbf{n} \tag{2.8}$$

The tangential component $\mathbf{F_s}$ is computed at each time step as function of the increment of tangential relative displacement Δu_s:

$$\Delta \mathbf{F_s} = F_s \mathbf{t} = k_t \Delta u_s \mathbf{t} \quad \rightarrow \quad \mathbf{F_s}^{(t)} = \mathbf{F_s}^{(t-\Delta t)} + \Delta \mathbf{F_s}^{(t)} \tag{2.9}$$

Other choices are possible, if a more realistic modelling of contact interactions is needed. A popular option is the Hertz-Mindlin contact model, based a nonlinear relation which takes into account the mechanical properties of the material the particles (of radius R) are made of (the shear modulus G and Poisson's ratio ν_d), and their deformation [65]. The expressions for the normal and tangential stiffnesses read:

$$k_n^* = \frac{dF_n}{d(\delta_c)} = \frac{G\sqrt{2R}}{1-\nu_d}\sqrt{\delta_c} \tag{2.10}$$

$$k_s^* = \frac{dF_s}{d(\delta_c)} = \frac{2(G^2 \cdot 3(1-\nu_d)R)^{1/3}}{2-\nu_d} F_n^{1/3} \tag{2.11}$$

Therefore, contact stiffnesses are updated at each iteration of a simulation.

Coulomb friction Coulomb's criterion is associated to the contact, defining its shear strength. Therefore, an upper limit is defined for the tangential force F_s as function of the normal force F_n and the intergranular friction angle ϕ_c (see fig.2.3b):

$$\| \mathbf{F}_s \| \leq \mathbf{F}_n tan\phi_c \tag{2.12}$$

Adhesion In case of absence of adhesion, only negative repulsive forces may arise at bodies interactions. If two bodies detach from one another loosing the contact, no effort will exist anymore between them.

However, it is possible to consider a condition of adhesion between two bodies, which would correspond to a resistance to traction and to shear stress. More precisely, it represents the maximum tensile force that have to act on two particles to break their contact [44] [83], and its counterpart contribution to shear resistance, known as *cohesion* in geomechanics. In case of models of dry materials (e.g. models of blocky structures) there won't be any traction resistance anymore between the two bodies, and their shear resistance will be described by eq.2.12.

Capillary effects In the case of wet granular materials, an extension of the basic interaction law can be defined to take into account the capillary effects [91], then the cohesive action ensured by liquid bridges that hold between neighbouring particles, resulting macroscopically to an *apparent cohesion* for the medium.

2.1.3 Critical time step

As mentioned in the introduction of this section, the time-stepping scheme used for the numerical integration of the equations of motions implies for the DEM a fine discretization of the time. The stability of an oscillating spring-mass system is function of the natural period of the system. In our simulations, a *critical* time step Δt_{crit} is computed at each iteration, computing the natural period of each particle, for all the degrees of freedom, supposed independent to each other. The natural period being expressed by the following relation,

$$T_N = \sqrt{m_i / K_i^j} \tag{2.13}$$

where m_i is the mass of the particle i and K_i^j an equivalent stiffness that is evaluated considering all the contacts of one particle, for each degree fo freedom ($j = 1,2,3,4$, $j = 4$ corresponding to the rotational stiffness). Finally, the *critical* time step is defined to coincide with the minimum natural period:

$$\Delta t_{cr} = min_{(i,j)}(\sqrt{m_i / K_i^j}) \tag{2.14}$$

2.1.4 Non-viscous damping

Each kind of action on the assembly generates a wave across the medium. In the case of waves of very small amplitude, the medium behave in purely elastic conditions and the friction may not dissipate energy at all. Then, the waves may never stop. To avoid such phenomenon that perturbates the numerical resolution, damping is often introduced, which can be of different types.

A classical choice is to introduce a viscous damper to particles interaction, proportional to the rate of sollicitation, which will result in a force to be added to the elastic force. Diversely, Cundall [30] proposed the introduction of a non-viscous damping which acts independently to each particle to limit their oscillation. For the translational and rotational motion, described by eq.(2.1), a damped force F_i^d and moment M_i^d are computed and applied to each particle i:

$$\begin{aligned} F_i^d &= -D_a \cdot \mid F_i \mid \cdot sign(\dot{x}_i) \\ M_i^d &= -D_a \cdot \mid M_i \mid \cdot sign(\dot{\omega}_i) \end{aligned} \tag{2.15}$$

$$\begin{cases} sign(a) = -1 & a < 0 \\ sign(a) = 1 & a > 0 \\ sign(a) = 0 & a = 0 \end{cases}$$

where F_i and M_i are the resultant interaction force and moment acting on the particle, D_a is a damping coefficient ($0 < D_a < 1$). The effect of such damping is finally to reduce the motive forces and to increase those forces which are opposed to the motion. Being a purely numerical trick, it has to be verified that the introduction of the damping doesn't influence the simulation results. In the case of presence of a fluid filling the pores, there is no need in employ such artifice, the fluid itself acting as a viscous damper.

2.1.5 Simulation of dry granular media

DEM models in three-dimensions are often based on the adoption of spherical-shaped particles. The advantages in terms of geometrical computation, for the detection of contact and the definition of interaction laws, are obvious. However, it is as much evident that this choice doesn't allow the quantitative reproduction of some property of real granular materials, whose particles are not spherical at all. Various authors proposed the adoption of polyhedric particles in order to reach realistic peak values of the friction angle, the relation between the microscopic and macroscopic friction angles being nonlinear [23].

Conceptually, sphere packings in DEM models, can be seen as *model materials* as the one constituted of rods for bidimensional stress-strain analysis, or glass beads in three-dimensional models. These materials have been used to study and analyze the microscopic origins of granular materials behaviour. In such context, DEM models show their unquestionable potential. Various characteristic phenomena have been reproduced through DEM simulations, like the stress-path dependence of the soil behaviour [27], the critical state concept [60], the shear localisation of deformation [8]. The direct comparison of numerical and experimental results remains complex, being difficult to reproduce the initial particle arrangement. Nevertheless, interesting results have been obtained on regular [73] and random [97] packings.

Quasi-staticity

In stress-strain analysis, the quasi-staticity of a simulation have to be ensured to access time-independent informations. By definition, quasi-staticity characterizes the evolution of a system consisting in a succession of static equilibrium states. To ensure such conditions, the inertial effects linked to the application of a charge must be controlled. Chareyre [23] analyzed the effect of the rate of deformation in triaxial tests simulations.

Mahboubi et al. [60] proposed a convenient measure to directly evaluate the quasi-staticity of a simulation,

$$\lambda = \frac{\| \sum_i^N \mathbf{F^{ext}}_i \|}{\| \sum_i^{N_i} \mathbf{F^c}_i \|} \tag{2.16}$$

where $\mathbf{F^{ext}}$ represents the resultant of all generic forces (external, body or contact forces) acting on all particles (N, number total of particles), while $\mathbf{F^c}$ refers to contact forces which arise at each interaction (N_i, number of interactions). $\lambda = 0$ in case of perfect staticity.

Representative Elementary Volume

As introduced in section 1.1.2, following a continuum approach, the description of the behaviour of a granular system is usually based on the definition of a Representative Elementary Volume (REV), defined as the smaller (elementary) volume portion of the whole system over which a constitutive relation can be defined, which will be representative of the mechanical behaviour as it can be observed at the macroscopic scale. In the case of discrete models, the definition of a relevant REV is tricky.

The definition of a REV in continuum mechanics being based on the uniqueness of the solution obtained, this concept had to be revised for the case of discrete models, in which a multitude of *exact* solutions exist as a result of a multitude of possible initial configuration of the packing. Calvetti et al. [21] and Biaretz and Hicher [11] experienced a good convergence of numerical results to laboratory experiments measures for a volume that would be at least ten times greater than the bigger particle size. Following a different approach, Chareyre [23] proposed a definition of the REV on the basis of the dispersion of the solution obtained, observing its influence on the number of particles employed in one simulation (see fig.2.4). Representativeness is finally related to the number of particles employed. The higher is the number of particles, the more homogeneous are the possible initial configuration of the packing, then the higher is the reliability of the estimated macroscopic properties.

Sample creation

In the simulation of laboratory tests or generic boundary problems, the generation of the sample is an operation of great importance. Indeed, it strongly influences the behaviour, via the initial density, granulometry, homogeneity and isotropy/anisotropy of the microstructure.

Two main techniques for the generation of the sample can be distinguished: geometrical methods based on algorithms for the positioning of the particles [49], or dynamical methods based on DEM simulations, during which particles may settle under the action

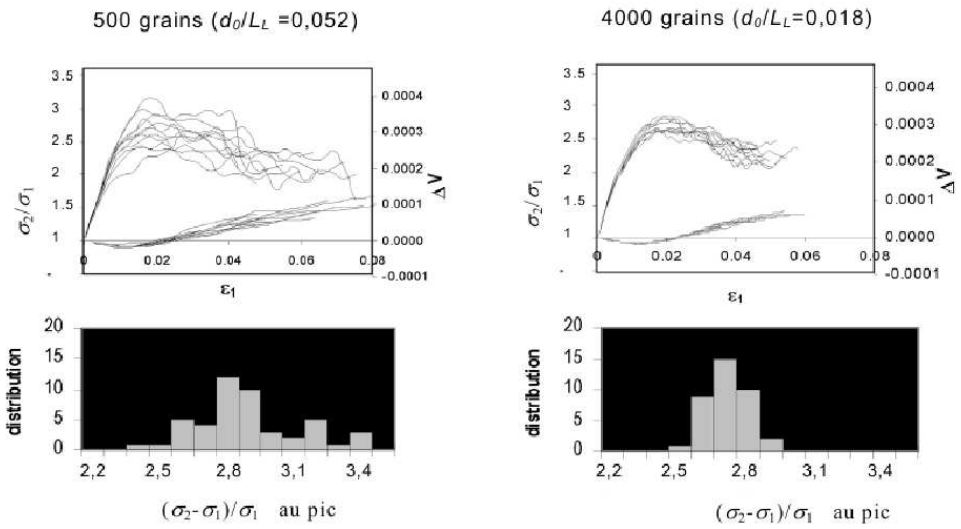

Figure 2.4: Dispersion of σ-ε curves for two samples of 500 and 4000 particles under biaxial test [23]

of gravity or may be compacted under the action of external load. The advantage of the dynamical method is that the generation process ends up with a sample which is mechanically stable and ready for the simulation, whereas in case of geometrical methods, the generated particles *cloud* needs of a mechanical stabilization process.

Pluviation of particles is well adapted for combined boundary/free surface problems, the properties of an unconsolidated sedimentary desposit being well reproduced through this process. A preferential orientation of contacts interactions, along the gravity direction, is noticed in this case [89]. On the other hand, the generation of the sample via external compaction allows to control the isotropy and the homogeneity of the packing, whose density may also be adjusted, by specifying an intergranular friction angle to incentivate or prevent the rearrangement of particles during the compaction process.

Boundary conditions

In order to subject a sample to a specified loading path, the boundary conditions are prescribed in terms of stress and/or strain, as it is the case in real laboratory or in situ tests. A classical solution is the use of a deformable box (fig.2.5a) whose faces are rigid walls in contact with the particles. The position and orientation of these walls will be function of the state of stress and strain specified by the user. As a consequence of the rigidity of the walls, the deformation field is forced to be homogeneous over the sample. For this reason, the adoption of flexible walls (fig.2.5b), whose effect is similar to the one of the membranes generally used in laboratory, was introduced. It was found that this type of boundary walls could facilitate the localization of the deformation in shear bands [47]. Furthermore, another effect of rigid walls is the perturbation of particles rearrangement within the sample, resulting in a higher porosity near boundaries. Such effect is generally addressed by the use of periodic boundary conditions (fig.2.5c), doing the hypothesis that the sample is part of a periodic space, so that the boundary conditions specified at one boundary are equivalent at the opposite boundary [27].

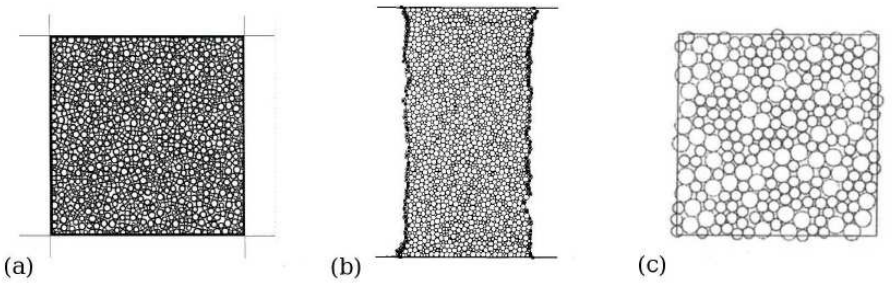

Figure 2.5: Types of boundary conditions: (a) rigid walls (b) flexible (c) periodic. [23]

2.1.6 Microscopic stress and strain

The definition of a per-particle stress tensor is detailed [101]. Each tensor represents the average stress in one particle, obtained from the contour integral of applied load as detailed below. This definition is considering each sphere as a continuum. It can be considered exact in the context of spheres at static equilibrium, interacting at contact points with negligible volume changes of the solid phase (this last assumption is not restricting possible deformations and volume changes at the packing scale).

First, we remark the identity:

$$\sigma_{ij} = \sigma_{ij}\delta_{ij} = \sigma_{ij}\nabla x_i^{[C]} = \nabla\cdot(x_i^{[C]}\sigma_{ij}) - x_i^{[C]}\nabla\cdot\sigma_{ij} \tag{2.17}$$

where $x_i^{[C]}$ is the vector containing the cartesian coordinates of the generic contact point.

At equilibrium, the divergence of stress is null: $\nabla\cdot\sigma_{ij} = 0$. Consequently, after divergence theorem:

$$\frac{1}{V}\int_V \sigma_{ij}dV = \frac{1}{V}\int_V \nabla\cdot(x_i^{[C]}\sigma_{ij})dV = \frac{1}{V}\int_{\partial V} x_i^{[C]}\sigma_{ij}n_j dS = \frac{1}{V}\sum_k x_i^{[k,C]}\mathbf{F}^{c,k} \tag{2.18}$$

where $\mathbf{F}^{c,k}$ represents the contact force, and k is an iterator over the number of contacts.

The last equality is implicitely based on the representation of external loads as Dirac distributions whose zeros are the so-called contact points: 0-sized surfaces on which the contact forces are applied, located at $x_i^{[C]}$ in the deformed configuration. A weighted average of per-body stresses will give the average stress inside the solid phase. There is a simple relation between the stress inside the solid phase and the stress in an equivalent continuum in the absence of fluid pressure. For porosity n, the relation reads:

$$\sigma_{ij}^{eq} = (1-n)\sigma_{ij}^{solid} \tag{2.19}$$

To define the strain tensor to be associated to each particle we follow an approach consisting in evaluating the strain of a particle's *neighbourhood*, as detailed in Chareyre (2003) [23]. Such neighbourhood is defined by bulding a Voronoï tessellation: a Voronoï cell will be associated to each particle, the smallest polygone satisfying the following conditions:

- the particle is inside the polygone;

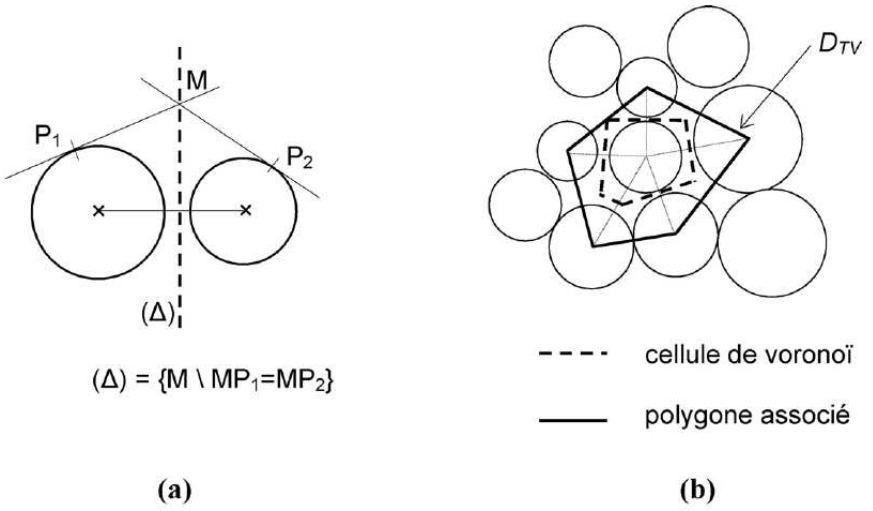

Figure 2.6: Definition of radical axis for a pair of neighbouring particles (a). Definition of a particle neighbourhood (b). [23]

- each edge of the polygone concides with the radical axis of the particle and one of its neighbours (see fig.2.6).

A larger polygon is finally associated to each particle, whose edges bind the neighbouring spheres centres. A polygonal domain D_{TV} is finally defined (see fig.2.6), whose surface is named S_{TV}, its boundary has length L_{TV} and is named C_{TV}. The macroscopic deformation to be associated to a particle is computed following the approach proposed by Cundall and Strack (1982) [28]. The gradient of average displacement of an equivalent continuum inside S_{TV} reads:

$$< \nabla \mathbf{dX} >= \frac{1}{S_{TV}} \int_{D_{TV}} \nabla \mathbf{dX} dS = \frac{1}{L_{TV}} \int_{C_{TV}} \mathbf{dX} \cdot \mathbf{n} dL \tag{2.20}$$

where **dX** is the the displacement field and **n** the boundary unit normal vector. Assuming that **dX** varies linearly between two vertices of the D_{TV} domain, we can easily compute the average gradient of displacement to be associated to one particle by knowing the displacement of the neighbouring particles. The equivalent strain tensor is finally obtained, by considering the symmetric part of $< \nabla \mathbf{dX} >$:

$$\varepsilon = \frac{1}{2}(\nabla < \mathbf{dX} > + \nabla^T < \mathbf{dX} >) \tag{2.21}$$

2.2 Coupled DEM-flow models

Various approaches have been adopted in the intent of describing the physics of flow through porous media and the mechanical interaction between the solid and the fluid phases. Each of these approaches is based on simplifications which depend on the scale at which the problem is observed, an aspect that determines also the range of validity and the fiability of the informations we can obtain from their adoption.

The existing and most popular coupling models, as they are adopted in the academic and professional frameworks, are presented. They essentially differ in the modelling techniques adopted for the description of fluid flow within the medium, to be then coupled with the DEM. A complete solution of the basic mechanical and fluid mechanical equations would determine quantities such as fluid-particle interaction forces and the resistance of the assembly to shear. Special emphasis will be put on the chosen scale in describing the physical processes that characterize the behaviour of a multiphase system, on the quality of the informations we can get by the application of such models and on the aspects which are linked on their implementation for numerical simulations.

2.2.1 Continuum-based models

In the application of fluid flow theory to two-phase flow problems the momentum and energy balance are usually applied in the integral form to finite volumes of the system under study. For fluidization studies, the whole fluidized bed can be taken as the reference volume [57]; for two-phase transport through conduits the volume element usually covers the whole cross-sectional area [100]. It is evident that in many other cases a differential analysis may lead to a better insight into the details of the flow phenomena and, utimately, to a better correlation of experimental information.

Following a continuum approach in the description of heterogeneous media, physical phenomena are observed and interpreted by a macroscopical point of view [103] [26]. The basis of continuum-based models is in fact the replacement of point mechanical variables at a specified point within a particle, by local mean variables obtained by averaging the point variables over regions which are larger than particle spacing but small compared with the complete system. This means that for a given application, it is assumed that a scale exists, defining the dimensions of a volume that would be physically and mechanically representative of the whole medium, as it was introduced in sections 1.1.2 and 2.1.5. It is worth noticing that the dimensions of such representative volume are uniquely determined by the application to which the model is intended to be applied. From Zeghal and Shamy [103], the space average of a point property h of the fluid phase, at location x, can be defined as follows:

$$\bar{h}_f(x) = \frac{1}{n(x)} \int_{RV_f} h(y) w(|x-y|) dv_y \tag{2.22}$$

where RV_f denotes the portion of a representative volume RV occupied by the pore fluid (such that $RV = RV_f + RV_p$, where RV_p is the part occupied occupied by the solid particles), $w(r)$ is a weighting function monotonically decreasing with the radial distance $r = |x-y|$ from location x, dv_y is the element of volume associated with the dummy location variable y, and $n(x)$ is the porosity in the neighbourhood of location x,

$$n(x) = \int_{RV_f} w(|x-y|) dv_y \tag{2.23}$$

Mechanical variables such as fluid velocity, the fluid pressure, or the velocity of solid matter appear as formal terms in continuum equations, and the form of these terms must be determined empirically, through the employment of phenomenological laws [3].

The dynamic flow of water and other viscous fluids through soil pores is generally addressed using Darcy's law (see section 1.2.2), to relate the pressure gradient ∇p to the fluid apparent velocity $\mathbf{u}_p$.

$$\mathbf{u}_p = -\frac{\kappa}{\mu}(\nabla p - \rho_f \mathbf{g}) \tag{2.24}$$

where κ is the intrinsic permeability expressed in [m^2], μ and ρ_f the viscosity and the density of the fluid, respectively. The permeability is often related to porosity by the Kozeny-Carman equation [46],

$$\kappa = c\frac{\bar{d_p}^2 n^3}{(1-n)^2} \tag{2.25}$$

where n is the porosity computed within the fluid cell, $\bar{d_p}$ the average particle diameter, c a geometric factor. Experimental studies show that pore fluid flow may deviate from Darcy's law for large interstitial velocities that may develop high hydraulic gradients [85]. Non-linear equations exist to evaluate the pressure gradient in these cases. Equation 2.26 shows Ergun's equation [103]:

$$\nabla p = -\left(150\frac{(1-n)^2}{n^3\bar{d}_p^2}\mu\rho_f\mathbf{u}_p + 1.75\frac{(1-n)}{n^3\bar{d}_p}\rho_f\mathbf{u}_p^2\right) \tag{2.26}$$

The continuum approach have been adopted for dilute particles suspensions as well as for dense materials at low strain rate (soils, rocks) and are commonly used in Computational Fluid Dynamics (CFD) codes. In coupled continuum-discrete models, classical schemes solve the continuity and Navier-Stokes equation numerically in eulerian cartesian coordinates, then derive pressure and velocity vector for each fluid cell. Individual forces on particles are then obtained through empirical relations as function of cell porosity and the fluid velocity as it can be computed with equations (2.24) or (2.26) [46]. Some limitations concern input parameters for those kind of coupled models. The fluid cell has to be large enough and contain at least *several* particles to obtain *good* results [46].

Continuum-discrete couplings succeed in making coupled problems affordable in terms of CPU cost. However, the use of phenomenological laws limit severely the predictive power of a model when new parameter ranges are explored. They are also incapable to render correctly the single particle behavior, and then they cannot apply for a series of problems inherently heterogenous at the particles scale and of high importance in porous solids : shear banding in cohesionless materials, fractures and microcracks in cohesive materials, segregating phenomena, internal erosion by transport of the smallest particles.

2.2.2 Microscale flow modelling

In certain situations, macroscopic phenomena depend so strongly on microscopic effects that continuum models fail. Furthermore, although quantities such as permeability are highly effective in describing flow in a homogeneous medium, they ultimately depend on fluid dynamics at the pore level. Hence, the desire to understand underlying fundamentals dictates the need for modelling at a smaller scale, supported by recent advances in porous media imaging techniques, which allow access to an unprecedented level of pore-space detail. Microscale models include the smallest length scales that affect the morphology of a medium.

The numerical solution of the Navier-Stokes equations is highly non-trivial and computationally demanding, especially for complex three-dimensional pore geometries. Finite Element Methods (FEMs) are often invoked for the numerical solution of flow problem in porous media [52] [69] [70], but their diffusion as an efficient tool have been finding more difficulties in the field of fluid mechanics than it has been in the field of structural and solid mechanics [37]. Although they allow to deal with irregular geometries and complex phases interfaces, because of the flexibility in the definition of the numerical mesh, the number of degrees of problem is too high if compared to other numerical schemes. As a consequence, the computer memory occupancy and the computational time needed to solve the associated system of nonlinear equations are often unaffordable, especially in case of three-dimensional problems [25].

In recent years, a numerical scheme which is having a widespread success for simulating fluid flows and modelling physics in fluids is the Lattice-Boltzmann method (LBM) [102] [62] [61] [56]. Like the finite element method, the scheme is particularly successful in fluid flow applications involving interfacial dynamics and complex boundaries. Unlike the finite element method, it does not resort to the solution of large systems of nonlinear equations. The fundamental idea is to construct simplified kinetic models that incorporate the essential physics of microscopic and mesoscopic processes so that the macroscopic averaged properties obey the desired macroscopic equations. The kinetic nature of the LBM introduces three important features that distinguish it from other numerical methods. First, the convection operator of the LBM in phase space (or velocity space) is linear. Simple convection combined with a relaxation process (or collision operator) allows the recovery of the nonlinear macroscopic advection through multi-scale expansions. Second, the pressure of the LBM is calculated using an equation of state, whereas in direct simulations of Navier-Stokes equations, the pressure satisfies a Poisson equation with velocity strains acting as sources. Third, the LBM utilizes a minimal set of velocities in phase space, being the phase space a complete functional space. It should be noted, however, that incompressible flow represents a high difficulty for the conventional LBM, which is entirely based on density fluctuations. This feature makes the LBM difficult in the situations of strong poromechanical coupling. One solution to this problem is to include the porosity as a field variable of the Navier-Stokes equation [41], thus upscaling the flow problem at the scale of the equivalent-continuum.

Such kinetic model incorporates many of the advantages of molecular dynamics, including clear physical pictures, easy implementation of boundary conditions, and fully parallel algorithms. While LB is generally faster than the FEM and has the possibility of being easily parallelized on multicore machines and GPUs (sailfish), commonly implemented fixed size grids can result in considerably larger computer memory occupancy. Only recently, grid refinement schemes have started to be implemented in open source LB codes (Palabos). Realistic microscale flow simulations in complex pore geometries still requires, however, access to computational resources beyond ordinary desktops due to the high number of grid nodes per particle.

2.2.3 Pore network models

Pore-network modelling covers a third class of models, based on a simplified representation of porous media as a network of pores and throats. Pore-network models have been

most commonly developed to predict the permeability of materials from microstructural geometry [19] [96] [7] [74] [45] [1], but have also been extended to include multiphase flow effects (e.g., air bubbles, immiscible two-phase flow) [17] [72] [18] [76]. Crucial for their success is an adequate definition of how fluids are exchanged between pores in term of the local pore geometry. This aspect will be discussed further in section 2.2.2.

Pore-network models studies have mostly focused on flow in passive rigid solid frames. Little attention, however, has been devoted to the definition of forces applied to individual particles in the solid phase. Early ideas of a coupled pore-network flow and DEM can be found in the works of Hakuno and Tarumi [43] and later by Bonilla [16]. These studies, however, were limited to 2D models of discs assemblies, where pores were defined by closed loops of particles in contact. Since such pore geometry does not offer any free path for fluid exchanges, 2D problems implied some arbitrary definition of the local conductivity, assuming virtual channels between adjacent voids. Adapting this approach to 3D spheres assemblies enables the definition of the local hydraulic conductivity using the actual geometry of the packing, as spheres packings always define an open network of connected voids. This in turns opens up the possibility of predicting both the macro-scale permeability and the forces acting on the individual particles rather than postulating it: this is one of the central themes of this work.

Conclusions

Far from being a complete introduction to the science of porous media, this chapter was conceived in the intent of introducing the reader to the complexity of these materials, and to the issues to be tackled to formulate a consistent mathematical and/or numerical model.

The fundamentals of fluid mechanics were presented, focusing primarly on the generic motion of fluids, described by the Navier-Stokes equations, then gradually introducing the possible simplifications, which were presented in relation to the aim of the work and the scenarios we'll present in next chapters. Darcy's law, the phenomenologically derived constitutive equation that describes the flow of a fluid through a porous medium, had been finally introduced.

The Biot's theory of poroelasticity has been briefly reported. The idea was to give an insight into the continuum description of the mechanics of saturated porous media, to be used as an introduction and a reference for the discrete description we propose in this work. Then, the main characteristics of the discrete element method, the powerful numerical tool for modelling heterogeneous materials, were presented. The numerical and mechanical aspects linked to the description of dry granular materials had been initially presented, being nearly completely independent from the issues related to the hydromechanical coupling.

A concise description of the existing families of coupled DEM-flow models concluded our introduction. The next part will be completely devoted to the description of the coupled Pore-scale Finite Volume (PFV) - DEM model we developed.

Part II

The DEM-PFV model

Chapter 3

The Pore-scale Finite Volume Model

As mentioned in the general introduction, the PFV coupling model follows a partitioned approach. The resolution of the elastic-plastic problem at particle interactions and of the flow problem are indeed independent and will be treated separately.

Discrete modelling is a framework that offers the possibility of modelling granular medium at the scale of its components. The PFV model is intended to provide a tool for the analysis of the behaviour of biphasic granular media, preserving the discrete nature of DEM models. This first chapter will concern the modelling of the fluid phase: viscous flow equations will be upscaled at the pore level, and approximated with a finite volume numerical scheme.

The comparison of the numerical results of the PFV model with FEM solutions will be presented. The void space being discretized by a fine mesh, FEM simulations provide a solution of Stokes equations with exceptional details. Assuming this as a reference, we will observe the cost of simplifications and approximations for the PFV model, in terms of *quality* of the solution obtained. A fixed solid skeleton will be considered at this stage. The forces on solid particles exterted by the fluid and the estimation of the intrinsic permeability of the granular packing will be directly compared.

3.1 Poral space discretization

Delaunay triangulations and their dual Voronoi graphs are widely used for structural studies of molecules, liquids, colloids, and granular materials [5]. More specifically, it has been applied to domain decompositions in sphere packings, for the definition of microscale strains and stresses [21, 6, 49], and pore-scale modelling of single-phase or multi-phase flow [17, 18, 96]. Delaunay triangulation is defined for a set of isolated points. In such case, the dual Voronoi graph of the triangulation defines polyhedra enclosing each point in the set, and facets of the polyhedra are parts of planes equidistant from two adjacent points. For mono-sized spheres, this construction gives a map of the void space. Delaunay-Voronoi graphs, however, present a number of misfeatures when applied to spheres of different sizes. Notably, branches and facets of the Voronoi graph can cross non-void regions, or divide regions in such a way that the splits are orthogonal to the actual void, as illustrated on fig. 3.1.

Luchnikov [59] proposed to define the split between spheres by means of curved surfaces equidistant from both sphere surfaces, thus defining *Voronoi S* cells. The use of

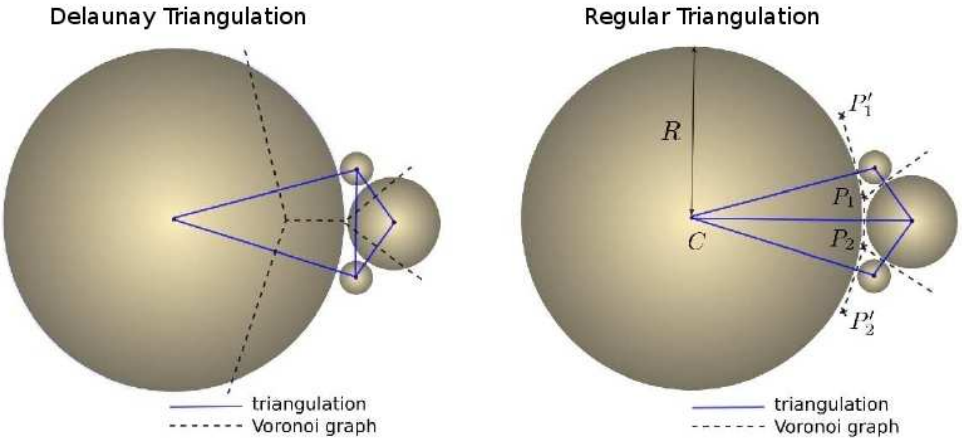

Figure 3.1: Comparison of 2D triangulations and dual Voronoi graphs: the Voronoi graph dual to Delaunay triangulation has branches inside discs, while the one dual to the regular triangulation gives all branches in the voids space. Observe that if R tends to infinity, $\{P_1',P_1,P_2,P_2'\}$ tends to aligned points.

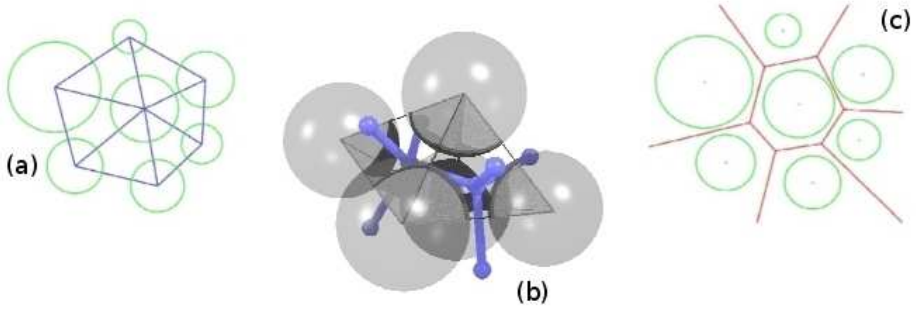

Figure 3.2: Adjacent tetrahedra in the regular triangulation and dual Voronoi network, in two dimensions (a,b) and three dimensions (c).

Voronoi S graphs is, however, computationally expensive for large numbers of particles. *Regular* triangulation (see fig. 3.1), while overcoming the problems associated with Delaunay triangulations, provides a computationally cheap alternative to the use of Voronoi S cells. Regular triangulation [35] generalizes Delaunay triangulation to weighted points, where weights account for the radius of spheres. It can be shown that the dual Voronoi graph of the regular triangulation is entirely contained in voids between spheres, as opposed to the dual of Delaunay triangulation, as seen on fig.3.1 (in 2-Dimensions) and fig.3.2 (2D/3D). Edges and facets of the regular Voronoi graph are lines and planes, thus enabling fast computation of geometrical quantities. In section 3.2 we will use a combination of regular Delaunay facets and regular Voronoi vertices to decompose the pore volume.

The only intrinsic restriction for this geometrical description is that the center of one sphere should not lie inside another sphere. In this case, the system degenerates. As such, contacts or even overlaps between adjacent spheres are allowed.

3.2 Fluxes

The partitioning described above results in a tethraedral mesh whose vertices coincide with the centres of the spheres. In three dimensions, each tethraedron of the triangulation represents one pore (see fig.3.2). Dual to the triangulation, the tessellation system, defined by branches linking the Voronoi centres computed for each pore, represents the path along which the fluid is assumed to flow within the medium. We are then ready to focus down at the pore scale, and start to describe the geometry we have to deal with at such scale.

Looking at fig.3.3a, we introduce the following notation: Ω denotes a domain occupied by a porous material, a tetrahedron of the triangulation comprising portions of spheres and of void space. Γ and Θ are the domains occupied respectively by the solid and the fluid: $\Omega = \Gamma \cup \Theta$, $\Gamma \cap \Theta = \emptyset$ (Θ is also called *pore space*). We denote by N_c the number of tetrahedral cells in the regular triangulation of the sphere packing, and by Ω_i the domain defined by tetrahedron i : $\Omega = \cup_{i=1}^{N_c} \Omega_i$. Similarly, N is the number of spheres, and Γ_i the domain occupied by sphere i, so that $\Gamma = \cup_{i=1}^{N} \Gamma_i$.

Continuity

We define Θ_i the portion of the tetrahedral element Ω_i not occupied by the solid particles. The volume V_i^f of Θ_i is filled by the fluid (fig. 3.3), since we are considering saturated porous media. The continuity equation for an incompressible fluid (1.14), cast into its surface integral form and using the divergence theorem, gives a relation between the time derivative of V_i^f and the fluid velocity:

$$\dot{V_i^f} = \int_{\partial\Theta_i} (\mathbf{v} - \mathbf{u}) \cdot \mathbf{n} \, \mathrm{d}s, \tag{3.1}$$

where $\partial\Theta_i$ is the contour of Θ_i, $\mathbf{n}$ the outward pointing unit vector normal to $\partial\Theta_i$, $\mathbf{u}$ the fluid velocity, and $\mathbf{v}$ the velocity of the contour. One part of the contour, noted $\partial^s\Theta_i$, corresponds to a solid-fluid interface. At any point in $\partial^s\Theta_i$, we have $(\mathbf{v} - \mathbf{u}) \cdot \mathbf{n} = 0$, so that the integration domain above can be restricted to $\partial^f\Theta_i$, the fluid part of the contour. By introducing $S_{ij}^f (j \in \{j_1, j_2, j_3, j_4\}$ the intersections of triangular surfaces S_{ij} with the fluid domain (fig. 3.3b), so that $\partial^f\Theta_i = \cup_{j=j_1}^{j_4} S_{ij}^f$, we can define four intergrals describing fluid fluxes q_{ij} from tetrahedron i to adjacent tetrahedra j_1 to j_4. Finally:

$$\dot{V_i^f} = \sum_{j=j_1}^{j_4} \int_{S_{ij}^f} (\mathbf{v} - \mathbf{u}) \cdot \mathbf{n} \, \mathrm{d}s = - \sum_{j=j_1}^{j_4} q_{ij} \tag{3.2}$$

In deformable sphere packings, $\dot{V_i^f}$ can be computed on the basis of particles motion (i.e. velocities of the vertices of the tetrahedra), thus linking fluid fluxes with the deformation of the solid skeleton.

Local conductances

Both Stokes (1.16) and Darcy (1.31) equations imply a linear relation between pressure gradients and fluxes. Here, we introduce an *inter-pore* gradient, defined as the ratio be-

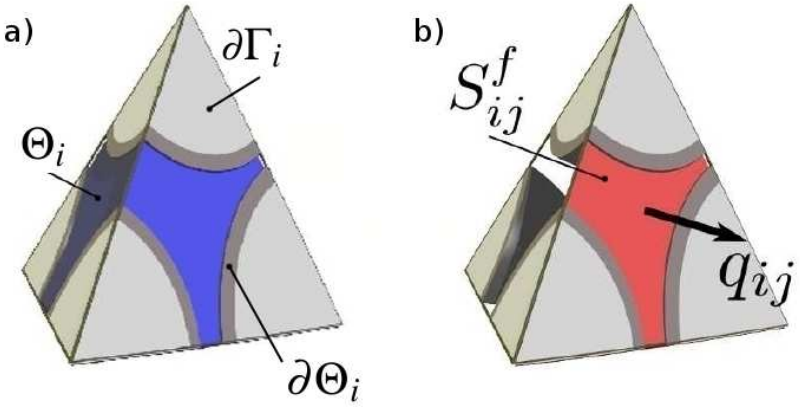

Figure 3.3: Ω_i - Tetrahedral element of the finite volume decomposition.

tween the pressure difference $p_i - p_j$ between two connected tetrahedral cells, and a relevant length L_{ij} - to be defined below. Being linear, the relation between q_{ij} and the inter-pore gradient can be expressed using the *local conductance* factor g_{ij} of facet ij:

$$q_{ij} = g_{ij} \frac{p_i - p_j}{L_{ij}}. \tag{3.3}$$

Considerable efforts have been devoted in the past literature to the definition of g_{ij} in pore-network models, with attempts to generalize Poiseuille's law to pores of different shapes, eventually mapping the microstructure of some real materials for permeability predictions [76, 45]. By analogy with the Hagen-Poiseuille relation, we define g_{ij} by introducing the *hydraulic radius* of the pore throat R_{ij}^h, and its cross-sectional area A_{ij} (the definitions of R_{ij} and A_{ij} are discussed below), by means of a non-dimensional conductance factor α reflecting the throat's shape (Hagen-Poiseuille for circular cross sections of radius $2R_{ij}^h$ is recovered with $\alpha = 1/2$):

$$g_{ij} = \alpha \frac{A_{ij} {R_{ij}^h}^2}{\mu} \tag{3.4}$$

L_{ij}, R_{ij}^h, and A_{ij} are geometrical quantities describing the throat geometry. Even though these variables are found in most of the papers cited above, there is no general agreement on their definition for pore-network modelling of arbitrary microstructural geometry. A detailed analysis of how non-circular cross-sections with variable constriction affect the flow path can be found in [74] and [66], while triangulated sphere packings were considered and discussed in [96], [7], [19]. Some of these models, however, do not clearly define a partition of the void space, and as such they need ad-hoc corrections for L_{ij} to ensure that the same pore volumes are not accounted for multiple times in different cells [19]. We observe here that in Delaunay-Voronoi graphs of spheres with polydispersed radii, circumcenters (and barycenters) may lie inside the solid phase [17], and definitions of L_{ij} based on distances between circumcenters become problematic.

For the present model, we take advantage of the regular Voronoi graph structure, whose edges and vertices are always contained in the pore space. A partition of the full domain is defined as the set of sub-domains Ω_{ij}, with Ω_{ij} the union of two tetrahedra constructed from facet S_{ij} and Voronoi vertices P_i and P_j : $\Omega_{ij} = (S_{ij}, P_i) \cup (S_{ij}, P_j)$. Keeping

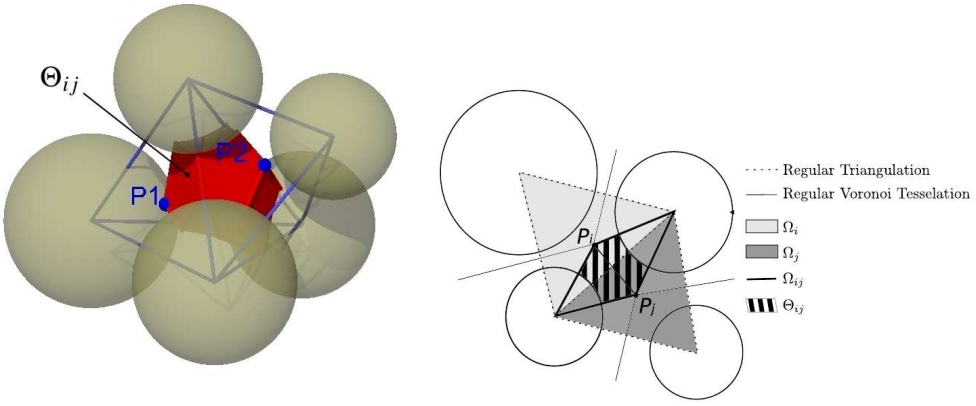

Figure 3.4: Construction of subdomain $\Theta_{ij}\Omega_{ij}$, defining the volume of the throat assigned to a facet for the definition of hydraulic radius R^h_{ij}; in 3D (left) and 2D (right).

only the part of Ω_{ij} that intersect the pore space, we define a throat connecting two pores, noted Θ_{ij} (see figs. 3.4 and 3.5). We define the hydraulic radius R^h_{ij} in eq. 3.4 as the ratio between the throat's volume and solid-fluid interfaces area. Denoting by ϕ_{ij} the volume of Θ_{ij}, and γ_{ij} the area of $\partial^s\Theta_{ij}$ (the part of the contour in contact with spheres), the *hydraulic radius* R^h_{ij} reads:

$$R^h_{ij} = \phi_{ij}/\gamma_{ij} \tag{3.5}$$

Note that, with the partition of the voids space proposed here, the definition of effective radii accounts for the exact total solid surface and void volume in the packing. Noting $\mathscr{F}$ the set of facets, we have $\Theta = \bigcup_{ij\in\mathscr{F}} \Theta_{ij}$, and $\partial\Theta = \bigcup_{ij\in\mathscr{F}} \partial^s\Theta_{ij}$.

We define the length of the throat as the distance between Voronoi vertices: $L_{ij} = \|P_iP_j\|$, and the throat's cross-sectional area as that of the fluid domain $A_{ij} = S^f_{ij}$ introduced in the previous section (fig. 3.3). In this model, the factor α is uniquely assigned to all throats of a packing and can be considered a calibration factor. A value of $\alpha = 1/2$ has been choosen as an initial guess, by analogy with the Hagen-Poiseuille law. The numerical simulations that will be presented in section 3.5 indicate that setting $\alpha = 1/2$ is indeed appropriate for the sphere geometries considered in this investigation. We observe that the values of α obtained analytically vary over a moderately wide range of values for compact throat sections [74]. It is also worth noting that, the factor α being the same for all throats, modifying this value will not modify the pressure distribution in the boundary value problems presented below (mixed Neumann-Dirichlet), and consequently it would not affect the values of forces applied on the particles.

Another possible definition of g_{ij} has been proposed by [17] for dense packings of mono-sized spheres. These authors defined g_{ij} as a function of an *effective radius* R^{eff}_{ij} (ER), thus accounting only for the effects of the narrowest cross section (surface S_{ij} in fig. 3.3) and disregarding the influence of the full volume of the flow path. The effective radius is defined [1] as $R^{eff}_{ij} = (r^{eq.}_{ij} + r^{inscr.}_{ij})/4$, where $r^{eq.}_{ij}$ is the radius of the disk with the same surface as S^f_{ij}, and $r^{inscr.}_{ij}$ is the radius of the circle inscribed in the three spheres

[1] For the convenience of comparisons, and consistently with the expression of conductance we are using, we introduce the effective radius R^{eff} as the half of its definition in the original paper from Bryant and Blunt. The final value of the conductance is preserved.

intersecting the facet. It represents the hydraulic radius of the circular tube that would have the same conductance as the throat:

$$g_{ij} = \frac{2\pi {R_{ij}^{eff}}^4}{\mu} = \frac{A_{ij}^{eff} {R_{ij}^{eff}}^2}{2\mu}, \tag{3.6}$$

where $A_{ij}^{eff} = \pi(2R_{ij}^{eff})^2$ is the cross-sectional area of the equivalent tube. The second expression is given for the purpose of comparison with eq. (3.4). The values of R_{ij}^{h} and R_{ij}^{eff} in random dense packings of polydispersed spheres, and the results they give in terms of fluxes and forces, are compared in section 3.5.

3.3 Forces on solid particles

The total force $\mathbf{F}^k$ generated on particle k by the fluid includes the effects of absolute pressure p^a and viscous stress τ, the divergence for which is the right-hand side of (1.16):

$$\mathbf{F}^k = \int_{\partial\Gamma_k} (p^a \mathbf{n} + \tau \mathbf{n}) \, \mathrm{d}s \tag{3.7}$$

We recall that the piezometric pressure governing the flow problem was defined as $p =$

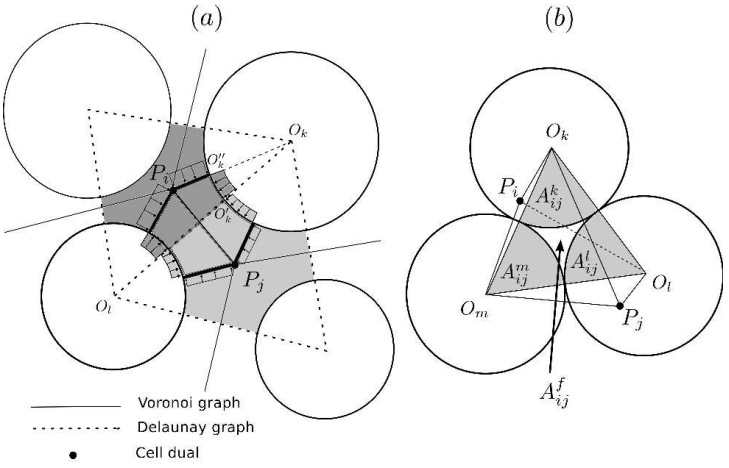

Figure 3.5: Volume decomposition for viscous drag force definition : (a) pressure distribution on $\partial\Theta_{ij}$ (in 2D for clarity), (b) definition of facet-spheres intersections in 3D.

$p^a - \rho_f \Phi(\mathbf{x})$. By introducing p in the previous equation, one can define $\mathbf{F}^k$ as the sum of three terms, noted $\mathbf{F}^{b,k}$, $\mathbf{F}^{p,k}$ and $\mathbf{F}^{v,k}$:

$$\mathbf{F}^k = \int_{\partial\Gamma_k} \rho_f \Phi(\mathbf{x}) \, \mathbf{n} \mathrm{d}s + \int_{\partial\Gamma_k} p \, \mathbf{n} \mathrm{d}s + \int_{\partial\Gamma_k} \tau \, \mathbf{n} \, \mathrm{d}s = \mathbf{F}^{b,k} + \mathbf{F}^{p,k} + \mathbf{F}^{v,k}. \tag{3.8}$$

$\mathbf{F}^{b,k}$ is the so-called buoyancy force, and can be computed independently. In the case of gravitational body forces, it will give the Archimede's force proportional to the volume

of Γ_k. $\mathbf{F}^{p,k}$ and $\mathbf{F}^{v,k}$ are terms resulting from viscous flow: $\mathbf{F}^{p,k}$ resulting from losses of piezometric pressure, and $\mathbf{F}^{v,k}$ resulting from viscous shear stress. Both $\mathbf{F}^{p,k}$ and $\mathbf{F}^{v,k}$ will be derived separately, at the scale of the domains Ω_{ij} that were introduced in the previous section, in the approximation of piecewise constant pressure.

3.3.1 Integration of pressure

The force generated by p on particle k in domain Ω_{ij} is the sum of two terms implying pressures p_i and p_j (see fig. 3.5),

$$\mathbf{F}_{ij}^{p,k} = \int\limits_{\partial\Gamma_k\cap\Omega_i\cap\Omega_{ij}} p_i\,\mathbf{n}\,\mathrm{d}s + \int\limits_{\partial\Gamma_k\cap\Omega_j\cap\Omega_{ij}} p_j\,\mathbf{n}\,\mathrm{d}s \tag{3.9}$$

In three dimensions, computing such integrals on spherical triangles could be computationally expensive. It is more convenient to project the pressure on the conjugate planar parts (angular sectors) of the closed domain $\Gamma_k\cap\partial\Omega_{ij}$, which trace in the plane of fig. 3.5 corresponds to segments OO' and OO''. Note that when iterating over all domains Ω_{ij} adjacent to one particle, the integral on sectors of type OO'' will appear twice with opposite normals and cancel out each other. Finally, the contribution to pressure force on particle k in domain Ω_{ij} is simply proportional to the area A_{ij}^k of sector $S_{ij}\cap\Gamma_k$ (trace OO'). If $\mathbf{n}_{ij}$ is the unit vector pointing from P_i to P_j, the force reads:

$$\mathbf{F}_{ij}^{p,k} = A_{ij}^k\,(p_i - p_j)\,\mathbf{n}_{ij} \tag{3.10}$$

3.3.2 Integration of viscous stresses

To integrate the viscous stresses, we first define the total viscous force $\mathbf{F}_{ij}^v$ applied on the solid phase in Ω_{ij}. Since Ω_{ij} intersects three spheres, $\mathbf{F}_{ij}^v$ will have to be later splitted into three terms. $\mathbf{F}_{ij}^v$ is defined as

$$\mathbf{F}_{ij}^v = \int\limits_{\partial^s\Theta_{ij}} \boldsymbol{\tau}\,\mathbf{n}\,\mathrm{d}s. \tag{3.11}$$

An expression of $\mathbf{F}_{ij}^v$ is obtained by integrating the momentum conservation equation (1.16)) in Θ_{ij}. The integral is cast in the form of a surface integral on contour $\partial\Theta_{ij}$ using the divergence theorem :

$$\int\limits_{\partial\Theta_{ij}} (p\,\mathbf{n} + \boldsymbol{\tau}\,\mathbf{n})\,\mathrm{d}s = 0.$$

This integral can be decomposed as in eq. (3.12), where the terms correspond respectively to $\mathbf{F}_{ij}^v$, to the sum of viscous stress on the fluid part $\partial^f\Theta_{ij}$ of the contour, and to the sum of pressure. By neglecting the second term (thus assuming that pressure gradients are equilibrated mainly by viscous stress on the solid phase), the expression of $\mathbf{F}_{ij}^v$ takes the form of equation 3.13, where the viscous force is simply proportional to the product of the throat's cross-sectional area A_{ij}^f and the pressure jump $p_j - p_i$.

$$\int\limits_{\partial^s\Theta_{ij}} \boldsymbol{\tau}\,\mathbf{n}\,\mathrm{d}s + \int\limits_{\partial^f\Theta_{ij}} \boldsymbol{\tau}\,\mathbf{n}\,\mathrm{d}s + \int\limits_{\partial\Theta_{ij}} p\,\mathbf{n}\,\mathrm{d}s = 0. \tag{3.12}$$

$$\mathbf{F}_{ij}^{v} \simeq -\int_{\partial\Theta_{ij}} p\,\mathbf{n}\,\mathrm{d}s \;=\; A_{ij}^{f}(p_j - p_i)\,\mathbf{n}_{ij} \tag{3.13}$$

In order to define the viscous forces applied on each of the three spheres intersecting Ω_{ij}, it is assumed that the force on sphere k is proportional to the surface of that sphere contained in the subdomain. If γ_{ij}^{k} denotes the area of the curved surface $\partial\Gamma_k \cap \Omega_{ij}$, the force on k then reads:

$$\mathbf{F}_{ij}^{v,k} = \mathbf{F}_{ij}^{v}\,\frac{\gamma_{ij}^{k}}{\sum_{k=1}^{3}\gamma_{ij}^{k}} \tag{3.14}$$

Finally, the total force on one particle is obtained by summing viscous and pressure forces from all incident facets with the buoyancy force:

$$\mathbf{F}^{k} = \sum_{(ij)_{incident}} \{\mathbf{F}_{ij}^{v,k} + \mathbf{F}_{ij}^{p,k}\} + \mathbf{F}^{b,k} \tag{3.15}$$

3.4 Boundary conditions

While rigid walls, as they have been presented in section 2.1, constitute those entities that allow an easy definition of boundary conditions for the resolution of the elastic boundary value-problem (see section 2.1.5), the numerical resolution of the flow problem needs of a specific treatment to ensure the relevance of space discretization in proximity to boundaries.

A consistent representation of boundaries for the flow model are *fictitious* spheres of infinite radius which are placed to be tangent to the assembly. They result, with a good approximation, in flat surfaces surrounding the spheres assembly (see fig.3.6 for a 2-D view). From such modelling, we take two main advantages: the first one is that the definition of pores shape and connections in proximity to the boundaries don't need in any additional assumption, the triangulation and tessellation system providing a consistent representation of them; the second one is that the *fictitious* spheres participate to the flow calculation as all the other spheres, and fluid forces are applied on them, making easily accessible the resultant fluid forces at boundaries. It is worth noticing that they don't have mechanical interactions with any other body (i.e. rigid walls or moving particles) during a simulation. As such, their position is periodically updated to take into account of solid skeleton deformations and boundaries displacement. Both "no-slip" or "symmetry" (slip) conditions can be considered at boundaries. They are reflected in the definition of conductivity and forces in the throats Θ_{ij} in contact with boundaries, as follows:

- For the "no-slip" condition, the surfaces of infinite spheres in contact with Θ_{ij} are accounted for in eq.s (3.5), (3.14);
- for the "symmetry" condition, these surfaces are ignored.

All the advantages of a relatively simple geometrical operations are kept through such modelling. Fig.3.7 shows a schematized view of boundary pores, represented by tethraedra which in turn can be built on a number of *real* and *fictitious* spheres. The approximation of prismatic-shaped pores is finally suggested by the geometry we deal with,

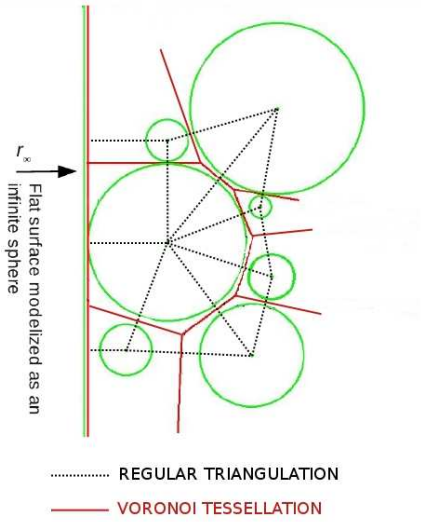

Figure 3.6: Regular triangulation and its dual Voronoi diagram near to boundaries.

assuming the perpendicularity between the boundary planes and the tethraedron edges. Faster computations are then possible using flat projected surfaces.

We will henceforth refer to two kind of boundary conditions:

- a *pressure* condition, which refers to a condition of imposed pressure;
- a *flux* condition, which refers to a condition of imposed flux, then free pressure.

3.5 Comparison with small-scale FEM simulations

In what follows particles will be assumed to be fixed, whereas the next chapter will be devoted to the validation of the model in the case of deformable packings. Here $\dot{V}_i^f$ is constant, thus the continuity equation (3.2) simplifies to:

$$\sum_{j=j_1}^{j_4} q_{ij} = 0 \tag{3.16}$$

Combining this equation with eq.(3.3), we can write the system to be solved as follows:

$$[\mathbf{G}]\{\mathbf{P}\} = 0 \tag{3.17}$$

where $\mathbf{G}$ is the conductivity matrix containing terms g_{ij}/L_{ij} and $\mathbf{P}$ the column vector containing all (unknown) values of pressure.

3.5.1 Numerical setup

We compare the results of the pore-scale finite volume (PFV) model with FEM Stokes flow simulations of a dense sphere packings subjected to an imposed pressure gradient, as described by eq.s (1.16),(1.14). We consider a sphere packing contained in a cube of size

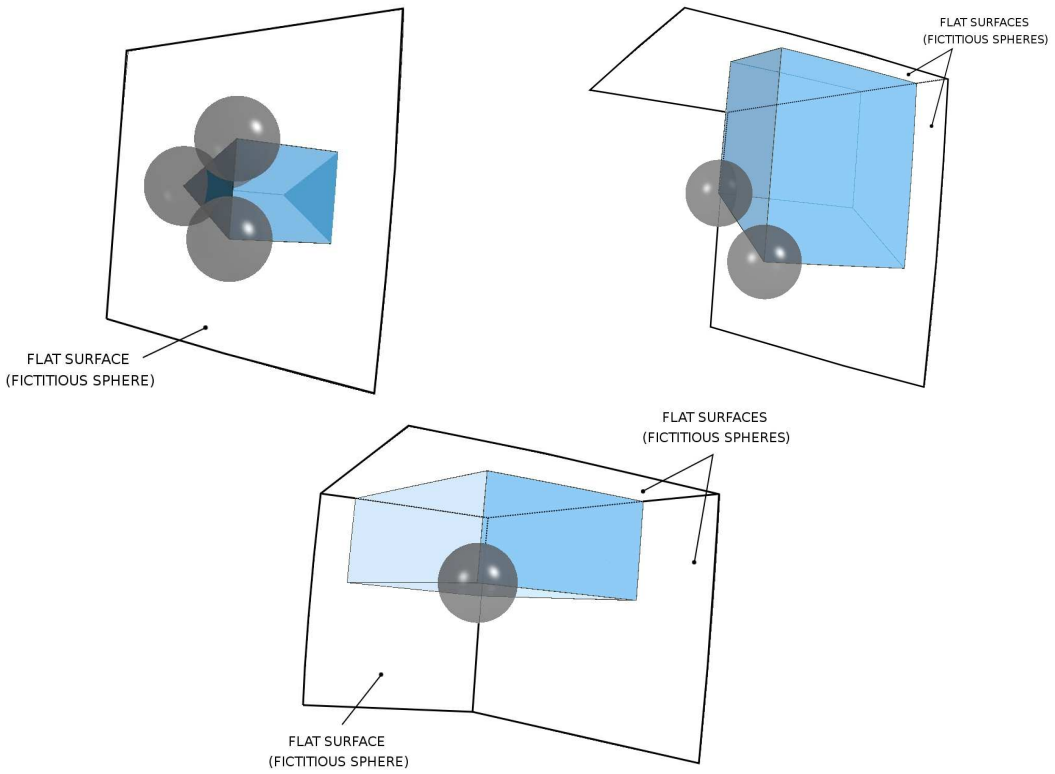

Figure 3.7: Pores at boundaries. One fictitious (a), Two fictitious (b) and three fictitious (c) cases.

l_0 (all results below will be normalized with respect to this reference length). Boundaries are accounted for in the triangulation process in the form of spheres with near-infinity radii ($10^6 \times l_0$). Hence, planes are not introducing special cases to handle in the algorithms, and equations presented in previous sections apply for boundaries as for any other sphere (see section 3.4).

The smallest test problem we consider is a regular cubic packing of eight spheres. Packings of nine spheres are obtained by placing an additional sphere (with variable size d) in the center of the cubic packing (fig. 3.8). Larger assemblies of 25, 54, and 200 spheres (fig. 3.9) are random packings that were generated using the DEM, by simulating the growth of spheres after random positioning, using the algorithm of Chareyre et al. [24]. Radii are generated randomly with respect to uniform distributions between radii r_{min} and r_{max}. In the 200-sphere assembly, sizes are narrow graded, with $r_{min}/r_{max} = 0.9$. Sizes in the 25-sphere and 54-sphere packings are more dispersed, with $r_{min}/r_{max} = 0.5$. After dense and stable packings are obtained, the spheres's positions are fixed.

For each packing geometry, the flow boundary conditions are the ones described on fig. 3.8: pressure is imposed on the top and bottom boundaries, while no-flux conditions are imposed on the lateral boundaries.

Both "no-slip" and "symmetry" conditions are considered on the lateral boundaries. Table 3.1 gives a comparison of problem sizes in terms of degrees of freedom (DOF) for the pressure field, and CPU times for solving. The data in this table is only an indication of how much is gained from the pore-scale formulation of Stokes flow.

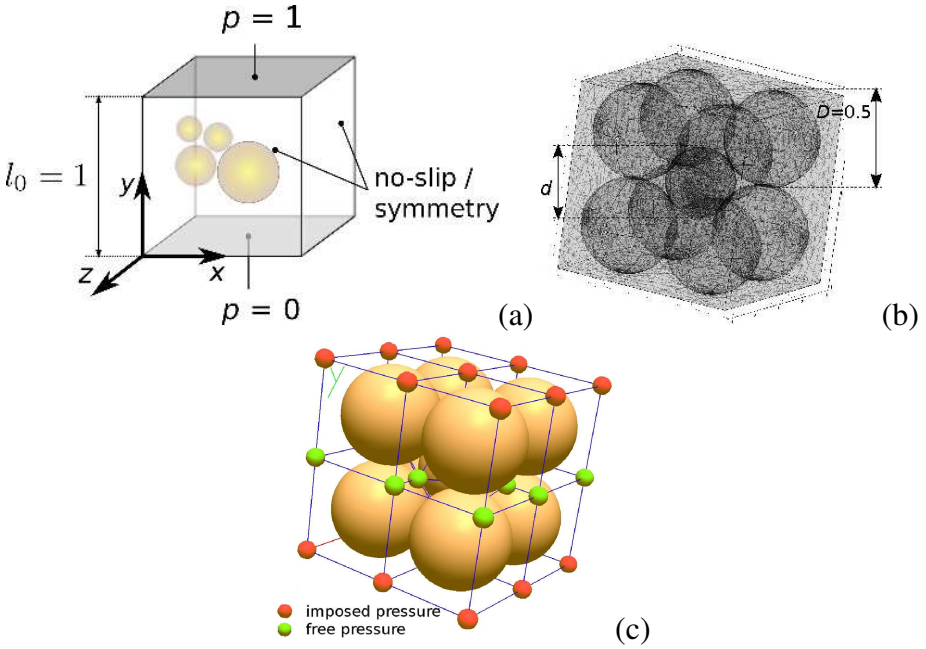

Figure 3.8: Boundary conditions of flow simulations (a), FEM mesh (b) and PFV mesh (c) of a 9-sphere packing. The PFV packings are plotted with Voronoi graph, where pressure values are defined at each point.

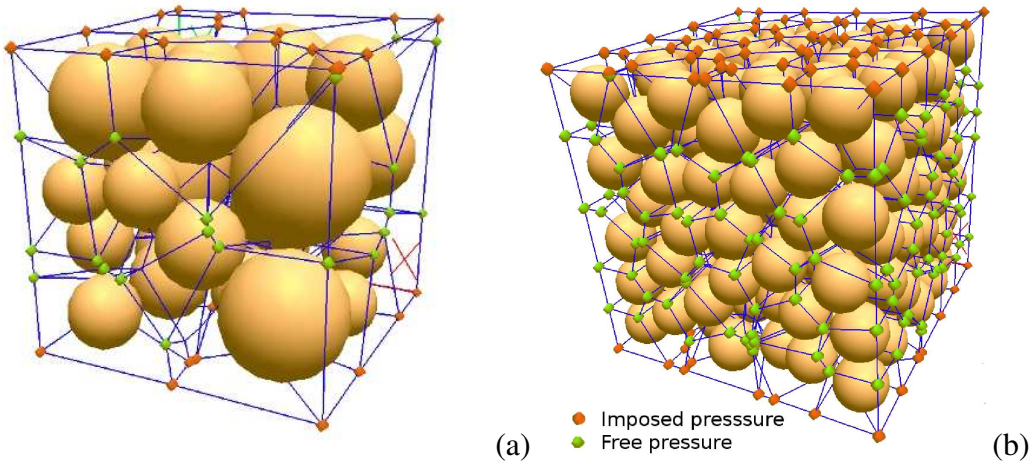

Figure 3.9: Packings of 25 and 200 spheres with corresponding Voronoi graph.

Nb. of spheres	FEM dof's	PFV dof's	FEM time$^{(a)}$ (s)	PFV time$^{(b)}$ (s)
9	1.7e5	45	300	0.00022
200	1.2e6	1093	5400	0.0046
2e3	(c)	11.6e3	(c)	0.091
2e4	(c)	11.3e4	(c)	2.21

Table 3.1: Compared DOF's and CPU time: (a) includes solving Stokes flow only, excludes preprocessing (e.g. mesh generation) and postprocessing (forces on spheres) done via a graphical user interface; (b) includes packing triangulation, solving, and computation forces on particles; (c) out-of-memory: no result.

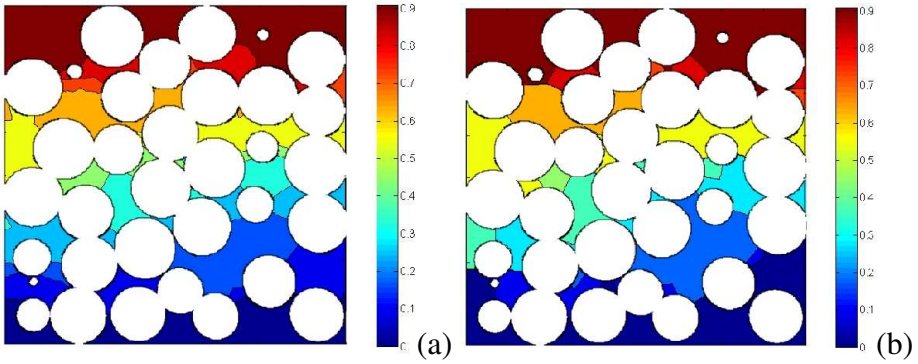

Figure 3.10: Isovalues of pressure in the 200 sphere packing on the plane $x = 0.5l_0$, obtained with FEM (a) and PFV (b).

3.5.2 Pressure Field

The pressure fields from FEM and PFV are compared on figure 3.10. Local conductances are defined as in eqs. (3.4-3.5). The isovalues in the PFV result are, by model definition (element-wise constant pressure), coincident with facets. Thus, the curvature of some isolines, as observed in FEM results, cannot be reproduced. The curvature of the isolines in the FEM solution is, however, usually very small, so that most of them are reasonably approximated by straight lines. Overall, the two fields compare well. The deviation from the horizontal isolines that would be obtained in an homogeneous continuum with same boundary conditions is relatively well reproduced by the PFV model.

On fig.3.11(a) it is shown the pressure field relative to an imposed horizontal pressure gradient. Fluid flow trajectories are represented as well. As it was the case on figure 3.10, most isolines are found near the necks of the flow paths, then it's here that the highest pressure gradients are expected to take place. On fig.3.11(b) the distribution of pressure gradients is shown, mainly concentrated at pores throats, thus justifying a posteriori the approximation of element-wise constant pressure used in the PFV scheme.

3.5.3 Fluxes

Two fluxes can actually be obtained from simulations: influx Q_i, and outflux Q_o at the respective boundaries (in the PFV model, they are computed by summing the q_{ij} of eq.(3.4) for elements where pressure is imposed). It was found that the difference between Q_i and

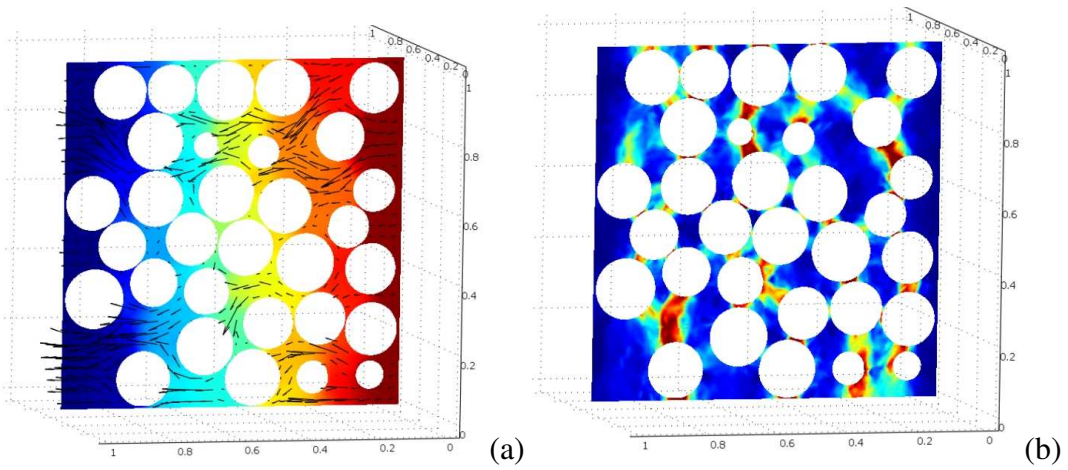

Figure 3.11: Local pressure gradients in the 200 sphere packing on the plane $x = 0.5l_0$, obtained with FEM.

Q_o is always negligible (less than $10^{-6} \times |Q_i|$). This is consistent with the incompressibility assumption and indicates a good convergence of the numerical solvers, be it in FEM (direct sparse solver Pardiso) or PFV (Gauss Seidel method). In the following, we define $Q = Q_i$. Fluxes are expressed in the form of normalized intrinsic permeability defined as $\kappa = \mu Q l_0/(\Delta P S^2)$ (see eq.(1.32) for the definition of κ), with $S = l_0^2$ the packing's cross-sectional area.

Permeabilities obtained with FEM and PFV for the different packings are compared on fig. 3.12. Both no-slip and symmetry conditions are considered for lateral boundaries. Comparison between the definitions of conductivity using the "hydraulic" radius (HR) of eq.(3.5) and Bryant's "effective" radius (ER) of eq.(3.6) are provided. This latter comparison only covers no-slip conditions, since the definition of effective radii in the symmetry case was ambiguous.

Symmetric boundary conditions give an average ratio of 1.01 between κ_{HR} and κ_{FEM}, with a maximum deviation of $+13\%$ for the 25-sphere packing. With no-slip conditions, the ratio are 0.78 for κ_{HR}/κ_{FEM} (max. deviation -40%) and 0.39 for κ_{HR}/κ_{FEM} (max. deviation -63%); κ_{HR} gives the best estimate of κ_{FEM} in all cases. The fact that the FEM results are better reproduced for symmetric conditions suggests that the fluxes along planes are underestimated. We consider, however, that the predictions of fluxes from hydraulic radii can be considered satisfactory overall.

The evolution of permeability in 9-sphere packings as a function of size d of the inner sphere's size (fig.3.8) is plotted on fig. 3.13. The evolution of κ with d/D is correctly reflected in HR-based results. Again, PFV results match FEM better for symmetric boundaries. ER-based simulations underestimate the fluxes by an average factor $\kappa_{ER}/\kappa_{FEM} = 0.43$.

It can be concluded that the initial value $\alpha = 1/2$ of the conductance factor entering eq. 3.4 tends to slightly underestimate fluxes on average. Although systematic comparisons could enable a better calibration of α, deviation from the FEM results is an inherent defect due to the approximations of the pore-scale description adopted here. Considering the small number of samples we tested, α has not been further adjusted to closely match FEM results.

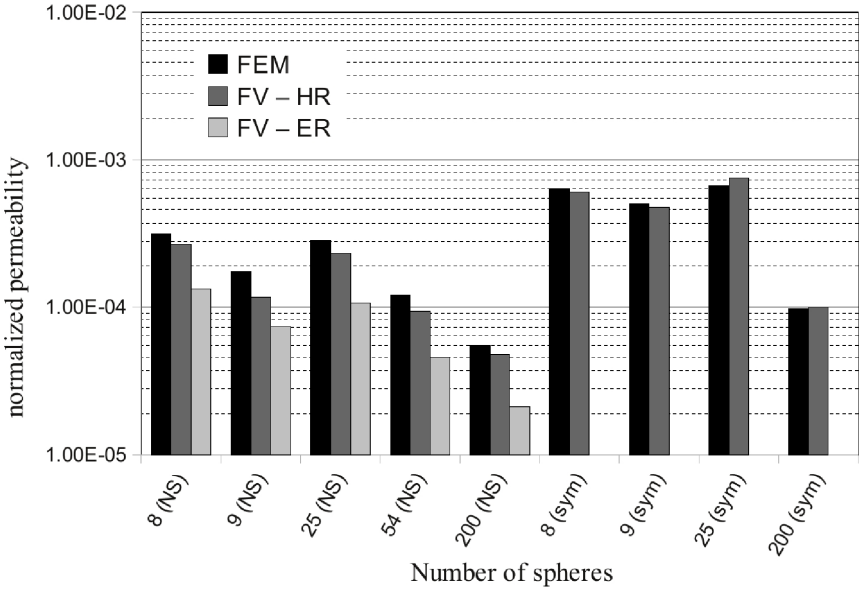

Figure 3.12: Predicted intrinsic permeability in FEM and PFV versus size of packing, for no-slip (NS) and symmetric (sym) boundary conditions. The PFV results include conductances defined using the hydraulic radius (HR - eq.(3.5)) and effective radius (ER - eq.(3.6)).

To investigate further the differences found between κ_{HR} and κ_{ER}, the values of R^h and R^{eff} obtained for all facets of the 200-sphere packing triangulation have been plotted (fig 3.14). Considering this distribution, it is obvious that the differences found between κ_{HR} and κ_{ER} reflect the fact that $R^h > R^{eff}$ on average at the local scale.

A small number of points fall outside the well-correlated cloud, for which $R^{eff} > R^h$. A close inspection of the outliers revealed that these correspond to special cases similar to the one represented on fig. 3.14, where a flat triangle results in the inscribed circle overlapping outside its original facet. In such a situation, the inscribed circle will eventually overlap other inscribed circles or spheres of the packing, thus losing physical consistency. It leads us to conclude that the hydraulic radius is overall a more robust description of the local void geometry.

3.5.4 Forces

Forces on particles and boundaries, as defined in section 3.3, have been obtained for all packings using the PFV scheme. In all cases, the sum of pressure and viscous forces on spheres and boundaries is, as expected, close to $\Delta P \times S$ ($\pm 10^{-5}\%$), where S is the packing's cross-sectional area. Comparison for the 8-sphere packing is trivial: $F_i = S \times \Delta P/8$ on each sphere for both FEM and PFV, modulo numerical errors. A detailed comparison is presented here only for the 9-sphere packings, for which contour integrals for fluid stress in the FEM models (the FEM results in table 3.2) have been collected.

Table 3.2 gives the total fluid forces per element for the solid phase, and details the viscous and pressure contributions. The viscous force on lateral boundaries, total force on big spheres, and total force on the center sphere are all approximated with an error smaller than 10%. Surprisingly, the prediction is less good for individual viscous and pressure contributions than for the total force. The viscous part is overestimated, while

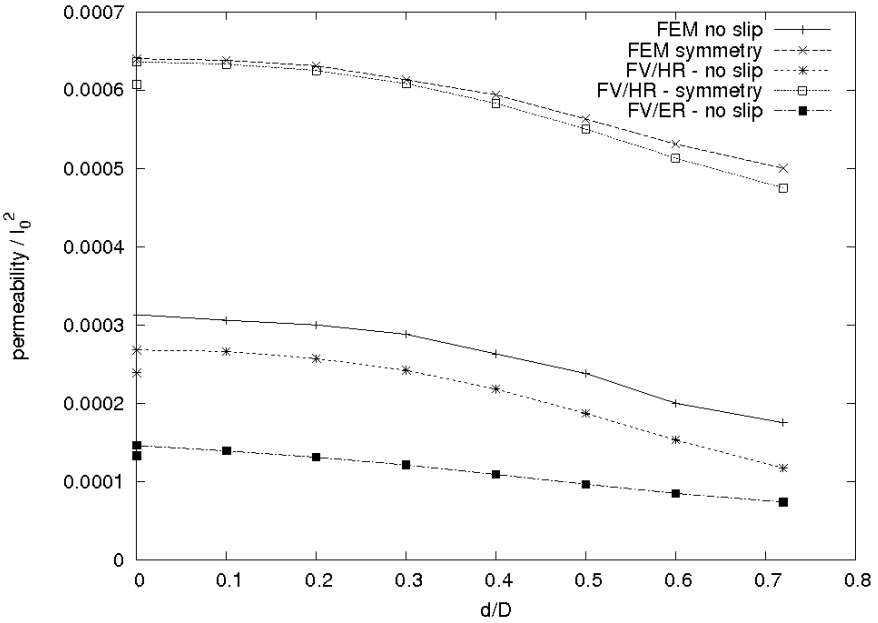

Figure 3.13: Permeability of 9-sphere packings versus size of the the central particle.

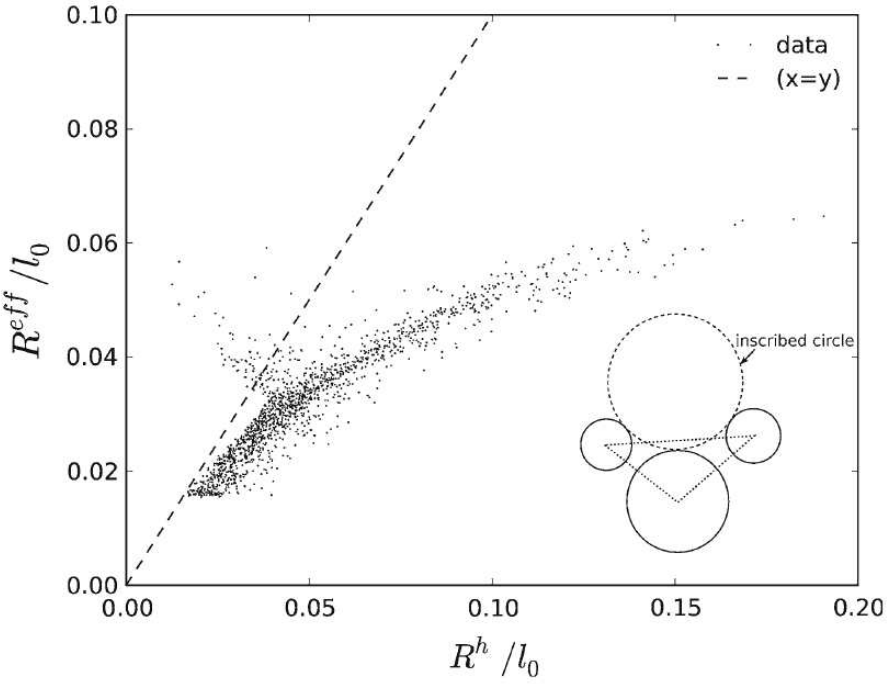

Figure 3.14: Effective radius versus hydraulic radius for all facets in the 200 grains packing (a), with example of a facet giving $R_{ij}^{eff} > R_{ij}^{h}$.

	FEM	PFV
Forces on one big sphere (y-component)		
viscous force	1.51×10^{-2}	1.06×10^{-2}
pressure force	9.09×10^{-2}	9.64×10^{-2}
total	1.06×10^{-1}	1.07×10^{-1}
Forces on the small sphere (y-component)		
viscous force	9.38×10^{-3}	5.83×10^{-3}
pressure force	5.17×10^{-2}	5.72×10^{-2}
total	6.04×10^{-2}	6.30×10^{-2}
Forces on boundary x=0		
viscous force (y-component)	2.27×10^{-2}	2.03×10^{-2}
pressure force (x-component)	$4.98 \times 10^{-}1$	$5.00 \times 10^{-}1$
Total force on the solid phase		
y-component	$1 - 5.56 \times 10^{-4}$	$1 + 1.18 \times 10^{-4}$

Table 3.2: Normalized forces in 9-sphere packings ($d/D = 0.72$). All forces are divided by $S \cdot \Delta P$, so that the sum of all forces should be exactly 1.

the pressure effect is underestimated. The two-error compensation results in a smaller error on the total force.

The evolution of force terms and error for the center sphere is given on fig. 3.15. This result shows an increasing error with decreasing d/D. For $d/D < 0.1$, the PFV scheme underestimates the force on the the center sphere by a factor 2. This suggest a limitation of the current formulation in the limit of (1) high contrasts in particles size, and/or (2) small particles "floating" in the voids between big ones. Here again, more investigations are needed in order to determine what situation exactly is generating this deviation from the FEM solution. As long as $d/D > 0.2$, though the predicted force is very well predicted, with error less than 10%. It is observed that similar forces are obtained with hydraulic radius (HR) and effective radius (ER).

We note that even if the total force were always increasing with d, the viscous component reaches a maximum near $d/D = 0.6$. The existence of this peak can be understood by considering the flow in a sufficiently long tube of diameter D obstructed by a sphere of diameter d as resulting from a fluid pressure dP imposed between the ends of the tube. For $d = D$, the total force on the sphere is maximum ($\pi D^2/4 \times dP$), while the viscous contribution is $F^v = 0$, as the fluid velocity and the corresponding viscous stress equal zero. On the other hand, when D tends to 0, then the viscous component F^v vanishes along with the total fluid force. When $0 < d < D$, then F^v takes on a finite value, implying the existence of a value of d for which F^v reaches a maximum. Such a maximum in the value of F^v can be also observed from our results (see fig. 3.15), although for more complex geometries.

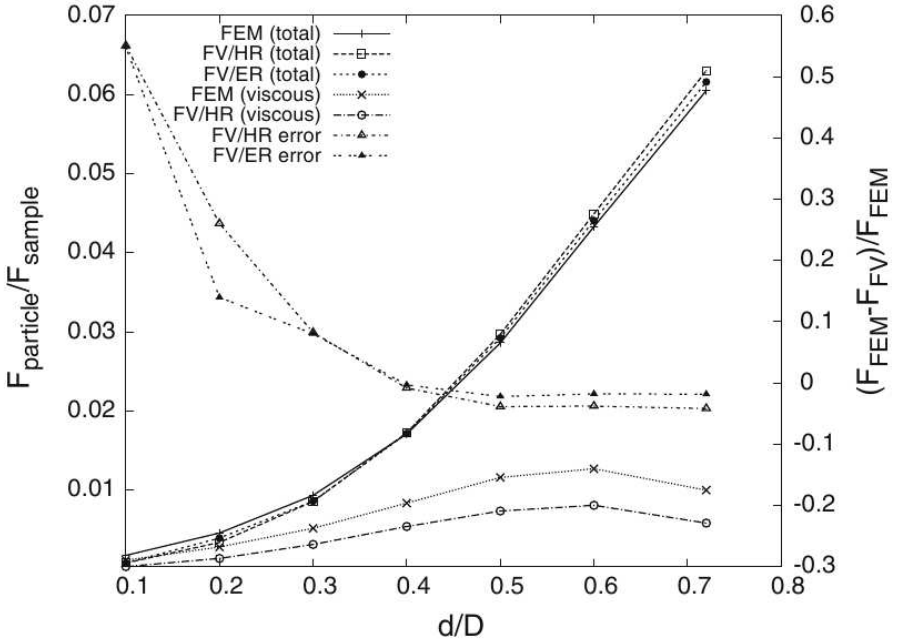

Figure 3.15: Total force and viscous force applied on a particle of size d, placed in the center of a cubic packing of eight particles of size D, in FEM simulations, PFV simulations based on hydraulic radius (HR), and PFV simulations based on effective radius (ER). Forces are normalized by F_{sample}, the total force on the packing.

Chapter 4

DEM-PFV coupling

This chapter will be devoted to the description of the coupling strategy of the PFV model with the discrete element method, as it has been implemented in the open-source code YADE [101]. The final algorithm will be presented. Considering a deformable porous media, we will see how the coupling equations we've presented may be seen as a discrete form of the field equations of conventional Biot's theory of poroelasticity. By such comparison, the DEM-PFV coupled model should be able to recover the results of classical poroelasticity in boundary value problems, provided they share similar assumptions. The 1D diffusion problem known as Terzaghi's consolidation is well suited for such comparison. It will be presented as a benchmark test for the validation of the model.

4.1 The solid phase

4.1.1 The open-source code YADE

The code Yade, "Yet Another Dynamical Engine", is an open-source C++ framework which allows the development of three dimensional discrete numerical models. Thanks to modularity and open source (GPL) licensing, the code capabilities are continuously evolving thanks to the contribution of users that have access to the code sources, can build their own model, and freely add ex-novo new modules or simply modify the existing ones. A few months usage of the code makes a user become a developer, a bugs finder and solver (and a source of new bugs at the same time!).

4.1.2 Contact definition

As in many other codes which implement the DEM, in YADE the solid particles are modelled as spheres interacting between each other according to the defined contact laws. These spheres are identified independently by their radius R, their mass m and moment of inertia I_0. At each time step, the position of each particle is computed by integration of the Newton's second law of motion, as function of the forces and moments that are applied on it. In the simplest case, the parameters which are defined at contacts are a normal and a tangential stiffness k_n and k_t, and an inter-granular friction angle ϕ_c. Such configuration may vary if a more complex description of local interactions is needed to derive a given

macroscopical effect, or in case of non-spherical shaped particles. For further details, refer to section 2.1.

Considering the objectives of the PFV model, there is no need in increasing the complexity of the interaction law from the case that was presented in section 2.1.2. Therefore, the computation of elastic forces and rotational moments to be applied to each particle will be based on eq.s (2.8, 2.9, 2.12), according to the contact law as it has been shown on fig.2.3 and fig.4.1.

The definition of contact stiffnesses is based on considerations regarding the consistency with the small lengths we deal with, at the scale of particle interactions. Thus, to ensure a relative position between two spheres in contact to be proportional to a characteristic dimension that could characterize such interaction, the normal and shear stiffnesses are computed as function of a global stiffness modulus E_{global}, and the harmonic mean of the interacting spheres' radius, R_1 and R_2, as follows:

$$k_n = 2E_{global} \cdot \frac{R_1 \cdot R_2}{R_1 + R_2} \tag{4.1}$$

$$k_t = a\,k_n \tag{4.2}$$

The shear stiffness k_t is defined as a fraction a of the normal stiffness. The introduction of E_{global} allows the homogenization of the elastic behaviour at the scale of the assemblies and ensures the independence of their global stiffness with the size of the particles.

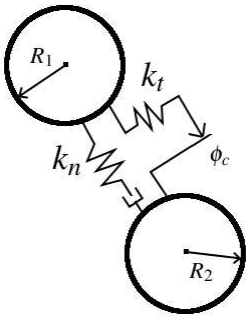

Figure 4.1: Normal and shear stiffnesses at contacts.

4.2 Coupled problem

The PFV model is finally ready to be implemented and coupled to the DEM model for the simulation of hydromechanical problems. Fig.4.2 shows the flow chart relative to the only flow model.

At the microscopic scale, the coupling is defined by two equations. One is eq.(3.2) where the left hand side is a function of the velocity of the solid particles. The other is obtained by introducing the fluid forces in the fundamental equation of the DEM (2.1), which becomes:

$$M_i \ddot{x}_i = F_i^c + M_i\, g + F_i^f, \tag{4.3}$$

where F_i^c and F_i^f are the contributions of contact forces and fluid forces, respectively.

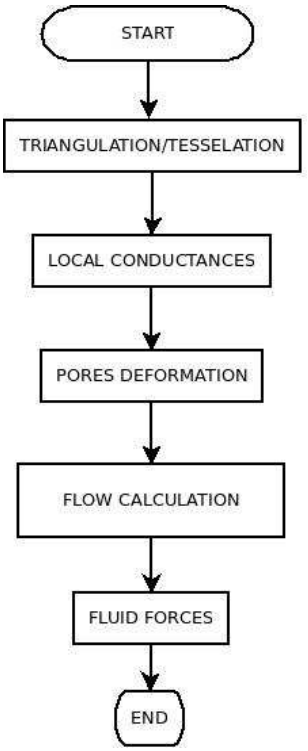

Figure 4.2: The PFV algorithm.

By assembling the continuity equation (3.2) and the law of motion (4.3) respectively for all volume elements Θ_i of fig.3.3 and all particles, we obtain two matrix relations linking the generalized displacements to the pressure field:

$$[\mathbf{G}]\{\mathbf{P}\} = [\mathbf{E}]\{\dot{\mathbf{X}}\} + \{\mathbf{Q_q}\} + \{\mathbf{Q_p}\} \tag{4.4}$$

$$[\mathbf{M}]\{\ddot{\mathbf{X}}\} = \{\mathbf{F^c}\} + \{\mathbf{W}\} + \{\mathbf{F^f}\} \tag{4.5}$$

where **G** and **P**, already defined in section 3.5 are the conductivity matrix containing terms g_{ij}/L_{ij} and the column vector containing all (unknown) values of pressure, respectively. **E** is the matrix defining the rates of volume change such that $\Delta\dot{V}_i^f = (\mathbf{E}\dot{X})_i$, **W** is the vector containing particles weights, $\mathbf{Q_q}$ and $\mathbf{Q_p}$ are the vectors containing respectively the source terms for imposed fluxes, and the products $p_i \cdot g_{ij}/L_{ij}$ for imposed pressures.

From the derivation of fluid forces described in section 3.3, one can write $\mathbf{F^f}$ in matrix form as a function of the pressure field **P** and a matrix **S** reflecting the local geometry of the pore space (eq.s 3.10, 3.13):

$$\{\mathbf{F^f}\} = [\mathbf{S}]\{\mathbf{P}\} \tag{4.6}$$

Combining equations (4.4) and (4.5), we end up with a differential equation, where X is the only remaining unknown:

$$\{\ddot{\mathbf{X}}\} = [\mathbf{M}]^{-1}(\{\mathbf{F^c}\} + \{\mathbf{W}\} + [\mathbf{S}][\mathbf{G}]^{-1}([\mathbf{E}] \cdot \{\dot{\mathbf{X}}\} + \{\mathbf{Q_q}\} + \{\mathbf{Q_p}\})) \tag{4.7}$$

4.2.1 Network definition

The network model has been implemented in C++, and is freely available as an optional package of the open-source software Yade [94]. The C++ library CGAL [36] is used for

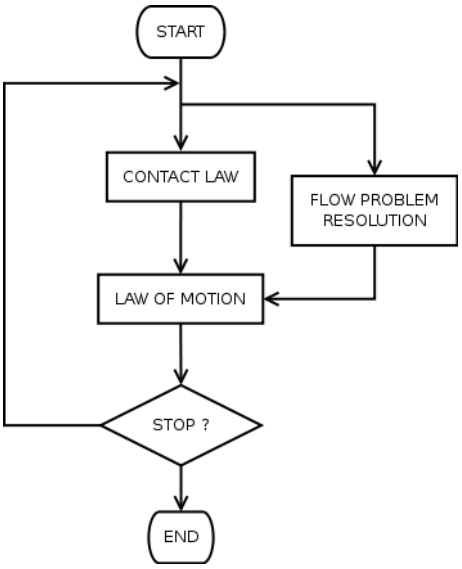

Figure 4.3: Coupled DEM-Flow computation cycle

the triangulation procedure. This library ensures exact predicates and constructions, and is one of the fastest computational geometry codes available [58]. It is worth noting that regular triangulation involves squared distance comparisons exclusively, thus avoiding time-consuming square roots and divisions. The computation of forces of eq. (3.15) also requires only simple vector multiplications. The only non-trivial operation is the computation of solid angles needed to define the volumes and surfaces associated to sphere-tetrahedron intersections, to be used in eq. (3.5). This cost can be reduced significantly, however, using the algorithm of Oosterom and Strackee [71].

4.2.2 Time integration

Although formally correct, the relation of eq. (4.7) won't be used directly, as it would result in the computation of the inverse of matrix $\mathbf{G}$, resulting in suboptimal performances of the scheme and large memory usage. Instead, $\mathbf{P}(\mathbf{t})$ will be obtained by solving the implicit relation (4.4) where $\dot{X}$ is approximated by a first order (explicit) backward Euler scheme:

$$[\mathbf{G}]\{\mathbf{P}(t)\} = [\mathbf{E}]\left(\frac{\mathbf{X}(t-\delta t)-\mathbf{X}(t)}{\delta t}\right) + \mathbf{Q_s}(t) + \mathbf{Q_p}(t). \tag{4.8}$$

The computed pressure field is then used in eq. (4.6) to compute fluid forces at time t. In turn, the fluid forces are injected in eq.(4.5), which is finally integrated with the explicit scheme of standard DEM.

Fig.4.3 shows a schematized view of the final coupled algorithm. To conclude, the discrete element method, as it is implemented in the open-source code YADE [101], had been used to model the mechanics of solid phase. The library CGAL was employed for the triangulation procedure [36]. To solve the system of eq.(4.4), the Gauss-Seidel method had been implemented, and the direct solvers for sparse linear systems PARDISO [86] [87] and TAUCS [98] have been also used.

4.2.3 Stability of the coupled algorithm

In coupled simulations, the fluid surrounding particles acts as a viscous damper, proportional to the rate of sollicitation, resulting in a force to be added to the elastic force, as it has been described in section 3.3. The expression of eq.(4.7) describes the dynamic of a mass-spring-dashpot MDoF (Multiple Degrees of Freedom) system and can be rewritten in its classical form:

$$[\mathbf{M}]\{\ddot{\mathbf{X}}(t)\} + [\mathbf{V}(t)]\{\dot{\mathbf{X}}(t)\} + [\mathbf{K}(t)]\{\mathbf{X}(t)\} = 0 \tag{4.9}$$

where $\mathbf{M}$,$\mathbf{V}(t)$ and $\mathbf{K}(t)$ express the global mass, viscosity and stiffness matrices. We can write eq. (4.9) for a single particle k:

$$M^k\ddot{X}^k(t) + V^k(t)\dot{X}^k(t) + K^k(t)X^k(t) = 0 \tag{4.10}$$

where $V^k(t)$ and $K^k(t)$ are the equivalent viscous and stiffness matrices that can be associated to the particle k, at time t. We can rewrite eq. (4.10) as follows:

$$\ddot{X}^k(t) + \frac{V^k(t)}{M^k}\dot{X}^k(t) + \frac{K^k(t)}{M^k}X^k(t) = 0 \tag{4.11}$$

Such expression describes the dynamic of a mass-spring-dashpot system, whose stability is influenced by both the viscous and the stiffness terms of eq.(4.11). Following a simplified approach, the influence of the two terms will be considered and treated independently: considering the viscosity effect as minor compared to the stiffness, a time step Δt_{M-K} is defined (see eq.(2.14)), in relation to the elastic-plastic problem, as it has already been described in section 2.1.3; otherwise, considering the viscosity effect as dominant compared to stiffness, a time step Δt_{M-V} will be defined, in relation to the viscous problem.

For the generic particle k, we consider the following relation:

$$M^k\ddot{X}^k(t) + V^k(t)\dot{X}^k(t) = 0 \tag{4.12}$$

where $V^k(t)$ is the viscosity matrix whose components $V^k_{ij}(t)$ are the viscous coefficients that can be associated to the particle k during its motion along the i direction ($i = 1,2,3$, translational degrees of freedom). We can write, for a given direction:

$$\frac{\dot{X}^k(t+\delta t) - \dot{X}^k(t)}{\delta t} + \frac{V^k(t)}{M^k}\dot{X}^k(t) = 0 \quad \rightarrow \quad \dot{X}(t+\delta t) = (1 - \frac{V^k(t)}{M^k}\delta t)\dot{X}^k(t) \tag{4.13}$$

A condition for the stability of an explicit integration scheme for the solution of such problem is ensured by imposing:

$$\mid 1 - \frac{V^k(t)}{M^k}\delta t \mid < 1 \tag{4.14}$$

We finally obtain:

$$\delta t = \Delta t_{M-V} < 2 \cdot min_k \left(\frac{M^k}{V^k(t)} \right) \tag{4.15}$$

In the following sections we will analyze the distribution of viscous coefficients for a dense granular sample, in order to extrapolate a unique formulation that could allow

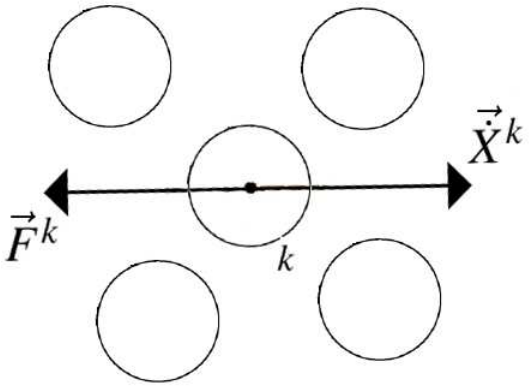

Figure 4.4: Evaluation of the magnitude and orientation of the viscous effects. $\vec{A}$

an easy computation of the critical time step for a coupled simulation. We will primarly investigate the fluid viscous response to particle motion, to justify the evaluation of the $V^k(t)/M^k$ ratio for the three translational degrees of freedom for each particle, supposing them independent to each other. Secondly, the dependence of viscous coefficients in the average size of the particles will be investigated on various samples, similar to each other, which are made vary homothetically. Finally, the influence of granular size polydipersity is investigated. This procedure allows the analysis of the distribution of the $V^k(t)/M^k$ ratios for the sphere packings we will use in our simulations, and define a final unique formulation to estimate the time step to ensure stable calculations.

Per-particle viscosity

The orientation and magnitude of the viscous effects will be investigated in this section, by imposing a non-zero velocity to a particle and measuring the resultant viscous force that results from its motion in the fluid. In a three-steps procedure, imposing a translational velocity $(\dot{X}^k)_i$ according to the cartesian global reference system ($\dot{X}_1^k = \{1,0,0\}$, $\dot{X}_2^k = \{0,1,0\}$, $\dot{X}_3^k = \{0,0,1\}$, see fig.4.4), we can easily build the particle viscosity matrix V^k of eq.(4.10).

$$\begin{bmatrix} F_1^k \\ F_2^k \\ F_3^k \end{bmatrix} = - \begin{bmatrix} V_{11} & V_{12} & V_{13} \\ V_{21} & V_{22} & V_{23} \\ V_{31} & V_{32} & V_{33} \end{bmatrix}^k \begin{bmatrix} \dot{X}_1^k \\ \dot{X}_2^k \\ \dot{X}_3^k \end{bmatrix}$$

We define, for a generic particle k:

$$V_{ij}^{*k}(t) = \frac{V_{ij}^k}{\mu} \tag{4.16}$$

where μ is the fluid viscosity, in Pa·s. V^* is thus only a function of the microstructure's geometry.

A monodisperse sphere packing have been initially considered, characterized by a ratio between the maximum and the minimum sphere diameter $d_{max}/d_{min} = 1.02$. Here is

a typical result that was obtained:

$$[V^{*k}(t)] = \begin{bmatrix} 85.7542744366 & 1.28216628154 & -1.93136379912 \\ 4.26512968579 & 46.211183304 & 0.858032308546 \\ -0.360344163069 & 2.79451599051 & 76.5480416898 \end{bmatrix}$$

The $V^{*k}(t)$ matrix is diagonal dominant, and non-diagonal terms are negligible compared to diagonal terms. The computed force is in fact aligned to the direction of the imposed displacement (drag force). This is confirmed having a look to the terms of D^{*k}, the diagonalized matrix of $V^{*k}(t)$,

$$[D^{*k}] = \begin{bmatrix} 85.90434703 & 0 & 0 \\ 0 & 45.97588642 & 0 \\ 0 & 0 & 76.63326597 \end{bmatrix}$$

Also the matrix E^{*k} is computed, containing on the diagonal the errors $E^{*k}_{ii} = \frac{|V^{*k}_{ii}(t) - D^{*k}_{ii}|}{V^{*k}_{ii}(t)}$:

$$[E^{*k}] = \begin{bmatrix} 0.2\% & 0 & 0 \\ 0 & 0.5\% & 0 \\ 0 & 0 & 0.1\% \end{bmatrix}$$

The informations we get by such results allow us this approach for the evaluation of the viscous terms $V_{k,ii}$ that will be used to evaluate the ratio $M^k/V^k(t)$ of eq. (4.15). Then, a viscous coefficient will be evaluated for each one of the three translational degrees of freedom, assumed as independent to each other.

Let's considere a polydisperse sphere packing, with $d_{max}/d_{min} = 10.0$. Here follows the result that was obtained:

$$[V^{*k}(t)] = \begin{bmatrix} 40.9920695914 & -5.38402761747 & -1.59448195147 \\ -5.38716958348 & 67.4306069655 & -6.48875764797 \\ -2.05057994865 & -0.771351357994 & 43.0371345081 \end{bmatrix}$$

Again, the computed matrix is diagonal dominant. As already done above, we diagonalize $V^{*k}(t)$:

$$[D^{*k}] = \begin{bmatrix} 38.55811208 & 0 & 0 \\ 0 & 68.57243018 & 0 \\ 0 & 0 & 44.3292688 \end{bmatrix}$$

and compute the errors E^{*k}_{ii}:

$$[E^{*k}] = \begin{bmatrix} 6.0\% & 0 & 0 \\ 0 & 1.7\% & 0 \\ 0 & 0 & 2.9\% \end{bmatrix}$$

As a consequence of the strong polydispersity, the errors which are committed neglecting the non-diagonal terms of $V^{*k}(t)$ are higher than in the monodisperse case. However, the scope being the estimation of the order of magnitude of the viscous coefficients to be used in eq. (4.15), the followed approach remains consistent.

In the following sections we compute the diagonal terms of the local viscous matrix for the generic sphere k, performing a parametric analysis that could allow us to characterize its relation in the particle size, expressed by the diameter d_k, in the packing characteristic dimension, generally addressed by the average diameter d_{av} and the dispersion degree, expressed by the ratio between the maximum and minimum particle diameter, d_{max}/d_{min}.

Average size dependence

We investigate here the dependence of the viscous coefficients in the average size of the sphere packing. A monodisperse sphere packing is considered ($d_{max}/d_{min} = 1.02$), and the size of all particles vary homothetically. The evolution of $V_{ii}^{*k}(t)$ as function of the homothety ratio is shown on fig.4.5a. A dependence on the average size of the particles that compose the packing is originally remarquable on fig.4.5a and confirmed on fig.4.5b, where the ratio $V_{ii}^{*k}(t)/d_k$ is plotted, where d_k represents the diameter of the particle. From fig.4.5b, we can write:

$$\frac{V_{ii}^{*k}(t)}{d_k} = cst = \beta_{ii}^k \tag{4.17}$$

and a first expression for the $M^k/V^k(t)$ ratio of eq. 4.15 can be formulated:

$$\frac{M^k}{V_{ii}^k(t)} = \frac{4/3\,\pi\,\rho_k\,(d_k/2)^3}{\beta_{ii}^k\,\mu\,d_k} = \frac{1}{6}\frac{\pi\,\rho_k\,\phi_k^2}{\beta_{ii}^k\,\mu} \tag{4.18}$$

where ρ_k expresses the particle density, in kg/m^3.

We can not already use such expression, because we don't know how the $M^k/V^k(t)$ ratio varies in case of strong polydispersity. That's the objective of the next section.

Polydispersity dependence

The variability of the $V_{ii}^{*k}(t)/M^k$ ratio as function of the dispersion degree is investigated on a particle k, whose diameter d_k is gradually reduced while keeping unchanged all the other spheres sizes. Fig.4.6a shows the evolution of the $V_{ii}^{*k}(t)/M^k$ ratio as function of the ratio between the particle diameter d_k and the average diameter d_{av}. Two zones can be distinguished: a first one, for $10^{-5} \leq d_k/d_{av} \leq 10^{-1}$, where the $V_{ii}^{*k}(t)/M^k$ ratio is observed to be highly sensitive to the variation of d_k, and a second one, for $10^{-1} < d_k/d_{av} \leq 1$, where the $V_{ii}^{*k}(t)/M^k$ ratio varies within a narrow range of values as d_k changes. Such consideration finds a confirmation on fig.4.6b: the $V_{ii}^{*k}(t)/M^k$ ratio is in the order of magnitude of units for the above-stated range of the ratio d_k/d_{av}.

Fig.4.7(a,b) clarifies our considerations, showing the evolution of $V_{ii}^{*k}(t)$ and comparing it to the squared and the cubic power of the diameter, d_k^2 and d_k^3, respectively. For $10^{-5} < d_k/d_{av} < 10^{-1}$ the evolution of $V_{ii}^{*k}(t)$ is found to be steadily proportional to the square of the diameter of the particle, whereas it deviates for $10^{-1} < d_k/d_{av} < 1$, where its evolution is proportional to the cubic power of the diameter, hence to the mass of the particle, as it can be seen on fig.4.6b. We can finally state that eq. (4.18) can be used to estimate the time step to be used in coupled simulations, provided that $10^{-1} < d_k/d_{av} < 1$, that is usually the case in simulations. However, the introduction of a safety factor is needed, to take into account of the (even if narrow) variability of the $V_{ii}^{*k}(t)/M^k$ ratio within such range of validity, as it was shown on fig.4.6b. If a higher degree of dispersion with respect to the average diameter is needed, eq. (4.18) could fail and the stability of the computation could not be guaranteed.

Damping distribution

To finally give a correct estimation of the β parameter of eq.(4.18) for the estimation of Δt_{M-V}, the value of the ratio $V_{ii}^{*k}(t)/d_k$ is computed for all the particles of three sphere

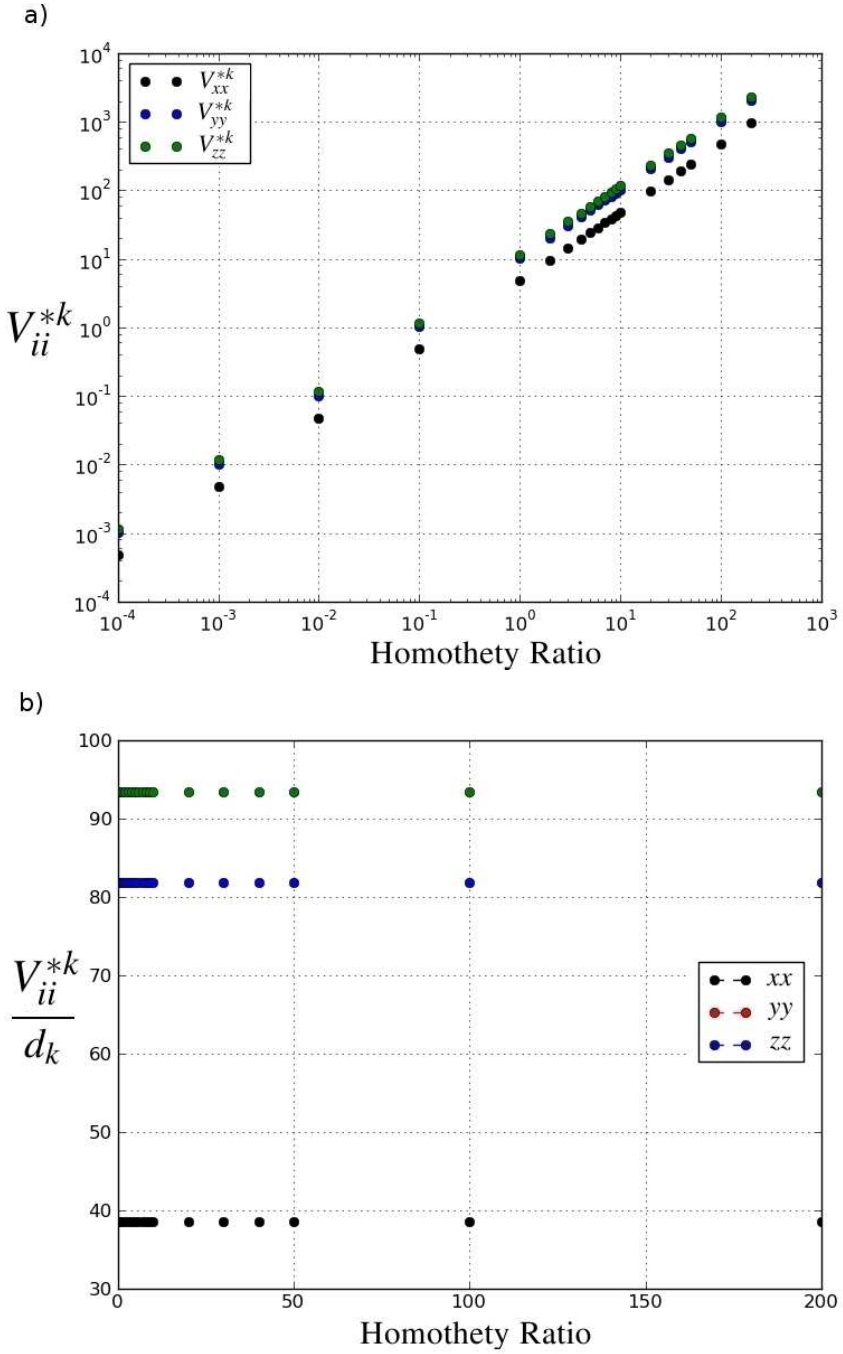

Figure 4.5: Variation of $V_{ii}^{*k}(t)$ parameter (a) and $V_{ii}^{*k}(t)/d_k$ ratio (b) as function of the homothety ratio.

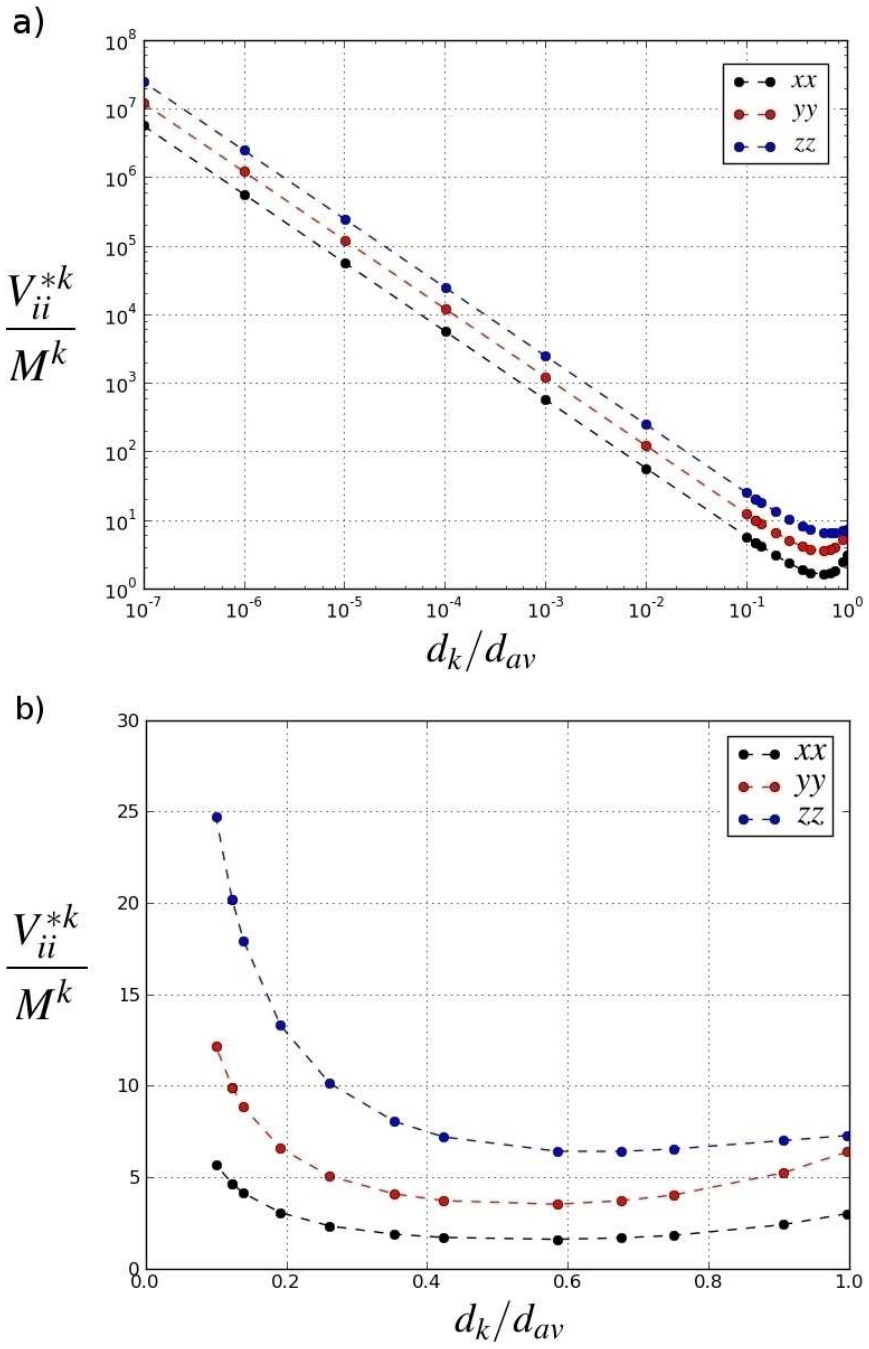

Figure 4.6: Evolution of the $V_{ii}^{*k}(t)/M^k$ ratio as function of the relative particle diameter.

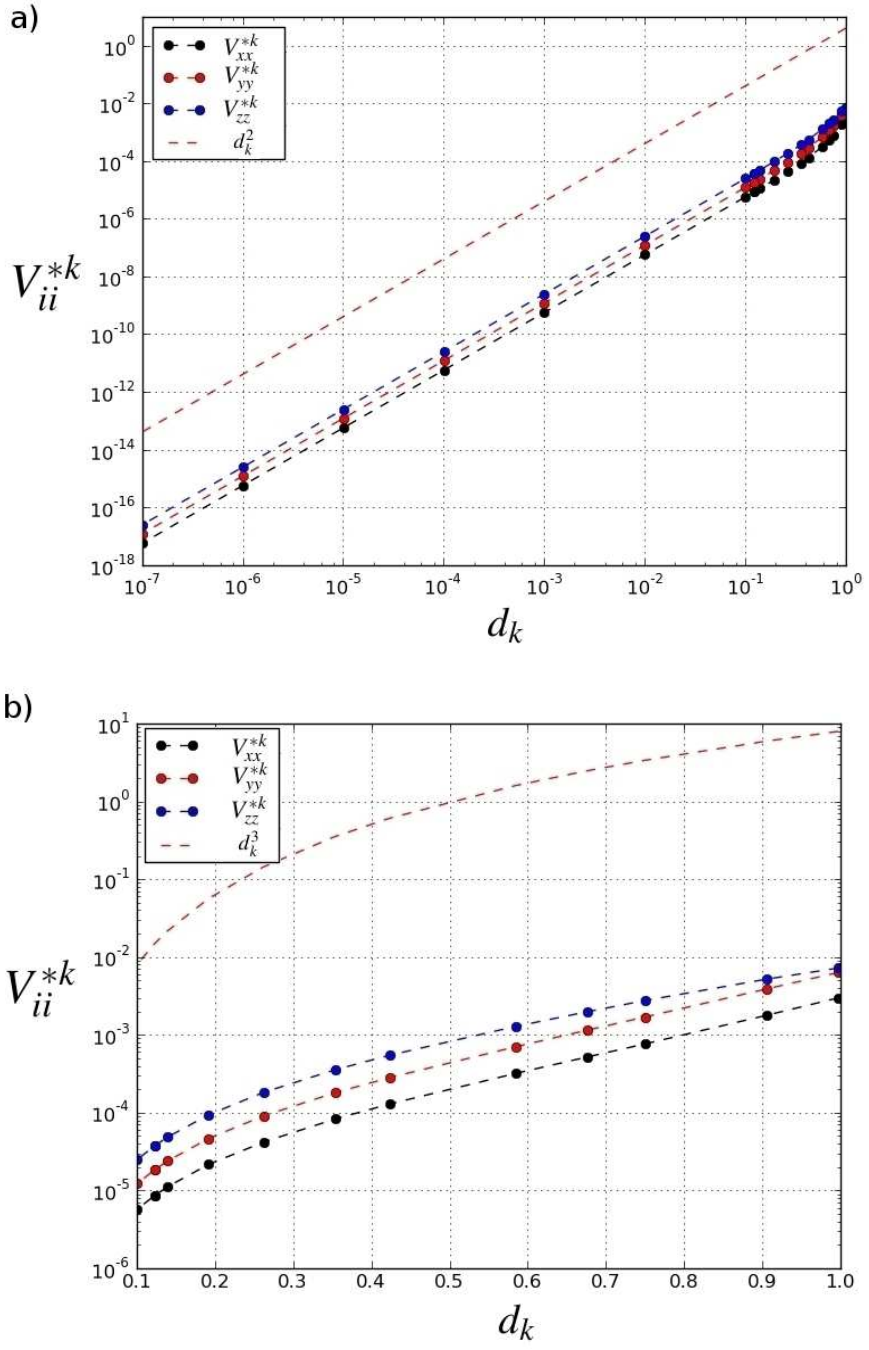

Figure 4.7: Evolution of the $V_{ii}^{*k}(t)$ ratio.

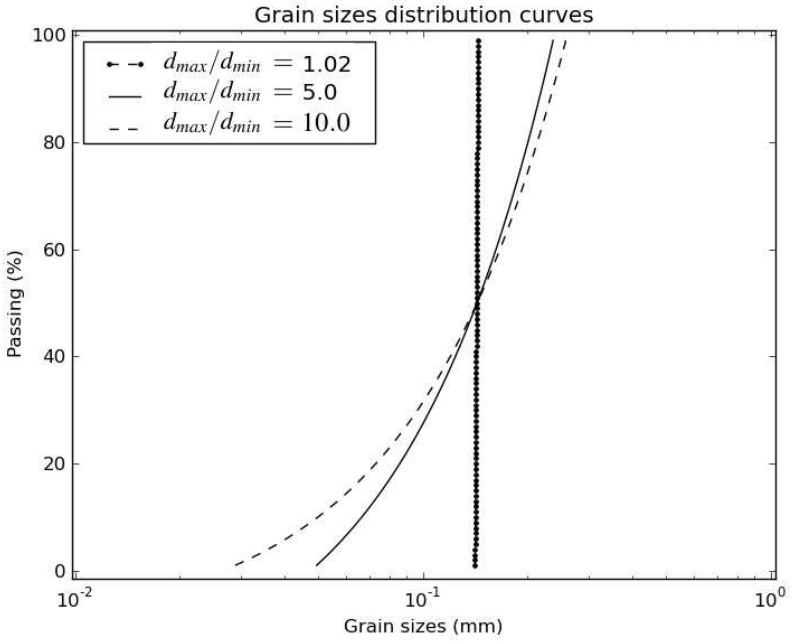

Figure 4.8: Granulometry of the sphere packings for the estimation of β parameter

packings characterized by a different degree of dispersion, a monodisperse and two polydisperse cases. The granulometry of these samples is shown on fig.4.8.

A frequency distribution of $V_{ii}^{*k}(t)/d_k$ ratio is obtained and shown on fig.4.10(a-b-c). As expected, the highest values are found for the packing characterized by the highest dispersion ($d_{max}/d_{min} = 10.0$). A relative homogeneous distribution is observed for the monodisperse case, as it is obvious. For the sake of completeness, a frequency distribution of the $V_{ii}^{*k}(t)/d_k$ ratio was obtained also for three loose samples, probing the influence in the grain sizes dispersion as done for the dense samples. Results are shown on fig.4.11(a-b-c). As it could be expected, the looser is the sphere packing, the lower are the viscous effects acting on a particle, the fluid encountering less narrow paths while flowing within the particles.

Assuming that a ratio between the biggest and the smallest particle $d_{max}/d_{min} = 10.0$ is large enough to cover all the cases of interest in our study, we finally adopt $\beta = 400.0$, we can rewrite eq. (4.18) as follows:

$$\frac{M^k}{V_{ii}^{*k}(t)} = \frac{1}{2400}\frac{\pi\rho_k d_k^2}{\mu} \tag{4.19}$$

The final expression to estimate the time step to estimate Δt_{M-V}, using eq. (4.15), become:

$$\Delta t_{M-V} < \frac{1}{1200}\frac{\pi\rho_k d_k^2}{\mu} \tag{4.20}$$

Fig.4.9 shows an example of application of eq.(4.20) for the estimation of a stable time step for a coupled simulation. The overall kinetic energy (summation of each particle's kinetic energy) is plotted as an indicator of the stability of the sample, as function of the time step, that is gradually increased up to a condition of instability, clearly identifiable

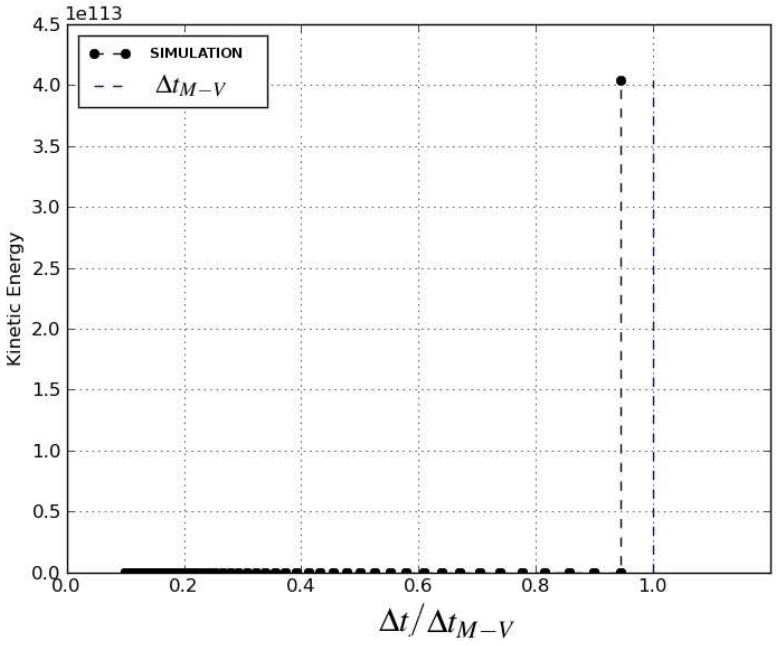

Figure 4.9: Application of eq.(4.20) for the estimation of the viscous time step Δt_{M-V}.

on the diagram. Instability occurs for a time step which is $\sim 0.95 * \Delta t_{M-V}$, confirming the consistency of our assumptions.

Critical time step for the coupled problem

We end up with the definition of an upper limit for the time step to ensure the stability of simulations, expressed by eq. (2.14) or eq. (4.15) in case of dominant effect of the stiffness or the viscosity, respectively. The time step to be used in a simulation will be:

$$\Delta t = min(\Delta t_{M-K}, \Delta t_{M-V}) \tag{4.21}$$

However, it is clear how such *limit condition* approach is susceptible to fail in cases where the stiffness and the viscous effects on the system dynamic are comparable. In such conditions, more complex factors have to be taken into account for a rigorous formulation of a stability condition for the algorithm. Our choice was to persist following the simplified approach, by introducing a safety factor to both Δt_{M-K} and Δt_{M-V}, which will be taken as a fraction of the time step previously defined, as follows:

$$\Delta t = \zeta \cdot min(\Delta t_{M-K}, \Delta t_{M-V}) \qquad \zeta < 1 \tag{4.22}$$

An example of application of eq.(4.22) with $\zeta = 0.8$, is shown on fig.4.12.

4.3 Relation with classical poromechanics

The coupling equations we've presented may be seen as a discrete form of the field equations of conventional Biot's theory of poroelasticity, as it was presented in section 1.3.1.

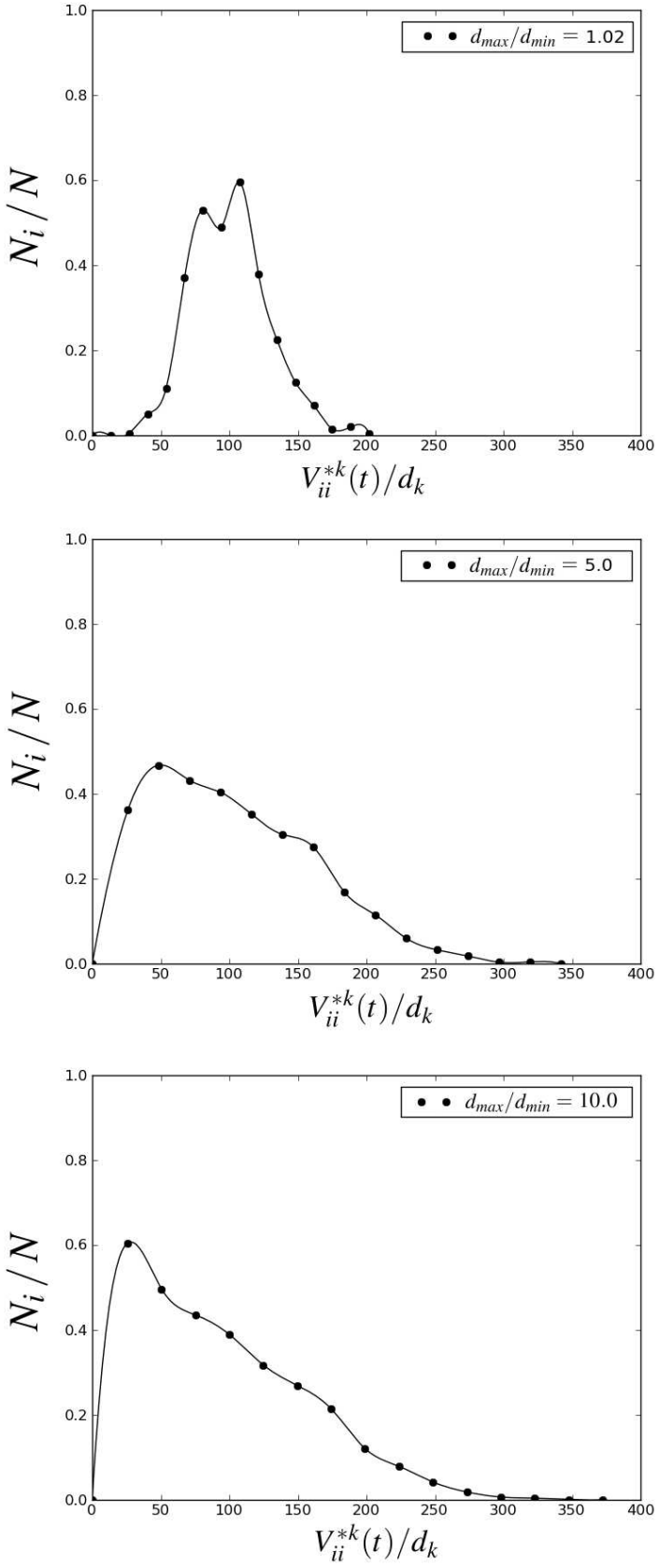

Figure 4.10: Dense samples - V_{ii}^{*k}/d_k distribution for a monodisperse (a), and two polydisperse samples (b, c) - N_i = occurrences, N=number of particles.

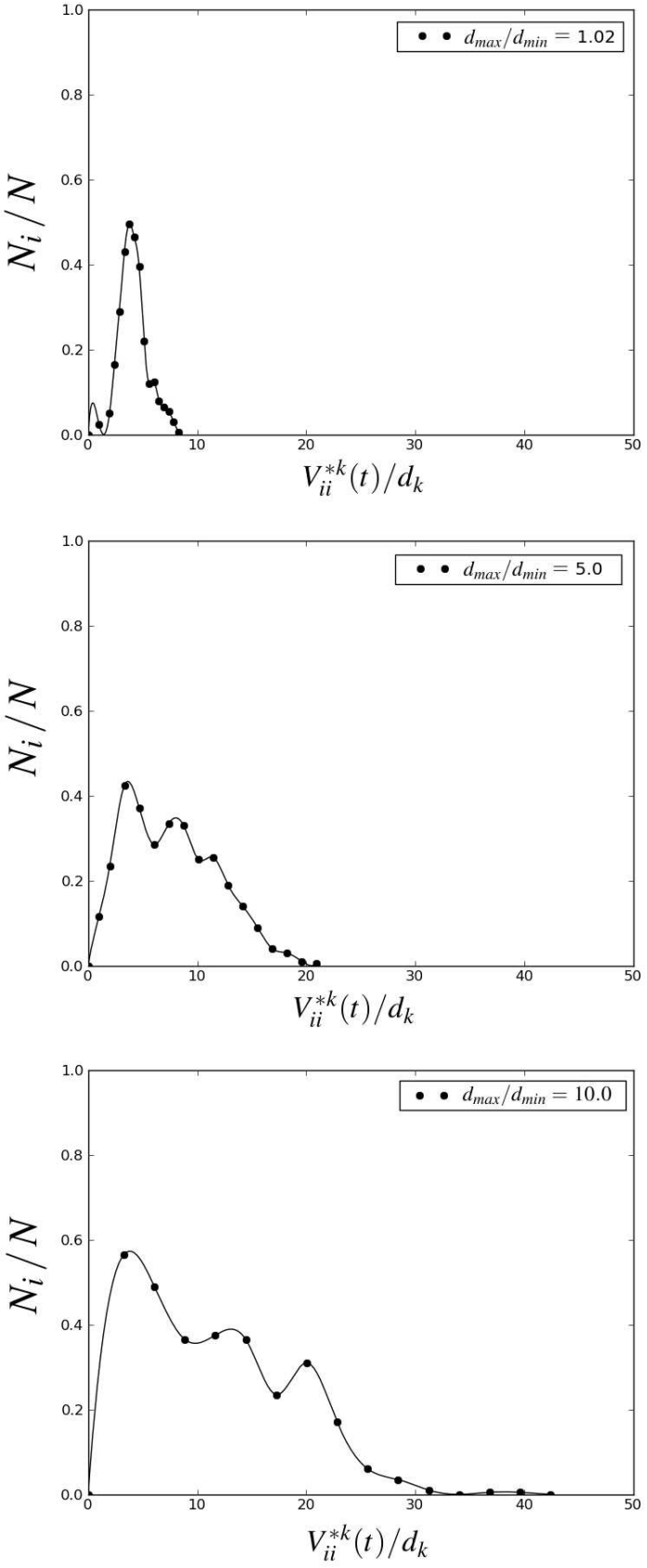

Figure 4.11: Loose samples - V_{ii}^{*k}/d_k distribution for a monodisperse (a), and two polydisperse samples (b, c) - N_i = occurrences, N=number of particles.

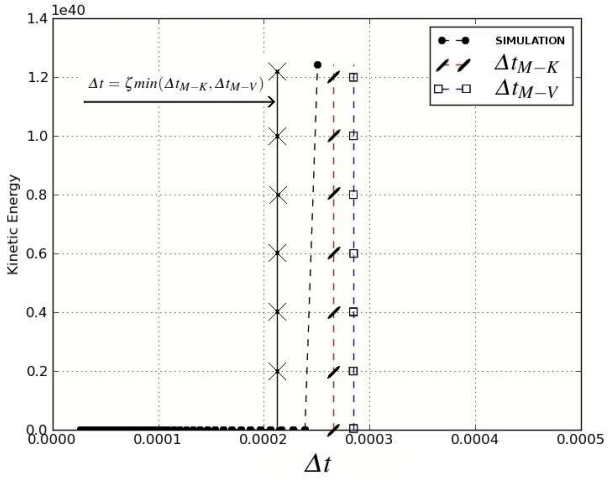

Figure 4.12: Estimation of a stable time step, using eq.(4.22) with $\zeta = 0.8$

In the case of incompressible phases (Biot's coefficient $\alpha_B = 1$), for a saturated granular medium, the continuity equation (1.41) can be rewritten as follows:

$$\frac{\partial}{\partial t}(\nabla \cdot \mathbf{dX}) + \nabla \cdot (-K_d \nabla p) = 0 \tag{4.23}$$

where the first term expresses the variation of fluid mass content $\partial \zeta / \partial t$, associated to the divergence of the solid displacement vector **dX**, and the second term is Darcy's law. The equation of local equilibrium (see eq.(1.40)), is rewritten as:

$$-\nabla \cdot \underline{\underline{\sigma'}} + \nabla p = (1-n)(\rho_s - \rho_f)\, g \tag{4.24}$$

where $p = p^a - \rho_f\, g\, z$ is the excess ("piezometric") pore pressure and $\underline{\underline{\sigma'}}$ represents Terzaghi's effective stress. In small strain linear elasticity (see eq.s (1.37), (1.45)), we have:

$$\underline{\underline{\sigma'}} = [\mathbf{C}]\frac{1}{2}(\nabla \mathbf{dX} + \nabla^T \mathbf{dX}) \tag{4.25}$$

with **C** the stiffness tensor. Substituting $\underline{\underline{\sigma'}}$ given by this expression in eq.(4.24) gives a Navier-type equation (see eq.s (1.42)), where ∇p can be seen as a body force:

$$-\nabla \cdot [\mathbf{C}]\,\frac{1}{2}(\nabla \mathbf{dX} + \nabla^T \mathbf{dX}) + \nabla p = (1-n)(\rho_s - \rho_f)\mathbf{g} \tag{4.26}$$

In the light of this system of partial difference equations, we can reconsider the equations of the pore-scale DEM-PFV formulation. Firstly, we observe that in the case of steady rates of deformation, $\ddot{\mathbf{X}}$ vanishes and eq.(4.7) becomes an equilibrium equation. Secondly, we note that in the special case when all contacts behave purely elastically, a linear relation exists between the contact force vector $\mathbf{F}^c$ and the generalized displacement **dX** via a global stiffness matrix $\mathbf{C}^s$ [2]. Hence, the system satisfies a relation of the form:

$$[\mathbf{C}^s]\,\{\mathbf{dX}\} + \mathbf{W} + [\mathbf{S}]\{\mathbf{P}\} = 0 \tag{4.27}$$

which we can also write for one particle alone, resulting in the following equilibrium condition for a particle i interacting with n_c particles in contact, and with n_f incident fluid cells:

$$\sum_{k=0}^{k=n_c} C_{ik}^s (dX_i - dX_k) + V_i \rho_s \mathbf{g} + \sum_{k=0}^{k=n_f} S_{ik} p_k = 0 \tag{4.28}$$

In this equation C_{ik}^s is the so called rigidity matrix [2], that is multiplied by the relative displacements $dX_i - dX_k$ to give the contact forces; the second term expresses the weigth of particle i (V_i = particle volume); the last term sums the contributions of fluid pressure in adjacent pores. Equation (4.28) can be seen as the discrete form of a Navier equation, where $\sum_{k=0}^{k=n_c} \mathbf{C}(\cdot - dX_k)$ is an operator defined for the discrete displacement field, and equivalent to the operator $\int_V \nabla \cdot C(\nabla \cdot + \nabla^T \cdot)$ that would arise in the conventional finite volume formulation for a continuum. Similarly, the third term is a discrete operator equivalent to the integral of the pressure gradient $\int_V \nabla \cdot$.
The analogy between eq.(4.23) and eq.(3.2) is more direct since in the latest, by definition, the two terms represent the local rate of volume change of the pore space and the divergence of the fluid velocity averaged in the pore.

Consistently, we also remark that the assembled matrices for the coupled boundary value problem, as given by equations (4.4) and (4.27), do not differ from the ones obtained through the discretization of Biot's equations using the FVM [68] or FEM [33] methods. As a last note, we can remark that the sets of elements that we obtain from the triangulation and the tessellation systems are also quite similar to the ones found in unstructured FV mesh.

From this comparison, we can conclude that the DEM-PFV coupled model should be able to recover the results of classical poroelasticity in boundary values problems, provided they share similar assumptions (the general theory is indeed not restricted to $\alpha_B = 1$ in general, for instance). The 1D diffusion problem known as Terzaghi's consolidation is well suited for such comparison. In the next section it will be presented as a benchmark test for the validation of the model.

4.4 Oedometer test simulation

The 1-D diffusion problem known as Terzaghi's consolidation is simulated with the DEM-PFV coupled model and will be used as a benchmark test. The consolidation process is a classical hydro-mechanical problem. The mechanisms that govern the evolution of the deformation of a granular medium filled by a viscous fluid depend on a variation of the state of stress, coupled to processes of diffusion of the interstitial fluid. Such phenomenon depends therefore on the properties of the porous medium, like permeability and deformability, and on the geometry of the problem, defined by the boundary conditions and the drainage patterns which characterize the medium.

The equation of monodimensional consolidation is a diffusion equation on p, that reads:

$$\frac{\partial p}{\partial t} = C_v \frac{\partial^2 p}{\partial z^2} \tag{4.29}$$

where p is the fluid pressure, z the height in the sample, C_v the consolidation coefficient, defined as follows:

$$C_v = \frac{K_d E_{oed}}{\rho_f g} \quad \left[\frac{L^2}{T}\right] \tag{4.30}$$

where K_d is the coefficient of hydraulic conductivity of the soil expressed in m/s (see eq.(1.32) and section 3.5.3), $E_{oed} = \Delta\sigma_v^{'}/\Delta\varepsilon_v$ the oedometric modulus, g the gravity acceleration and ρ_f the density of the fluid. A non-dimensional time parameter is introduced, T_v, defined as:

$$T_v = \frac{C_v t}{L^2} \tag{4.31}$$

where t is the effective time, and L the longest drainage path for the generic fluid particle. Then, $T_v = 0$ at the begin of consolidation, whereas $T_v = 1$ (100%) at the end of the process.

4.4.1 Numerical results

The DEM-PFV model is consistent with Terzaghi's assumptions, provided that:

- c1) The deformation is small and the stress-strain behaviour is linear;
- c2) Biot's coefficient is $\alpha_B = 1$;
- c3) The displacement is unidirectional;
- c4) The permeability and the oedometric modulus are constant in space and time.

The c1) condition can be obtained with the DEM for small deformations. c2) is one hypothesis of the DEM-PFV model, as we've seen in section 4.2. Our boundary conditions will be consistent with the c3) condition, but the displacement inside the material will not be purely unidirectional due to local fluctuations in the displacement field. By definition, a discrete model generally does not satisfy the c4) condition since one of its desirable features is to reflect local heterogeneities and volume changes in the local conductivity, and to take into account of the deformation of the solid skeleton. In the first simulation, however, at least for validation purpose, the permeability and the oedometric modulus will be constant in time as the deformation will be very small. It will be seen that the spatial and temporal variability of κ, the intrinsic permeability of the medium, does not prevent a good agreement with the analytical solution in such case. In the second simulation, conditions c1) and c4) conditions will be relaxed and the consequences will be commented.

Boundary conditions are shown on figure 4.13. Lateral displacement are prevented ($\varepsilon_{xx} = \varepsilon_{yy} = 0$). Both upward and downward drainage are activated by imposing an external fluid pressure $p_{ext} = 0\,kPa$ ($L = H/2$ in eq.(4.31)). A relative dense sample was created, to minimize the dispersion of pores' dimension and avoid strong heterogeneities within the sample. 5000 slightly polydispersed grains were employed to build a cubic sample ($l = 0.1m$) which was then subjected to an axial external load $\Delta\sigma_{ext} = 5\,kPa$. A compression test, in dry conditions, was used to evaluate the oedometric modulus for the

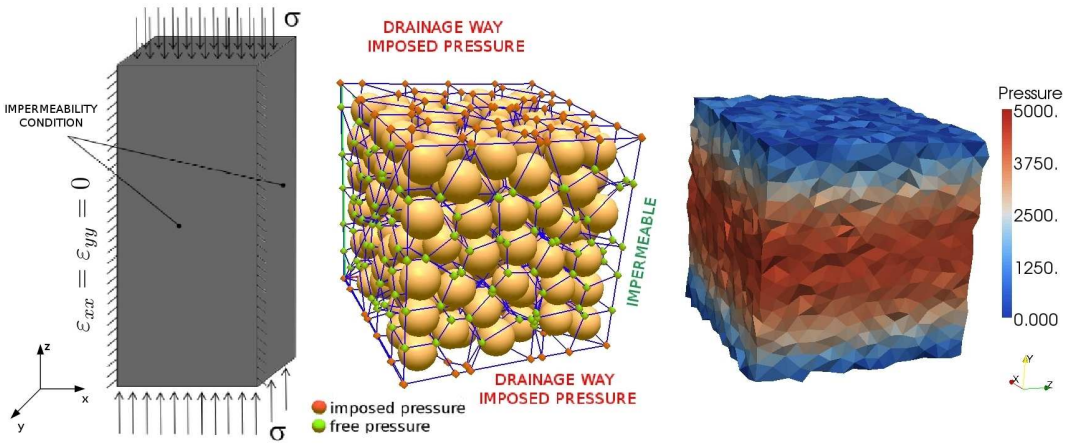

Figure 4.13: Boundary conditions (left). Pressure field at $T_v = 0.1$ (10% of consolidation completed) (right).

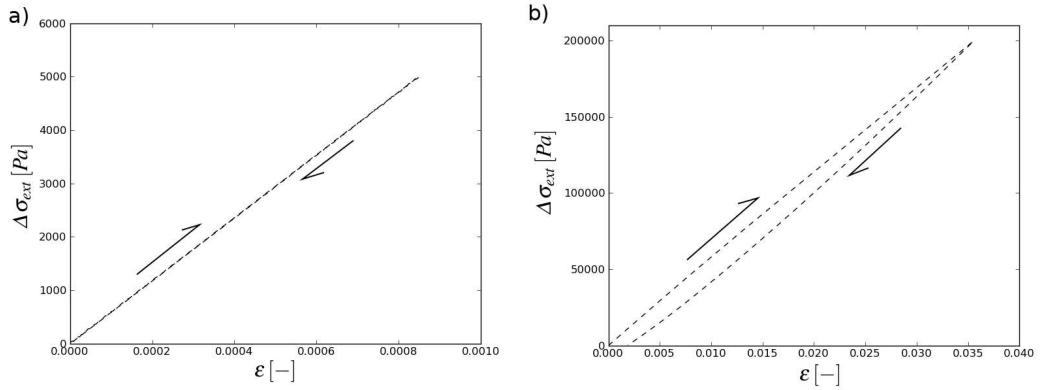

Figure 4.14: Compression tests on dry samples. $\Delta\sigma_{ext} = 5\,kPa$ (a), $\Delta\sigma_{ext} = 200\,kPa$ (b)

sample. Unloading the sample, the total strain was recovered, showing that we are in the purely elastic regime at such stress-strain level (see fig.4.14(a)).

Table 4.1 reports the main parameters of the simulation.

The numerical results that were obtained are summarized in table 4.2. Fig.4.15 shows the evolution of excess pore pressure at half the total height of the sample. The plotted value is in fact an average computed on the plane $z = H/2$. Fig.4.16 (left) shows the evolution of pore pressure in space (z/H) and time (T_v). The pore pressures values are normalized to the external stress value $\Delta\sigma_{ext}$. Fig.4.16 (right) shows the evolution of strain ε, normalized to its final value ε_{final}.

The final strain we could measure was $\varepsilon_{final} = 0.08\%$ (for both the dry and saturated compression tests). The oedometric modulus is $E_{oed} = 5895\,kPa$, the permeability $K_d = 7.07623 \cdot 10^{-5}\,m/s$. Both these last two parameters remain constant during the simulation. The excess pore pressure, plotted on fig.4.15, instantaneously rose up to $5\,kPa$ (= σ_{ext} = p_{max}) and then gradually decreased. We remind that in Terzaghi's formulation, the initial condition is $p = \sigma_{ext}$, at $t = 0$ ($T_v = 0$). In our simulation we had $p = \sigma_{ext}$ at $T_v = 3.2 \cdot 10^{-5} \simeq 0$. The evolution in space and time of the pore pressure is found to be in good agreement with the analytical solution, as it can be seen on fig.4.16 (left). The same

INPUT DATA		
Number of grains	[-]	5000
Sample dimensions	[m]	0.1 x 0.1 x 0.1
μ	[kPa · s]	0.25
$\Delta\sigma_{ext}$	[kPa]	5
σ_0	[kPa]	0
p_0	[kPa]	0
E	[kPa]	15000
a	[-]	0.5

Table 4.1: Oedometer test - Input data of the test of fig.s 4.15,4.16.

RESULTS		
ε_{final}	[-]	0.08%
E_{oed}	[kPa]	5895
K_d	[m/s]	$7.07623 \cdot 10^{-5}$

Table 4.2: Oedometer test - Numerical result (see fig.s 4.15,4.16).

consideration can be done for the evolution of the settlement, shown on fig.4.16 (right).

Fig.4.17 (left) shows the profiles of fluid pressure p, strain ε and effective stress σ', evaluated at the microscopic scale (see eq.s (2.18),(2.21)), along the relative height of the sample, z/H, at $T_v \simeq 0.10$ (10% of consolidation). As it was expected, fluid pressure and effective stress profiles are complementary, as stated by the Terzaghi's effective stress principle $\sigma = \sigma' + p$. The nearly linear relation between the stress and the strain can also be observed in the left diagram, and even clearer on the right diagram (fig.4.17 (right)). Fig.4.18 shows a 3D-visualization of the deformation field within the sample, at the same istant $T_v \simeq 0.10$. A profile similar to the ones of fig.4.17 can be observed, although the strain field reflects more local fluctuations than the pressure field.

4.4.2 Nonlinear consolidation problem

It is worth noticing that the final settlement as it would result from a coupled analysis, at the end of the consolidation process, is equal to the one that would be obtained in dry conditions, only in case of hyperelastic behaviour, for which the soil response is expected to

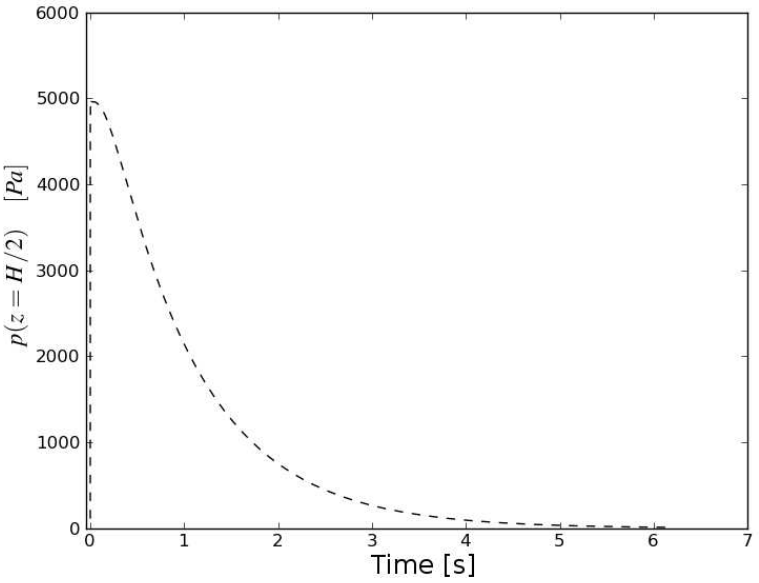

Figure 4.15: Oedometer test - Fluid pressure measured at $z = H/2$ during the consolidation process.

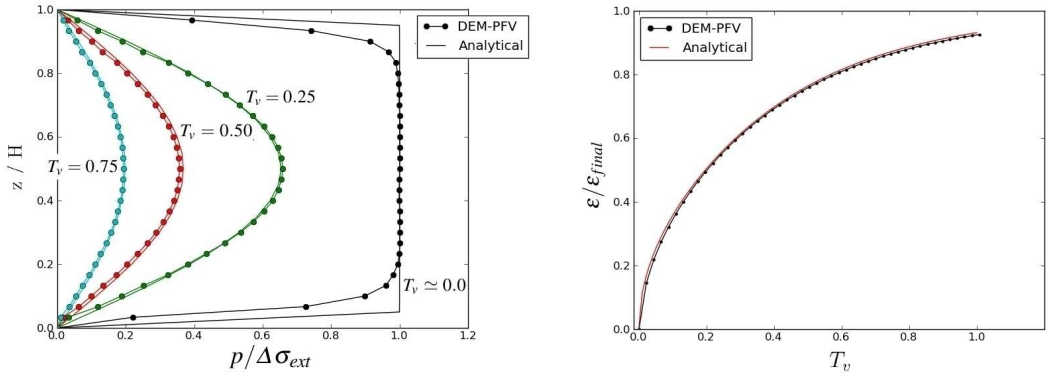

Figure 4.16: Oedometer test - Evolution of pore pressure ($\Delta\sigma_{ext} = 5\,kPa$) (left) and settlement (right)

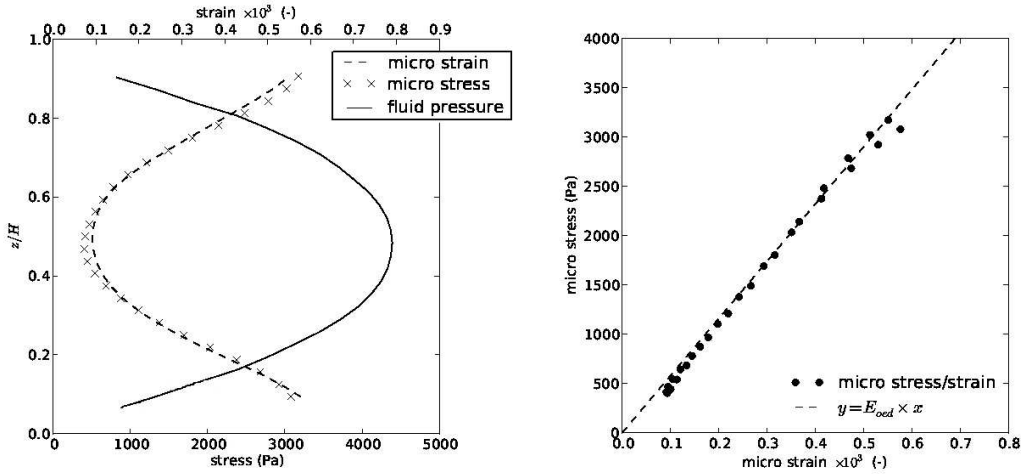

Figure 4.17: (left) Profile of fluid pressure p, micro effective stress σ' and micro strain ε. (right) Relation between micro effective stress σ' and micro strain ε

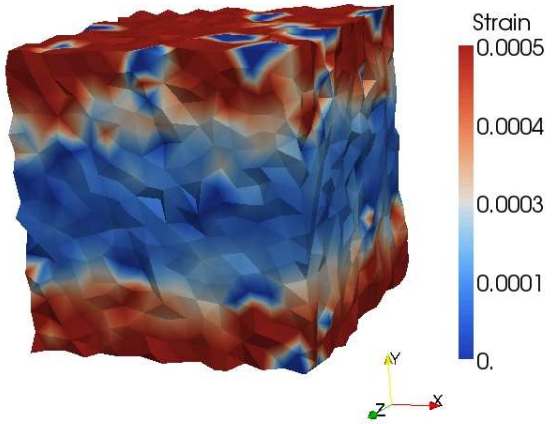

Figure 4.18: Strain field at $T_v = 0.10\%$ - 3D-visualization.

	RESULTS	
ε_{final}	[-]	3.94%
Initial Permeability $K_{d,init}$	[m/s]	$7.07623e-09$
Final Permeability $K_{d,final}$	[m/s]	$6.41317e-09$
Initial $E_{oed,init}$	[kPa]	5895
Final $E_{oed,final}$	[kPa]	5620
$Cv_{initial}$	[-]	0.0417
Cv_{final}	[-]	0.0360

Table 4.3: Nonlinear oedometric consolidation - Numerical result.

depend on the initial and the final state of stress, and not depend to the stress path applied [20]. In this section the influence of conditions c1) and c4) (see previous section) on the final solution, in case of large deformations imposed to the sample, will be investigated. The input data are the same than the ones summarized in table 4.1, expected $\Delta\sigma_{ext}$. A higher load is applied, $\Delta\sigma_{ext} = 200$kPa.

Table 4.3 summarizes the results for this new simulation. The final strain that was obtained through a dry compression test was $\varepsilon_{dry} = 3.94\%$. On fig.4.14(right) it can be seen how the total strain is not recovered by unloading the sample, during the compression test on the dry sample. The initial and final values of the permeability and of the oedometric modulus (secant modulus) are reported, as well as the respective consolidation coefficients, computed using eq.(4.30).

Fig.4.19 shows the results that were obtained by adopting the initial values of K_d and E_{oed}, then $Cv = Cv_{initial}$. Such choice leads to a discrepancy between the analytical and the numerical solutions, in terms of evolution of pore pressure and settlement. More precisely, tha rate of deformation is underestimated. On the contrary, on fig.4.20 we present the results that are obtained by adopting the final values of K_d and E_{oed}, then $Cv = Cv_{final}$. The analytical and the numerical solutions are then found to be in good agreement.

4.5 Immersed granular deposition

In this section the evolution of fluid pressure and effective stress is observed in a granular deposition problem. The simulation was set in order to reproduce a fluid-filled vessel in which a number of spheres is placed and left to deposit under the action of gravity. No fluxes are allowed through lateral and bottom boundaries, while an external fluid pressure $p_{ext} = 0$ is set at top boundary. A cloud of immersed spheres is created, as represented on fig.4.21. The fluid pressure is measured and recorded at six different heights during the simulation (fig.4.21). Table 4.4 reports the parameters of the simulation.

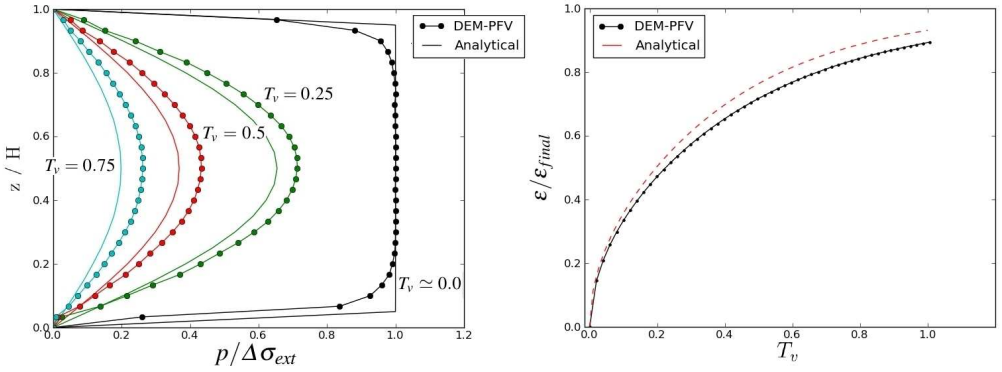

Figure 4.19: $Cv = Cv_{initial}$ - Evolution of pore pressure (left) and settlement (right).

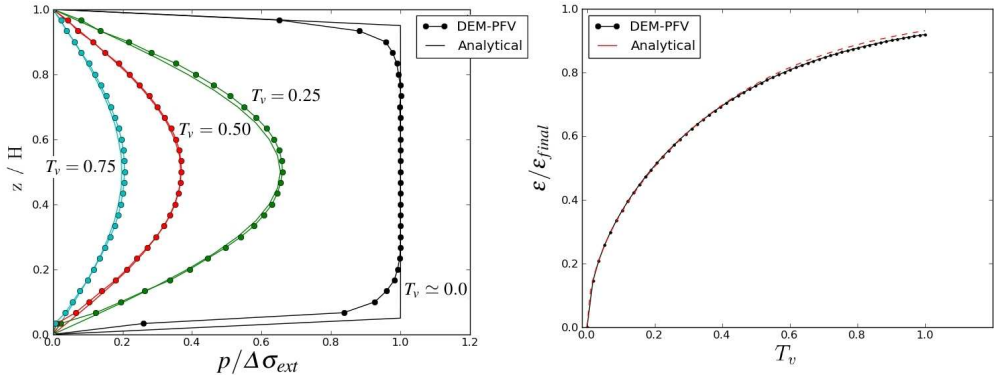

Figure 4.20: $Cv = Cv_{final}$ - Evolution of pore pressure ($\Delta\sigma_{ext} = 200\,kPa$) (left) and settlement (right).

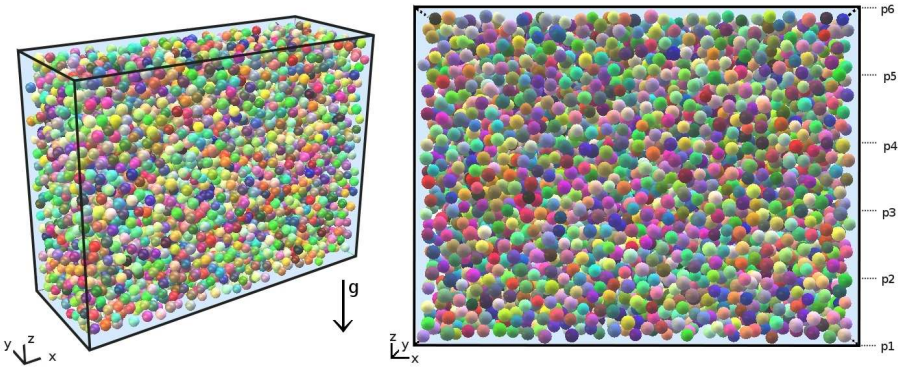

Figure 4.21: Simulation of an immersed granular deposition (a). Position of fluid pressure sensors p_i (b).

INPUT DATA		
Number of grains	[-]	5000
Sample dimensions	[m]	2.00 x 1.50 x 0.75
μ	[kPa · s]	0.10
d_{50}	[m]	0.06
ρ_s	[kg/m^3]	2600
ρ_f	[kg/m^3]	1000
p_{ext}	[kPa]	0
E	[kPa]	15000
a	[-]	0.5

Table 4.4: Immersed granular deposition - Input data.

4.5.1 Critical gradient of liquefaction

By definition, the condition of *complete liquefaction* of soils consists in the complete transfer of the weight of solid particles from intergranular forces to the interstitial fluid. In such case, the effective stress reduced to almost zero, and the fluid-solid mixture behaves as a viscous material. In the problem we are analyzing, we will analyze and discuss such phenomenon.

The critical gradient of liquefaction is defined as:

$$i_c = \frac{\gamma'}{\gamma_f} = \frac{\gamma_{sat} - \gamma_f}{\gamma_f} = \frac{\nabla p}{\gamma_f} \tag{4.32}$$

where γ_{sat} indicates the specific weight of the saturated soil, $\gamma_{sat} = \gamma_s(1-n) + \gamma_f(n)$. We can directly evaluate the gradient of pressure ∇p, considering the value of porosity that characterizes the particles suspension, $n = 0.61$:

$$\nabla p = \gamma_{sat} - \gamma_f = \gamma_s(1-n) + \gamma_f(n) - \gamma_f = 6,120 kN/m^3 \tag{4.33}$$

And finally the critical hydraulic gradient of liquefaction:

$$\frac{\nabla p}{\gamma_f} = \nabla H_c = \frac{6,120 kN/m^3}{9,80665 kN/m^3} = 0.624[-] \tag{4.34}$$

The result in terms of fluid pressure measured along the height of the vessel is plotted on fig.4.22(a). The gradient of fluid pressure, evaluated for each couple of consecutive sensors, is plotted as well (b). On fig.4.22a, when the pressure measured at a certain layer equals the one measured at an adjacent layer, it means that at that depth the spheres are newly in contact and the layer has stabilized. It can be observed, on fig.4.22b, how the

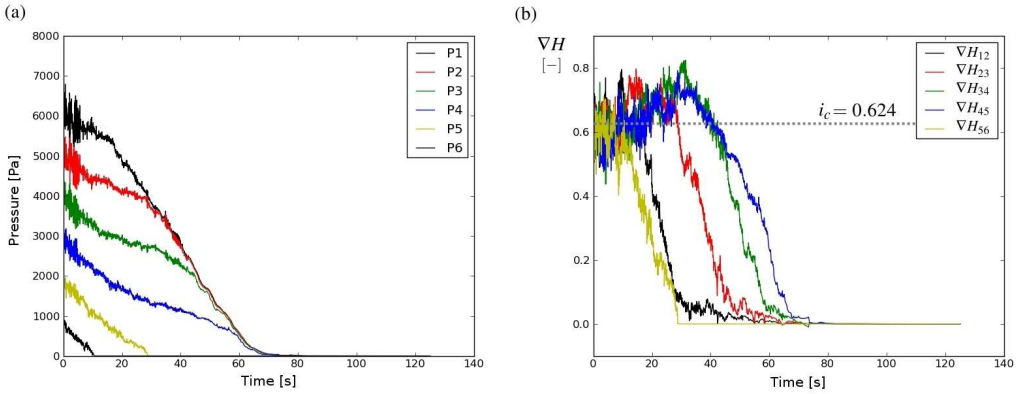

Figure 4.22: Immersed grain deposition, case of tab.4.4. Fluid pressure measurements (a). Hydraulic gradient (b).

initial values of the hydraulic gradient are close to the *suspension* gradient computed with the expression (4.34), and finally goes to zero as the packing stabilizes. On fig.4.23 a sequence of stress states is represented (for the definition of stresses at particles scale, see eq.(2.18)). The initial load is entirely carried by the fluid phase, and the effective stress is none (a). As long as the lower strata get stable, the consolidation process starts, and the stress is transferred from to liquid phase to the grains (b-c). Finally, once the fluid pressure is fully dissipated and the consolidation process completed, the load is entirely carried by the solid skeleton (d).

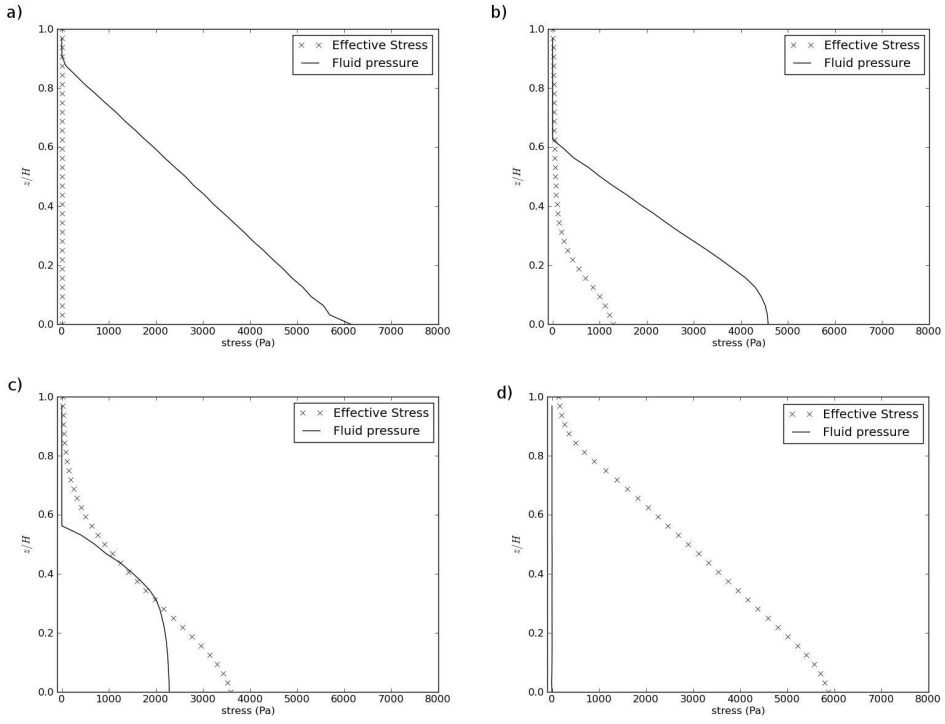

Figure 4.23: Effective stress and fluid pressure evolution during the granular deposit.

Chapter 5

Numerical aspects

The modelling strategy of the PFV-DEM coupled model result in a low ratio, of the order of magnitude of units, between the number of unknowns relative to the resolution of the fluid and the solid problem, finally ensuring good performances for a detailed description of fluid-soil interactions. This chapter will be then devoted to the analysis of the performances of the DEM-PFV model. The cost in terms of computational time and RAM utilization will be examined, and possible optimizations will be discussed and integrated into the model.

5.1 Performance and optimization

The PFV-DEM model purpose is to allow the analysis of a single particle interaction with the fluid flowing past it, by introducing some assumption to simplify the formulation of the coupled hydromechanical problem and containing the costs of its numerical resolution. In this section the model performances will be analysed and discussed. Potential optimizations are presented and introduced to the model, in order to appreciate their effects on the solution.

The cost in terms of time of each operation concerned by a cycle of computation of the PFV-DEM model will be analysed. They are summarized on fig.5.1. We name T the total time which is taken by the model for the whole simulation. The two contributions T_{DEM} and T_{PFV} can be isolated, referring to the time which is needed for the DEM computation cycle, as it has been described in section 2.1, and to the time associated to the operations which are needed to solve the flow problem, respectively. Then, we can write:

$$\begin{aligned} T &= T_{DEM} + T_{PFV} \\ T_{PFV} &= T_{TRG} + T_G + T_{DEF} + T_{LS} + T_F \end{aligned} \tag{5.1}$$

where,

- T_{TRG} refers to the triangulation/tessellation procedure, described in section 3.1;
- T_G refers to the the computation of local conductances of eq.(3.4);
- T_{DEF} refers to the computation of pores' volumetric deformation rate $\Delta\dot{V}_i^f$ (see eq.(3.2));

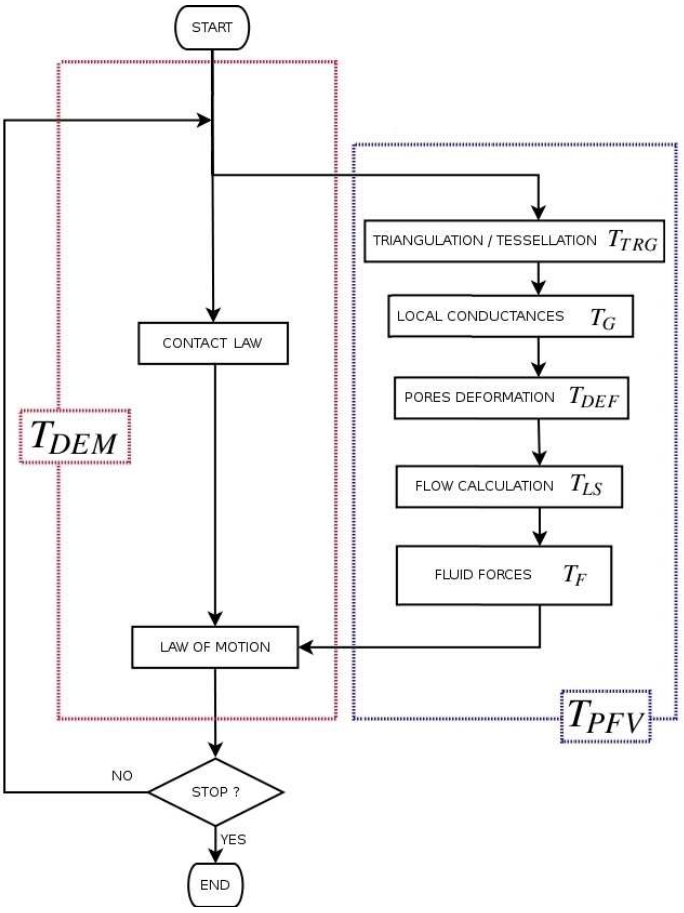

Figure 5.1: The PFV-DEM coupled model - The scheme mirrors the partitioned approach that characterizes the coupling strategy. Note that the current implementation is sequential, not parallelized as this scheme could suggest.

- T_{LS} refers to the resolution of the linearized system of eq.(4.4);
- T_F refers to the computation of the fluid forces (see section 3.3).

The flow chart of the implemented algorithm is represented on fig.5.1, with a graphical representation of the two contributions to the total cost, T_{DEM} and T_{PFV}. The cost proportions of each operation for the simulation of the consolidation problem are represented on fig.5.2.

5.1.1 Computational geometry

The size of the problem, determined by the number of particles employed for one simulation, will be analyzed in this section as it influences the cost of the operations that have been explicited in the eq.(5.1). The reported times were obtained on a computer equipped with a 64bit Intel Xeon 2.67Ghz processor and 8GB of RAM and are shown on figures 5.3 and 5.4. The total number of tetrahedra scales with the number of spheres and is of the order of $5 \cdot N$. Therefore the costs T_G, T_{DEF} and T_F should scale linearly with N, theoretically.

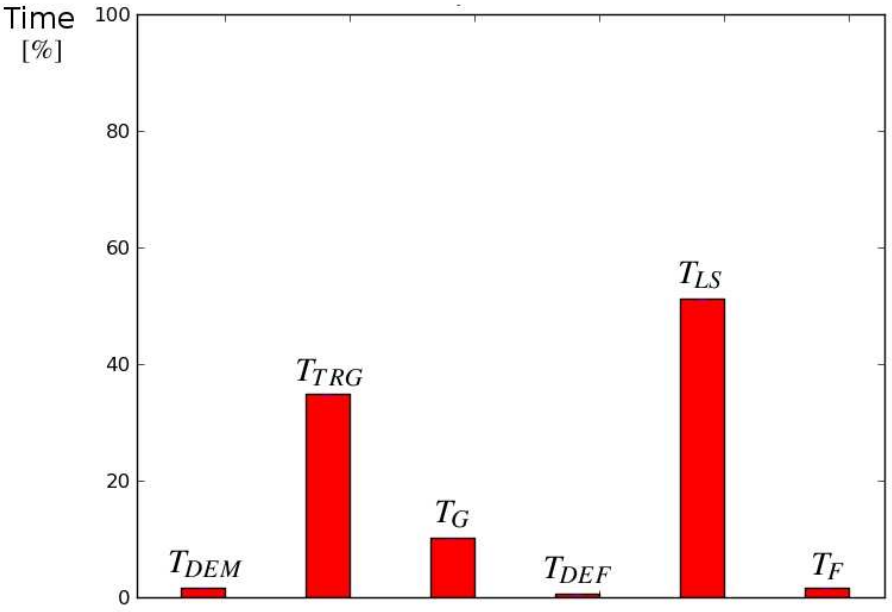

Figure 5.2: Cost proportion of each operation of eq.(5.1). The resolution of flow problem takes the 90% of the total time.

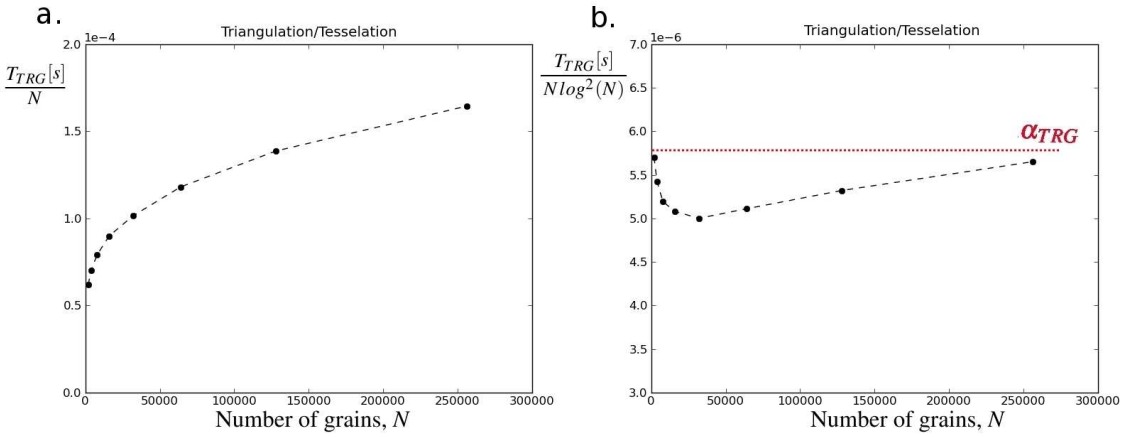

Figure 5.3: Running time for the construction of the triangulation and the tessellation systems (a-b).

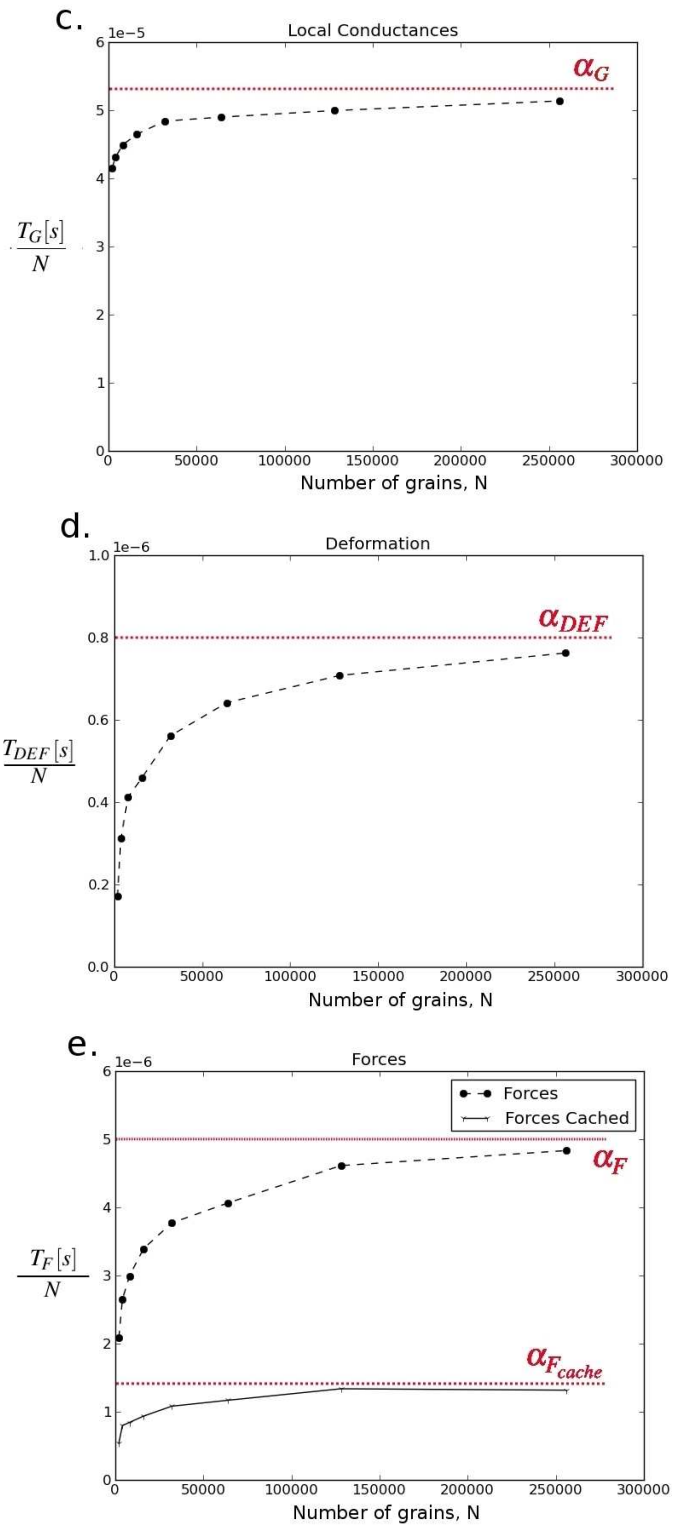

Figure 5.4: Running time for the computation of local permeabilities (c), the computation of pores volumetric deformation rate (d) and fluid forces (e). In (e) the "Forces" cost is relative to the definition of matrix $[\mathbf{G}]$ and the solution of the product $[\mathbf{G}]\{\mathbf{P}\}$. "Forces cached" cost is relative to the only cost of product $[\mathbf{G}]\{\mathbf{P}\}$.

On CGAL documentation [75], the reported running time per node of the triangulation (in case of *regular triangulation*) attains rapidly an asymptotic value as the size of the problem increases. Liu and Snoeyink (2005) [58], comparing CGAL and other softwares performances, experienced a quasi-linear dependence in the number of points. In our experience, the results were best fitted by a $N \cdot log^2(N)$ scaling (see fig.5.3 a-b). Although we don't have a clear explanation for such scaling, we will use the following relation to estimate the cost of the triangulation operation:

$$\frac{T_{TRG}}{N log^2 N} = 5.8 \cdot 10^{-6} = \alpha_{TRG} \tag{5.2}$$

The triangulation system constitutes the base of the formulation of the problem. The computation of local conductances of eq.(3.4), the rate of volumetric deformation of pores $\Delta \dot{V}_i^f$ of eq.(3.2) and the derivation of fluid forces to be applied on solid particles as described in section 3.3, are all triangulation-based operations. The cost of these operations is shown on fig.5.4 (c-d-e). The per-sphere running time tends to an asymptotic value as the size of the problem increases, whereas it shows a slight variability for the smallest packings. The asymptotic values that were found are:

$$\frac{T_G}{N} = 5.4 \cdot 10^{-5} = \alpha_G \qquad \frac{T_{DEF}}{N} = 8 \cdot 10^{-7} = \alpha_{DEF} \qquad \frac{T_F}{N} = 5 \cdot 10^{-6} = \alpha_F \tag{5.3}$$

5.1.2 Solving the linear system

The system we have to solve, as it is shown in eq.(4.4) and recalled hereafter, is large ($5xN$ unknowns approx.) and the associated matrix $\mathbf{G}$ is sparse and symmetric. Sparse direct solvers are based on a direct elimination of equations, as opposed to iterative solvers, where the solution is obtained through an iterative process that successively refines an initial guess to a solution that is within an acceptable tolerance of the exact solution. Both iterative and direct methods have been tested and compared, and will be presented in the next sections.

$$[\mathbf{G}]\{\mathbf{P}\} = [\mathbf{E}]\{\dot{\mathbf{X}}\} + \{\mathbf{Q_q}\} + \{\mathbf{Q_p}\} \tag{5.4}$$

The Gauss-Seidel algorithm

The iterative Gauss-Seidel method has been implemented to solve the linear system of eq.(4.4). Such method is based on the introduction of a convergence criterion, namely the definition of a parameter (*error*) that expresses the quality of the solution and a threshold (*tolerance*) to be compared to it, to automatically stop the iterative process.

The error as it has been defined in the model, reads:

$$e = \frac{\Delta p_{max}}{p_{max}} \Rightarrow e < tol \quad (1e-03 < tol < 1e-12) \tag{5.5}$$

Fig.5.5 shows the influence of the tolerance and the size of the problem on the computational time which is needed by the iterative solver to converge to the solution. Obviously, the lower is the tolerance, the higher is the time needed to satisfy the convergence criterion. So, which tolerance shall we adopt to get an *accurate* solution in a *acceptable* time? In what follows we will propose a criterion to do such choice.

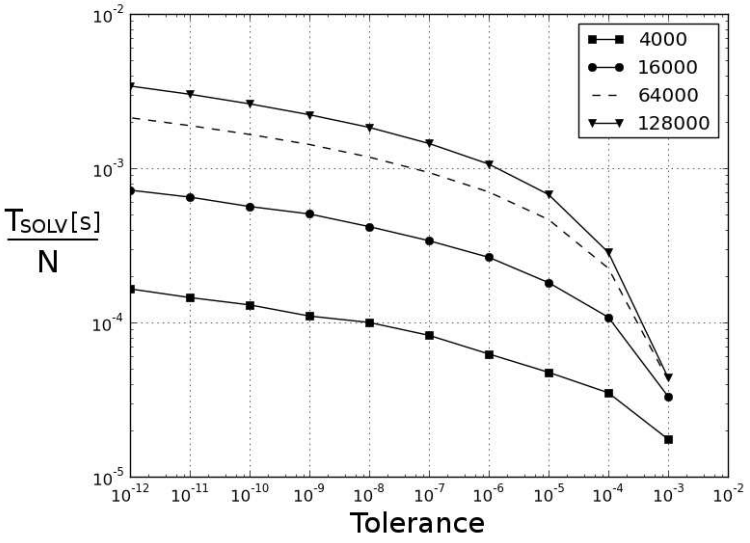

Figure 5.5: GS iterative method - Influence of tolerance and number of grains on the computation time.

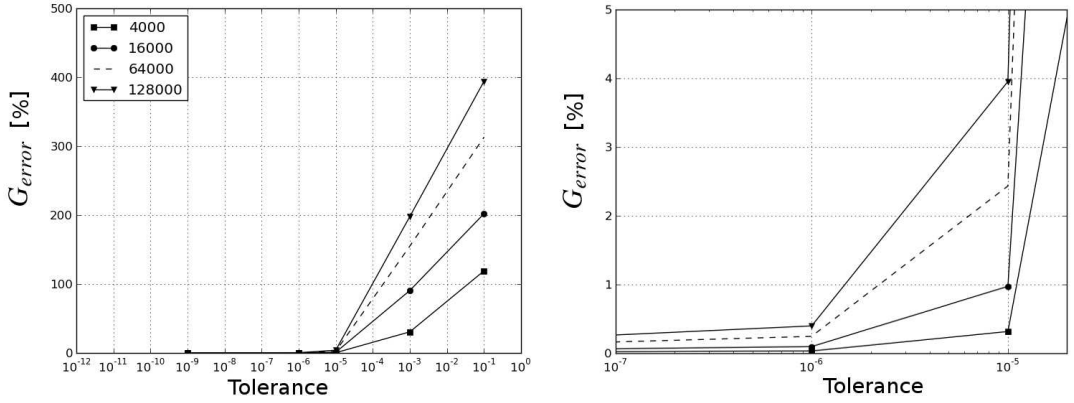

Figure 5.6: Influence of tolerance on model predictions. Evolution of $G_{error} = \frac{|Q_i - Q_o|}{Q_i}$.

Imposing a macroscopic pressure gradient to ensure a vertical seepage flow allows the prediction of the permeability of a sample, as it has already been described in section 4.4.1. An important feedback about the quality of the solution comes from the equality between the inlet and the outlet flow rates Q_i and Q_o. A good indicator of the quality of the solution is the difference $Q_i - Q_o$, which is none in case of exact solution. Thus, we define a new parameter, G_{error}:

$$G_{error} = \frac{\mid Q_i - Q_o \mid}{Q_i} \tag{5.6}$$

Fig. 5.6 shows the results that were obtained. G_{error} stays close to zero up to a tolerance of $1e-06$, then rises up rapidly for the highest tolerances. In the zoomed window it can be seen how for $tol = 1e-06$, $G_{error} < 1\%$ for all the tested samples. This is considered an acceptable error, which allow a sensible saving of time as it can be seen on fig.5.5.

Sparse direct solvers

Direct elimination requires the factorization of an initial very sparse linear system of equations into a lower triangular matrix followed by forward and backward substitution using these triangular systems. The lower triangular matrix factors are typically much larger than the initial assembled sparse matrix, hence the large disk or in-core memory requirements for direct methods.

TAUCS and PARDISO libraries have been tested. They are two of the fastest available sparse solvers [40]. Both libraries are high-performance softwares for direct solving large sparse symmetric (and non-symmetric) linear systems of equations of the form $Ax = b$, by a Cholesky factorization of matrix A ($PAP^T = LL^T$) based on BLAS and LAPACK [98].

The PARDISO package, of Schenk and Gärtner [86] [87], offers serial and parallel solvers for the direct solution of unsymmetric and symmetric sparse linear systems on shared memory multiprocessors. PARDISO algorithms are based on a Level-3 BLAS update. Pipelining parallelism is exploited with a combination of left- and right-looking supernode techniques to improve sequential and parallel sparse numerical factorization performance. TAUCS has been developed since 2001 by Sivan Toledo's research group [98]. Both a multifrontal algorithm and a left-looking algorithm are implemented. The documentation states the latter is slower than the former but requires less memory. Both libraries are based on a compressed-column-storage (CCS) structure and support a variety of preconditioning algorithms. The ordering method provided by METIS [51] was recommended for large problems and was used in our tests. TAUCS is able to factorize a matrix whose factor is larger than the main memory by holding the factor out-of-core. The factor is held in multiple files, each at most 1 Gbyte in size [82].

Let's compare such methods to Gauss-Seidel algorithm performances. Fig.5.7a compares the cost of the different methods. Raw data are reported on table 5.1, whereas table 5.2 reports the error on predicted permeabilities, as it has been already defined in eq.(5.6).

As in section 5.1.1, we can extrapolate some useful expression to estimate the T_{LS} term of eq.(5.1). For the Gauss-Seidel, we have:

$$\frac{T_{LS}}{N} = 1.07 \cdot 10^{-7} N^{0.786} = \alpha_{LS,GS} \tag{5.7}$$

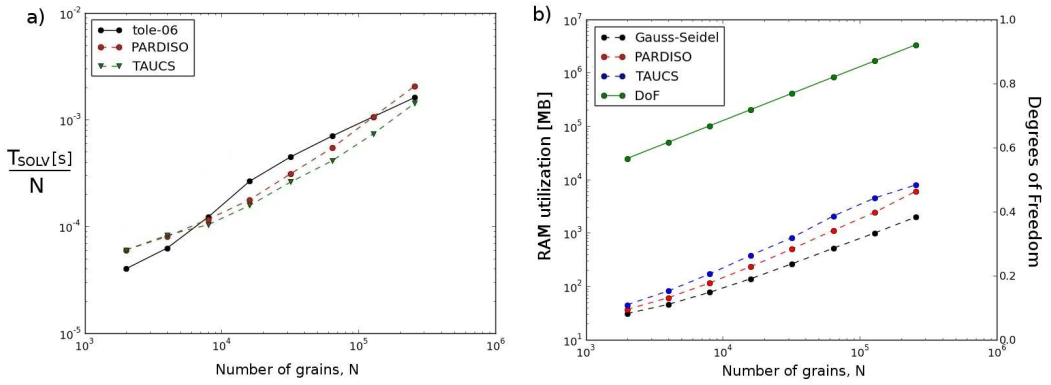

Figure 5.7: Direct comparison between TAUCS, PARDISO and Gauss-Seidel performances (a) and RAM utilization (b).

In the case of adoption of PARDISO or TAUCS direct solvers, we have:

$$\frac{T_{LS}}{N} = 7.84 \cdot 10^{-9} N + 5 \cdot 10^{-5} (pardiso) \tag{5.8}$$

$$\frac{T_{LS}}{N} = 5.28 \cdot 10^{-9} N + 6.72 \cdot 10^{-5} (taucs) \tag{5.9}$$

It can be concluded that direct solvers result in a faster and more accurate solution, compared to Gauss-Seidel method. Fig.5.7b shows the RAM occupancy that we could measure for each solver, and the number of degrees of freedom for the packings that were tested.

Solving multiple Right-Hand-Side

For linear systems of the form $[A]\{x\} = \{b\}$, direct methods provide an effective means of solving with the same $[A]$ but different right-hand sides b, because the factorization needs only to be performed once. Tables 5.3 and 5.4 report detailed timings when direct methods are employed. It can be seen how in both cases the time which is spent for the matrix factorization is much more higher than the time needed for solving the system (see also table 5.5). It is finally possible to decompose the T_{LS} term of eq.(5.1) in two components, relative to the factorization (LTL) and the solving (SLV) operations, respectively.

$$T_{LS} = T_{LTL} + T_{SLV} \tag{5.10}$$

Both terms are approximately quadratic in N. We found:

$$\frac{T_{LTL,P}}{N} = 7.8 \cdot 10^{-9} N + 4.8 \cdot 10^{-5} = \alpha^{LTL,P} N + \alpha_0^{LTL,P} \tag{5.11}$$

$$\frac{T_{SLV,P}}{N} = 9.4 \cdot 10^{-8} N^{0.36} = \alpha^{SLV,P} N^{\alpha_0^P}$$

Whereas, for TAUCS direct solver, we have:

$$\frac{T_{LTL,T}}{N} = 5.3 \cdot 10^{-9} N + 6.4 \cdot 10^{-5} = \alpha^{LTL,T} N + \alpha_0^{LTL,T} \tag{5.12}$$

$$\frac{T_{SLV,T}}{N} = 1.7 \cdot 10^{-7} N^{0.3} = \alpha^{SLV,T} N^{\alpha_0^T}$$

Nspheres	GS (1e-06) [s]	PARDISO [s]	TAUCS [s]
2000	0.08	0.12	0.12
4000	0.25	0.32	0.33
8000	0.98	0.93	0.83
16000	4.23	2.84	2.51
32000	14.36	9.97	8.34
64000	44.88	34.72	26.29
128000	136.16	135.77	94.22
256000	411.31	526.17	363.04

Table 5.1: Solvers performances. Gauss-Seidel (tolerance=1e-06), TAUCS and PARDISO libraries.

Nsph	Q $[m^3/s]$	GS (tol=1e-06)	Err GS [-]	PARDISO	Err PAR [-]	TAUCS	Err TCS [-]
4000	Q_{in} Q_{out}	0.00316319 0.00316511	0.03%	0.00316415 0.00316415	$< 10^{-6}$	0.00316415 0.00316415	$< 10^{-6}$
16000	Q_{in} Q_{out}	0.0919755 0.0921494	0.09%	0.092063 0.092063	$< 10^{-6}$	0.092063 0.092063	$< 10^{-6}$
64000	Q_{in} Q_{out}	2.54168 2.55406	0.24%	2.54783 2.54783	$< 10^{-6}$	2.54783 2.54783	$< 10^{-6}$
128000	Q_{in} Q_{out}	13.098 13.2017	0.39%	13.1498 13.1498	$< 10^{-6}$	13.1498 13.1498	$< 10^{-6}$

Table 5.2: Permeameter simulation. Inlet/Outlet flow rates computed with Gauss-Seidel (tolerance=1e-06), TAUCS and PARDISO methods

N	Matrix Assembly [s]	Reordering [s]	Factorization [s]	Solve [s]	Total Time [s]
2000	0.01	0.06	0.057	0.003	0.120
4000	0.02	0.133	0.181	0.007	0.321
8000	0.04	0.299	0.614	0.019	0.932
16000	0.08	0.657	2.132	0.047	2.836
32000	0.19	1.448	8.399	0.122	9.969
64000	0.46	3.245	31.16	0.315	34.72
128000	1.11	7.263	127.70	0.813	135.77
256000	2.52	16.057	508.01	2.099	526.17

Table 5.3: Time cost detail of PARDISO method.

N	Matrix Assembly [s]	Reordering [s]	Factorization [s]	Solve [s]	Total Time [s]
2000	0.01	0.04	0.08	0.005	0.12
4000	0.02	0.11	0.22	0.007	0.33
8000	0.03	0.22	0.58	0.028	0.83
16000	0.09	0.49	1.95	0.070	2.51
32000	0.18	1.03	7.13	0.175	8.34
64000	0.43	2.29	23.58	0.419	26.29
128000	1.01	4.97	88.19	1.059	94.22
256000	2.27	10.35	350.02	2.668	363.04

Table 5.4: Time cost detail of TAUCS method.

	Factorization [s]	Solve [s]	Total Time [s]
PARDISO	98.56%	1.44%	100%
TAUCS	97.49%	2.51%	100%

Table 5.5: TAUCS and PARDISO. Factorization and solving time cost proportions.

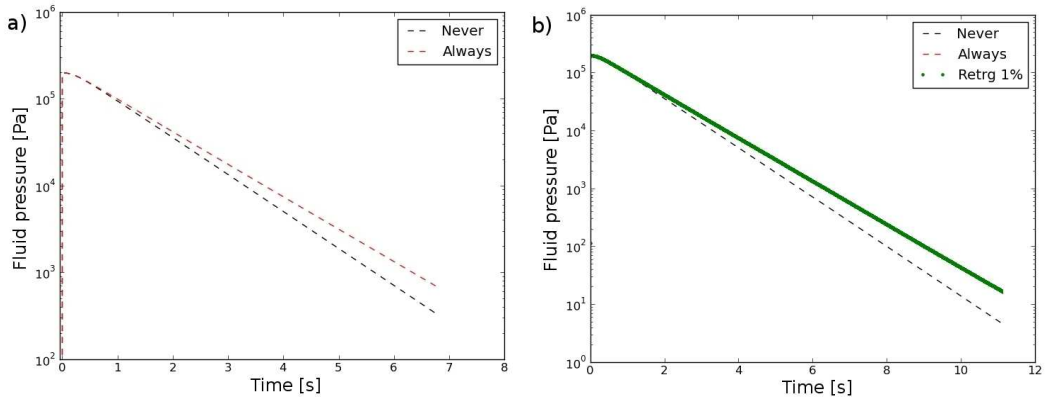

Figure 5.8: a) Influence of retriangulation frequency on the computed pore pressure. b) Effects of the retriangulation criterion on the computed pore pressure.

The performances of the two libraries are relatively similar. It is clear from these results that the factoring stage is the expensive part of this procedure. Therefore, a significant speedup can be obtained by using the same factors for many time steps, solving with a different right-hand side $\Delta\dot{V}$ the system of eq.(4.4).

5.1.3 Frequency of permeability updates

The results that were presented in last section show the advantage that would result from keeping the same conductivity matrix $[\mathbf{G}]$ of eq.(4.4) for many timesteps. A criterion has to be defined, to fix an appropriate frequency of retriangulation of the packing. The optimal frequency will be the one that allow a considerable save of time provided that the triangulation remains representative of the state of the medium.

Let's try to analyse the effects of the frequency of retriangulation on the numerical solution of the consolidation problem, by primarly evaluating two limit conditions. Fig.5.8a shows the fluid pressure that can be measured at half height of the granular sample, comparing two cases:

- The system is never retriangulated during the simulation;
- The system is retriangulated at each iteration.

The effect of never retriangulating the system is that the local hydraulic conductivities are kept unvaried during the whole simulation, equal to the ones computed on the initial configuration. Such effect necessarely influence negatively the solution obtained, and an error is committed on the estimation of the time needed for the dissipation of the excess pore pressure, as shown on fig.5.8a.

The parameter which was chosen to control the retriangulation frequency was ε_{RTRG}, defined as follows:

$$\varepsilon_{RTRG} = \sum_{t=t_0}^{t=t_{RTRG}} max(\varepsilon_{vol,pore_i}(t)) \tag{5.13}$$

ε_{RTRG} is therefore a cumulative parameter which is augmented at each iteration of the maximal pore deformation that can be measured inside the medium. Then, the system will be retriangulated each time ε_{RTRG} crosses a fixed threshold.

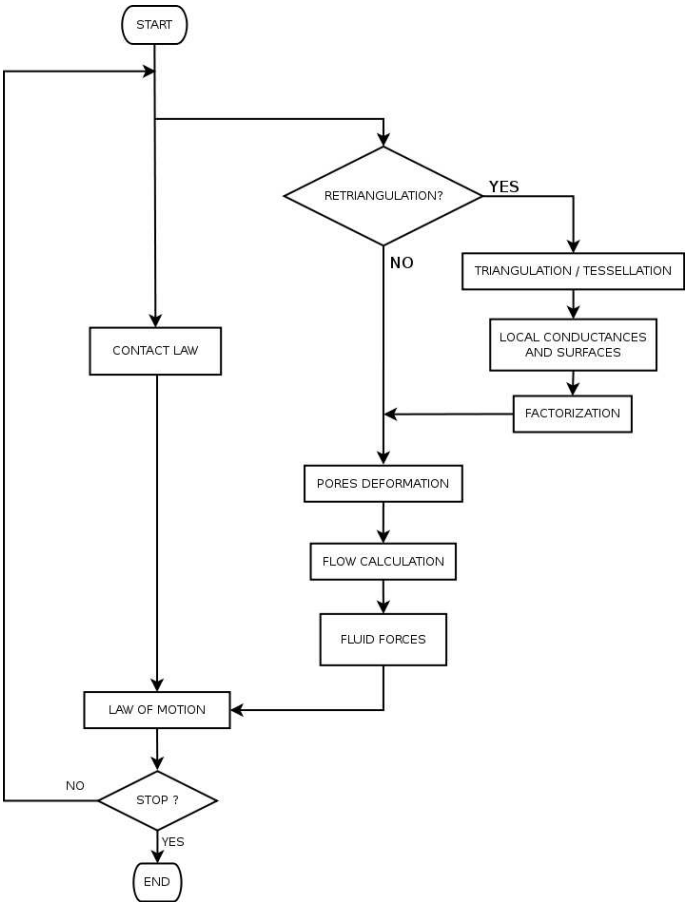

Figure 5.9: An optimized version of the PFV-DEM coupled model.

Fig.5.8b shows the result that was obtained by fixing the following threshold:

$$\varepsilon_{RETRG} < 1\% \tag{5.14}$$

By the direct comparison with the solution that was obtained retriangulating the system at each iteration it can be concluded that such criterion seems to be sufficient to assure that the triangulation-based geometrical and mechanical variables are effectively representative of the state of the medium during the whole simulation.

A new flow chart is shown on fig.5.9, including the verification, at each iteration, of the need for a new triangulation of the system.

5.1.4 Optimization of fluid forces calculation

Keeping the triangulation system unchanged allows the use of a sort of "cached" informations stocked in the memory (matrix $[\mathbf{G}]$ of eq.(4.4)), with a consistent save of computational time. It can be noticed how in the computation of fluid forces by eq.(3.15) the geometrical variables remain unchanged as long as the triangulation is not updated (see the chart of fig.5.9). This operation becomes more than three times faster, as it can be seen on fig.5.4(e).

$$\frac{T_{F_{cache}}}{N} = 1.35 \cdot 10^{-6} = \alpha_{F_{cache}} \tag{5.15}$$

5.1.5 Total computational cost

An estimation of the average computational time needed for one cycle of computation of the coupled PFV-DEM model is obtained by summing eq.s (5.1), (5.2), (5.3), (5.15), (5.11), (5.12). A unique expression can be formulated, which will be function of the number of particles N, and the period of retriangulation P_R:

$$P_R = \frac{I}{N_{TRG}} \tag{5.16}$$

where I is the total number of iterations and N_{TRG} is the number of retriangulation events. We can rewrite eq.(5.1) in the following way:

$$\begin{aligned} T &= T_{DEM}(N) + T_{PFV}(N,P_R) \\ &= T_{DEM}(N) + T_{TRG}(N,P_R) + T_G(N,P_R) + T_{DEF}(N) + T_{LS}(N) + T_F(N,P_R) \end{aligned} \tag{5.17}$$

The terms which depend on both N and P_R are triangulation-based operations, which are made only N_{TRG} times in one simulation.
From [94], we have the estimate:

$$T_{DEM} = 1.8 \cdot N log(N) = \alpha_{DEM} \cdot N log(N) \tag{5.18}$$

Finally, we can write:

$$\begin{aligned} T &= T_{DEM}(N) + T_{PFV}(N,P_R) = \\ &= T_{DEM}(N) + T_{TRG}(N,P_R) + T_G(N,P_R) + T_{DEF}(N) + T_{LTL}(N,P_R) + T_{SLV}(N) + T_F(N,P_R) = \\ &= \alpha_{DEM} \cdot N log(N) + \alpha_{TRG}\frac{N log^2 N}{P_R} + \alpha_G \frac{N}{P_R} + \alpha_{DEF} N + \alpha^{LTL}\frac{N^2}{P_R} + \alpha_0^{LTL}\frac{N}{P_R} + \\ &+ \alpha^{SLV} N^{(1+\alpha_0^{SLV})} + \alpha_F \frac{N}{P_R} + \alpha_{F_{cache}} N \end{aligned} \tag{5.19}$$

Table 5.6 reports the values of the factors to be used in such expression, for the estimation of the total computational time of one simulation. In fig.5.10 it is shown, for the simulation of the oedometer test, the effect of the frequency of retriangulation P_R on the time cost proportion between the "dry" *DEM* and the coupled DEM-PFV.

α_{TRG}	$5.8 \cdot 10^{-6}$
α_G	$5.4 \cdot 10^{-5}$
α_{DEF}	$8 \cdot 10^{-7}$
α_{LTL}	$7.813 \cdot 10^{-9}$ (pardiso) - $5.25 \cdot 10^{-9}$ (taucs)
α_0^{LTL}	$4.84 \cdot 10^{-5}$ (pardiso) - $6.38 \cdot 10^{-5}$ (taucs)
α^{SLV}	$9.4 \cdot 10^{-8}$ (pardiso) - $1.72 \cdot 10^{-7}$ (taucs)
α_0^{SLV}	0.36 (pardiso) - 0.33 (taucs)
α_F	$5 \cdot 10^{-6}$
$\alpha_{F_{cache}}$	$1.35 \cdot 10^{-6}$
α_{DEM}	1.8

Table 5.6: Factors for the estimation of the total computational time.

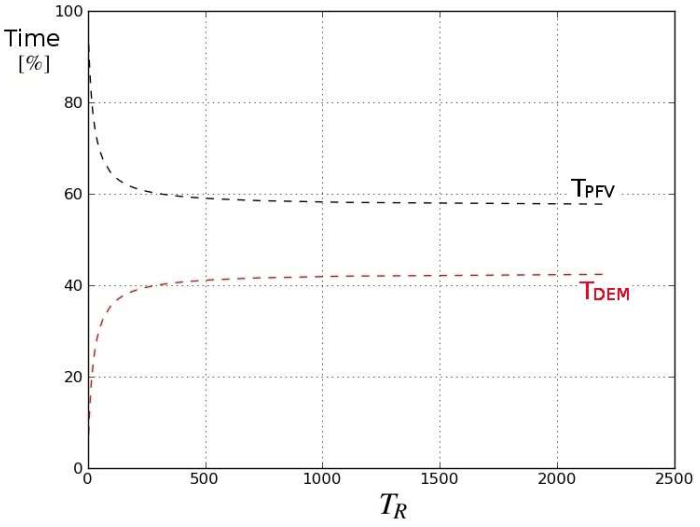

Figure 5.10: Example of time cost proportions between the DEM and PFV calculations for N=5000. Effect of the retriangulation frequency (case of PARDISO direct solver).

Conclusions

This part was entirely devoted to the presentation of the DEM-PFV coupled model, based on a discretization of the void space in finite volumes for the approximation of the viscous flow equations, upscaled at the pore level, and on the discrete element method for the modelling of solid particles interaction (section 4.1).

A key feature of the model is the description of the interaction between the solid and the fluid phases, that is done at the scale of pores and particles. The analysis of the interaction of a single particle with the fluid surrounding it is made possible by modelling at such scale. The employment of spherical particles provides an easy-to-handle geometric computations. The discrete nature of DEM models is preserved in the PFV model, and their coupling results naturally adapted. The final algorithm uses a semi-implicit finite difference scheme for time integration. The stability of the coupled model was also discussed. By the introduction of further simplifications, with the hypothesis of piecewise constant pressure, the number of unknowns for the resolution of the flow problem remains comparable to the case of the solid elastic-plastic problem.

Taking the FEM results as reference, the permeabilities obtained with the pore-scale modeling are in most cases within the range of $\pm 20\%$, usually below the reference value. Considering only symmetric boundary conditions, the permeabilites are better predicted (in the range $\pm 10\%$), which indicates that fluxes along planar no-slip boundaries are underestimated. The model predictions were found in good agreement with permeability measurements on bi-dispersed glass beads assemblies, as it was found by Anh-Tuan Tong during his PhD thesis [99].

The effective radius proposed by Bryant et al. [19] for mono-sized spheres also gives acceptable predictions of permeabilities for polydispersed sphere packings, but it is computationally more expensive and underestimates fluid fluxes more than the hydraulic radius proposed in this investigation. It is important to note that the pore network model of Bryant et al. includes a reduction of L_{ij}, accounting for overlapping cylindrical throats. This correction has not been implemented because it requires relatively complex computations of cylinders intersections. By maximizing micro-gradients, this correction could have at least partly balanced the underestimation of permeabilities in our results. Hence, our findings cannot be considered in disagreement with the Bryant et al. model in itself. They only indicate that the effective radius should not be used in connection with the regular Delaunay partitioning we are developing.

The pressure field compares well with the FEM results. In all cases, the sum of forces applied on the solid phase in a unit cube under unit gradient is close to one, showing the correct implementation and validity of the model at the mesoscale. Forces applied by the fluid on individual particles, and viscous forces on no-slip boundaries, are found to be correct, with errors typically less than 10%: the error, though, grows larger when the size ratio d/D of the particles is less than 0.2. The modelling of fluid forces gives a sound basis for fluid-particle systems.

The ability of the model to solve transient problems was tested by analyzing the consolidation process of a saturated sample subjected to axial load. The solution obtained, in the case of small deformations, is in good agreement with Terzaghi's analytical solution, in terms of evolution of the excess pore pressure and settlements, in time and space. In case of large deformations, the limitations of Terzaghi's formulation linked to the adop-

tion of a unique constant value for the permeability and the oedometric modulus for the granular medium, influenced as well our simulations.

It is worth noticing that in the PFV model, the description of stress and strain in the fluid is limited to their isotropic component, as it is the case in the Biot model of poroelasticity. Donia Marzougui integrated into the model the contribution, in terms of fluid-solid interaction, which arises from taking into account the deviatoric component of the fluid stress and strain tensors [63]. New viscous shear forces arise from taking into account such component. In the next part we will show an example of numerical result obtained with this new contribution.

Many numerical aspects, concerning the performances of the model, have been finally analyzed. At each iteration, a linearized system of the form $Ax = b$ have to be solved, where A was in this case a positive defined symmetric matrix, expressing the hydraulic conductivity of the porous medium. Various approaches had been tested in order to solve such system, notably the Gauss-Seidel iterative procedure, and two direct solvers, based on PARDISO and TAUCS libraries. It has been shown how the adoption of direct solvers allows a significative boost of performances. For the simulations we have presented in this thesis, the total computational cost that was measured was only the double with respect to uncoupled "dry" simulations. This can be considered as innovative in the framework of modern fluid-solid coupling models.

The parallelization of the model is conceivable and constitutes a perspective on further developments. The structure of the algorithm, as represented on fig.5.1, suggests an easy parallelization of the code, in order to utilize multiple processors simultaneously in a shared-memory multiprocessor machine. Forces at contacts betweeen particles and fluid forces can in fact be computed independently. The DEM, as implemented in the open-source code YADE, is already parallelized [101], whereas in regard to triangulations in CGAL, works are in progress [9]. The TAUCS version we employed is sequential [98], while PARDISO is fully parallelized [86], [87]. The Gauss-Seidel method, also, can be easily parallelized [53].

Part III

Sediment hydrodynamics

Chapter 6

Sediment hydrodynamics

The interaction between the solid and the fluid (liquid or gas) phases, strongly influences the behaviour of granular materials, and is crucial to interprete phenomena as internal or external erosion, sediment transport, wave or seismic-induced instability of structures and foundations, soil liquefaction, etc.

It has been shown in the previous chapters how the PFV-DEM model could provide a relevant tool to analyse the behaviour of fluid-particle systems. Pore-scale modelling allows to link the macroscopic behaviour to the local properties that characterize the microstructure (solid fraction, particle size), and may help the interpretation of the above mentioned complex mechanisms, on the base of micromechanical considerations.

In this chapter we will present the application of the model to the poro - visco - elastoplastic problem that characterizes of the interaction between fluid flow and internal deformation in coastal sediments. This study is part of the Hydro-Fond[1] project (”Hydromécanique des Géomatériaux de Fondation Immergés“). The aim is the characterisation of the instability induced by cyclic loading associated to the action of waves. This problem is of special interest since it has rarely been studied and is at the interface between fluid mechanics and geomechanics-based disciplines. It is out of the scope of this work analyze processes of suspension, erosion and deposition of solid particles, and generally the complex mechanism involved with sheet flow at seabed surface. Instead, the consequences of the action of sea waves on the stability of the seafloor, the influence of initial state conditions such as porosity and the relation existing between the period of wave loading and the characteristic time of consolidation of the packing will be presented and discussed.

[1]Realised with the support of the Department of Ecology, of the sustainable development, transports and housing, general direction of substructures, transports, and the sea,within the C2D2 program of RGCU.

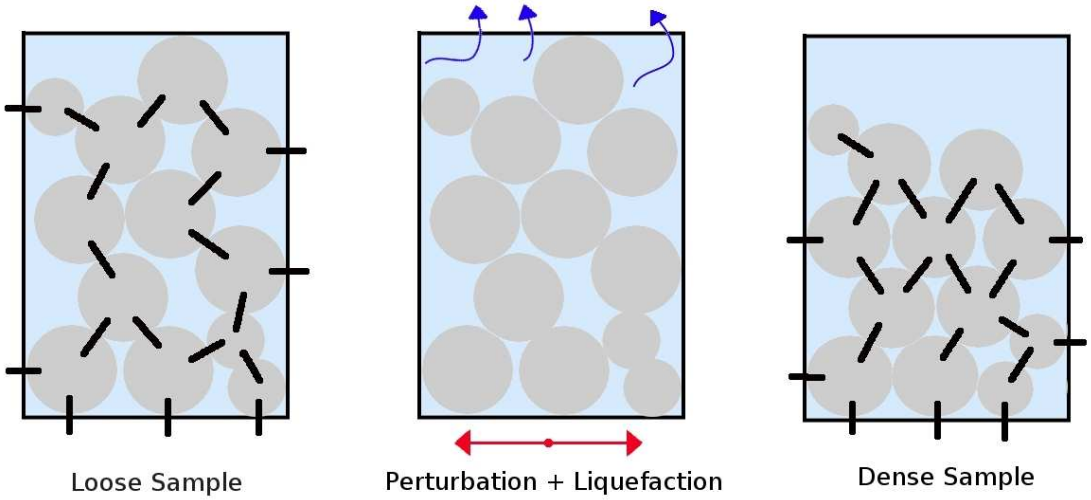

Figure 6.1: Soil liquefaction: schematized mechanisms.

6.1 Soil liquefaction

Soil liquefaction is a phenomenon in which soil loses much of its strength or stiffness for a generally short time. It arises with cyclic loading and static overloading of soil, usually but not exclusively from earthquakes. Liquefaction develops rapidly, often with minimal warning in what appears to be a safe situation. It has caused many failures worldwide, with both deaths and some very large financial losses.

As long as the grains are in contact, the average pore pressure is the hydrostatic one. If subjected to a mechanical perturbation, the soil tends to compact. Once the soil tends to compact, the intergranular contacts are broken and the external load is carried by the fluid, leading to the increase of the pore pressure p. Therefore, soil liquefaction is generally associated to an increase of the pore pressure p, such that the effective stress σ' vanish.

An example of a situation where such criterion is satisfied is represented on fig.6.1, where a loose saturated material under gravitational loading liqeufies as an effect of a perturbation (a typical case is seismic-induced liquefaction).

6.2 Simulation of the wave action

The accurate reproduction of the load of a natural wave on a seabed would demand a modelling of turbulent fluid flow. This is, for the moment, out of the scope of this work. Our simplifying choice was to represent the wave action by specifying a sinusoidal-shaped pressure condition at the top boundary of the packing. The periodicity of such representation can be observed on fig.6.2. The simulations we will be present henceforth employ a half period, then a condition of symmetry is imposed on lateral boundaries (see fig.6.3), while the bottom boundary is impermeable.

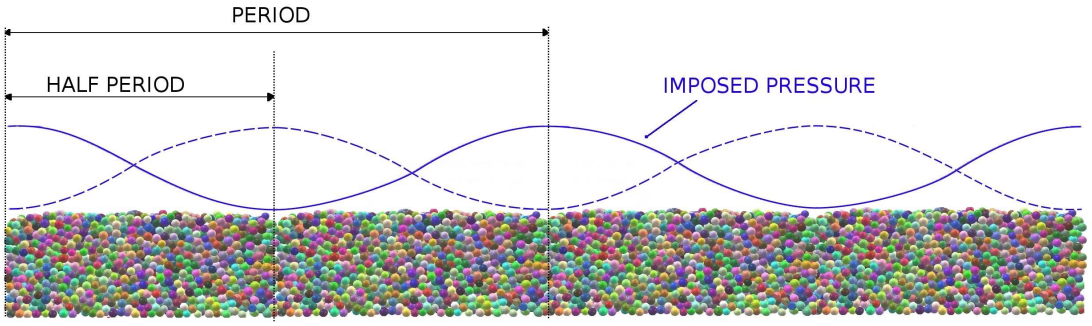

Figure 6.2: Simplified wave action: sinusoidal pressure condition.

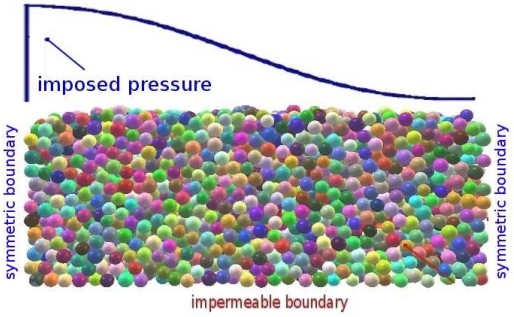

Figure 6.3: Seabed representation for the study of the sediment hydrodynamics (half period on fig.6.2) - Symmetric conditions are specified on lateral boundaries.

Analytical solution

For the specified boundary conditions, the *Darcy* velocity field can be computed analytically, considering a fixed solid skeleton. We present the solution for the 2D problem. The field is governed by Darcy's law (1.31), recalled here:

$$\mathbf{q} = K_d \nabla H \tag{6.1}$$

where q_i is the specific discharge in m/s, H is the hydraulic potential of eq.1.28, K_d is the coefficient of *hydraulic conductivity* expressed in m/s. By imposing the condition of divergence of fluid velocity is zero,

$$div\,\mathbf{q} = 0 = K_d \nabla^2 H \tag{6.2}$$

it can be stated that the potential H is harmonic. The condition of impermeability reads $\mathbf{u} \cdot \mathbf{n} = 0$ or $\nabla H \cdot \mathbf{n} = 0$. A harmonic problem, with mixed Neumann-Dirichlet conditions

at boundaries, has to be solved:

$$\nabla^2 H = 0 \tag{6.3}$$

$$x = 0 \quad \rightarrow \quad \frac{\partial H}{\partial x} = 0 \tag{6.4}$$

$$x = L \quad \rightarrow \quad \frac{\partial H}{\partial x} = 0 \tag{6.5}$$

$$z = -h \quad \rightarrow \quad \frac{\partial H}{\partial z} = 0 \tag{6.6}$$

$$z = 0 \quad \rightarrow \quad H(x,0) = H_{lim}(x) \tag{6.7}$$

The general solution can be written as:

$$H(x,z) = M(x)N(z) \tag{6.8}$$

Eq. (6.3) can be rewritten as:

$$\frac{M''}{M} = -\frac{N''}{N} = \pm\theta^2 \tag{6.9}$$

where M' indicates the ordinary derivative dM/dx.

Case 1 Making the choice of $+\theta^2$, we have:

$$M(x) = Ae^{\theta x} + Be^{-\theta x} \tag{6.10}$$

Combining with the conditions of eq.s (6.4) and (6.5), we end up with a homogeneous system in A and B, as follows:

$$A - B = 0 \tag{6.11}$$

$$Ae^{\theta L} - Be^{-\theta L} = 0 \tag{6.12}$$

which has a non-zero solution if $e^{2\theta L} = 1$, resulting in $\theta = 0$. Such condition would bring to a constant M, which is not physically consistent.

Case 2 Making the choice of $-\theta^2$, we have:

$$M(x) = Acos(\theta x) + Bsen(\theta x) \tag{6.13}$$

$$N(z) = Ccosh\,\theta(z+h) + Dsinh\theta(z+h) \tag{6.14}$$

Conditions of eq.(6.4),(6.6) can be rewritten as:

$$M'(0) = 0 \tag{6.15}$$

$$N'(-h) = 0 \tag{6.16}$$

which implies $B = D = 0$. Condition (6.5) becomes:

$$M'(L) = -A\theta sin(\theta L) = 0 \tag{6.17}$$

from which, excluding the non-physical solution $A = 0$, we have $sin(\theta L) = 0$, with θ that may assume infinite values:

$$\theta = \frac{n\pi}{L} \quad n = 0, 1, ... \tag{6.18}$$

We solve a Sturm-Lioville problem, whose solution reads:

$$H = A_0 + \sum_{n=1}^{\infty} A_n cosh\,\theta_n(z+h)cos\,\theta_n x \tag{6.19}$$

with the constants A_0 and A_n that will be determined by specifying the condition of eq.(6.7).

Rewriting condition (6.7) to consider the sinusoidal pressure condition represented on fig.6.3, we have:

$$z = 0 \quad \rightarrow \quad H(x,0) = \frac{H_0}{2}\left(1 + cos\frac{\pi x}{L}\right) \tag{6.20}$$

which is already written as a Fourier serie. Then, we can write, term-by-term:

$$A_0 = \frac{H_0}{2} \tag{6.21}$$

$$A_1 = \frac{H_0}{2}\frac{1}{cosh\,\frac{\pi h}{L}} \tag{6.22}$$

$$A_2 = A_3 = ... = 0 \tag{6.23}$$

Finally the solution reads:

$$H(z,x) = \frac{H}{2}\left(1 + \frac{cosh\,\frac{\pi}{L}(z+h)}{cosh\,\frac{\pi h}{L}} cos\frac{\pi}{L}x\right) \tag{6.24}$$

and the velocity field is easily computed:

$$u(x,z) = K_d\frac{\pi}{L}\frac{H_0}{2}\frac{cosh\frac{\pi}{L}(z+h)}{cosh\frac{\pi h}{L}} sin\frac{\pi}{L}x \tag{6.25}$$

$$v(x,z) = -K_d\frac{\pi}{L}\frac{H_0}{2}\frac{sinh\frac{\pi}{L}(z+h)}{cosh\frac{\pi h}{L}} cos\frac{\pi}{L}x \tag{6.26}$$

Fig.6.4 shows the velocity field superimposed to the equipotential lines.

Numerical solution

Fig.6.5 shows the pressure field that was obtained numerically over the 3D sample that was employed in our simulation. A 2D visualization (depth/height=2.0 as in the analytical case) of the equipotential lines and of the pressure field are represented as well. Fig.6.6 compares directly the numerical and the analytical solution, in terms of equipotential lines and velocity field, that are found in good agreement. The two velocity fields show a very similar pattern. It is worth noticing that only 5000 grains have been employed to obtain this result. The adoption of a higher number of particles would smooth further the equipotential lines and avoid some irregularities as they can be observed in the velocity field.

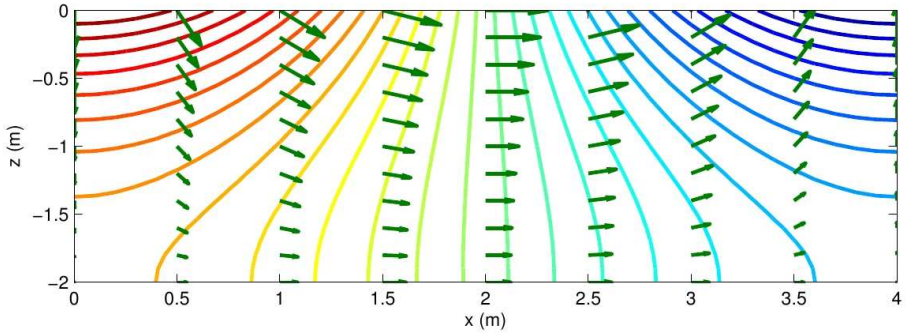

Figure 6.4: Analytical solution. Equipotentials and fluid velocity field (Depth / Height = 2.0).

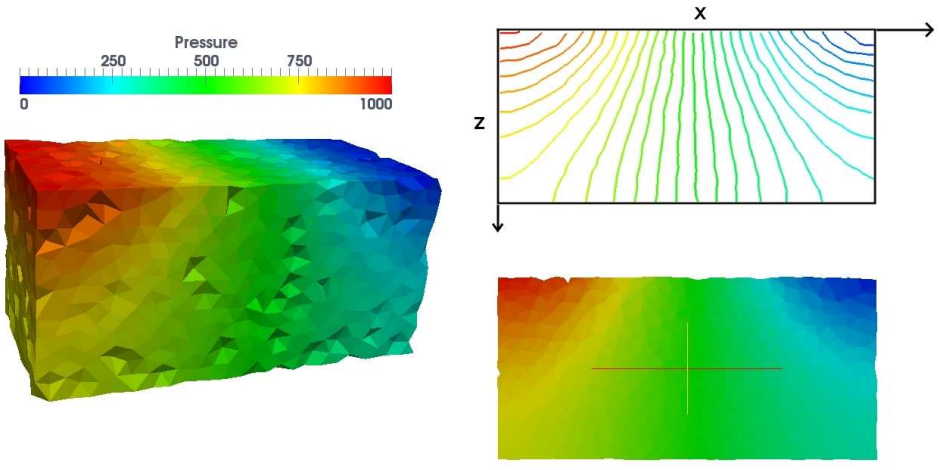

Figure 6.5: Numerical solution. Equipotential lines and pressure field (Depth / Height = 2.0).

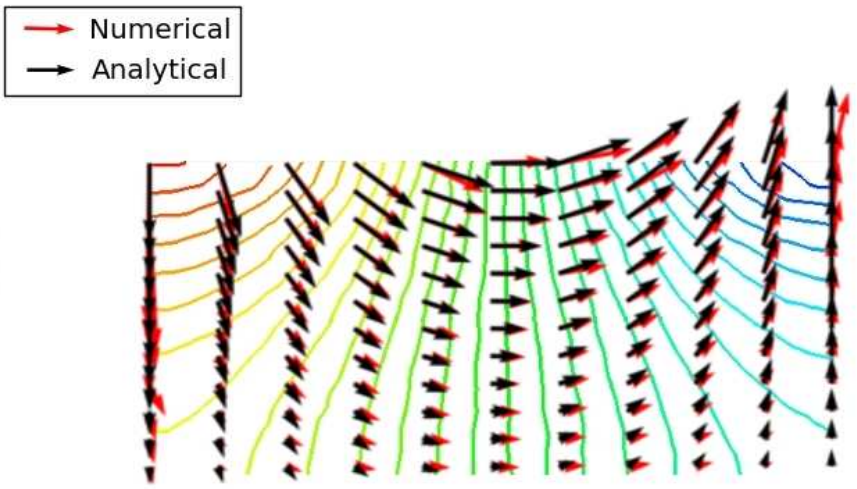

Figure 6.6: Fluid velocity field - Numerical and analytical solution.

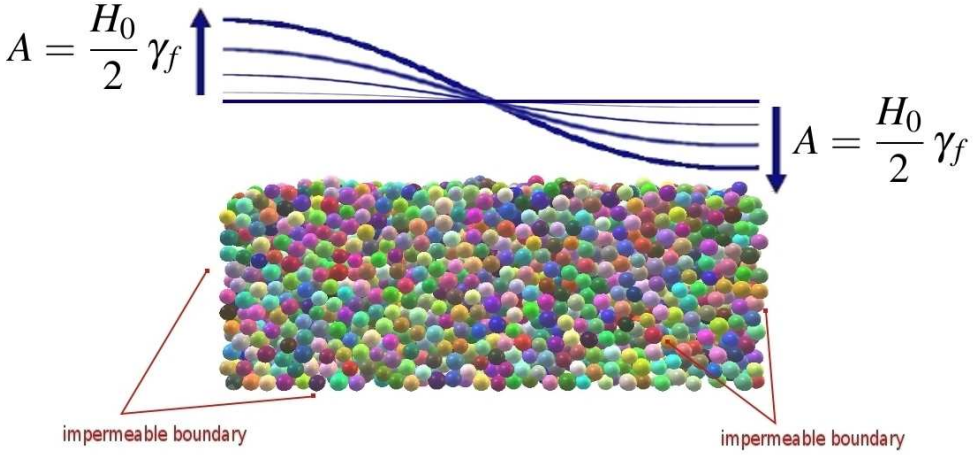

Figure 6.7: Simulation of a pressure wave of increasing amplitude.

6.3 Wave action on a deformable granular medium

The effect of the wave action on a sphere packing will be presented in this section, considering a deformable solid skeleton. The boundary conditions are the ones presented in section 6.2, with a sinusoidal pressure profile imposed at the top boundary. The amplitude A ($A = \frac{H_0}{2}\gamma_f$, [Pa], see fig.6.7) of the wave, is increased linearly with time. Each increment of the amplitude corresponding to a higher pressure gradient imposed to the packing, the analysis will consist of the observation and interpretation of its response. Two main scenarios are reproduced, differing in the value of initial porosity of the granular medium; we will refer henceforth to the *loose* case ($n = 0.436$) and the *dense* case ($n \simeq 0.368$).

During the simulation, a fluid pressure measurement is taken at six equally spaced points (p1, p2, .. p6 on fig.6.8) along five verticals (v1, v2, .. v5 on fig.6.8).

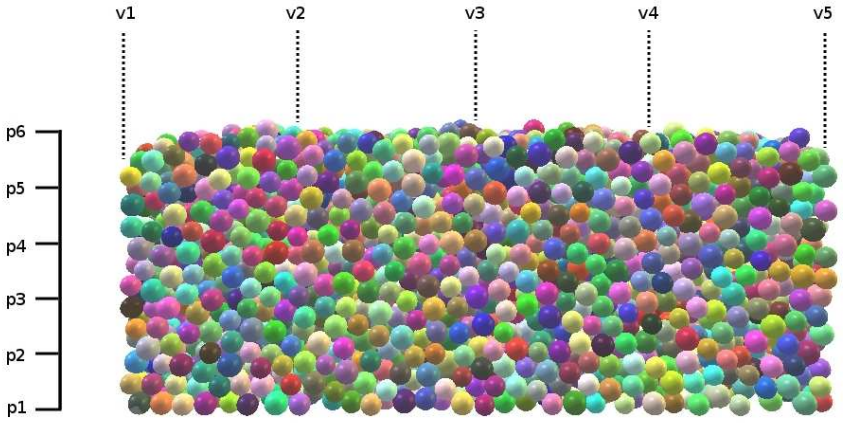

Figure 6.8: Scheme of fluid pressure measurements.

6.3.1 Preparation of the sample

To properly prepare a sphere packing that could represent at best the real conditions of a seabed, an expectable choice would be an immersed granular deposition as it has been presented in section 4.5. By the way, due to the relatively high computational cost that would be linked to the preparation of stable packings following this procedure, a dry pluviation process is preferred, a choice that allows the reproduction of all the configurations that we need to analyze different scenarios.

The preparation of a looser or denser packing is ensured by smartly specifying an intergranular friction angle, which would prevent more or less effectively the slip of particles at contacts and their mutual rearrangement. It is worth noticing that the friction angle that is adopted during the phase of preparation of the packing, ϕ_{c1}, has to be smaller or equal the intergranular friction angle that is adopted during the simulation, ϕ_{c2} in eq.(2.12). Otherwise unstable packings are obtained.

Triaxial test

Triaxial testing is a classical tool that is adopted in geomechanics in order to characterize the mechanical behaviour of granular soils. We will present and discuss in this section the results that were obtained on two samples, whose granulometry and initial porosity are the same than the dense and the loose seabeds which were prepared following the procedure described in section 6.3.1.

A dense ($n \simeq 0.37$) and a loose cubic samples ($n \simeq 0.44$) were created, by imposing an isotropic confining stress of $50\,kPa$ to the sample. Table 6.1 summarizes the parameters of the simulation. The results that were obtained are plotted on fig.6.9, in terms of axial stress and strain (a), and volumetric and axial strain (b). The resulting curves are classical: for the dense case, a peak is clearly remarquable on the $\varepsilon_{zz} - \sigma_{zz}$ curve, while a contractant-dilatant behaviour is observed on the $\varepsilon_{zz} - \varepsilon_v$ curve; for the loose case, a purely contractant behaviour is observed (b), and no peak is remarquable on the $\varepsilon_{zz} - \sigma_{zz}$ curve (a). The stress-strain curves converge at the same value at the critical state. These limit configurations were reproduced for the simulation of the wave action on the seabed,

INPUT DATA		
N	$[-]$	5000
d_{50}	$[m]$	0.06
ρ_s	$[kg/m^3]$	2600
ρ_f	$[kg/m^3]$	1000
σ_{iso}	$[kPa]$	50
n	$[-]$	0.37 - 0.44
E	$[kPa]$	15000
a	$[-]$	0.5

Table 6.1: Numerical triaxial tests - Input data.

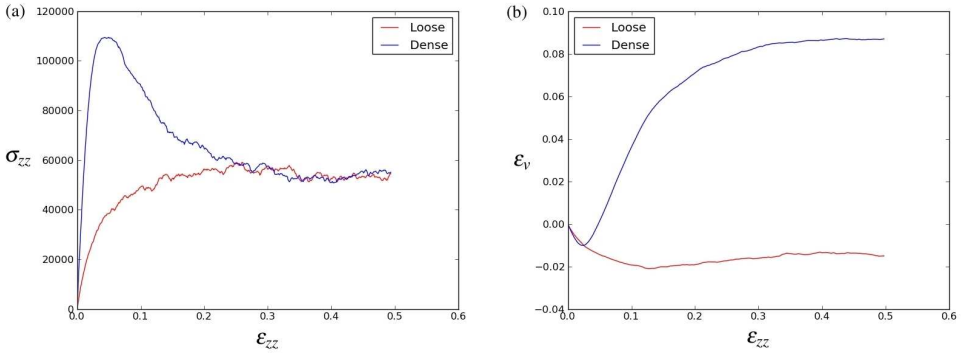

Figure 6.9: Triaxial tests on a loose ($n \simeq 0.37$) and a dense ($n \simeq 0.44$) packing.

in order to analyze the effects of a such different behaviour on the global response of the packing. This makes the object of the next sections.

6.3.2 Dense sphere packing

We will present in this section the results that were obtained by simulating the action of a wave on an initially dense sphere packing. As it has been described in section 6.3.1, a dense particles arrangement is obtained by specifying a low intergranular friction angle, hence favouring the slip at contacts. Table 6.2 summarizes the input parameters of the simulation.

State and kinetic parameters

The evolution of some indicative parameter, useful to analyze the state and the kinetic of the system during the simulation, is plotted on fig.6.10. The amplitude of the wave A, on

INPUT DATA		
N	$[-]$	5000
ϕ_{c1}	$[deg]$	1
ϕ_{c2}	$[deg]$	30
E	$[kPa]$	15000
a	$[-]$	0.5
d_{50}	$[m]$	0.066
d_{max}/d_{min}	$[m]$	1.22
μ	$[kPa \cdot s]$	0.1

Table 6.2: Wave action on a dense sphere packing. Input parameters.

the top plot, linearly increases with the time. The evolution of the kinetic energy KE and of the parameter λ (see eq.(2.16)), are plotted as well. The former parameter is defined as the summation of each particle's kinetic energy, while the latter is defined for each body as the norm of the ratio between the resultant of all external forces acting on particles over the resultant of contact forces ($= 0$ at static equilibrium, see eq.(2.16)). They give essential informations to detect the onset of instabilities during the simulation. Notably the kinetic energy's evolution (y-semilogarithmic scale plot) appears noisy, with some motion event that can be recognized up to an amplitude of $1500\,Pa$, related to some local rearrangement of particles. For higher amplitudes, after $t = 15$s, the particles accelerate suddenly. The evolution of λ confirms these indications. The last two plots report the maximum y-coordinate (y_{max}) of the packing and the porosity (n) of the medium. Both parameters don't show any significative variation, except in the last part of the simulation.

It appears clear that the packing remains globally stable up to an amplitude $A = 1500\,Pa$. Beyond this value, the drag force which result from the flow gradient is high enough to induce an overall instability of the packing. Any localization of the deformation is optically remarquable. On fig.6.11 four snapshots of the simulation at times $t = 5\,s$, $t = 10\,s$, $t = 15\,s$, $t = 19.3\,s$ are presented. The fluid pressure profile and the grain velocity field are represented. It can be seen how the pressure profile remains similar to the hydrostatic one all along the simulation. This means that, solving the system of eq.(4.4), here recalled ($\{\mathbf{Q_q}\} = 0$),

$$[\mathbf{G}]\{\mathbf{P}\} = [\mathbf{E}]\{\dot{\mathbf{X}}\} + \{\mathbf{Q_p}\} \tag{6.27}$$

the right-hand side term which mainly influences the solution $\{\mathbf{P}\}$ is $\mathbf{Q_p}$, the vector of imposed pressures, whereas is weakly influenced by the vector containing the rates of pores volumetric strain, $\mathbf{E\dot{x}}$.

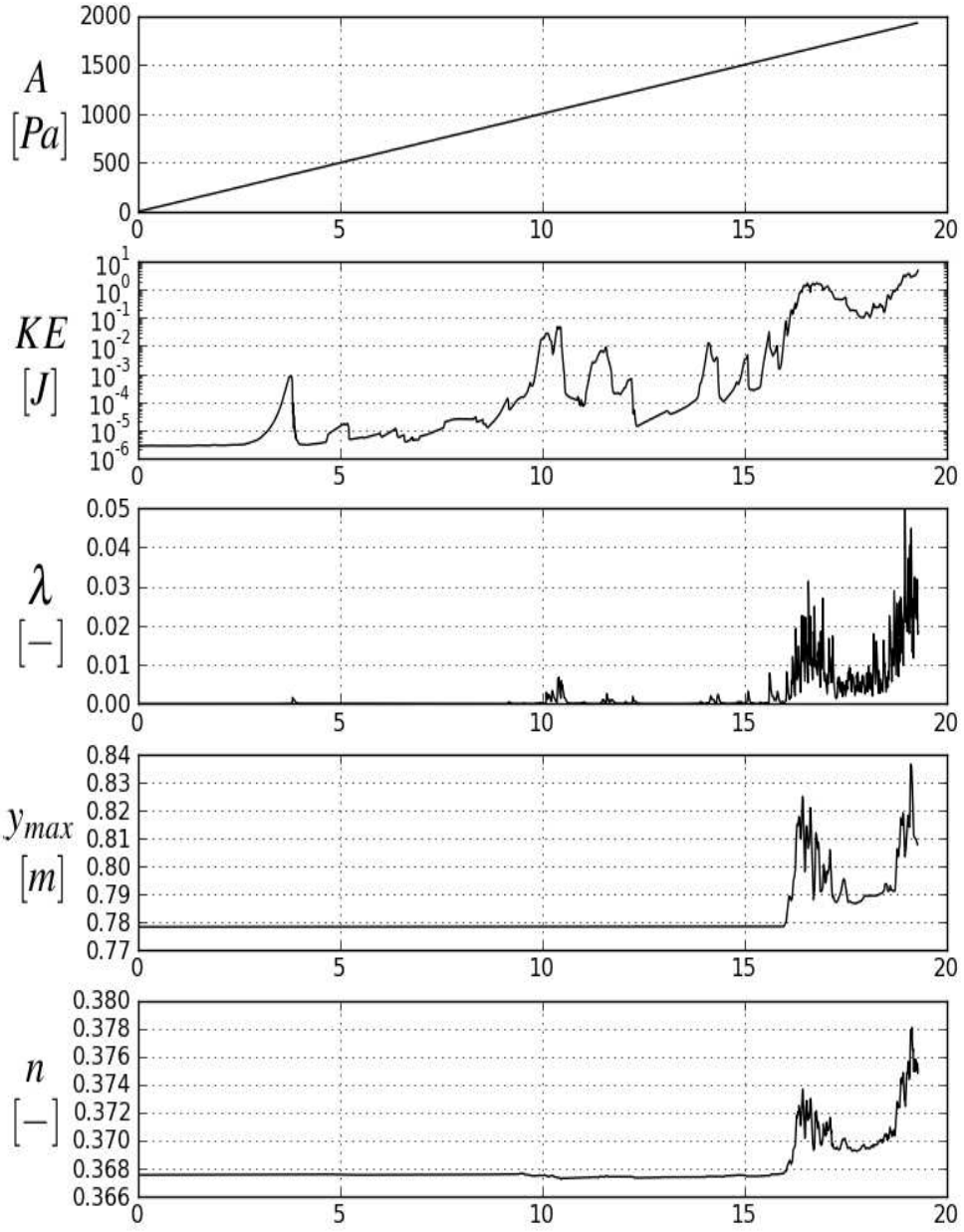

Figure 6.10: Wave action on a dense seabed - Evolution of kinetic parameters for the wave actino defined by input data of table 6.2.

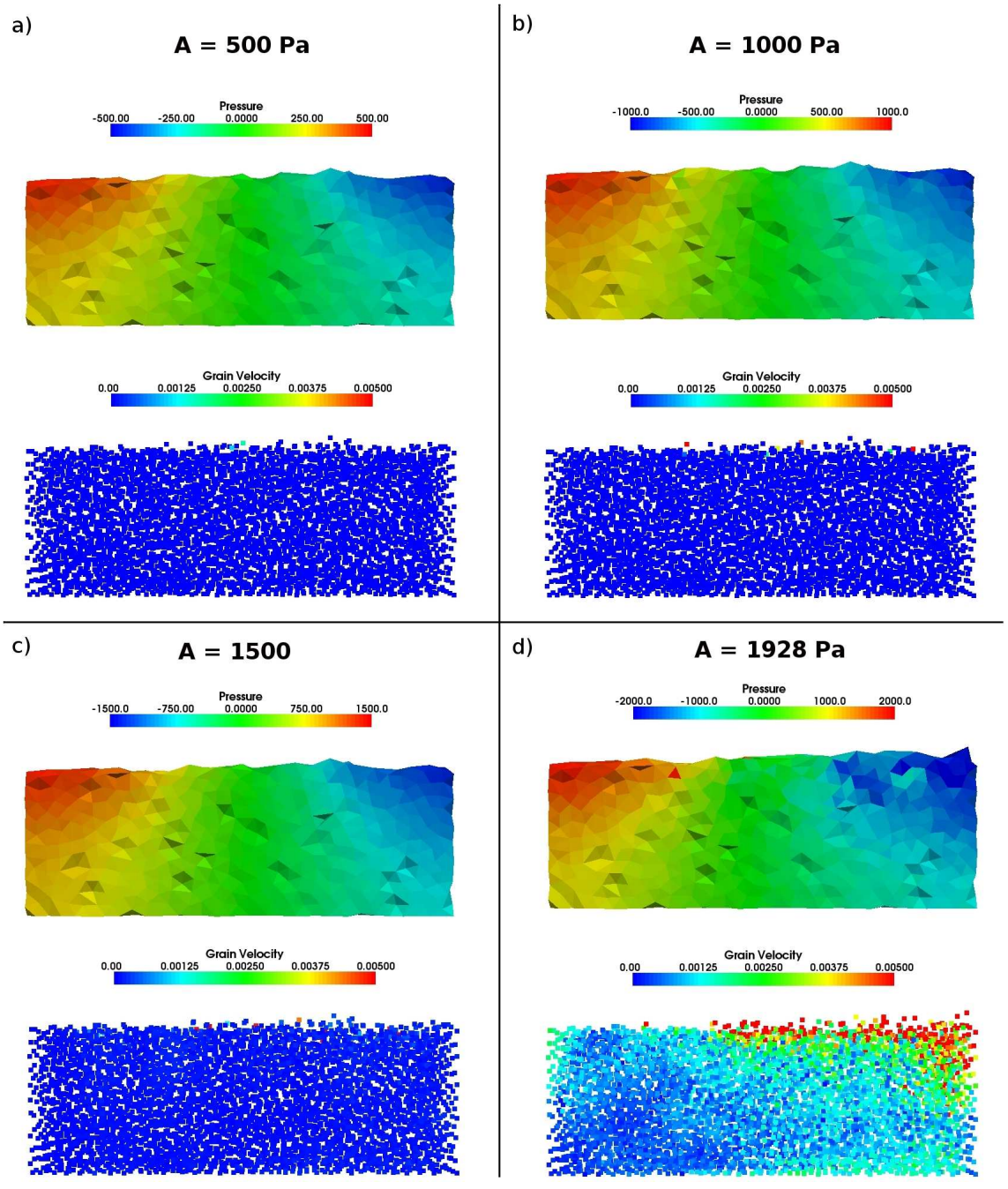

Figure 6.11: Simulation snapshots at $t = 5s$ (a), $10s$ (b), $15s$ (c), $19.3s$ (d). Fluid pressure in [Pa], grain velocity in [m/s].

Fluid pressure measurements

The values of fluid pressures, which are measured according to the scheme presented on fig.6.8, are plotted on fig.6.12(left). Their evolution indicates clearly that the pressure profile doesn't deviate from the hydrostatic one, except in the last part of the simulation ($t > 15s$), when an instability mechanism arises.

On the same figure, the ratio between the gradient of charge ∇H and the critical gradient of liquefaction, i_c, defined in eq.s (4.32) and (4.33), is plotted. It's defined as follows:

$$\frac{\nabla H}{i_c} = \frac{\nabla H \gamma_f}{\gamma'} = \frac{\nabla P}{\gamma'} = \frac{\Delta p}{\gamma' \Delta z} \tag{6.28}$$

where Δp is the pressure difference between each couple of consecutive sensors (whose distance between each other is Δz), and γ' is the buoyant unit weight of the soil (see eq.(4.32)), whose initial porosity is $n \simeq 0.368$. In case of liquefaction, $\nabla H / i_c = 1$.

As expected, the evolution of this ratio is linear as long as the packing remains stable. Once the instability occurs, the grains are dragged by the flow, and a noisy evolution is observed.

Result interpretation

An interpretation of what happens in the last part of the simulation is suggested by the simulation snapshot of fig.6.13, where the motion of the particles is represented by arrows whose color and length represent their velocity and acceleration, respectively. The motion is found to concern mainly the grains at the seabed surface that tend to be dragged as a result of the pressure gradient which is imposed to the seabed, and to pile up next to the right wall. Considering that a condition of symmetry is specified on lateral boundaries (see fig.s 6.2,6.3), this result can be interpreted as the formation of a sediment dip. The strain deviator field represented on fig.6.14 confirms this interpretation.

6.3.3 Loose sphere packing

We will present now the results that were obtained by performing the same experience on a loose seabed, prepared by specifying a high intergranular friction angle, preventing in this way the slip at particles contacts. Table 6.3 summarizes the input parameters of the simulation.

State and kinetic parameters

Looking at fig.6.15, many differences may be noticed comparing to the *dense* case. The amplitude A at which we observe the onset of instabilities is much lower: the kinetic energy KE, plotted on logarithmic scale, already indicates the presence of moderate motion events by the beginning of the simulation. A more significative motion can be observed from around $t \simeq 5\,s$: the kinetic energy and the parameter λ show a sudden increase, followed by a slightly shifted reduction of the maximum y-coordinate y_{max} and of the porosity n. The packing is consolidating.

The interpretation of what follows is tricky using the data of fig.6.15. The kinetic parameters (KE, λ) indicate that the packing is moving, with a nearly constant velocity,

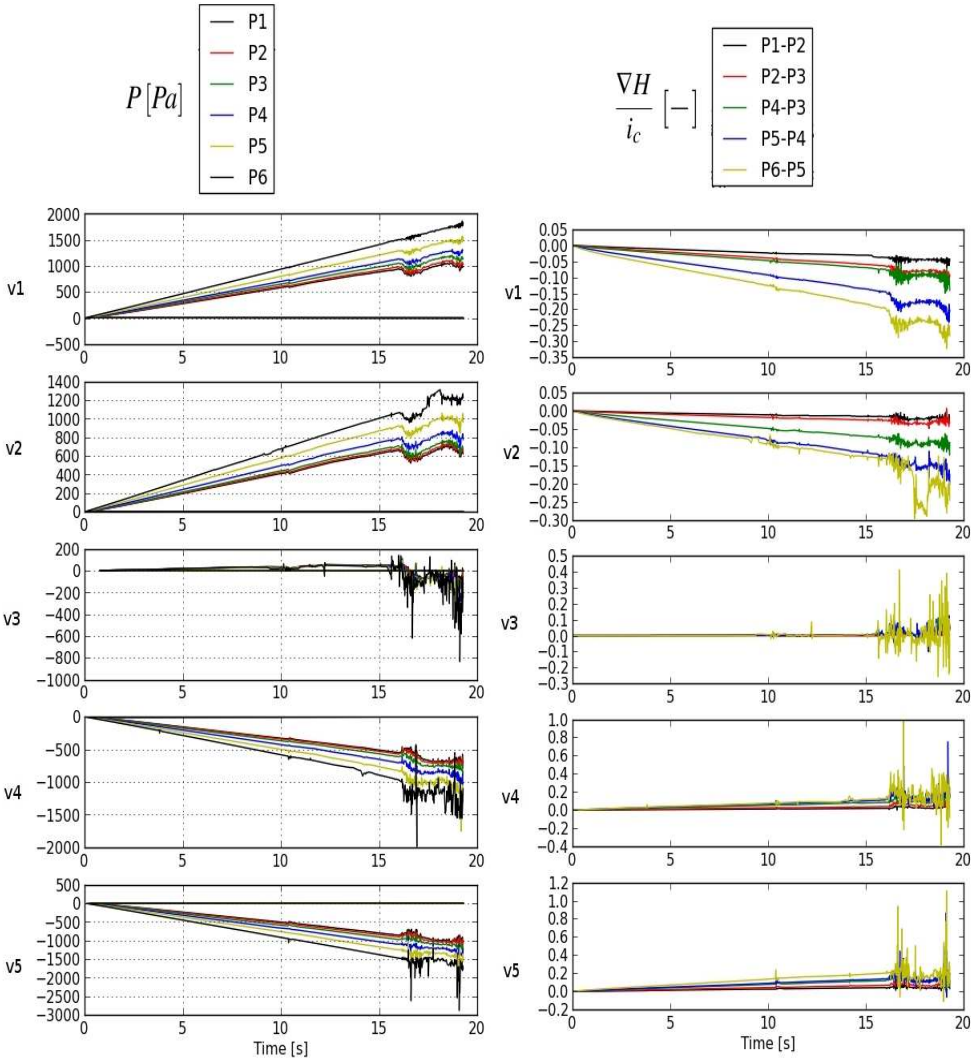

Figure 6.12: Wave action on a dense seabed - Fluid pressure measurements.

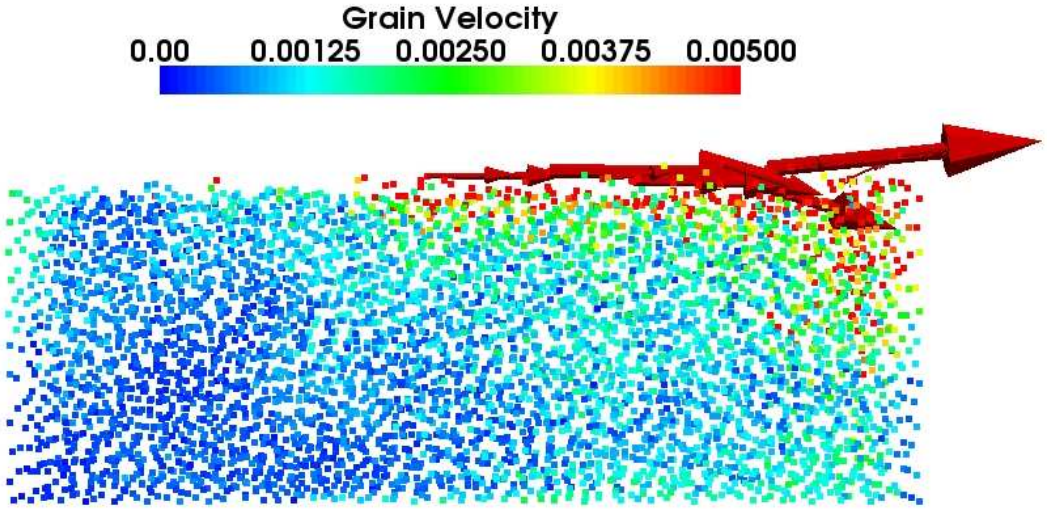

Figure 6.13: Wave action on a dense seabed - Grain velocities (arrows color) and accelerations (arrows length).

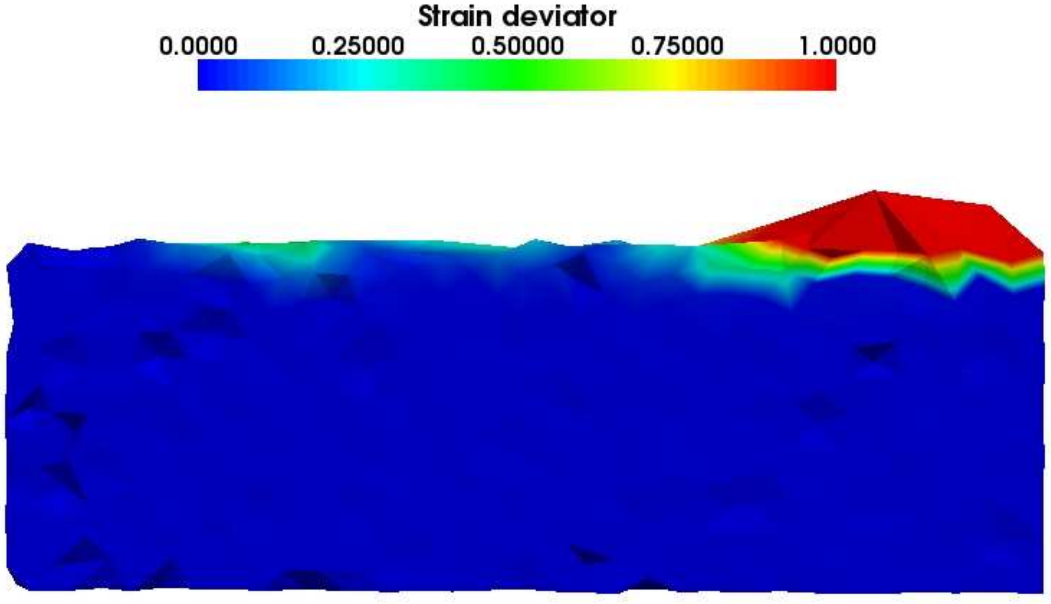

Figure 6.14: Wave action on a dense seabed. Strain deviator field.

INPUT DATA		
N	$[-]$	5000
ϕ_{c1}	$[deg]$	30
ϕ_{c2}	$[deg]$	30
E	$[kPa]$	15000
a	$[-]$	0.5
d_{50}	$[m]$	0.06
d_{max}/d_{min}	$[m]$	1.22
μ	$[kPa \cdot s]$	0.1

Table 6.3: Wave action on a loose sphere packing. Input parameters.

the porosity also remaining almost constant. This phase ends at $t \simeq 7.5\,s$, followed by a state of instability, with the rapid increase of all kinetics quantities. On fig.6.16 four snapshots of the simulation at times $t \simeq 1s$, $t \simeq 4\,s$, $t \simeq 6\,s$, $t \simeq 8.5\,s$ are presented. The fluid pressure profile and the grain velocity field are represented. The fluid pressure profile is observed to be initially closed to the hydrostatic one (a), then to start to deviate from it as a result of a contraction of pores which concern a part of the packing (b). It finally evolves to a generalized overpressure resulting in a fluid pressure field that completely deviates from the hydrostatic one (c). The packing is consolidating and the fluid is carrying its entire weight. The overpressure has the effect of reducing the effective stress, then the shear resistance of the packing, that starts to deform. The last snapshot (d) shows the deformed packing, which still persist in a liquefied state. The most important deformations are observable mainly at the seabed surface. Rolling and suspension processes concern the surface grains, whose analysis is out of the scope of our treatment. The simulation is stopped. As a last remark, comparing the simulations performed on the initially loose and dense packings, the value of the amplitude for which the instability arises is much lower (25%) in the former case.

Fluid pressure measurements

The fluid pressure measurements during the simulation, plotted on fig.6.17(left), gives evidence to the phenomena we have just observed and commented. Two phases can be distinguished. A first, stable one, from $t = 0$s to $t = 3$s, during which the pressure measurements attest the persistence of the hydrostatic conditions. During this phase, the right-hand side term of eq.(4.4) that mainly influences the pressure field is again $\mathbf{Q_p}$, the vector of imposed pressures. A second one, during which the packing liquefies, with an overpressure that concerns the whole packing, resulting from the pores contraction due to

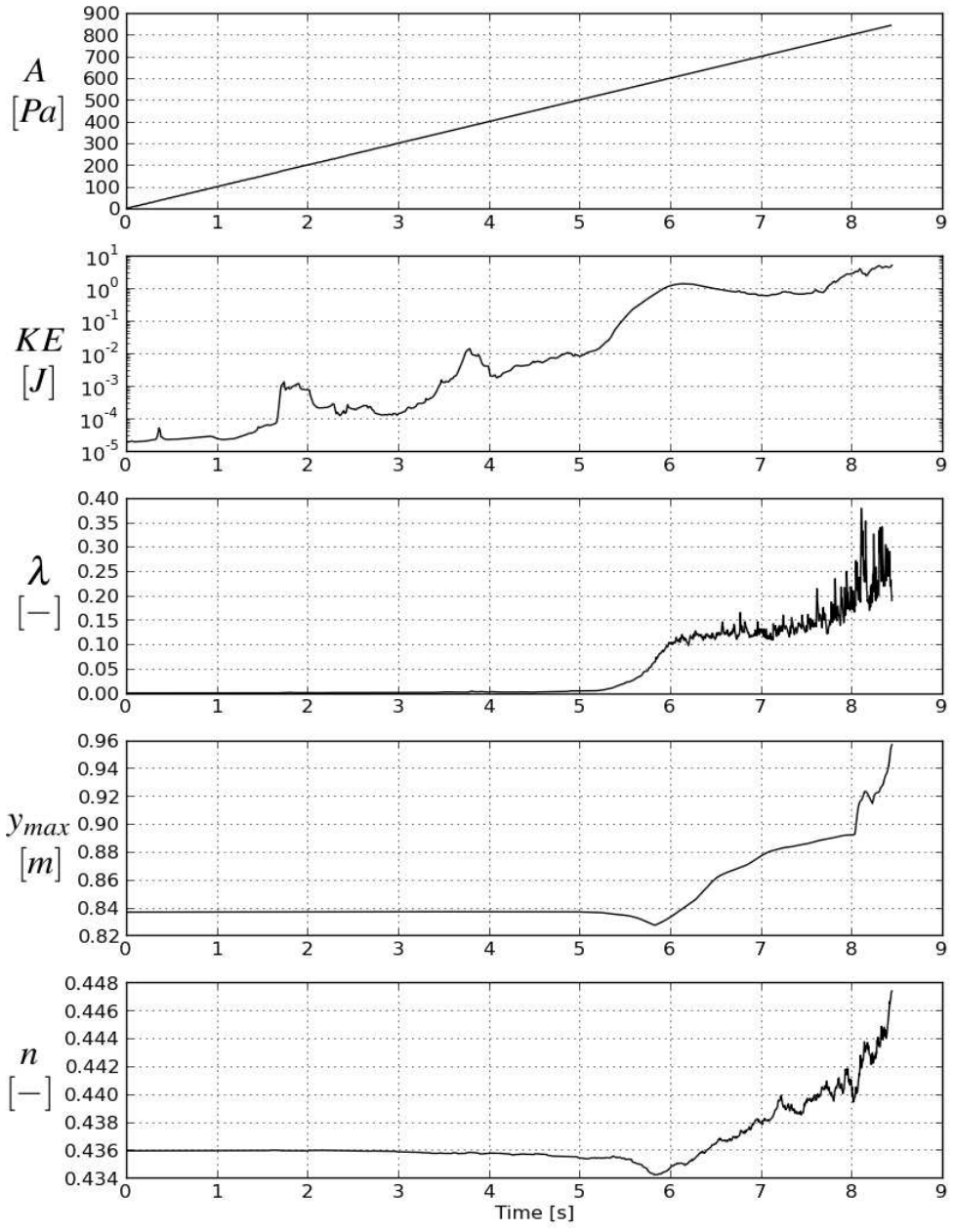

Figure 6.15: Wave action on a loose seabed - Evolution of kinetic parameters.

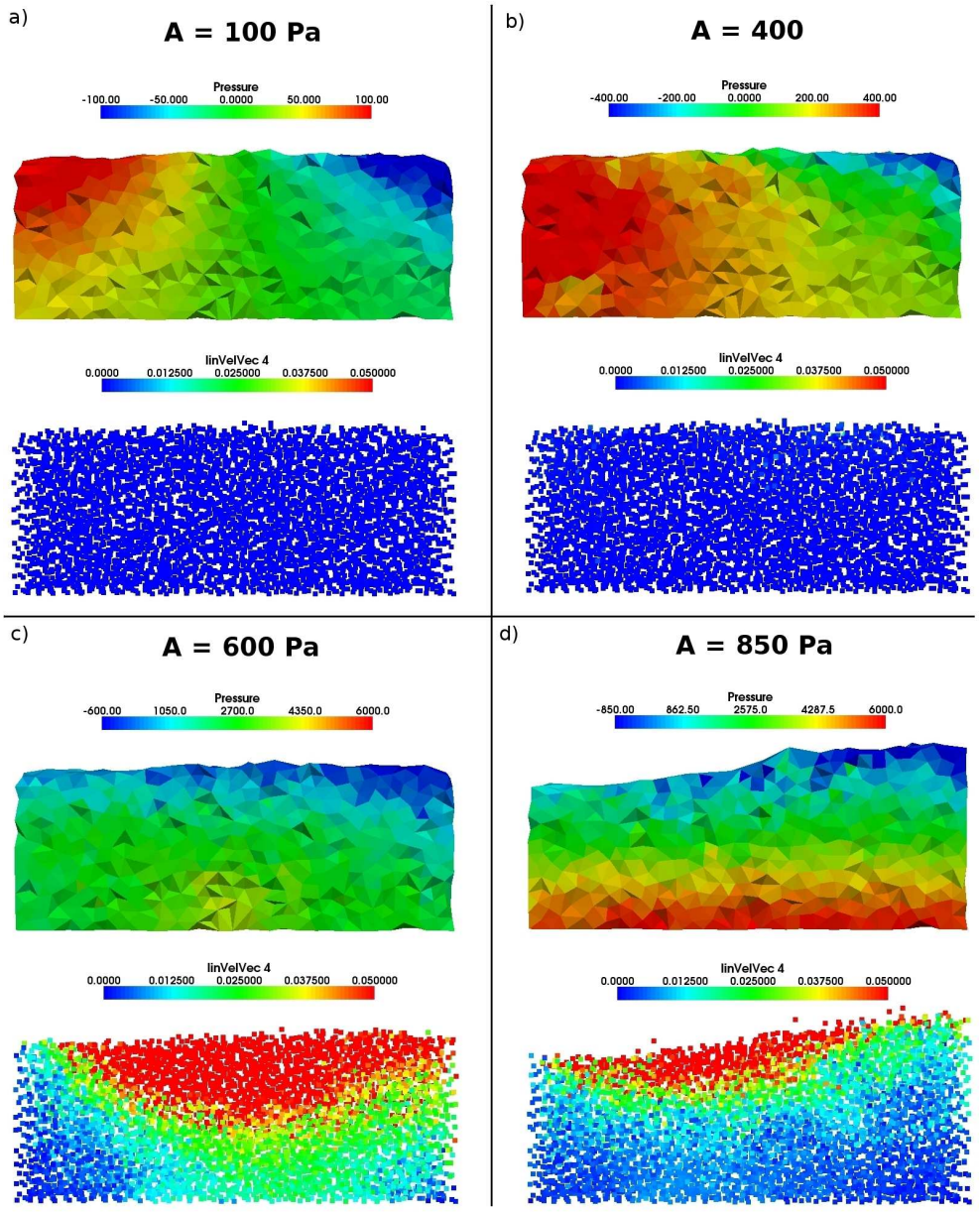

Figure 6.16: Simulation snapshots at $t \simeq 1s$ (a), $t \simeq 4s$ (b), $t \simeq 6s$ (c), $t \simeq 8.5s$ (d). Fluid pressure in [Pa], grain velocity in [m/s].

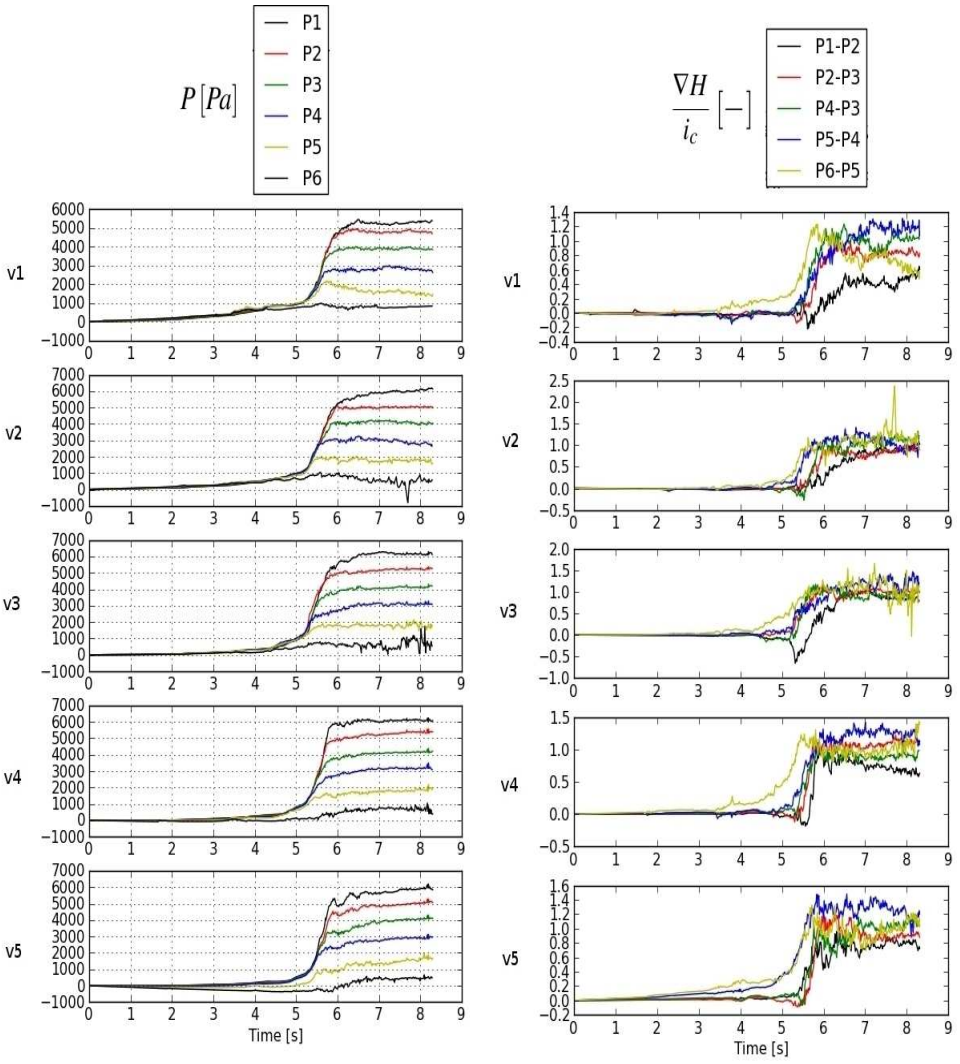

Figure 6.17: Wave action on a loose seabed - Fluid pressure measurements.

the particles mutual rearrangement. During this phase, it's the term expressing the rate of pores volumetric deformation, $\mathbf{E}\dot{\mathbf{x}}$ that mainly influences the solution of the system of eq.(4.4). The two phases are easily distinguished looking at the evolution of the $\frac{\nabla H}{i_c}$ ratio (fig.6.17(right)). Once the packing liquefies, the ratio approaches the unity, nearly homogeneously within the medium, and even exceeds the unity, as the particles get accelerated.

Result interpretation

On fig.6.18 an interpretation in terms of fluid pressure profile (along the $v3$ vertical) and effective stress is proposed. The hydrostatic conditions corresponds to a none fluid pressure measured all along the symmetrical axis of the packing, as represented on the first plot (a). The effective stress profile is nearly linear in this phase. On the plots (b-c-d), the fluid pressure and the effective stress, as expected, evolve as two complementary quantities. The progressive increase of the fluid pressure indicates the progressive deviation from the hydrostatic conditions. Parallely, the effective stress reduces and goes close to

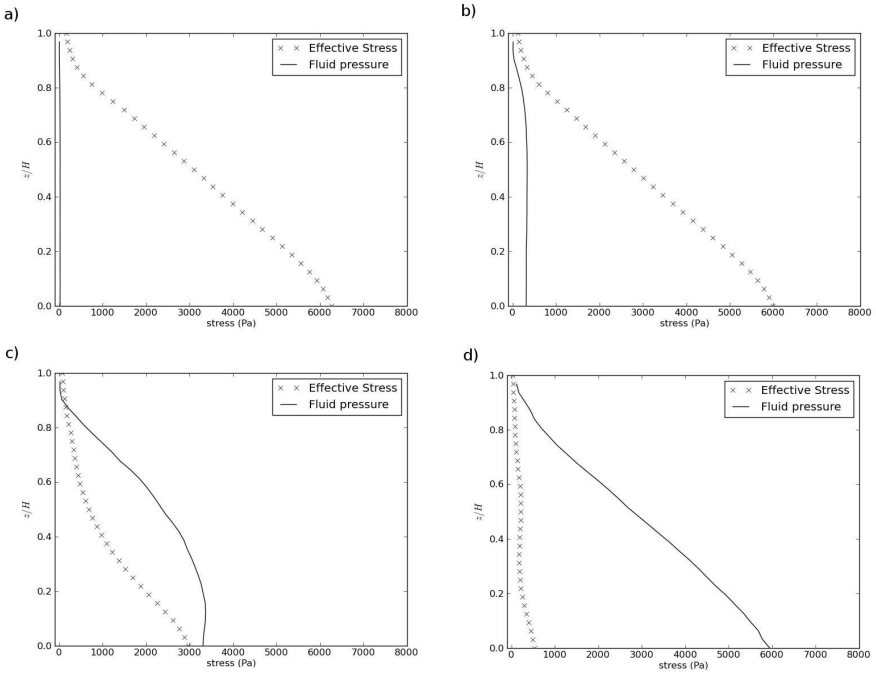

Figure 6.18: Effective stress σ' and fluid pressure p evolution at $t \simeq 1s$ (a), $t \simeq 4s$ (b), $t \simeq 6s$ (c), $t \simeq 8.5s$ (d)

zero (d). Fig.6.19 finally shows the strain deviator field, that gives further informations on the deformation pattern, giving evidence to its localisation along a shear band. As already

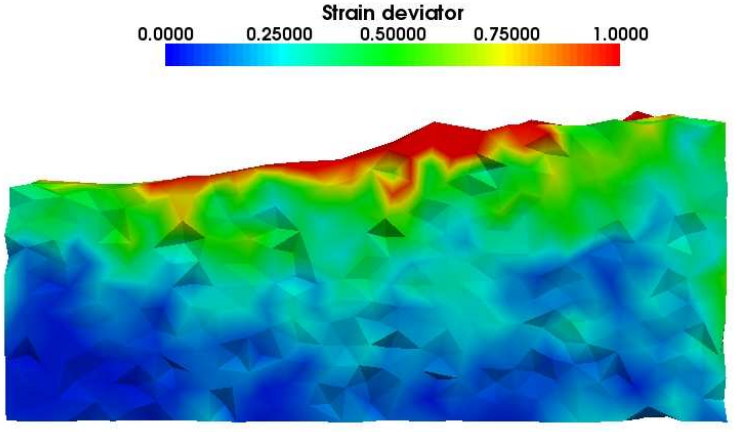

Figure 6.19: Wave action on a loose seabed. Strain deviator field.

seen for the case of the dense packing, on fig.6.20 the motion of the particles is visualized by means of arrows whose color and length represent their velocity and acceleration, respectively. The mechanism of instability, with the localization of the deformation into a shear band, is confirmed by this new visualization.

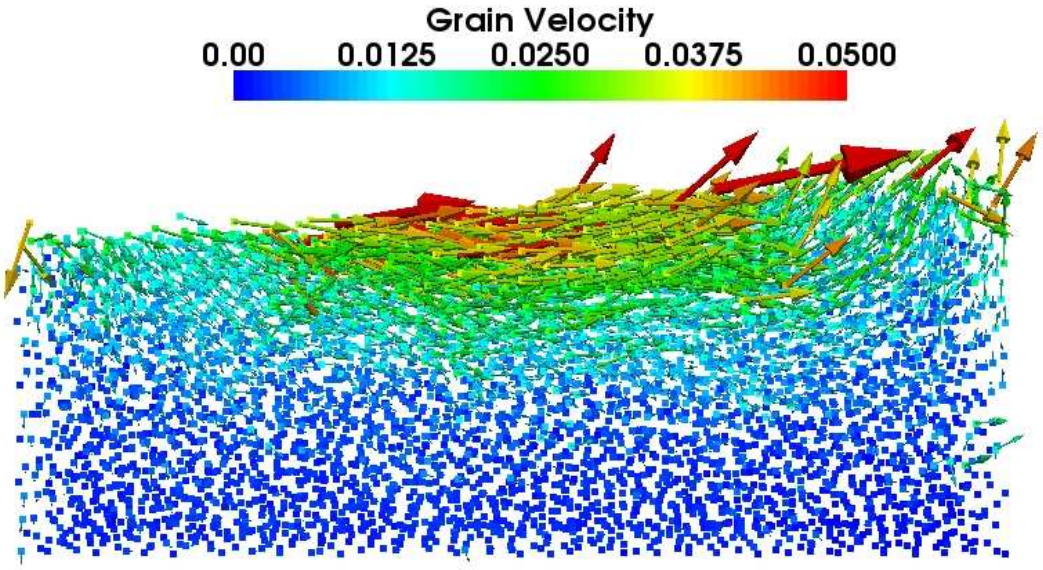

Figure 6.20: Wave action on a loose seabed - Grain velocities (arrows color) and accelerations (arrows length).

6.3.4 The role of initial permeability

In this section a new set of simulations is presented, whose goal is to analyze the response of a seabed subjected to the action of a wave, trying to characterize its dependence in the hydraulic properties of the packing. Three configurations are tested, differing in the value of the hydraulic conductivity for the packing, K_d. A sinusoidal-shaped wave of constant amplitude $A = 300$ Pa (see fig.6.7) is assumed to act on the packing.

The lower is the hydraulic conductivity of a soil, the slower is the slip velocity and the process of transfer of the load from the liquid phase, which initially carries the entire load (external load + soil weight), to the solid phase (intergranular contacts). We've already observed this process of load transfer in section 4.4, in the case of the oedometric consolidation test. In that case, the final result (deformation) didn't depend on the fluid properties. The sole duration of the transient phase was affected. This was due to the symmetricity (geometry and load) of the problem.

Considering the effect of a wave on a seabed, a combination of two different mechanisms of deformation takes place. On the one hand, the sample tends to consolidate to reach a denser and more stable configuration. On the other hand, it tends to deform as an effect of the fluid pressure gradient which results from the specified boundary conditions. We will present in this section how the hydraulic properties of the packing may entail the former mechanism to be dominant over the latter or viceversa.

State and kinetic parameters

Fig.6.21(b) shows the evolution of λ, defined in eq.(2.16), that gives an indication of the overall stability of the sample (λ) and of the acceleration of the particles ($\lambda' = \partial\lambda/\partial t$). As expected, the lower is K_d, the hydraulic conductivity of the sample, the more the particles acceleration is *damped*, and as such it's longer the time needed by the sample to reach a

new stable configuration. The evolution of the porosity n is plotted on fig.6.21(c), from which it can be stated that the lower is the hydraulic conductivity of the sample, the lower is the value of porosity relative to the final configuration.

Fluid pressure measurements

The fluid pressure plotted on fig.6.22 provide useful informations to interprete such result. They globally give account of the state of the packing, notably if soil liquefaction occurs. This is the case for the less permeable samples (b-c), where liquefaction occurs and concerns the nearly whole sample, except the lowest layer (p1−p2) that liquefies only partially. The duration of the liquefied state is inversely proportional to the hydraulic conductivity. During this time, deviatoric deformation occurs, being the shear resistance of the soil nearly none. Three snapshots of the packing, on the same figure 6.22, show the deviatoric strain field. The longer the liquefied state persist, the higher is the observed final deviatoric strain. In the highly permeable case (a), the packing does not liquefy. This explains the nearly absence of deviatoric strain.

Porosity-deformation relation

Fig.6.23 finally shows the classical relation between deviatoric strain and porosity for a contractant material (see section 6.3.1). For this kind of materials, the higher is the induced deviatoric strain, the lower is the resultant porosity. This consideration provides a key to interprete the results that we have just discussed, in which the packing that underwent the most important strain, was also the one to which the lowest final porosity was associated.

6.3.5 Influence of fluid deviatoric stress

As it was recalled in part II, only the isotropic part of the stress in the fluid is taken into account in both our PFV-DEM model and Biot's theory. In a recent extension of our work, however, Donia Marzougui in [63] defined the fluid forces linked to the deviatoric stress and integrated them into the PFV-DEM model. These forces are known as the shear viscous forces. They can be written as:

$$F^{sv} = T\,S \tag{6.29}$$

where T is the shear component of fluid stress acting on the surface S. Shear stress was put in relation with the tangential component of the relative velocity between neighbouring spheres, ΔV^t, the hydraulic radius R^h_{ij} of eq.(3.5), and the fluid viscosity μ.

$$T = \frac{\Delta V^t}{R^h_{ij}}\mu \tag{6.30}$$

The surface S is derived from the triangulation system, and corresponds to the polygonal facet separating two spheres in the Voronoi diagram. For further details, please refer to Marzougui's master thesis [63].

The contribution of these shear viscous forces is evaluated in this section, as they influence the result we have just presented in last section, by considering the presence of

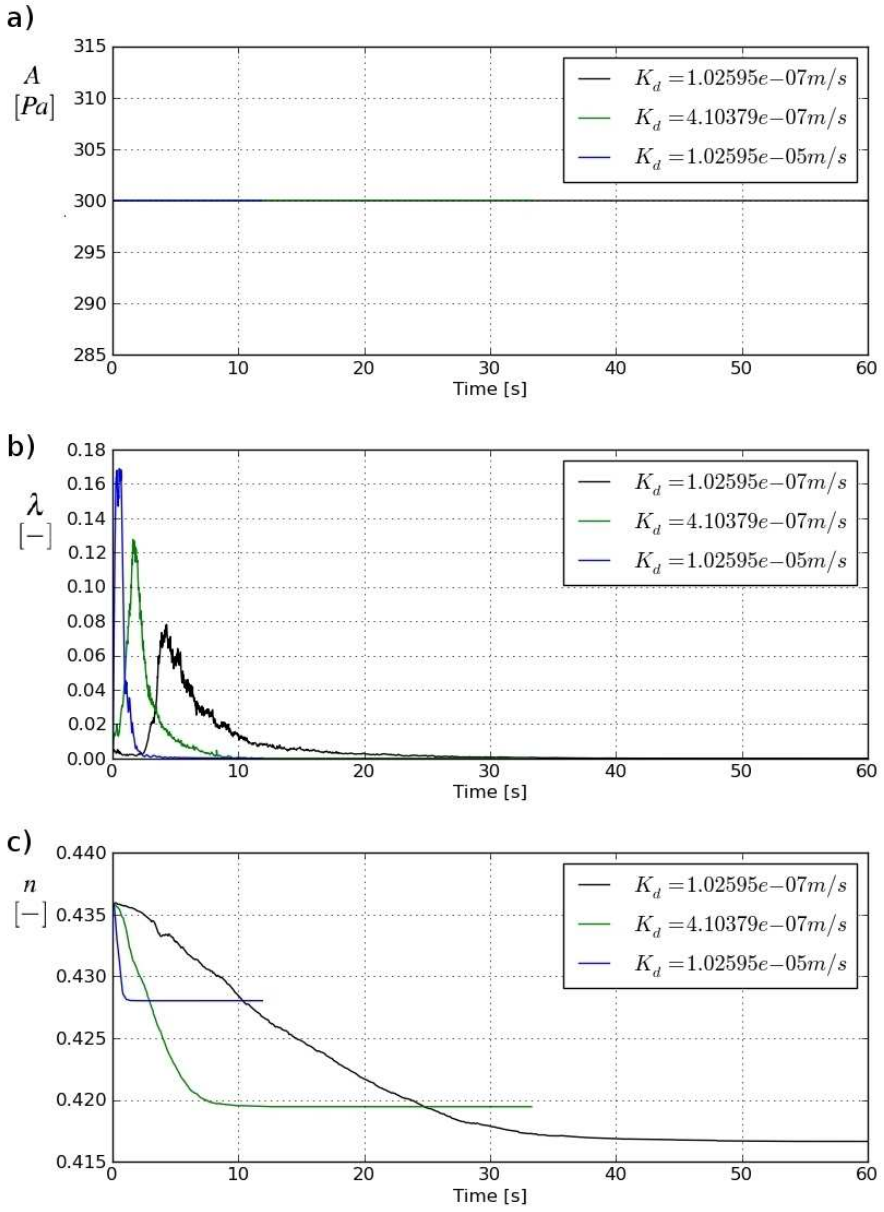

Figure 6.21: Hydraulic conductivity influence on seabed kinematic.

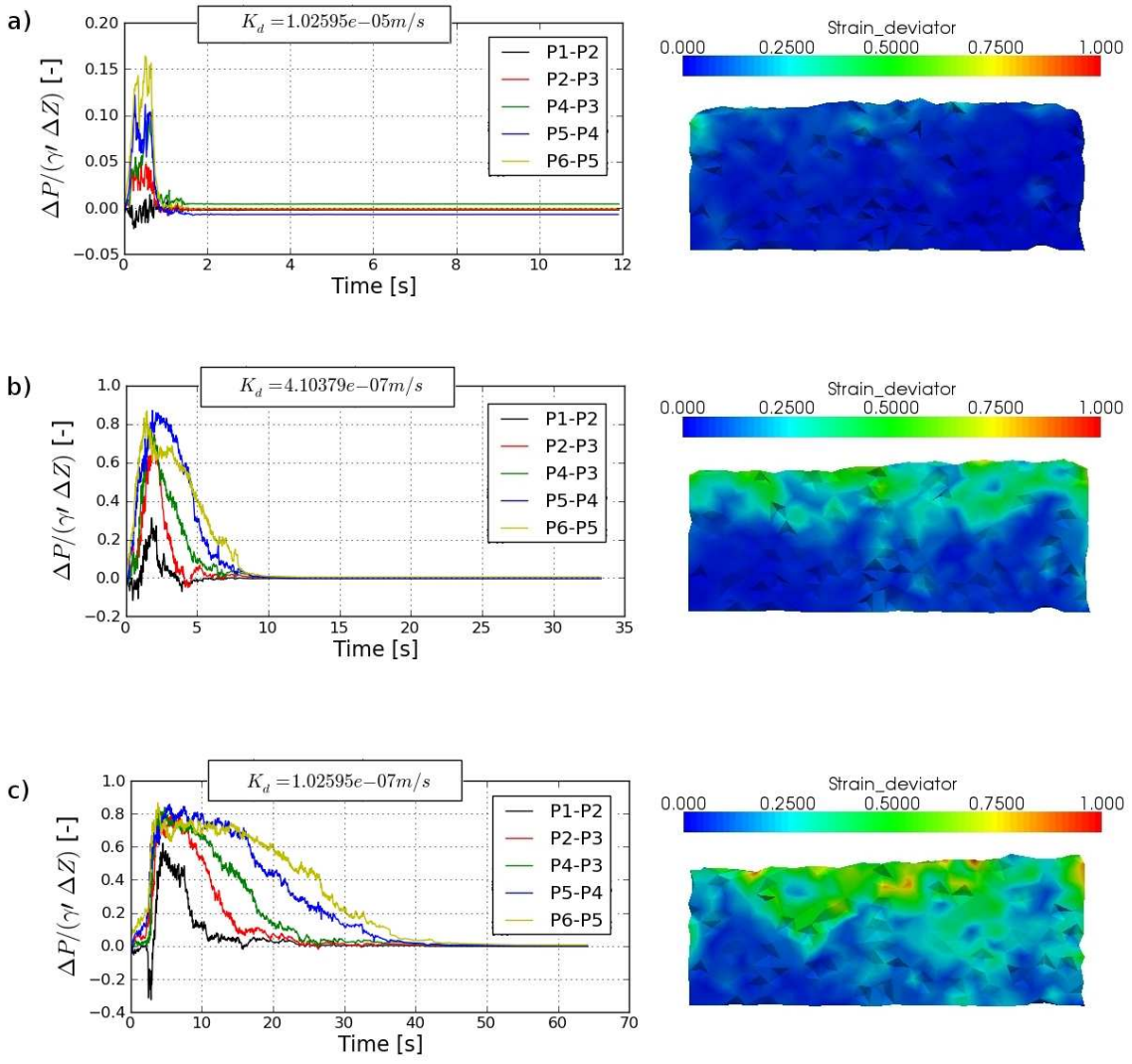

Figure 6.22: Hydraulic conductivity influence on seabed deformation.

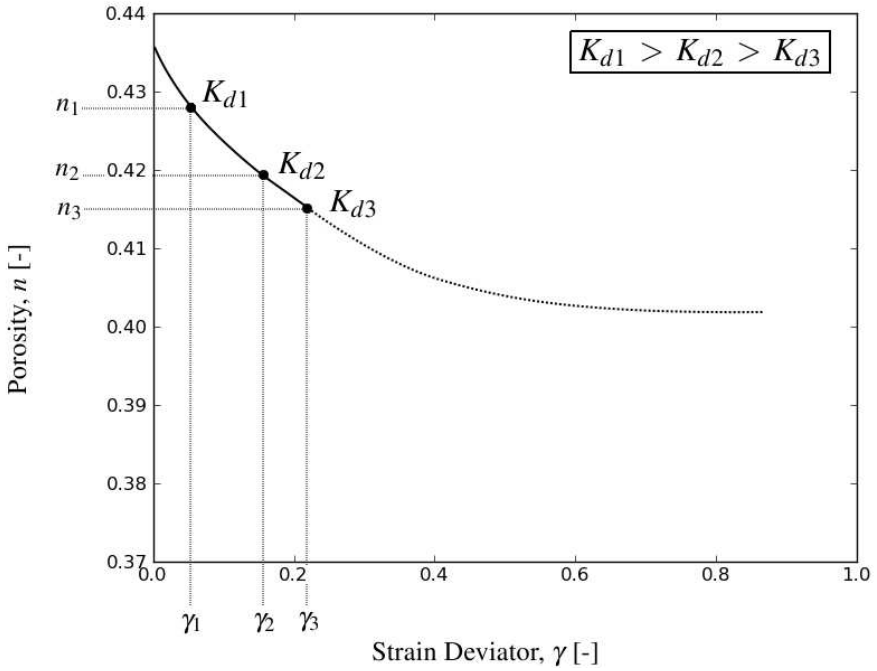

Figure 6.23: Typical strain deviator vs porosity curve of a loose packing.

water ($\mu = 10^{-3}$ Pa·s). The effect is expected to be conservative, the forces associated to the shear component of fluid stress behaving as a damper, thus preventing acceleration of the particles. The results are compared on fig.6.24. The time t - porosity n curves relative to the two cases, seem to coincide perfectly. A slight effect of shear viscous forces $\mathbf{F}^{\mathbf{sv}}$ can be observed for the less permeable packing, the one for which a liquefied state was found to persist enough to induce a remarkable deviatoric strain of the packing. The action of shear viscous forces seem to slighly restrain the final deformation of the packing, the final value of porosity being higher than in the former case. On fig.6.25 the deviatoric strain fields relative to the two cases are subtracted and visualized. It can be consluded from this comparison that the neglect of shear viscous forces is an acceptable assumption in this problem.

6.4 Stationary wave simulations

In this section we will present the numerical results that were obtained by defining a more complex hydraulic charge profile at the packing surface, in order to simulate a bit more realistic action of the wave on the seabed. Notably, a stationary wave is defined, oscillating with a certain period within a maximum and a minimum value of the amplitude A, as represented on fig.6.26.

The packing that was used is the loose packing whose response to the standing wave action has been discussed in section 6.3.3. The aim was the analysis of the relation between the period of oscillation of the wave with the characteristic time of consolidation associated to the packing. The relation between these two quantities is supposed to determine the mechanical response of the packing. That is, if the period of the wave loading is longer than the characteristic time of consolidation, the packing is supposed to have

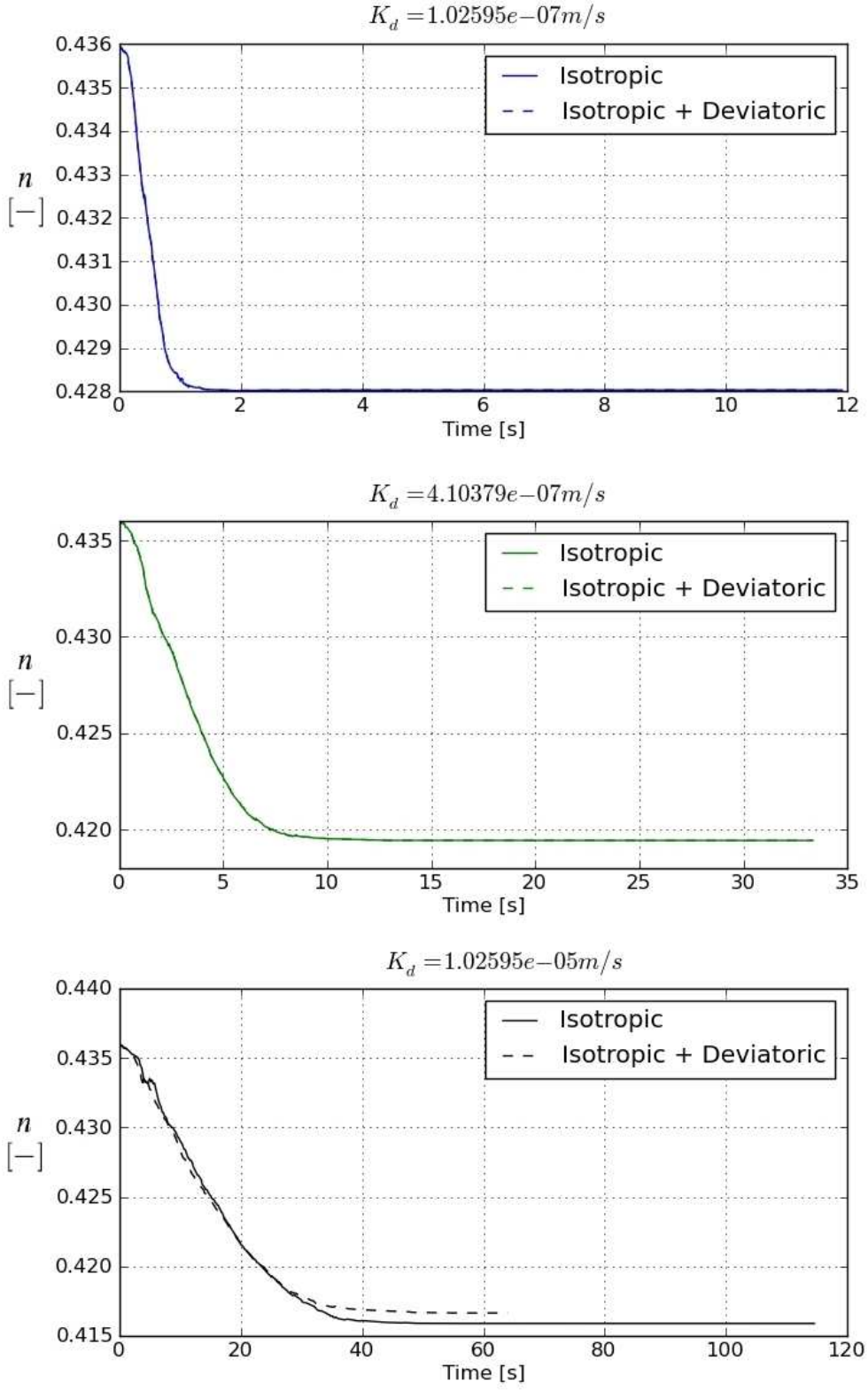

Figure 6.24: Influence of shear viscous forces on seabed deformation.

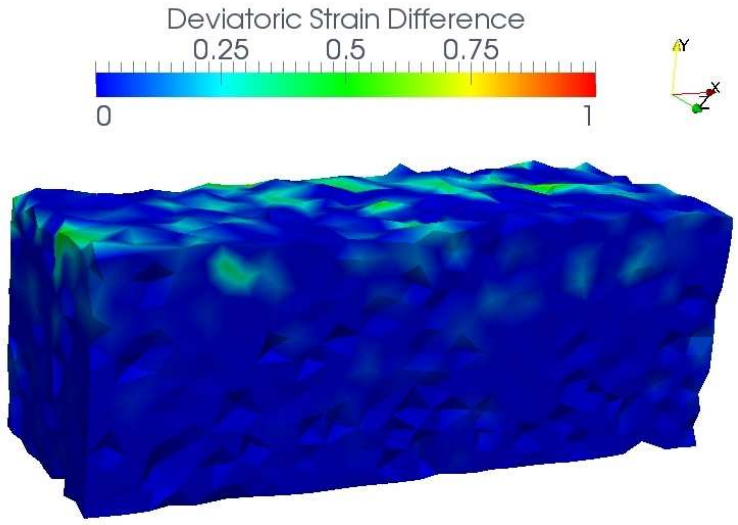

Figure 6.25: Deviatoric strain deviation as an effect of the deviatoric component of fluid stress.

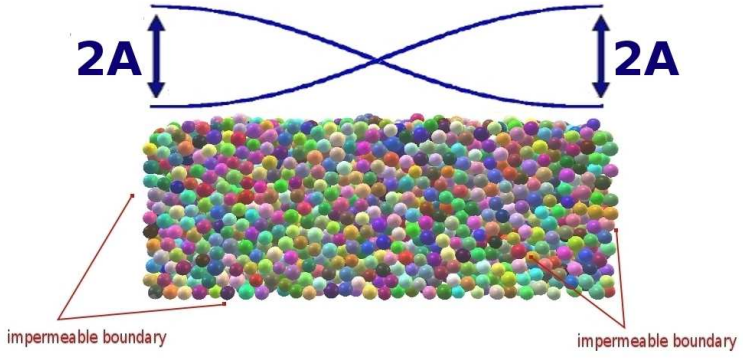

Figure 6.26: Sketch of the packing (depth/height = 2.0) we will use to simulate the effects of a stationary wave on a loose seabed. Fluid pressure sensors are placed according to fig.6.8.

the time to consolidate and get a stable configuration without undergoing into deviatoric strain. In the opposite case the packing wouldn't have time to consolidate. Deviatoric strain would occur and might become more important in case of liquefaction of the packing.

The parametric analysis that was performed will be presented henceforth, by making vary the value of the amplitude A and the period of oscillation of the wave.

6.4.1 Loose packing response

We will present primarly the result that was obtained by defining at the seabed surface a wave oscillating with a period of 1 s, within a max/min amplitude $A = 150$ Pa. It is worth noticing that the amplitude A at which the instability occurred in the case of the standing wave, as it was presented in section 6.3.3, was much higher than the one we are now imposing and making oscillate at the packing surface. The simulation parameters are the ones reported in table 6.3.

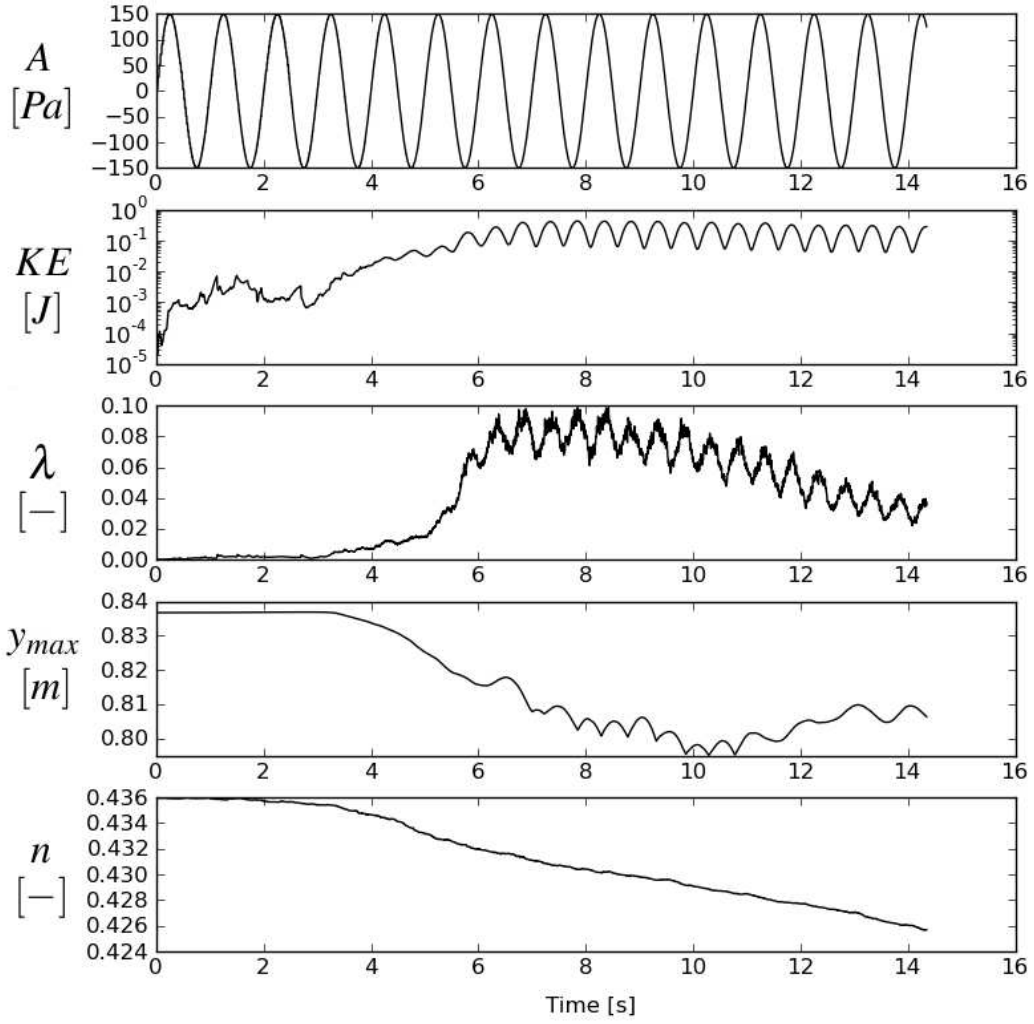

Figure 6.27: Stationary wave (period = 1s) on a loose seabed ($n \simeq 0.436$) - State and kinetic parameters time evolution.

State and kinetic parameters

On fig.6.27, as already done in previous sections, some state and kinetic parameters are reported, tracking the evolution of the fluid-particle system for this simulation. The amplitude A evolution is plotted on the top plot. The kinetic parameters (kinetic energy KE and λ) indicate the presence of motion events from the early iterations already, up to $t \simeq 3$s. After this first phase, the packing starts to settle, as it can be deduced from the simultaneous reduction of the porosity n and the max y-coordinate y_{max}. Particles are accelerated, then λ and KE increase. After $t \simeq 6s$, the packing continues to settle and consolidate, reducing its porosity. However, the oscillating evolution of the kinetic parameters λ and KE and of the maximum y-coordinate y_{max}, suggests that the mechanism of deformation in act is more complex. The interpretation of what happens in this phase will be presented in the next section.

Fluid pressure measurements

The fluid pressure measurements allow a better interpretation of the numerical result that was obtained. On fig.6.28, the evolution of the fluid pressure is plotted at the symmetric axis of the sample ($x \simeq 1$m), and at two vertical axis by the left ($x \simeq 0$m) and the right ($x \simeq 2$m) walls. Deviating from the hydrostatic profile from the early stages of the simulation, the seabed liquefies under the action of the wave. The evolution of the dimensionless ratio $\frac{\nabla H}{i_c}$ indicates that at $t \simeq 6$ s the packing is liquefied, and remains under these conditions up to end of the simulation. The liquefaction induces a reduction of the shear resistance of the packing, that more easily deforms under the action of the wave. That's the reason of the oscillating-shaped evolution of the kinetic and state parameters we have observed in fig.6.27.

Characteristic time of consolidation

To estimate the order of magnitude of the characteristic time of consolidation for the packing we are employing, we can use the definition of eq.4.31,

$$T_v = \frac{t}{t_c} \quad \rightarrow \quad t_c = \frac{L^2 \gamma_w \varepsilon_c}{K_d \sigma_c} \tag{6.31}$$

by adapting it to the case we want to study. L, the longest drainage path for the generic fluid particle, corresponds now to the height H of the sample. The stress term σ_c is associated to the weight of the particles, $\rho' H$, while the strain term ε_c can be estimated to be around 0.01. We obtain:

$$t_c \simeq 10 s \tag{6.32}$$

This estimation allows the interpretation of the result that was obtained by comparing it to the period of oscillation of the wave. In the case we have just presented, the period of the wave was 1s. Then the packing have no time to consolidate, the pressure gradient effects dominate its global response to the load, an aspect emphasized by the liquefaction of the packing.

It is conceivable that for other periods of oscillation, around the order of magnitude of the tens of seconds, we could experience other types of mechanical behaviour of the packing. This makes the object of the next section.

6.4.2 Various Amplitude - Period combinations

To better characterize the packing behaviour under the action a stationary wave, a number of combinations amplitude A - period of oscillation were tested. The onset of packing liquefaction determines strongly the packing response. That's why the choice was to resume the results that were obtained by focusing on either the packing liquefies or not, as represented on fig.6.29. It is worth noticing that the criterion that was chosen to define the packing liquefaction was based on the computation of the dimensionless ratio $\nabla H / i_c$, that reaches the unity when the hydraulic gradient induced by the pores deformation equalizes the critical gradient of liquefaction. Also the states of nearly complete liquefaction ($\nabla H / i_c > 0.80$), have been coloured in red on the plot.

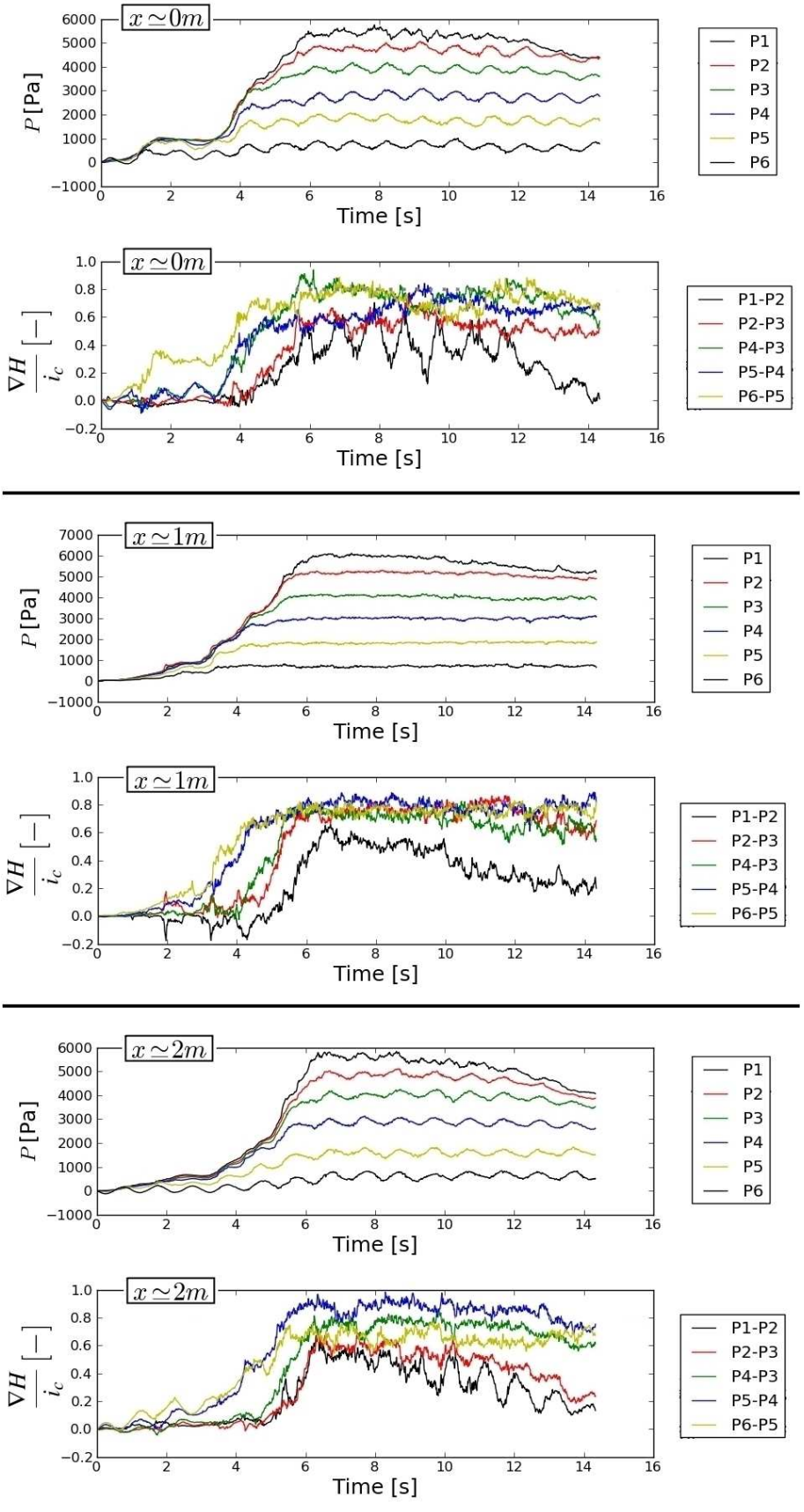

Figure 6.28: Stationary wave (period = 1s) on a loose seabed ($n \simeq 0.436$) - Fluid pressure measurements.

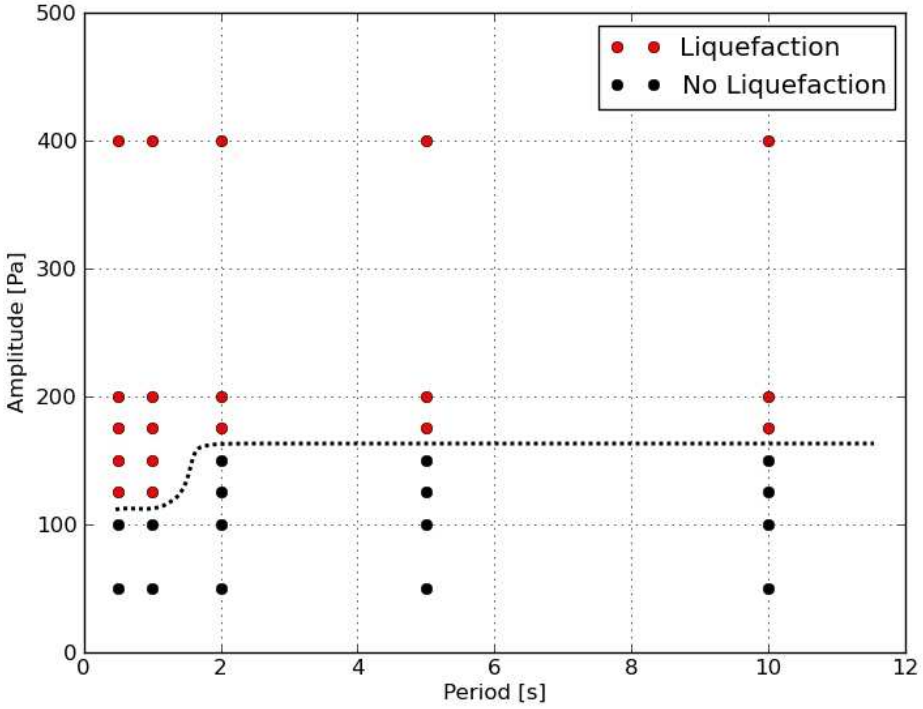

Figure 6.29: Liquefaction events for various amplitude/frequency combinations.

For the lowest amplitudes ($A = 50\,/100\,\text{Pa}$), we didn't experience any liquefaction events for all the periods that were tested. At the contrary, for the highest amplitudes ($A = 200\,/400\,\text{Pa}$) the packing liquefied in all tests. For some intermediate amplitude ($A = 125\,/150\,\text{Pa}$) we experienced liquefaction events for the lowest periods that were tested ($0.5/1$ s), while for longer periods the packing didn't liquefy.

Our interest not being limited to know if the packing liquefies or not, rather to analyze how the deformation of the packing is influenced by such condition, we deepened the investigations by plotting the horizontal displacements of the particles that stay along the symmetric axis. This is presented and discussed in the next section.

Influence of the period of oscillation

The resuming plot of fig.6.29 indicated that for certain amplitudes the packing shows a mechanical response sensitive to the specified period of oscillation of the wave. Notably, the packing liquefies for the shortest periods, while it doesn't liquefy for the highest periods. Important informations regarding this aspect are plotted on fig.6.30. The horizontal displacement of the particles that stay on the symmetric axis of the packing is plotted. Four curves are plotted, relative to four different periods of oscillation.

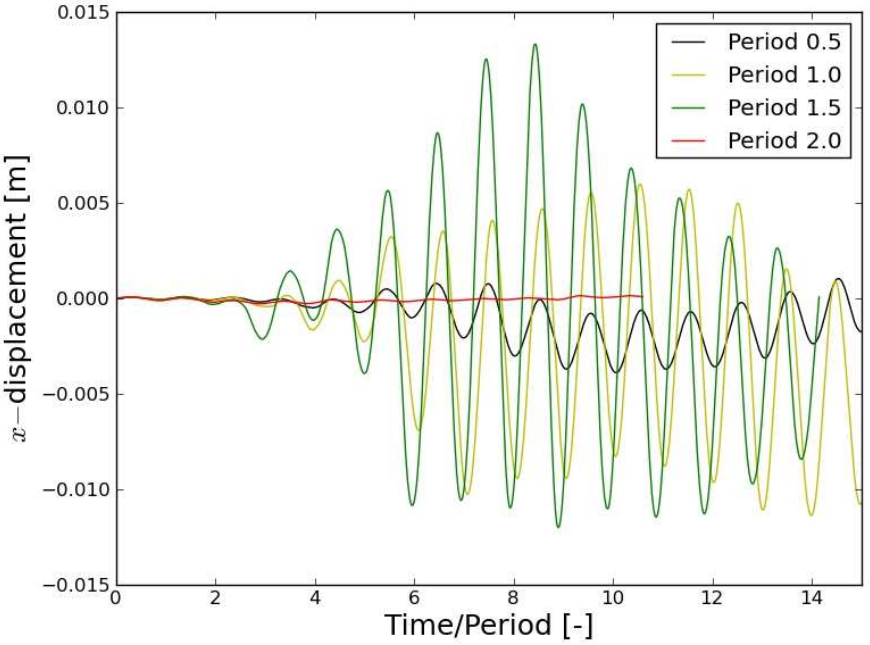

Figure 6.30: Horizontal displacement of particles on the symmetric axis for various periods of oscillation.

When liquefaction doesn't occur (period = 2.0s, see also fig. 6.39) the measured horizontal displacements are nearly none. For shortest periods, the packing liquefies (see fig.s 6.33, 6.35, 6.37) and the displacements become more important. Under these conditions, it's the relation between the period of oscillation of the wave and the inertial time associated to the weight of the particles that governs the evolution of the fluid-particle system. When the period is very short (0.5s), the particles have no time to get accelerated but just oscillate around their initial position (fig. 6.30). The measured horizontal displacements are very low but incentivate in some way the particle rearrangement to a more compact configuration (see fig. 6.33). At the contrary, for longer periods (period = 1.0s/1.5s), the horizontal displacements become more important (fig.s 6.30, 6.35, 6.37). Fig.6.31 reports the maximum absolute horizontal displacement that was measured for each one of the simulations that were presented.

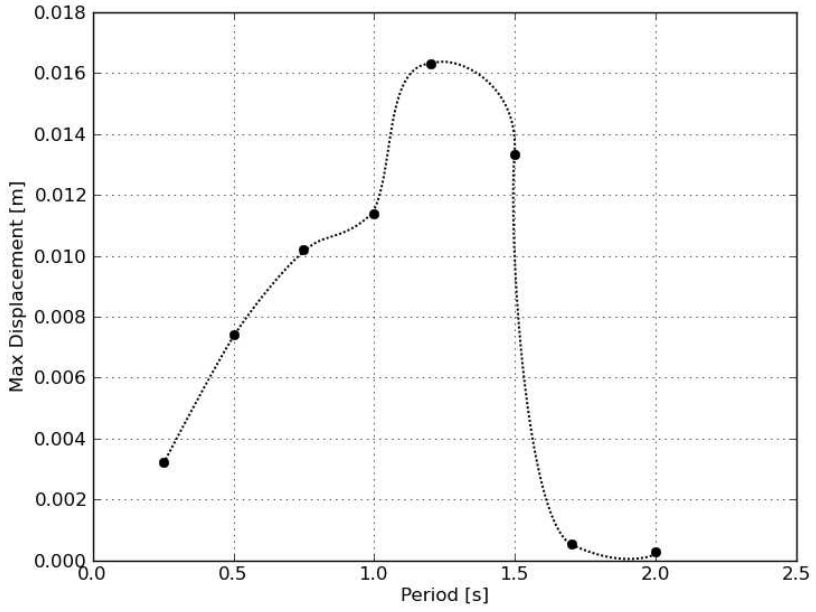

Figure 6.31: Maximum horizontal displacement for various periods of oscillation.

Conclusions

The application of PFV-DEM model to the analysis of the hydrodynamics of a granular sediment have been presented in this chapter. A rigorous fluid mechanics-based modelling of turbulent flow would be needed to recover more realistic hydraulic charge profiles at the sediment-fluid interface. However, the simplified approach we followed by considering the wave action equivalent to a sinusoidal pressure profile allowed the reproduction and the analysis of some characteristic scenarios.

The analysis have been organized in two main parts. A first one was characterized by a standing wave of increasing amplitude. The response of the packing has been analyzed by looking at the evolution of state and kinetic parameters. Fluid pressure measurements were regularly taken, giving precious informations to interprete and understand the behaviour of the fluid-particle system. Two main *limit* scenarios were reproduced, differing in the initial state of the packing. A dense ($n \simeq 0.368$) and a loose packing ($n \simeq 0.436$) were created. The response that was observed was qualitatively different. More specifically, solving the system of eq.(4.4),

$$[\mathbf{G}]\{\mathbf{P}\} = [\mathbf{E}]\{\dot{\mathbf{X}}\} + \{\mathbf{Q_p}\} \tag{6.33}$$

the right-hand side terms which more influenced the solution were not the same.
In the case of the dense packing, the problem was entirely governed by the pressure conditions $\mathbf{Q_p}$ that were specified at the boundaries. The hydrostatic conditions were kept all along the simulation, up to a condition of instability due to a gradient of charge high enough to make the solid particles at the seabed surface move as in effect of the horizontal component of the hydraulic gradient.
Differently, in the case of the loose packing, the solution of the system of eq.(4.4) was

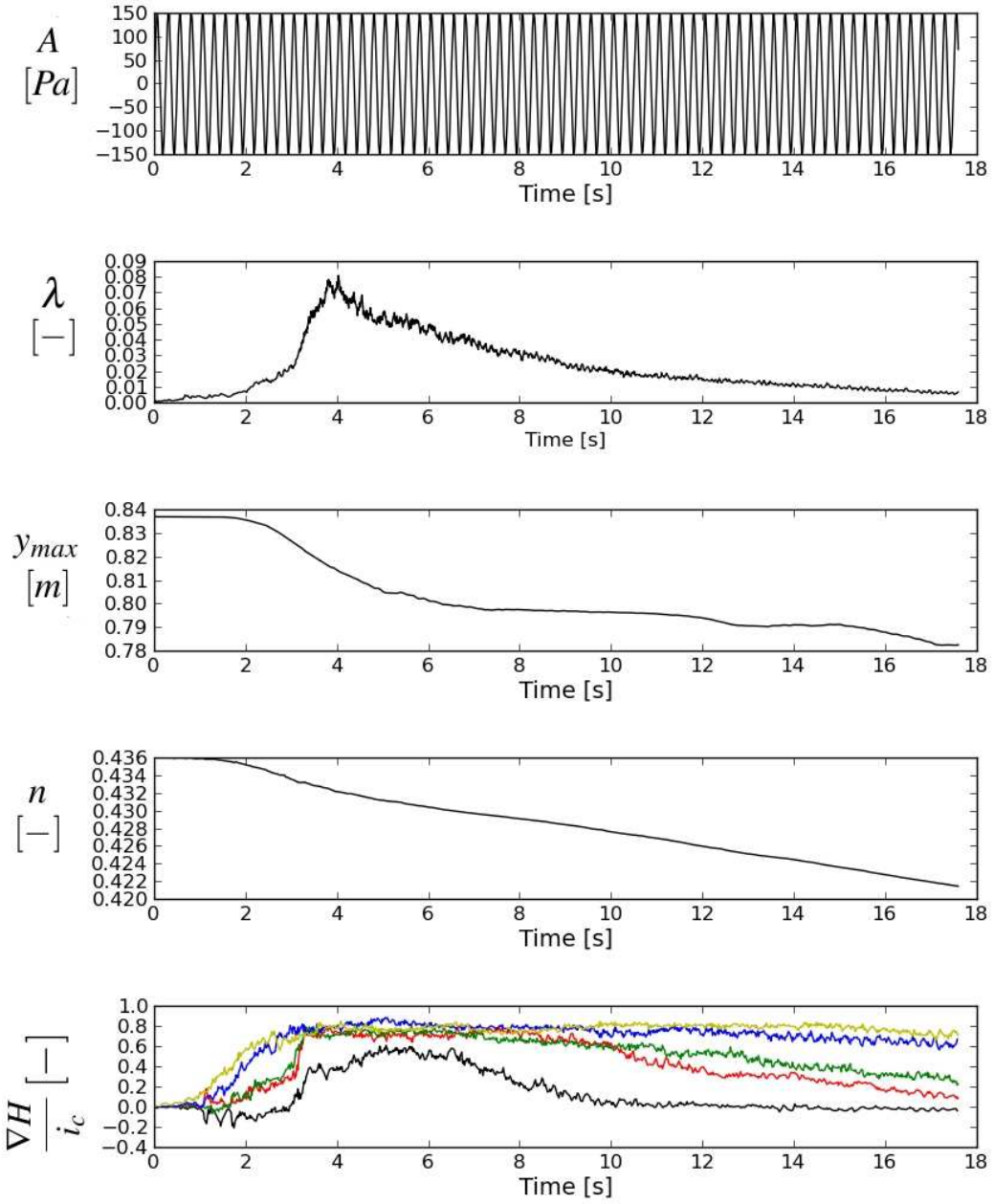

Figure 6.32: Stationary wave action on a loose seabed - Period = 0.25s.

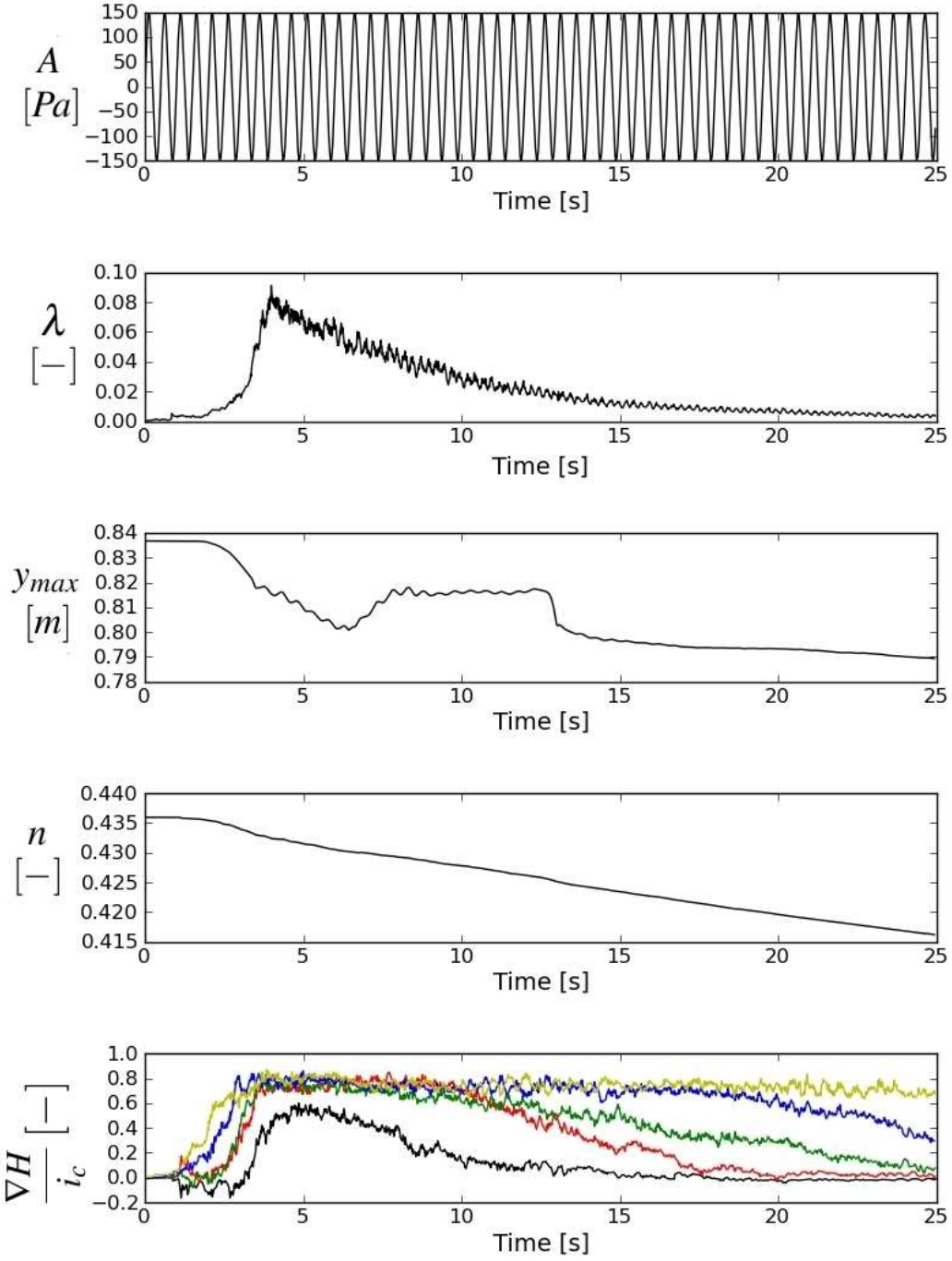

Figure 6.33: Stationary wave action on a loose seabed - Period = 0.5s.

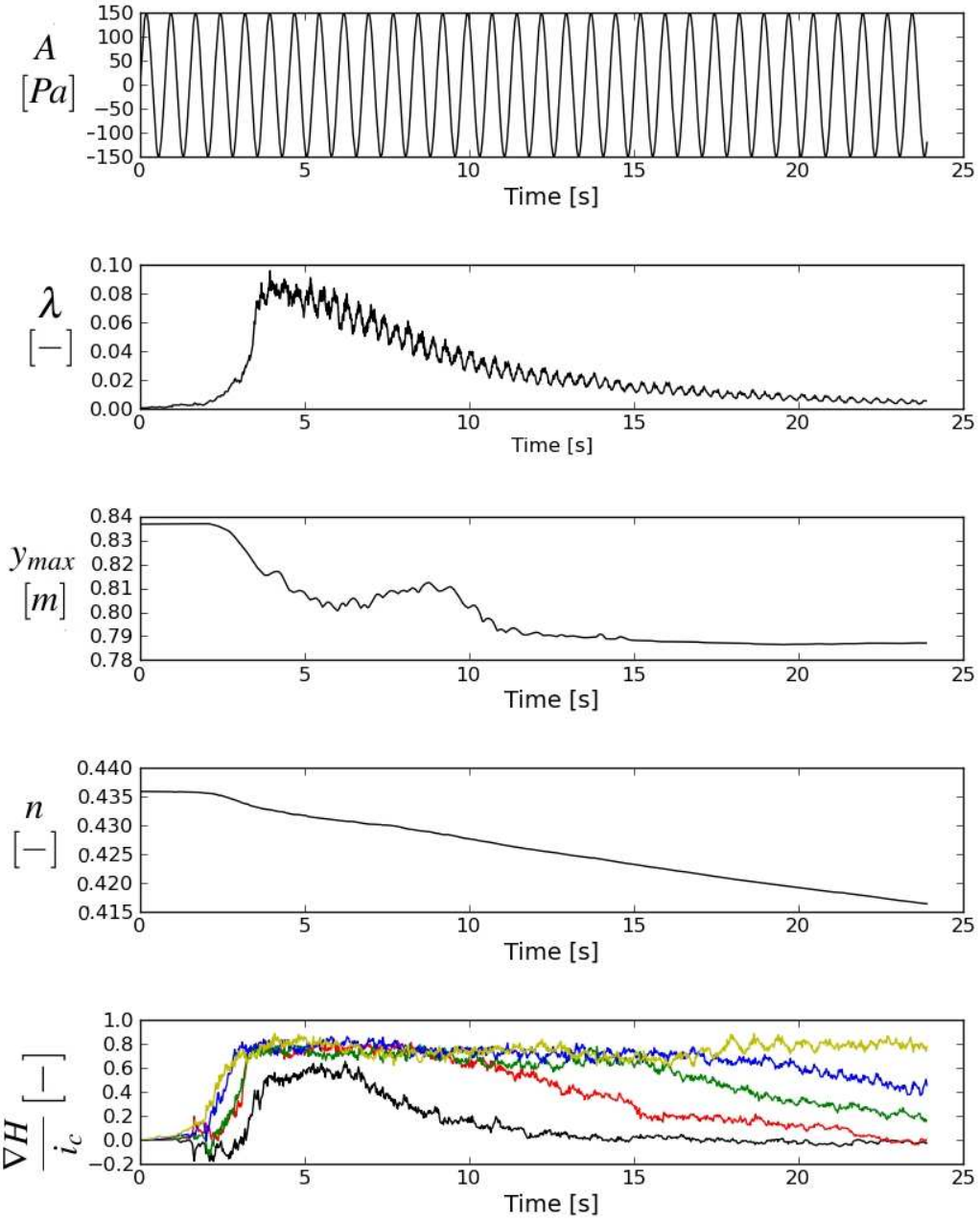

Figure 6.34: Stationary wave action on a loose seabed - Period = 0.75s.

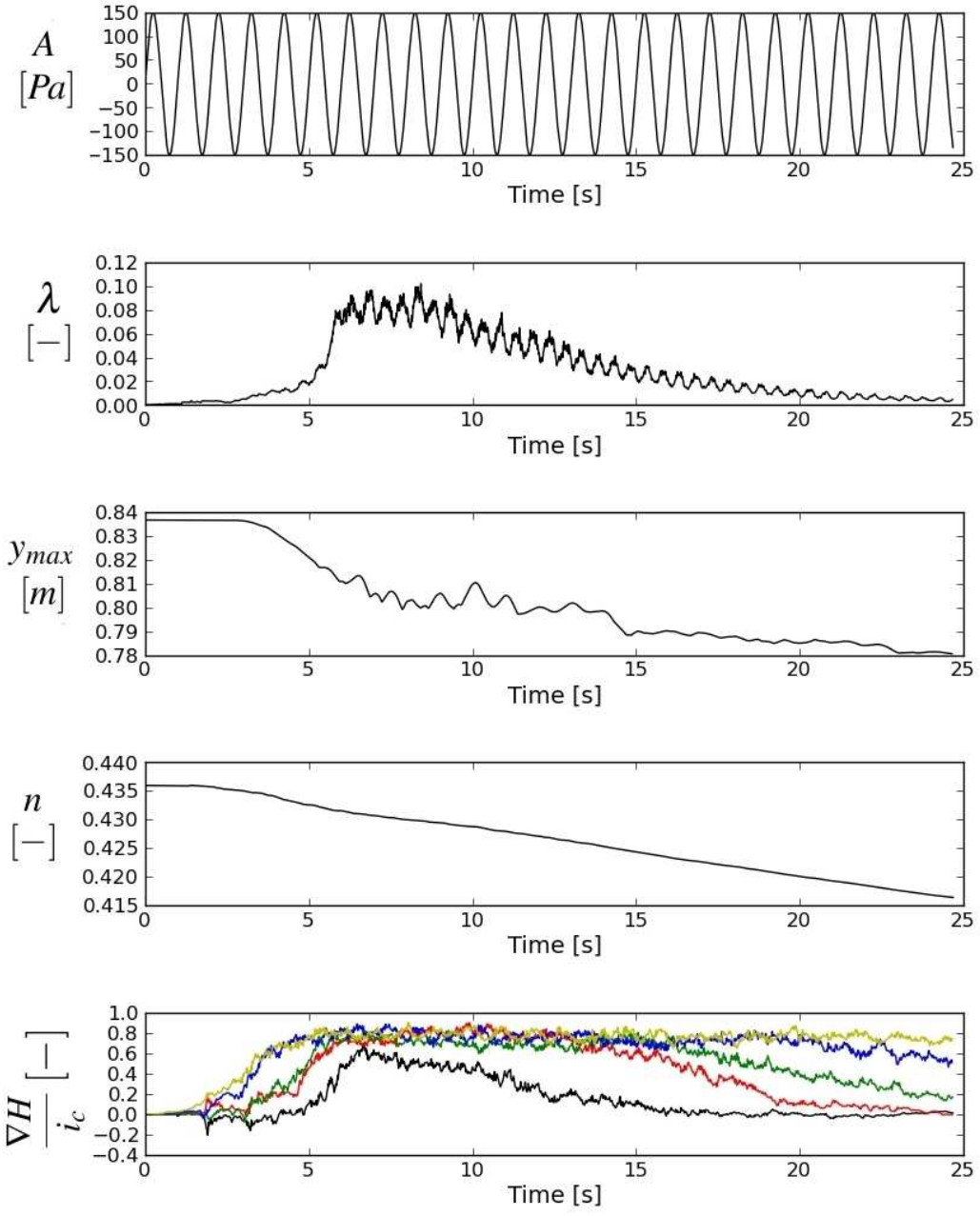

Figure 6.35: Stationary wave action on a loose seabed - Period = 1.0s.

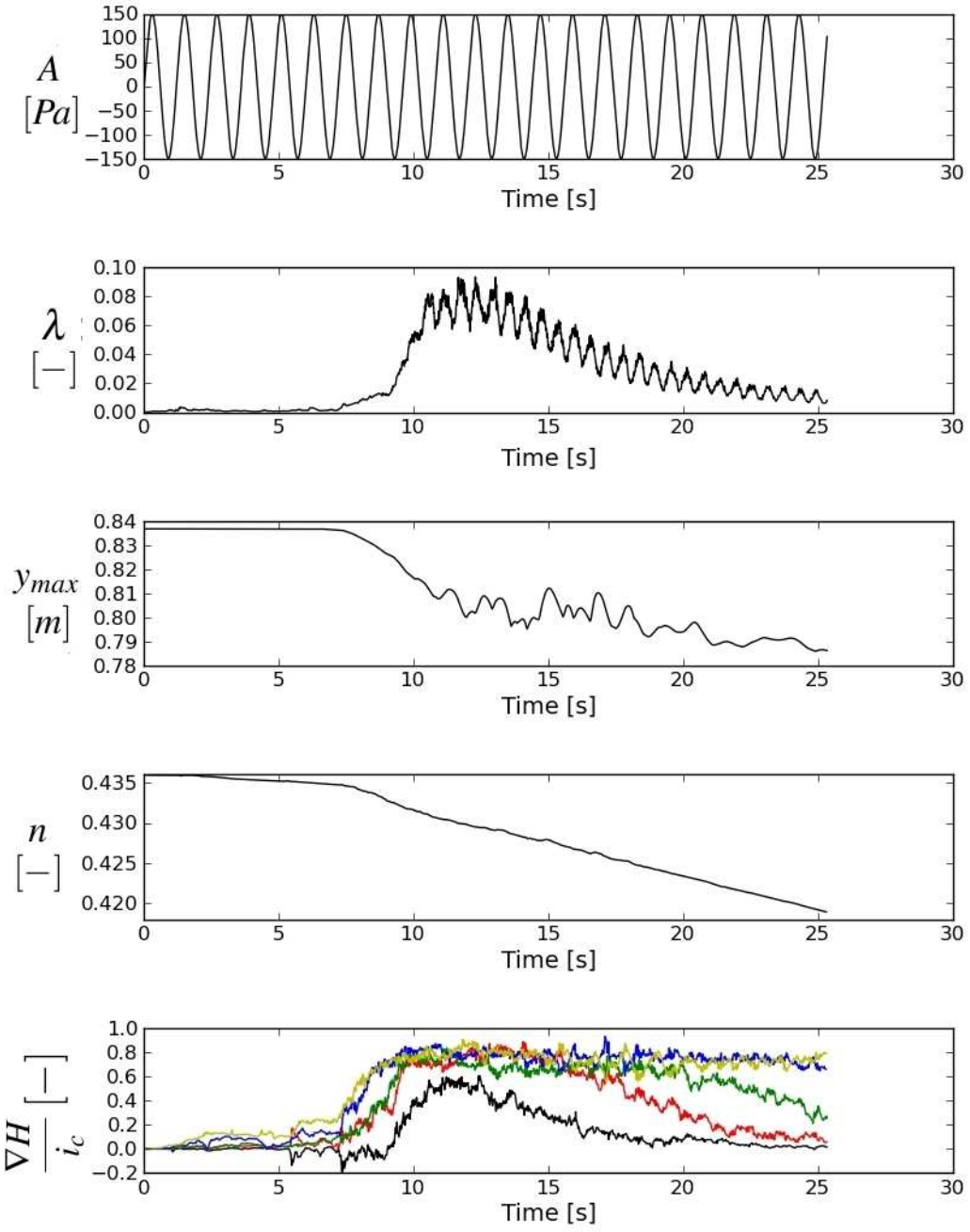

Figure 6.36: Stationary wave action on a loose seabed - Period = 1.2s.

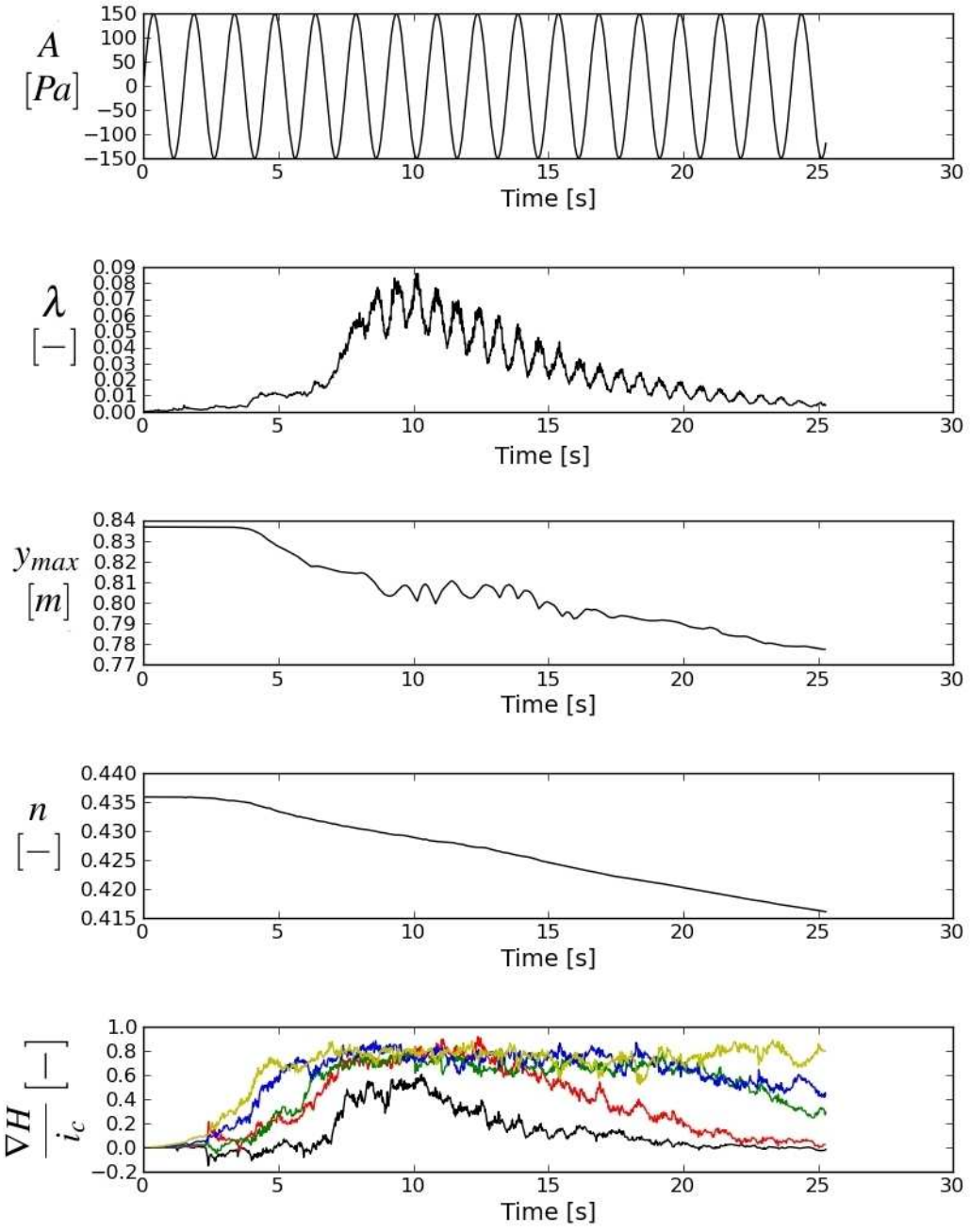

Figure 6.37: Stationary wave action on a loose seabed - Period = 1.5s.

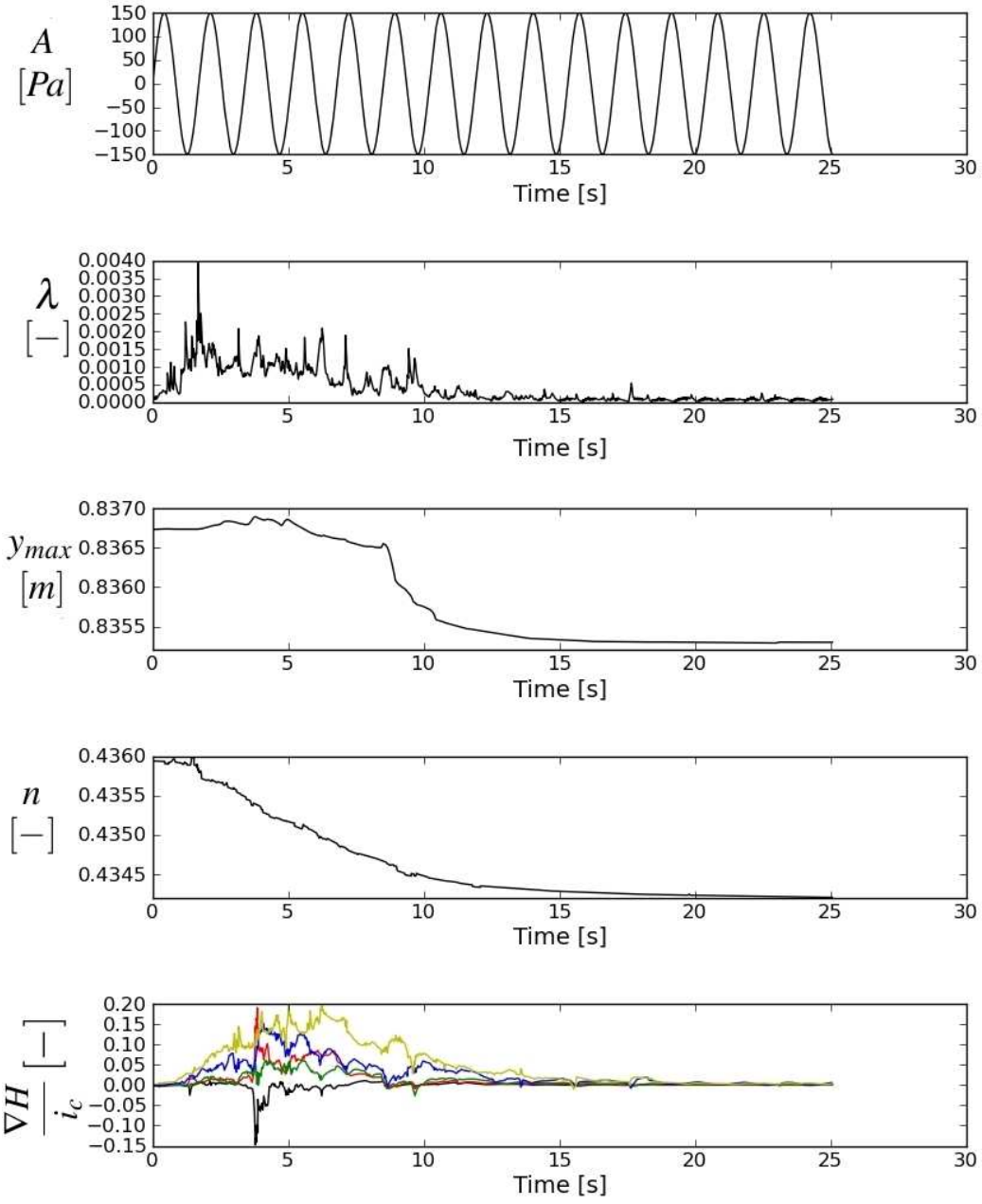

Figure 6.38: Stationary wave action on a loose seabed - Period = 1.7s.

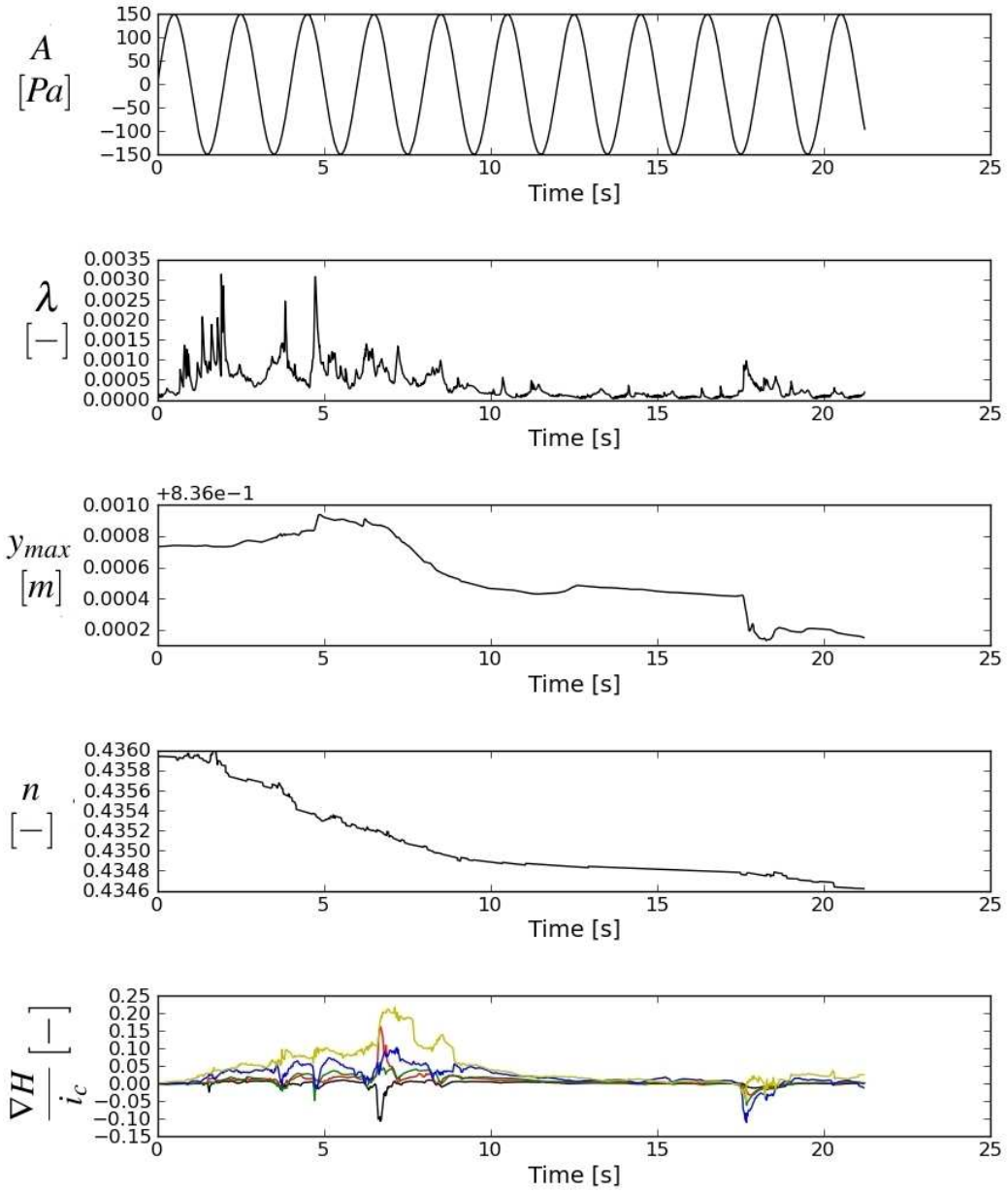

Figure 6.39: Stationary wave action on a loose seabed - Period = 2.0s.

highly influenced by the term expressing the pores volumetric deformation rate, $[\mathbf{E}]\{\dot{\mathbf{X}}\}$. Then, the evolution of the fluid-particle system was significatively different than the former case. The packing liquefied as an effect of the particle rearrangement due to the load that was applied, inducing the nearly complete reduction of the shear strenght. The amplitude of the wave at which the onset of instability was observed was 75% lower than the dense case. The deviatoric strain pattern gave evidence of the localization of the deformation in the proximity of the seabed surface.

This first set of simulations allowed us to access some informations to characterize the behaviour of a sphere packing of a given particle size distribution and particles density. On one side, from the simulation on the initially dense packing we had access to the amplitude that triggers surface movements. The information comes from the independence of the result from the deformation mechanism that was induced by the action of the wave. On the other side, the simulation on the loose packing gave evidence of the influence of particles rearrangement on the mechanical behaviour of the packing.

The second part of our analysis was characterized by a more complex representation of the wave loading on the packing. The effects of a stationary wave, oscillating with a certain frequency within a maximum and a minimum value of the amplitude, were analyzed. The aim was the characterization of the behaviour of the packing by focusing on the relation between the period of oscillation of the wave, the characteristic time of consolidation of the packing, and the characteristic time associated to the inertia of the particles. The period of oscillation was supposed to be the dominant variable determining the mechanical response of the packing. Notably, the packing liquefies if the period of oscillation is lower than the characteristic time of consolidation. When these two times become comparable, the packing has the time to reach a stable configuration, compatible with the fluid pressure gradient. For the frequencies of oscillation that induced liquefaction of the packing, the relation between the period of oscillation and the inertial characteristic time of the packing governs the behaviour of the fluid-particle system. For very short periods of oscillation, the particles have not enough time to be accelerated, then the final induced deformation remains very low. As long as those quantities become comparable, the induced deformation becomes more important. For the highest period of oscillation, the packing does not liquefy, but rather consolidates as an effect of the particles rearrangement induced by the wave loading. The deviatoric strain becomes negligible.

Conclusions and Perspectives

The objective of this survey was the development of a numerical hydromechanical coupled model to be applied to the analysis of the interaction between fluid flow and internal deformation in saturated granular media.

The discrete element method (DEM) was employed for the description of the mechanical interaction between solid particles. This numerical model allows the representation of granular materials by means of independent bodies which interact between each other, following a user-defined local interaction law. Solid particles were represented by spherical bodies. This over simplified choice allows however the evaluation of the influence of the particle arrangement to the behaviour of the packing, and at the same time provides an easy-to-handle geometry at the particles scale. There was no need in increasing the complexity of particles texture, since the behaviour we wanted to reproduce did not originate from such property.

The guiding consideration that characterized the choices we had taken defining the flow model was the preservation of the discrete nature of the DEM, in order to access all the necessary informations we needed to define a per-particle fluid force. The exisisting coupled models usually reach this level of detail in the description of particles-fluid interaction at high computational cost. This is the case for microscale flow models, based on a fine discretization of the poral space, that provide a highly detailed solution, in terms of fluid pressure, on particles contour. This is not the case for continuum-based models, that are generally based on phenomenological laws that reduce their predictive power and are not able to render correctly the single particle interaction with fluid flow. The pore-scale finite volume (PFV) model's valuable asset was the characterization of the local particle-fluid interaction, ensuring acceptable performances that could allow the employment of thousands of particles in 3D simulations, while keeping an affordable computational cost.

Main hypothesis

The literature review of the theoretical background concerning the description of pore flow in porous media allowed us to introduce some simplification to Navier-Stokes equations and formulate a tractable mathematical model for the flow system. An incompressible fluid is assumed to steadily flow between adjacent pores in the laminar regime. This a consistent assumption considered that we deal with problems characterized by a very slow velocity of the fluid, then very low values of the Reynolds and Mach numbers. Under these conditions, the inertial term in Navier-Stokes equations can be neglected if compared to the viscous term. A simplification that constitutes a very substantial simplification, since the equations become linear. Laminar flow is finally assumed to be described by a

generalized Poiseuille's law.

The PFV-DEM coupled model

The resolution of the flow problem was based on an algorithm using an implicit finite difference scheme. The coupling with the DEM results therefore naturally adapted. A criterion to ensure the stability of the coupled model was defined and supported by a parametric study. By the introduction of further simplifications, with the hypothesis of piecewise constant pressure, the number of unknowns for the resolution of the flow problem remains comparable to the case of the solid elastic-plastic problem.

Taking the FEM results as reference, the permeabilities and the pressure field obtained with the pore-scale modeling are well predicted. The model predictions were found also in good agreement with permeability measurements on bi-dispersed glass beads assemblies, as it was found by Anh-Tuan Tong during his PhD thesis [99]. Forces applied by the fluid on individual particles, and viscous forces on no-slip boundaries, are found to be correct, by comparison with FEM results. The modelling of fluid forces gives a sound basis for fluid-particle systems.

A set of coupling equations have been derived for the coupled DEM-PFV model. The analogy of these equations with Biot's theory of poroelasticity, briefly reported in *part 1*, suggested how the DEM-PFV coupled model should be able to recover the results of classical poroelasticity in boundary values problems. The 1D diffusion problem known as Terzaghi's consolidation was then used as a benchmark test for the validation of the model. The solution obtained was in good agreement with Terzaghi's analytical solution, in terms of evolution of the excess pore pressure and settlements, in time and space.

Many numerical aspects, concerning the performances of the model, especially regarding the resolution of the flow problem, had been analyzed. The Gauss-Seidel iterative procedure, and two direct solvers, based on PARDISO and TAUCS libraries, were tested. It was shown how the adoption of direct solvers allows a significative boost of performances. For the simulations we have presented in this thesis, the total computational cost that was measured was only the double with respect to uncoupled "dry" simulations. This can be considered as innovative in the framework of modern fluid-solid coupling models.

Sediment hydrodynamics

The PFV-DEM model was applied to the analysis of the hydrodynamics of a granular sediment, subjected to a wave-induced loading. The simplified approach we followed by considering the wave action equivalent to a sinusoidal pressure profile allowed the reproduction and the analysis of some characteristic scenarios.

The effect of the load of a standing wave of increasing amplitude had been initially considered to act on the granular sediment. Two main *limit* scenarios were reproduced, differing in the initial state of the packing. A dense and a loose packing were created. The response that was observed was qualitatively different. In the case of the dense packing, the problem was entirely governed by pressure conditions that were specified at the boundaries. The hydrostatic conditions were kept all along the simulation, up to a condition of instability due to the horizontal component of the gradient of charge which results

to be high enough to make the solid particles at the seabed surface be dragged. Differently, in the case of the loose packing, the solution of the system of eq.(4.4) was highly influenced by the term expressing the pores volumetric deformation rate, thus evidencing a strong poromechanical effect. The packing liquefied as an effect of the particle rearrangement inducing the nearly complete reduction of the shear strenght. The amplitude of the wave at which the onset of liquefaction was observed was 75% lower than the dense case. The deviatoric strain pattern gave evidence of the localization of the deformation at the seabed surface.

The second part of the analysis was dedicated to a more complex representation of the wave loading on the packing. The effects of a stationary wave, oscillating with a certain frequency within a maximum and a minimum value of the amplitude, were analyzed. The packing was found to liquefy when the period of oscillation was lower than the characteristic time of consolidation. When these two times become comparable, the packing has the time to reach a stable configuration, compatible with the fluid pressure gradient. For the frequencies of oscillation that induced liquefaction of the packing, the relation between the period of oscillation and the inertial characteristic time of the packing governed the behaviour of the fluid-particle system. For very short periods of oscillation, the particles have not enough time to be accelerated, then the final induced deformation remains very low. As long as those quantities become comparable, the induced deformation becomes more important. For the largest period of oscillation, the packing does not liquefy, but rather consolidates as an effect of the particles rearrangement induced by the wave loading. The deviatoric strain becomes negligible.

Our results suggest that occurrence of compaction associated to liquefaction does not produce any spontaneous evolution of the material. There is, indeed, a relation between the magnitude of porosity changes and the amplitude of the wave: the higher the amplitude, the higher the settlement. In this regard, there is no instability in the usual sense (an arbitrary large resposne to a small perturbation). It has been shown how the hydromechanical coupling can lead to liquefaction events in loose sediments. This origin of liquefaction has not been reported before to our knowledge. It is a result of particular importance since it can significantly enhance sediment mobility.

Perspectives

Regarding the possible extensions of the model we proposed, both physical and the numerical aspects could be concerned.

Regarding the physical description of the fluid-particles interaction, as it was recalled in the last chapter, in the PFV model, the description of stress and strain in the fluid is limited to their isotropic component, as it is the case in the Biot model of poroelasticity. Donia Marzougui integrated into the model the contribution, in terms of fluid-solid interaction, which arises from taking into account the deviatoric component of the fluid stress and strain tensors [63]. New viscous shear forces arise from taking into account such component.

The introduction of the module of compressibility of the fluid is also a potential extension which can be easily integrated into the model. Also in this case, works are in progress (post-doc of Luc Scholtès in Laboratoire 3SR).

From a numerical point of view, the parallelization of the model is conceivable and constitutes a perspective on further developments. The structure of the algorithm, as represented on fig.5.1, suggests an easy parallelization of the code, in order to utilize multiple processors simultaneously in a shared-memory multiprocessor machine.

In terms of applications of the model, the analysis of internal erosion, with the analysis of the phenomenon of fine particles migration in granular porous media, whose preliminary results may be found in [84] may be further deepened, as well as the transport of solid particles at the sediment surface. The implementation of periodic boundary conditions is under development (PhD of Donia Marzougui) and may open to more complex analysis of granular sediment hydrodynamics as well as to slope stability and debris flow.

Bibliography

[1] T. Abichou, C. H. Benson, and T. B. Edil. Network model for hydraulic conductivity of sand-bentonite mixtures. *Can. Geotech. J.*, 41(4):698–712, 2004.

[2] I. Agnolin and J.-N. Roux. Internal states of model isotropic granular packings. i. assembling process, geometry, and contact networks. *Phys. Rev. E*, 76, 2007.

[3] T. Anderson and R. Jackson. Fluid mechanical description of fluidized beds. equations of motion. *Industrial & Engineering Chemistry Fundamentals*, 6(4):527–539, 1967.

[4] E. Ando, S. Hall, G. Viggiani, J. Desrues, and P. Bésuelle. Grain-scale experimental investigation of localised deformation in sand: a discrete particle tracking approach. *Acta Geotechnica*, pages 1–13, 2011.

[5] F. Aurenhammer. Voronoi diagrams - a survey of a fundamental geometric data structure. *ACM Comput. Surv.*, 23(3):345–405, 1991.

[6] K. Bagi. Analysis of microstructural strain tensors for granular assemblies. *Int. J. of Solids and Structures*, 43(10):3166–3184, 2006.

[7] S. Bakke and P. Øren. 3-d pore-scale modelling of sandstones and flow simulations in the pore networks. *SPE Journal*, 2(2):136–149, 1997.

[8] J. Bardet and J. Proubet. Numerical investigation of the structure of persistent shear bands in granular media. *Geotechnique*, 41(4):599–613, 1991.

[9] V. Batista, D. Millman, S. Pion, and J. Singler. Parallel geometric algorithms for multi-core computers. *Computational Geometry*, 43(8):663–677, 2010.

[10] J. Bear. *Hydraulics of groundwater*, volume 569. McGraw-Hill New York, 1979.

[11] J. Biarez and P. Hicher. *Elementary Mechanics of Soil Behaviour: Saturated Remoulded Soil*. AA Balkema, 1994.

[12] M. Biot. Theory of elasticity and consolidation for a porous anisotropic solid. *Journal of Applied Physics*, 26(2):182–185, 1955.

[13] M. Biot. Theory of propagation of elastic waves in a fluid-saturated porous solid. i. low-frequency range. *J. Acoust. Soc. Am*, 28(2):168–178, 1956.

[14] F. Blake. The resistance of packing to fluid flow. *Transactions of the American Institute of Chemical Engineers*, 14:415–421, 1922.

[15] R. Boer and W. Ehlers. The development of the concept of effective stresses. *Acta Mechanica*, 83(1):77–92, 1990.

[16] R. R. O. Bonilla. *Numerical simulation of undrained granular media*. PhD thesis, University of Waterloo, 2004.

[17] S. Bryant and M. Blunt. Prediction of relative permeability in simple porous media. *Phys. Rev. A*, 46(4):2004–2011, 1992.

[18] S. Bryant and A. Johnson. Wetting phase connectivity and irreducible saturation in simple granular media. *J. of Colloid and Interface Science*, 263(2):572–579, 2003.

[19] S. Bryant, P. King, and D. Mellor. Network model evaluation of permeability and spatial correlation in a real random sphere packing. *Transp. Porous Med.*, 11(1):53–70, APR 1993.

[20] C. Callari. *Appunti del corso di meccanica dei mezzi porosi*. Università degli studi di Tor Vergata, 2007.

[21] F. Calvetti, G. Combe, and J. Lanier. Experimental micromechanical analysis of a 2d granular material: relation between structure evolution and loading path. *Mech. Cohes.-Frict. Mater.*, 2(2):121–163, 1997.

[22] B. Cambou and M. Jean. *Micromécanique des matériaux granulaires*. Hermes Science, 2001.

[23] B. Chareyre. *Modélisation du comportement d'ouvrages composites sol-géosynthétique par éléments discrets-application aux tranchées d'ancrage en tête de talus*. PhD thesis, PhD thesis at Grenoble University, 2003.

[24] B. Chareyre, L. Briançon, and P. Villard. Theoretical versus experimental modelling of the anchorage capacity of geotextiles in trenches. *Geosynthetics International*, 9(2):97–123, 2002.

[25] B. Chareyre, A. Cortis, E. Catalano, and E. Barthélemy. Pore-scale modeling of viscous flow and induced forces in dense sphere packings. *Transport in Porous Media*, 92:473–493, 2012.

[26] F. Chen, E. Drumm, and G. Guiochon. Coupled discrete element and finite volume solution of two classical soil mechanics problems. *Computers and Geotechnics*, 2011.

[27] P. Cundall. Computer simulations of dense sphere assemblies. *Micromechanics of granular materials*, 4:113–123, 1988.

[28] P. Cundall, A. Drescher, and O. Strack. Numerical experiments on granular assemblies; measurements and observations. In *IUTAM Conference on Deformation and Failure of Granular Materials, Delft, Holland, 1982*, pages 355–370. eds. P.A. Vermeer and H.J. Luger, Delft, Balkema, 1982.

[29] P. Cundall and O. Strack. A discrete numerical model for granular assemblies. *Geotechnique*, (29):47–65, 1979.

[30] P. A. Cundall. *Distinct element models of rock and soil structure. In Analytical and Conlputational Methods in Engineering Rock Mechanics,*. E.T. Brown (Ed.), Allen and Unwin, London.

[31] H. Darcy. Les fontaines publiques de la ville de dijon, 1856. *Dalmont, Paris*.

[32] J. Degroote, K.-J. Bathe, and J. Vierendeels. Performance of a new partitioned procedure versus a monolithic procedure in fluid–structure interaction. *Computers & Structures*, 87(11–12):793–801, 2009.

[33] E. Detournay and H. Alexander. Fundamentals of poroelasticity1. 1993.

[34] J. Dupuit. *Traité théorique et pratique de la conduite et de la distribution des eaux*. Dunod, 1854.

[35] H. Edelsbrunner and N. R. Shah. Incremental topological flipping works for regular triangulations. *Algorithmica*, 15(6):223–241, 1996.

[36] A. Fabri, G. Giezeman, L. Kettner, S. Schirra, and S. Schönherr. The cgal kernel: A basis for geometric computation. *Applied Computational Geometry Towards Geometric Engineering*, pages 191–202, 1996.

[37] R. Gallagher, R. Glowinski, P. Gresho, J. Oden, and O. Zienkiewicz. Finite elements in fluids. volume 7. *Chichester, England and New York, Wiley-Interscience, 1988, 325 p.*, 1, 1988.

[38] J. A. Gili and E. E. Alonso. Microstructural deformation mechanisms of unsaturated granular soils. *International Journal for Numerical and Analytical Methods in Geomechanics*, 26(5):433–468, 2002.

[39] R. Glowinski, T. W. Pan, T. I. Hesla, D. D. Joseph, and J. Periaux. A fictious domain approach to the direct numerical simulation of incompressible viscous flow past moving rigid bodies: Application to particulate flow. *Journal of Computational Physics*, 169(2):363–426, 2001.

[40] N. Gould, J. Scott, and Y. Hu. A numerical evaluation of sparse direct solvers for the solution of large sparse symmetric linear systems of equations. *ACM Transactions on Mathematical Software (TOMS)*, 33(2):10, 2007.

[41] Z. Guo and T. Zhao. Lattice boltzmann model for incompressible flows through porous media. *Physical Review E*, 66(3):036304, 2002.

[42] M. Hakuno. Simulation of the dynamic liquefaction of sand. In *Earthq. geotechnical engineering*, pages 857–862. Balkema, 1995.

[43] M. Hakuno and Y. Tarumi. A granular assembly simulation for the seismic liquefaction of sand. In *Proc. of Japan Society of Civil Engineers*, volume 398, pages 129–138, 1988.

[44] S. Hentz, F. Donzé, and L. Daudeville. Discrete element modelling of concrete submitted to dynamic loading at high strain rates. *Computers & structures*, 82(29):2509–2524, 2004.

[45] M. Hilpert, R. Glantz, and C. T. Miller. Calibration of a pore-network model by a pore-morphological analysis. *Transp. Porous Med.*, (51):267–285, 2003.

[46] C. Itasca. Pfc 3d-user manual. *Itasca Consulting Group, Minneapolis*, 1999.

[47] K. Iwashita and M. Oda. Micro-deformation mechanism of shear banding process based on modified distinct element method. *Powder Technology*, 109(1):192–205, 2000.

[48] M. Jean. The non-smooth contact dynamics method. *Computer Methods in Applied Mechanics and Engineering*, 177(3–4):235–257, 1999.

[49] J.-F. Jerier, B. Hathong, V. Richefeu, B. Chareyre, D. Imbault, F.-V. Donze, and P. Doremus. Study of cold powder compaction by using the discrete element method. *Powder Tech.*, In Press, 2010.

[50] T. Kambe. *Elementary fluid mechanics*. World Scientific Pub Co Inc, 2007.

[51] G. Karypis and V. Kumar. A fast and high quality multilevel scheme for partitioning irregular graphs. *SIAM JOURNAL ON SCIENTIFIC COMPUTING*, 20(1):359–392, 1998.

[52] K. M. Khanafer and A. J. Chamkha. Mixed convection flow in a lid-driven enclosure filled with a fluid-saturated porous medium. *International Journal of Heat and Mass Transfer*, 42(13):2465–2481, 1999.

[53] D. Koester, S. Ranka, and G. Fox. A parallel gauss-seidel algorithm for sparse power system matrices. In *Proceedings of the 1994 conference on Supercomputing*, pages 184–193. IEEE Computer Society Press, 1994.

[54] J. Kozeny. Ueber kapillare leitung des wassers im boden. *Wien, Akad. Wiss*, 136(2a):271, 1927.

[55] J. Kozeny and P. Carman. Flow of gases through porous media. *Acadwmic, NewYork*, 1956.

[56] M. Krafczyk, P. Lehmann, O. Philippova, D. Hänel, and U. Lantermann. Lattice boltzmann simulations of complex multi-phase flows. *Multifield Problems*, pages 50–57, 2000.

[57] M. Leva and U. S. B. of Mines. *Fluid flow through packed and fluidized systems*. USGPO, 1951.

[58] Y. Liu and J. Snoeyink. A comparison of five implementations of 3d delaunay tessellation. In J. Pach, J. E. Goodman, and E. Welzl, editors, *Combinatorial and Computational Geometry*, pages 439–458. MSRI Publications, 2005.

[59] V. A. Luchnikov, N. N. Medvedev, L. Oger, and J.-P. Troadec. Voronoi-delaunay analysis of voids in systems of nonspherical particles. *Phys. Rev. E*, 59(6):7205–7212, Jun 1999.

[60] A. Mahboubi, A. Ghaouti, and B. Cambou. La simulation numérique discrète du comportement des matériaux granulaires. *Revue française de géotechnique*, (76):45–61, 1996.

[61] M. Mansouri, J.-Y. Delenne, A. Seridi, and M. E. Youssoufi. Numerical model for the computation of permeability of a cemented granular material. *Powder Technology*, 208(2):532–536, 2011.

[62] M. Mansouri, J.-Y. Delenne, M. E. Youssoufi, and A. Seridi. A 3d dem-lbm approach for the assessment of the quick condition for sands. *Comptes Rendus Mécanique*, 337(9–10):675–681, 2009.

[63] D. Marzougui. Hydromechanical modeling of the transport and deformation in bed load sediment with discrete elements and finite volume. Master's thesis, Ecole Nationale d'Ingenieurs de Tunis, 2011.

[64] S. McNamara, E. G. Flekkøy, and K. J. Måløy. Grains and gas flow: Molecular dynamics with hydrodynamic interactions. *Phys. Rev. E*, 61(4):4054–4059, Apr 2000.

[65] R. D. Mindlin and H. Deresiewicz. Elastic Spheres in Contact Under Varying Oblique Forces. *J. of Appl. Mech.*, 20, 1953.

[66] N. Mortensen, F. Okkels, and H. Bruus. Reexamination of hagen-poiseuille flow: Shape dependence of the hydraulic resistance in microchannels. *Physical Review E.*, 71(5):057301–1–057301–4, 2005.

[67] H. Nakasa, T. Takeda, and M. Oda. A simulation study on liquefaction using dem. In *Earthquake geotechnical engineering*, pages 637–642. Balkema, 1999.

[68] A. Naumovich. On a finite volume discretization of the three-dimensional biot poroelasticity system in multilayered domains. *Computational methods in applied mathematics*, 6(3):306, 2006.

[69] P. Nithiarasu, K. Seetharamu, and T. Sundararajan. Natural convective heat transfer in a fluid saturated variable porosity medium. *International Journal of Heat and Mass Transfer*, 40(16):3955–3967, 1997.

[70] P. Nithiarasu, K. Seetharamu, and T. Sundararajan. Finite element modelling of flow, heat and mass transfer in fluid saturated porous media. *Archives of Computational Methods in Engineering*, 9:3–42, 2002.

[71] A. V. Oostreom and J. Strackee. The solid angle of a plane triangle. *IEEE Trans. on Biomedical Eng.*, BME-30(2):125–126, 1983.

[72] P. Øren, S. Bakke, and O. Arntzen. Extending predictive capabilities to network models. *SPE Journal*, 3(4):324–336, 1998.

[73] C. O'Sullivan, J. Bray, and M. Riemer. 3-d dem validation using steel balls with regular packing arrangements. In *Third International Conference on Discrete Element Methods: Numerical Modelling of Discontinua*. ASCE, 2002.

[74] T. Patzek and T. Silin. Shape factor and hydraulic conductance in noncircular capillaries: I. one-phase creeping flow. *J. of Colloid and Interface Science*, 236(2):295–304, 2001.

[75] S. Pion and M. Teillaud. 3d triangulations. *CGAL Editorial Board, editor, CGAL-3.2 User and Reference Manual*, 2006.

[76] M. Piri and M. J. Blunt. Three-dimensional mixed-wet random pore-scale network modeling of two- and three-phase flow in porous media. i. model description. *Phys. Rev. E*, 71(2):026301, Feb 2005.

[77] J. Poiseuille. *Recherches expérimentales sur le mouvement des liquides dans les tubes de très-petits diamètres*. Imprimerie Royale, 1844.

[78] F. Radjai. Contact dynamics method. *European Journal of Environmental and Civil Engineering*, 12(7-8):871–900, 2008.

[79] F. Radjai and V. Richefeu. Contact dynamics as a nonsmooth discrete element method. *Mechanics of Materials*, 41(6):715–728, 2009.

[80] J. Rayleigh. *Notes on hydrodynamics*. 1876.

[81] V. Richefeu, M. El Youssoufi, and F. Radjaï. Shear strength properties of wet granular materials. *Physical Review E*, 73(5):051304, 2006.

[82] V. Rotkin and S. Toledo. The design and implementation of a new out-of-core sparse cholesky factorization method. *ACM Transactions on Mathematical Software (TOMS)*, 30(1):19–46, 2004.

[83] J. Rousseau, E. Frangin, P. Marin, and L. Daudeville. Multidomain finite and discrete elements method for impact analysis of a concrete structure. *Engineering structures*, 31(11):2735–2743, 2009.

[84] H. Sari, B. Chareyre, E. Catalano, P. Philippe, and E. Vincens. Investigation of internal erosion processes using a coupled dem-fluid method. In *Particles 2011 II International Conference on Particle-Based Methods, E. Oate and DRJ Owen (Eds), Barcelona*, 2011.

[85] A. Scheidegger. *The physics of flow through porous media*. University of Toronto Press, 1960.

[86] O. Schenk and K. Gärtner. Solving unsymmetric sparse systems of linear equations with pardiso. *Future Generation Computer Systems*, 20(3):475–487, 2004.

[87] O. Schenk and K. Gärtner. On fast factorization pivoting methods for sparse symmetric indefinite systems. *Electronic Transactions on Numerical Analysis*, 23:158–179, 2006.

[88] E. M. Schlueter. *Predicting the Transport Properties of Sedimentary Rocks from Microstructure*. PhD thesis, LBL University of California, 1995.

[89] L. Scholtés. *Modélisation micromécanique des milieux granulaires partiellement saturés*. PhD thesis, Institut National Polytechnique de Grenoble, 2008.

[90] L. Scholtès, B. Chareyre, F. Nicot, and F. Darve. Micromechanics of granular materials with capillary effects. *International journal of engineering science*, 47(1):64–75, 2009.

[91] L. Scholtes, P. Hicher, F. Nicot, B. Chareyre, and F. Darve. On the capillary stress tensor in wet granular materials. *Int. J. Numer. Anal. Meth. Geomech.*, 33(10):1289–1313, 2009.

[92] A. Skempton. Significance of terzaghi's concept of effective stress. *From Theory to Practice in Soil Mechanics. John Wiley & Sons Inc*, 1960.

[93] C. Slichter and G. S. U. G. W. Branch. *Theoretical investigation of the motion of ground waters*. 1899.

[94] V. Smilauer, E. Catalano, B. Chareyre, S. Dorofeenko, J. Duriez, A. Gladky, J. Kozicki, C. Modenese, L. Scholtes, L. Sibille, J. Stransky, and K. Thoeni. Yade Reference Documentation. In V. Smilauer, editor, *Yade Documentation*. 2010. http://yade-dem.org/doc/.

[95] K. Terzaghi. Die berechnung der durchlassigkeitsziffer des tones aus dem verlauf der hydrodynamischen spannungserscheinungen. *Sitzungsberichte der Akademie der Wissenschaften in Wien, Mathematisch-Naturwissenschaftliche Klasse, Abteilung IIa*, 132:125–138, 1923.

[96] K. E. Thompson and H. S. Fogler. Modeling flow in disordered packed beds from pore-scale fluid mechanics. *AIChE Journal*, 43(6):1547–5905, 1997.

[97] C. Thornton and J. Lanier. Uniaxial compression of granular media: numerical simulations and physical experiment. *Powders and Grains*, 97:223–226, 1997.

[98] S. Toledo, D. Chen, and V. Rotkin. Taucs: A library of sparse linear solvers, 2003.

[99] A.-T. Tong, E. Catalano, and B. Chareyre. Numerical simulation of hydro-mechanical couplings by combined discrete element method and finite volumes: model predictions versus experiments on bi-dispersed granular assemblies. *Oil & Gas Science and Technology (accepted)*, 2012.

[100] J. Van Deemter and E. Van der Laan. Momentum and energy balances for dispersed two-phase flow. *Applied Scientific Research*, 10(1):102–108, 1961.

[101] V. Šmilauer and B. Chareyre. Yade dem formulation. *Yade Documentation*, 2010.

[102] Z. Yu and L.-S. Fan. Lattice boltzmann method for simulating particle–fluid interactions. *Particuology*, 8(6):539–543, 2010.

[103] M. Zeghal and U. E. Shamy. A continuum-discrete hydromechanical analysis of granular deposit liquefaction. *Int. J. Numer. Anal. Meth. Geomech.*, 28(14):1361–1383, 2004.

Résumé en français

Introduction Générale

Le comportement des matériaux multiphasiques couvre une multitude de phénomènes qui suscitent un grand intérêt dans le domaine scientifique et professionnel. Les propriétés mécaniques de ces types de matériau trouvent leur origine dans les phases dont ils sont composés, leur distribution et interaction. Idéalement, tester chaque phase séparément serait fondamentale pour comprendre et contrôler le comportement mécanique du matériaux dans l'ensemble. Cependant, même si les technologies modernes permettent l'observation de ces matériaux à une très petite échelle et l'identification de la distribution et de la texture de chaque phase, il est généralement difficile de caractériser la relation entre les évidences expérimentales microscopiques et macroscopiques.

Parmi les matériaux multiphasiques existants, l'étude du comportement des matériaux pulvérulents est central pour des sciences tels que la mécanique des solides, des sols, et certaines branches de l'ingénierie physique et chimique. La géométrie des assemblages de particules, la distribution de leur taille, ainsi que leur propriétés électriques, optiques, etc. constituent les problématiques à la base de ces disciplines. Une phase solide, une liquide et une gazeuse sont identifiables dans un matériau pulvérulent présent dans la nature. On a de plus en plus tendance à ne considérer que les deux premières, le phase gazeuse pouvant être considérée comme une phase liquide avec des propriétés spécifiques.

L'interaction entre la phase solide et la phase fluide constitue la problématique centrale de notre étude. Priorité sera donnée aux applications en mécanique des sols. L'érosion interne ou de surface, les études d'instabilité d'ouvrages en terre et fondations, retrait/gonflement des matériaux poreux suite à changements de la teneur en eau, etc. sont des exemples de problèmes classiques qui ont une origine hydromécanique, et impliquent des questions complexes auxquelles on doit faire face sur la base de la mécanique des fluides et des solides granulaires.

Parallèlement à l'évolution de technologies en optique et tomographie qui a caractérisé les dernières décades, en donnant accès à des informations détaillées sur la structure et le comportement des systèmes complexes, des nouveaux outils numériques, puissants et efficients, ont été développés pour interpréter, analyser et prédire leur comportement. Dans ce contexte, il devient clair que l'échelle à la quelle les scientifiques observent et décrivent la physique de tels systèmes devient de plus en plus petite jusqu'à atteindre l'échelle microscopique.

La méthode des éléments discrets (DEM) est un des ces outils numériques qui connaît un succès grandissant parmi les communautés scientifiques. La DEM fournie une plateforme performante pour la modélisation du comportement des matériaux granulaires.

Basée sur la définition des interactions entre particules, la DEM permet la reproduction du comportement de matériaux purement frottants [22] ainsi que de matériaux multiphasiques [90] [38] [81] en définissant des lois microscopiques spécifiques.

Dans ce travail, on propose le couplage de la DEM avec un modèle d'écoulement, ce dernier basé sur la définition des équations relatives à l'écoulement visqueux à l'échelle des pores, ensuite approximées par un schéma numérique aux volumes finis. La nature discrète de la DEM est ainsi préservée. L'avantage obtenu par cette stratégie de modélisation réside dans la possibilité de considérer indépendemment chaque phase et ainsi accéder à une série d'informations qui seraient inaccessible expérimentalement. L'interaction de chaque particule avec le fluide est définie. Ce niveau de détail est normalement atteint par les modèles d'écoulement basées sur une discrétisation fine de l'espace porale. L'objective du modèle est d'introduire des simplifications qui puissent permettre à la fois de réduire le nombre des degrés de liberté relatifs au problème d'écoulement et de décrire l'interaction entre la phase solide et la phase fluide à l'échelle des pores et des particules.

Le modèle DEM-PFV ("Pore-scale Finite Volume") est un modèle couplé suivant une approche partitionnée: les résolutions du problème élasto-plastique aux contacts entre particules et du problème d'écoulement seront donc traités séparément. Le modèle DEM-PFV sera appliqué à l'analyse de l'interaction entre l'écoulement et la déformation interne d'un sédiment côtier.

Description du problème

Ecoulement dans les milieux poreux

Les équations de Navier-Stokes

Les équations de Navier-Stokes décrivent le mouvement des fluides newtoniens. Ces équations sont obtenues par application de la deuxième loi de Newton, en faisant l'hypothèse que la contrainte fluide est la somme d'un terme visqueux, proportionnel au gradient de vitesse, et d'un terme de pression isotropique.

L'équation de continuité est obtenue par application du principe de conservation de la masse sur un élément infinitésimal de volume fluide:

$$\frac{\partial \rho_f}{\partial t} = -\nabla \cdot (\rho_f \mathbf{u}) \tag{6.34}$$

où ρ_f représente la densité du fluide, $\mathbf{u}$ sa vitesse locale, $\frac{\partial}{\partial t}$ l'opérateur de dérivée temporelle. Le vecteur $\rho_f \mathbf{u}$ exprime la densité de l'écoulement, sa divergence exprimant la vitesse de l'écoulement par unité de volume. En cas d'hypothèse de fluide incompressible (ρ_f constant), l'équation de continuité s'écrit:

$$\nabla \cdot \mathbf{u} = 0 \tag{6.35}$$

On considère ensuite l'équation bilan de la quantité de mouvement:

$$\frac{\partial (\rho_f \mathbf{u})}{\partial t} + \mathbf{u} \cdot \nabla \rho_f \mathbf{u} = \nabla \cdot \Pi + \rho_f \mathbf{f}^{\mathbf{V}} \tag{6.36}$$

où le premier terme exprime le taux d'augmentation de la quantité de mouvement volumique, le deuxième le taux de diminution de la quantité de mouvement volumique par convection à travers la surface; les termes de droite représentent les forces externes, exercées par la contrainte fluide (tenseur Π) sur la surface de l'élément (troisième terme) et par les forces volumiques (quatrième terme).

Le tenseur de contrainte peut être décomposé en sa partie isotropique et déviatorique, comme il suit:

$$\Pi = -p\mathbf{I} + \mathbf{T} \tag{6.37}$$

et peut être réécrit, en accord avec la théorie des fluides newtoniens, comme:

$$\Pi = -p\mathbf{I} + \kappa_b(\nabla \cdot \mathbf{u})\mathbf{I} + 2\mu\,\Delta \tag{6.38}$$

où p est la pression hydrostatique, $\mathbf{I}$ le tenseur identité, κ_b la viscosité volumique, μ la viscosité de cisaillement et $\Delta = \frac{1}{2}[\nabla\mathbf{u} + (\nabla\mathbf{u})^T] - \frac{1}{3}\mathbf{I}(\nabla \cdot \mathbf{u})$ le tenseur de taux de déformation déviatorique. La viscosité volumique met en relation la contrainte avec le taux de déformation volumique. Ce terme est important dans le cas de fluides soumis à des forces en rapide évolution (par ex. en cas de vibrations ultrasoniques). Il sera négligé dans la suite.

Avec ρ_f constant (fluide incompressible, $\nabla \cdot \mathbf{u} = 0$) et viscosité μ constante, on obtient une forme des équations de Navier-Stokes, telle que:

$$\rho_f \left(\frac{\partial \mathbf{u}}{\partial t} + \mathbf{u} \cdot \nabla\mathbf{u} \right) = -\nabla p + \mu\nabla^2\mathbf{u} + \rho_f \mathbf{f}^{\mathbf{V}} \tag{6.39}$$

Écoulement de Stokes

La résolution des équations de Navier-Stokes constitue encore un challenge mathématique important. Généralement des simplifications sont introduites. Le mouvement du fluide peut être *turbulent* ou *laminaire*. Dans le régime turbulent, les variables dépendantes telles que la vitesse ou la pression ne sont pas fonction que du temps et l'espace, mais doivent être décrites par des lois stochastiques. Bien que les formes indépendantes du temps des équations de continuité (6.34) et de mouvement (6.38) restent valides, leur solution en termes de vitesse et de pression instantanée n'est pas possible. Généralement, l'hypothèse d'écoulement laminaire est adoptée quand la vitesse de fluide est suffisamment lente et les effets visqueux peuvent être dominant sur les effets inertiels. Le traitement mathématique en devient fortement simplifié.

Un paramètre adimensionnel qui détermine l'importance relative des effets visqueux et inertiels est le nombre de Reynolds:

$$Re = \frac{\rho_f \mathbf{u} \cdot \nabla\mathbf{u}}{\mu\nabla^2\mathbf{u}} \simeq \frac{\| \mathbf{u} \| L}{\nu} \tag{6.40}$$

où $\mathbf{u}$ exprime la vitesse du fluide, L est une longueur caractéristique du problème (diamètre d_T de la conduite), μ et ν sont la viscosité absolue et cinématique du fluide, respectivement ($\nu = \mu/\rho_f$). Quand le nombre de Reynolds est petit, on parle d'*écoulement visqueux*. Les forces visqueuses due à l'écoulement cisaillant du fluide dominent sur les forces inertielles associées à l'accélération et la décélération des particules de fluide. Dans le contexte de notre recherche, le nombre de Reynolds est suffisamment petit ($Re \simeq 10^{-8}$)

pour adopter l'hypothèse d'écoulement laminaire.

Un autre paramètre qui décrit le comportement de particules en suspension dans un fluide est le nombre de Stokes:

$$S_t = \frac{\tau_V}{\tau_F} \tag{6.41}$$

où τ_V est le temps de relaxation associé à la particule et τ_F est un temps caractéristique du champ d'écoulement, le temps caractéristique $d_T / \parallel \mathbf{u} \parallel$ de l'écoulement au travers d'un venturi par exemple, où d_T est le diamètre de la gorge, et $\parallel \mathbf{u} \parallel$ la vitesse d'écoulement. Le nombre de Stokes devient ainsi:

$$S_t = \frac{\tau_V \parallel \mathbf{u} \parallel}{d} \tag{6.42}$$

Si $S_t << 1$, le temps de réponse des particules est petit par rapport au temps carateristique associé au champs d'écoulement. La particule aura largement le temps pour répondre aux changements de vitesse fluide. Par conséquent la particule et le fluide auront quasiment la même vitesse. $S_t >> 1$ représente la condition pour laquelle la particule n'a pas le temps de répondre aux changements de vitesse fluide, sa vitesse restant donc quasiment unchangée.

Un dernier paramètre qui nous permet d'introduire les hypothèse du modèle est le nombre de Mach. En mécanique de fluides, ce paramètre (Ma ou M) représente la vitesse d'un objet en mouvement dans l'air ou n'importe quel autre fluide, divisé par la vitesse du son dans le fluide considéré.

$$M = \frac{V_R}{c} \tag{6.43}$$

où V_R est la vitesse de la source relative au milieu et c la vitesse du son dans ce milieu. L'estimation du nombre de Mach nous permet d'assumer l'hypothèse d'écoulement incompressible si $M < 0.2 - 0.3$. Dans le contexte de notre recherche, le nombre de Mach est estimé au tour de 10^{-8}. Il est donc possible faire l'hypothèse d'écoulement incompressible.

En cas d'écoulement incompressible et laminaire (qui est le cas dans notre étude) le terme inertiel $\rho_f \mathbf{u} \cdot \nabla \mathbf{u}$ peut être négligé par rapport au terme visqueux $\mu \nabla^2 \mathbf{u}$, et les équations de Navier-Stokes (eq.(6.39)) prennent la forme suivante:

$$\nabla p = \mu \nabla^2 \mathbf{u} \quad (Re << 1) \tag{6.44}$$

$$\nabla \cdot \mathbf{u} = 0 \quad (S_t >> 1) \tag{6.45}$$

Cela constitue une simplification essentielle, puisque les équations sont désormais linéaires. En présence d'un potentiel Φ (i.e. gravité), la pression piézométrique p est liée à la pression absolue p^a par l'expression suivante:

$$p = p^a - \rho_f \Phi \tag{6.46}$$

L'équation de Stokes devient alors:

$$\nabla p = \mu \nabla^2 \mathbf{u} - \rho_f \nabla \Phi \tag{6.47}$$

Approche macroscopique - Loi de Darcy

En 1856, Henry Darcy étudia l'écoulement de l'eau au travers de filtres homogènes verticaux, dans le cadre de travaux destinés à la mise en place d'un système de distribution d'eau pour la ville de Dijon. De ses expériences, Darcy arriva à la conclusion que le débit de fluide, Q, était proportionnel à la surface de la section A et au gradient de charge hydraulique, défini comme:

$$i = \frac{\Delta H}{L} \quad [-] \tag{6.48}$$

où H exprime la charge hydraulique et L la longueur du filtre. La loi de Darcy assuma donc la forme suivante:

$$\mathbf{q} = K_d \nabla H \tag{6.49}$$

où $\mathbf{q}$ est le débit spécifique (m/s), ∇H est le gradient hydraulique et K_d est la conductivité hydraulique du milieu (m/s). La perte de charge serait due au frottement qui caractérise le passage du fluide au travers les gorges étroites du milieu poreux. La vitesse qui peut être calculée en utilisant la loi de Darcy est en réalité une vitesse apparente du fluide, plus faible que la vitesse effective du fluide interstitiel dans les pores V_p ($V_p \simeq V/n$). En outre, l'éq.(6.49) inclut implicitement les effets de viscosité et de frottement interne, en permettant l'analyse d'un écoulement de filtration sans prendre directement en compte de ces effets. Dans ce sens, la loi de Darcy peut être vu comme une représentation statistique équivalente aux équations de Navier-Stokes.

A l'augmentation du débit spécifique, la relation avec le gradient hydraulique dévie de la relation linéaire exprimée par la loi de Darcy (fig.6.40), dont le domaine de validité est donc remis en discussion. Par analogie avec la définition du nombre de Reynolds (eq.(6.40)), une nouvelle expression est proposée pour ce genre de problématique:

$$Re = \frac{qd}{\nu} \tag{6.50}$$

où d est une longueur représentative de la matrice poreuse, généralement mise en relation avec la dimension moyenne des particules, et ν est la viscosité cinématique du fluide. Des évidences expérimentales montrent que la loi de Darcy est valide tant que le nombre de Reynolds calculé avec l'expression (6.50) ne dépasse pas une valeur comprise entre 1 et 10 [10].

Modèles numériques d'un milieu granulaire saturé

La méthode des éléments discrets (DEM)

Généralités

Une possibilité pour obtenir des informations sur le comportement des milieux granulaires est l'expérimentation. Une alternative consiste à effectuer des simulations avec la méthode

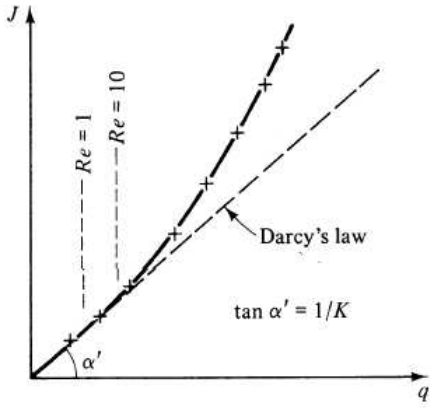

Figure 6.40: Relation débit spécifique q - gradient hydraulique $J = \nabla H$ [10].

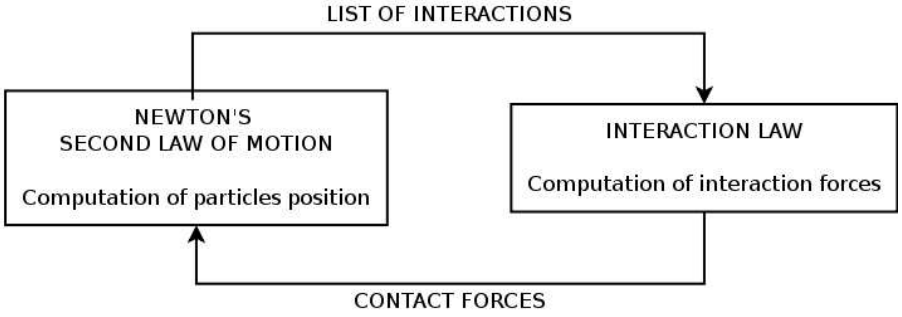

Figure 6.41: Cycle de calcul d'un modèle DEM.

des élément discrets (DEM) [29]. Cette méthode sera présentée par la suite, en essayant de fournir les aspects principaux qui en font une des méthodes numériques de plus en plus utilisée dans les domaines académique et industriel.

Le dénominateur commun des modèles discrets existants réside dans le fait que le particules dont un milieu granulaire est composé sont considérés comme des corps rigides indépendants. Le comportement de ces derniers sera donc le résultat de ce qu'il se passe au niveau des contacts entre les particules, avec les variables cinématiques qui seront dérivées selon les degrés de liberté (translations et rotations) des particules. De ce fait, il est évident que ce qui est le plus attractif dans les modèles discrets est la possibilité de décrire la physique et la mécanique des discontinuités qui caractérisent les matériaux naturels, en utilisant un nombre de paramètres relativement faible. Lié à cet aspect est la possibilité de mesurer les grandeurs mécaniques à l'échelle des discontinuités qui seraient inaccessibles expérimentalement. Le coût en calcul pour la résolution du problème est proportionnel au nombre de particules qui sont adoptées dans une simulation, qui sera donc le résultat d'un compromis entre les ressources disponibles en CPU et RAM et la représentativité de l'échantillon pour le problème à étudier ou le mécanisme à reproduire.

Le cycle de calcul d'un modèle DEM est schématisé en fig.6.41. Le problème étant résolu par petit pas temporels, le mouvement des particules est décrit par des fonctions régulières, donc deux fois dérivables, et les équations de la dynamique sont intégrées avec

l'aide de lois d'interaction régissant les contacts entre particules. Dans le cas de particules sphériques, qui sera le cas dans notre étude, dans un espace orienté de dimension *i* (*i=1,2,3* in 3D), le mouvement des particules est défini par leur position x_i et leur vitesse translationnelle $\dot{x}_i$ et rotationnelle ω_i. L'accélération des particules est calculée à chaque pas de temps par application du principe fondamentale de la dynamique.

$$\begin{aligned} \ddot{x}_i &= F_i/m_i \\ \dot{\omega}_i &= M_i/J_i \end{aligned} \tag{6.51}$$

En suivant l'évolution du système particulaire dans le temps, la position des particules est mise à jour à chaque pas de temps Δt par intégration des accélérations $\ddot{x}_i$ et $\dot{\omega}_i$ selon un schéma centré aux différences finies. On obtient:

$$\begin{aligned} \dot{x}_i^{[t+\Delta t/2]} &= \dot{x}_i^{[t-\Delta t/2]} + (\ddot{x}_i^{[t]} + g)\cdot\Delta t \\ \omega_i^{[t+\Delta t/2]} &= \omega_i^{[t-\Delta t/2]} + \dot{\omega}_i^{[t]}\cdot\Delta t \end{aligned} \tag{6.52}$$

où les vitesses translationnelle et rotationnelle des particules sont évaluées au temps $t + \Delta t/2$. Les positions des particules sont ainsi calculées, au temps $t + \Delta t$:

$$x_i^{[t+\Delta t]} = x_i^{[t]} + \dot{x}_i^{[t+\Delta t/2]}\cdot\Delta t \tag{6.53}$$

Une fois les nouvelle positions calculées, la liste des interactions entre particules est mise à jour, et les nouvelles forces de contact sont calculées.

Loi d'interaction

La définition d'une loi d'interaction entre deux particules constitue un aspect central d'un modèle DEM, car c'est à ce niveau de la modélisation que le comportement microscopique et macroscopique des assemblages des particules est déterminé. Les forces résultent du contact qui est assumé avoir lieu en un point. Un repère locale est défini par ce point, *C*, et deux axes définis respectivement par un vecteur normal **n** dont la direction est définie par le segment reliant les centre de gravité des deux particules, et un vecteur tangentiel, **t**, orthogonal au précédent.

La force de contact est donc définie par une composante normale et une composante tangentielle, fonction respectivement du déplacement normale et de l'incrément de déplacement relatif tangentiel:

$$\mathbf{F_n} = F_n\mathbf{n} = k_n\delta_c\mathbf{n} \tag{6.54}$$

$$\Delta\mathbf{F_s} = F_s\mathbf{t} = k_t\Delta u_s\mathbf{t} \quad \rightarrow \quad \mathbf{F_s}^{(t)} = \mathbf{F_s}^{(t-\Delta t)} + \Delta\mathbf{F_s}^{(t)} \tag{6.55}$$

où k_n et k_t sont des raideurs constantes définie au niveau de chaque contact (fig.6.43) [29], [24], [91].

Frottement de Coulomb

Un critère de Coulomb est associé à chaque contact, définissant sa résistance au cisaillement. Il en résulte une limite supérieure pour la force tangentielle F_s, fonction de la force normale F_n et d'un angle de frottement intergranulaire ϕ_c (fig.6.43b):

$$\| \mathbf{F}_s \| \leq \mathbf{F}_n tan\phi_c \tag{6.56}$$

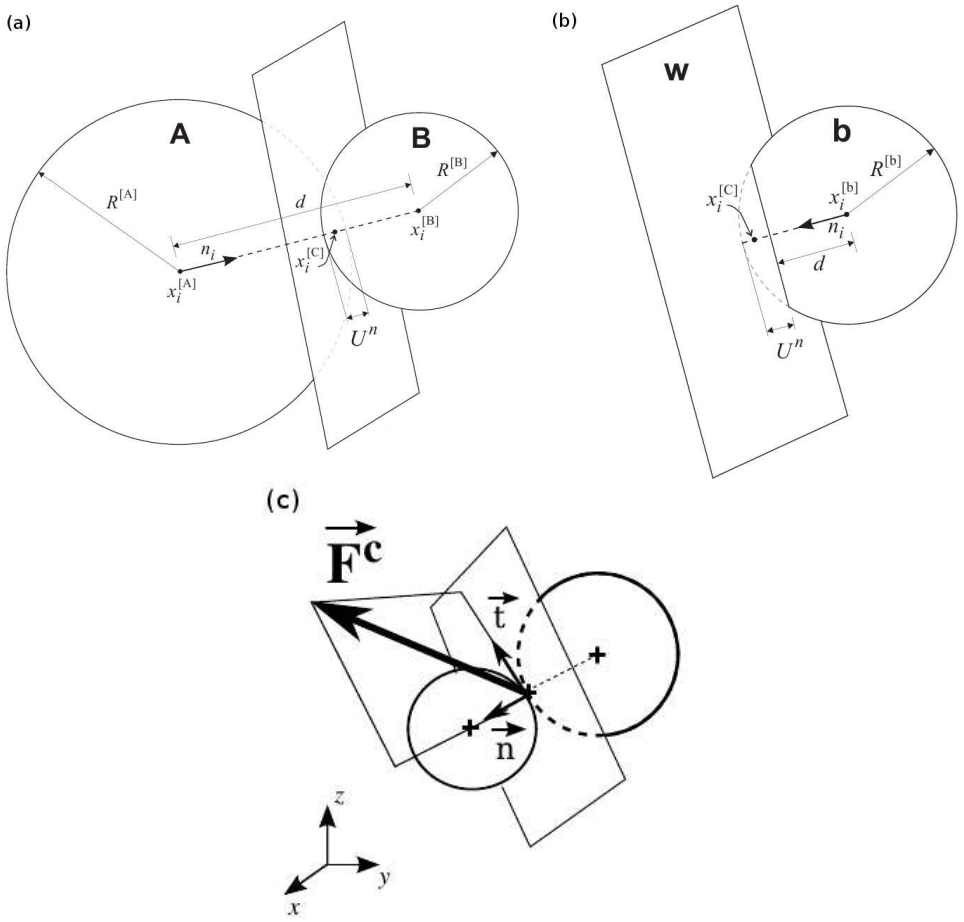

Figure 6.42: Géométrie locale de l'interaction ([46], [89]).

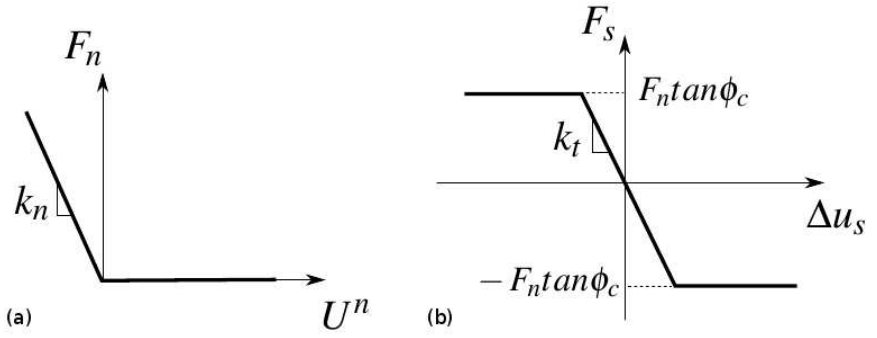

Figure 6.43: Modèle de contact élastique-plastique. Loi d'interaction normale (a) et tangentielle (b) [89]

Modèles couplés DEM-écoulement

Différentes stratégies ont été adoptées pour le couplage de la DEM avec des modèles d'écoulement, qui diffère essentiellement dans la façon dont la partie fluide du problème est traitée. Ceux-ci peuvent être regroupés en trois familles:

- *Modèles microscopiques*, généralement basés sur une discrétisation fine de l'espace porale. La méthode des élément finis (FEM) est souvent évoquée étant donné sa flexibilité dans le définition de la maille numérique [39], mais généralement implique un temps de calcul très élevé. Les modèles Lattice-Boltzmann (LB) [64] ne nécessitent pas la résolution d'un grand système d'équations non-linéaires. Ils sont plus rapides que la FEM, même si la maille fixe communément implémenté peut engendrer une large occupation de mémoire en cas de modèles 3D;

- *Modèles continus*, dans lesquels l'écoulement et les interactions fluide-solide sont définis à l'aide de modèle simplifié basés sur la loi de Darcy. Ils en résultent des temps de calcul normalement acceptables [67]. Il n'y a pas de couplage direct à l'échelle locale: les forces agissantes sur chacune des particules sont définies en fonction de la vitesse de fluide moyennée sur une méso-échelle regroupant plusieurs particules, à l'aide d'estimations de la perméabilité basées sur les valeurs locales de la porosité. Le comportement d'une particule seule n'est donc pas bien reproduit par ces modèles, ce qui limite leur application pour des problèmes tels que la localisation de la déformation, le ségrégation, érosion interne et d'autres problème pour lesquels les phénomènes principaux ont lieu à l'échelle des hétérogénéités qui caractérisent l'échelle microscopique.

- *Modèles pore-network*, généralement développé pour la prédiction de la perméabilité des matériaux à partir de leur géométrie microstructurelle, mais qui ont été aussi enrichis avec la prise en compte d'effets multiphysiques [17]. Leur succès dépend fortement de comment les fluides sont échangés entre les pores, relativement à la géométrie locale. D'autres idées pour le couplage de modèles pore-network avec la DEM peuvent être retrouvées dans les travails de Hakuno and Tarumi [42], et Bonilla [16]. Les études réalisés dans ce cadre, cependant, étaient limités à des modèles 2D. La géométrie 2D des pores n'offrant pas un parcours libre du fluide au sein du milieu poreux, des hypothèses ultérieures sont nécessaires dans la définition des conductivités locales. En adaptant ces approches à des assemblages des sphères en 3D, au contraire, les conductivités locales peuvent être définies en fonction de la géométrie des assemblages, qui résulte par définition en un réseaux de pores connectés. Les estimation de la perméabilité à l'échelle macroscopique est ainsi rendue possible.

Le modèle couplé PFV-DEM

Modélisation de la phase solide

Le code YADE ("Yet Another Dynamical Engine") est un environnement open-source (C++, license GPL) qui permet le développement de modèles numériques discrets en trois

dimensions. Grace à sa modularité les capabilités du code sont en évolution constante, fruit de la contribution des utilisateurs qui ont accès aux sources du code, créent leur propre modèle, ajoutent des nouveaux modules ou modifient les existants.

Définition des contacts

Comme dans des autres codes qui implémentent la DEM, les particules solides dans YADE sont modélisées comme des corps de forme sphérique interagissant entre eux selon des lois d'interaction définie par l'utilisateur. Ces sphères sont identifiées par leur rayon R, leur masse m et leur moment d'inertie I_0. A chaque pas de temps la position de chacune des sphères est calculée par intégration de la deuxième loi de Newton, ou principe fondamental de la dynamique, en fonction des forces et moments qui lui sont appliqués. Dans le cas plus simple, les paramètres qui sont définis aux contacts sont une raideur normale et tangentielle k_n et k_t, et le frottement intergranulaire ϕ_c. Une telle configuration peut varier lorsqu'on désire reproduire des comportement macroscopiques plus complexes. L'adoption de particules non-sphériques est aussi possible [94].

Considérant les objectifs du modèle PFV, l'adoption d'une lois de contact plus complexe que celle qui a été présentée en section 6.4.2 ne se rend pas nécessaire. Le calcul des forces élastiques et moments à appliquer aux particules sera donc basé sur les équations (6.54, 6.55, 6.56) selon la loi de contact exprimée par les diagrammes des figures 6.43 et 6.44.

La définition des raideurs de contact est basée sur l'idée de trouver une formulation qui puisse résulter en une position relative entre deux sphères toujours proportionnelle à une dimension caractéristique associée à leur interaction. Elle seront donc définies en fonction d'une raideur globale E_{global} et de la moyenne harmonique des rayons des sphères en contact, R_1 et R_2:

$$k_n = 2\,E_{global} \cdot \frac{R_1 \cdot R_2}{R_1 + R_2} \tag{6.57}$$

$$k_t = a\,k_n \tag{6.58}$$

La raideur tangentielle k_t est définie comme une fraction a de la raideur normale. L'introduction de E_{global} permet l'homogénéisation du comportement élastique à l'échelle des assemblages et assure l'indépendance de leur comportement globale de la taille des particules.

Modélisation de la phase fluide

Écoulement visqueux

Comme introduit dans les sections précédentes, on considère un milieu poreux saturé d'un fluide dont l'écoulement est régi par l'équation de Stokes, qui exprime la conservation de la masse de fluide et du moment pour des petits nombres de Reynolds et de Stokes:

$$\nabla p = \mu \nabla^2 \mathbf{u} - \rho^f \nabla \Phi \tag{6.59}$$

$$\nabla \cdot \mathbf{u} = 0 \tag{6.60}$$

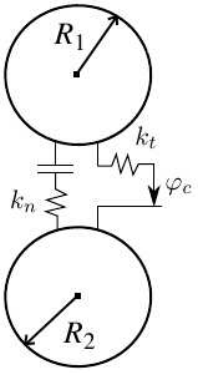

Figure 6.44: Raideur normale et tangentielle définies aux contacts.

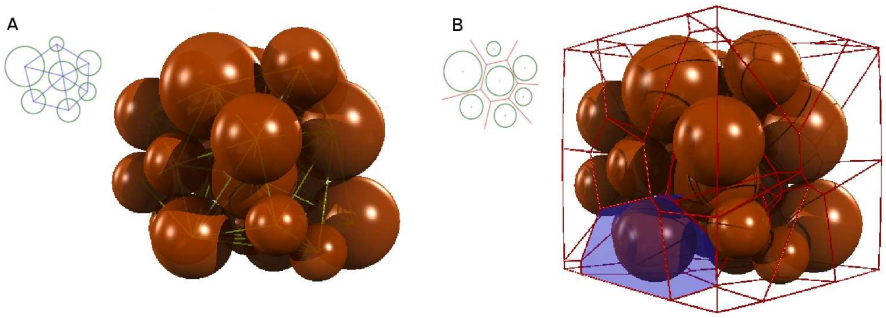

Figure 6.45: Triangulation régulière (A) et diagramme duale de Voronoi (B).

où $\mathbf{u}$, et p sont respectivement la vitesse de fluide et la pression piézometrique, μ est la viscosité dynamique du fluide, et Φ est un champ potentiel (e.g. gravité). La condition $\mathbf{u} = 0$ est spécifiée aux contour des grains, qui est essentiellement responsable des pertes d'énergie visqueuse à l'échelle microscopique et résulte en une perte de charge le long du parcours d'écoulement.

Le modèle PFV

Une triangulation régulière et le diagramme dual de Voronoi sont utilisés pour la discrétisation de l'espace des vides. En 3D, cela résulte en un système de tétraèdres en résulte en 3D, chaque tétraèdre représentant un pore (fig.6.45(A) et fig.6.46). Les sommets de la triangulation sont représentés par les centre de gravité des particules. Les déplacement des particules déterminent donc la déformation des éléments de la maille. La diagramme dual de Voronoi constitue un réseau dont les arêtes ne croisent jamais la phase solide (fig.6.45(B)) et forment des régions clos, chacune contenant une et une seule particule fig.6.45(B)). Ce réseau représente le chemin du fluide au sein du milieu poreux et permet la formulation et la résolution du problème fluide de Stokes à l'échelle des pores. L'équation de conservation de la masse intégrée dans le pore i, reformulée en une intégrale de surface par le théorème de la divergence, donne:

$$\Delta \dot{V}_i^f = \int_{S_{ij}} (\mathbf{u} - \mathbf{v}) \cdot \mathbf{n} ds = \sum_{j=j_1}^{j_4} q_{ij} \tag{6.61}$$

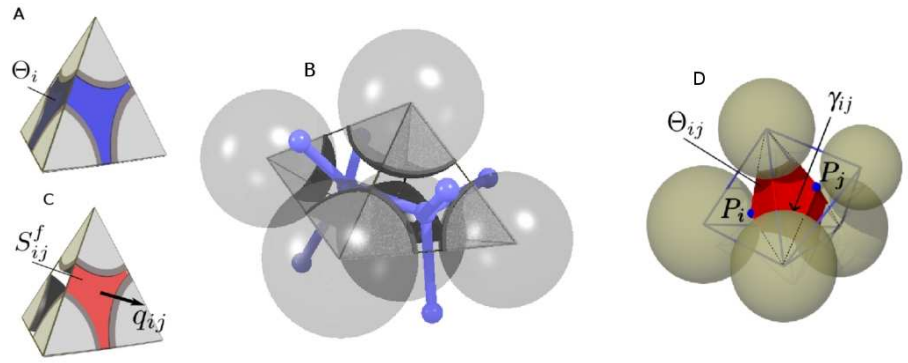

Figure 6.46: Volume de fluide dans le pore (A), pores adjacents et connectivité locale (B), domaine fluide du contour du pore (C), partition du pore pour la définition du rayon hydraulique (D) [25]

où $(\mathbf{u}-\mathbf{v})$ exprime la vitesse du fluide relative à celle des particules. L'intégrale de ce terme sur la facette S_{ij} donne le fluide échangé entre deux tétraèdres adjacents, q_{ij} (fig.6.46C), leur somme sur toutes les facettes étant équilibrée par la vitesse de déformation de l'élément pore $\Delta\dot{V}_i^f$.

Un des aspects clé du modèle est l'expression de q_{ij} en fonction de la géométrie locale et la pression dans les pores. Les équations de Stokes et Darcy impliquent une relation linéaire entre le gradient de pression et le débit. On peut donc écrire:

$$q_{ij} = g_{ij}\frac{p_i - p_j}{l_{ij}} \tag{6.62}$$

où le gradient de pression local est défini comme le rapport entre le saut de pression $p_i - p_j$ et la distance l_{ij} entre les pores i et j (distance euclidienne entre les centres de Voronoi associés aux deux pores), et g_{ij} est un terme qui exprime la conductivité hydraulique de la région Θ_{ij} telle qu'elle est représentée en fig.6.46D. La combinaison entre les équations (6.61) et (6.62) donne la relation entre le champ de pression de fluide et la vitesse des particules:

$$\Delta\dot{V}_i^f = \sum_{j=j_1}^{j_4} \frac{g_{ij}}{l_{ij}}(p_i - p_j) \tag{6.63}$$

La conductivité hydraulique g_{ij} est définie par l'expression suivante [25]:

$$g_{ij} = \frac{S_{ij}^f {R_{ij}^h}^2}{2\mu} \tag{6.64}$$

où R_{ij}^h est le rayon hydraulique, S_{ij}^f est la portion de la facette S_{ij} occupée par le fluide et μ est la viscosité du fluide. Le rayon hydraulique est défini comme le rapport entre le volume de Θ_{ij} occupé par le fluide et la surface γ_{ij} représentant l'interface fluide-solide (fig.6.46D).

La pression dans chaque pore est obtenu par la résolution du système linéaire (6.63),

en fonction des condition aux limites spécifiées. Les forces exercées par le fluide sur les particules solides sont ainsi calculées à partir du champ de pression obtenu. La force totale F^k sur la particule k est défini comme:

$$F^k = \int_{\partial\Gamma_k} (p^a \mathbf{n} + \tau \mathbf{n}) ds \tag{6.65}$$

où $\partial\Gamma_k$ dénote la surface solide de la particule k, p^a la pression de fluide absolue et τ la contrainte visqueuse. F^k peut être ainsi calculé par la somme de trois termes:

$$F^k = \int_{\partial\Gamma_k} \rho\Phi(x)\mathbf{n} ds + \int_{\partial\Gamma_k} p\mathbf{n} ds + \int_{\partial\Gamma_k} \tau\mathbf{n} ds = F^{b,k} + F^{p,k} + F^{v,k} \tag{6.66}$$

où $F^{b,k}$ dénote la force d'Archimède, $F^{p,k}$ la résultante des forces de pression et $F^{v,k}$ la résultante des forces visqueuses.

Couplage hydromécanique

Les équations relatives au problème couplé peuvent donc être détaillées, et la relation de cette formulation avec la théorie classique de la poroélasticité discutée.

Équations de couplage

A l'échelle microscopique, le couplage est défini par deux équations. La première est l'éq.(6.63) où le terme de gauche est une fonction de la vitesse des particules solides. L'autre est obtenue par introduction des forces fluides dans l'équation fondamentale de la DEM (6.51), qui dévient:

$$M\ddot{X} = F^c + W + F^f, \tag{6.67}$$

où F^c et F^f expriment les contributions des forces de contact et des forces fluides, respectivement, et M est la matrice globale des masses.

La combinaison des équations (6.61) et (6.67) respectivement pour tous les éléments de la maille et toutes les particules amène à une relation matricielle reliant les déplacements globaux au champ de pression:

$$\mathbf{G}\{P\} = \mathbf{E}\dot{x} + Q_q + Q_p, \tag{6.68}$$

$$[\mathbf{M}]\{\ddot{\mathbf{X}}\} = \{\mathbf{F^c}\} + \{\mathbf{W}\} + \{\mathbf{F^f}\} \tag{6.69}$$

où G est la matrice de conductivité contenant les termes g_{ij}/l_{ij}, P le vecteur colonne contenant les valeurs inconnues de pression, $\mathbf{E}$ est la matrice définissant les vitesses de changement de volume tel que $\Delta\dot{V}_i^f = (\mathbf{E}\dot{x})_i$, Q_q et Q_p sont les vecteurs contenants respectivement les termes sources pour les débits imposés, où les produits $p_i \cdot g_{ij}/l_{ij}$ pour les pression externes imposées, W est le vecteur colonne des poids des particules. F^f peut être donc exprimée sous forme matricielle comme une fonction du champ de pression P et la matrice $\mathbf{S}$, qui exprime la géométrie locale de l'espace porale:

$$F^f = \mathbf{S}P \tag{6.70}$$

La combinaison des équations (6.68) et (6.69) amène à une équation différentielle, où x est la seule inconnue:

$$\ddot{X} = M^{-1}(F^c + W + \mathbf{S}G^{-1}(\mathbf{E}\cdot\dot{X} + Q_s + Q_p)) \tag{6.71}$$

Validation du modèle

L'analogie du problème ainsi formulé avec la théorie classique de la poroélasticité de Biot suggère que le modèle DEM-PFV peut bien s'adapter à la simulation des problèmes classiques hydrodynamiques, tel que le processus de consolidation des sols, présenté dans la suite.

Essai oedomètrique

Le problème de consolidation monodimensionnelle de Terzaghi est simulé avec la modèle DEM-PFV et sera utilisé comme test de validation. La consolidation est un problème hydromécanique classique. Les mécanismes qui gouvernent l'évolution de la déformation d'un milieu granulaire saturé d'un fluide visqueux dépendent de la variation de l'état de contrainte, couplé aux procès de diffusion du fluide interstitiel. Ce phénomène dépend donc des propriétés du milieu poreux, tels que la perméabilité et la déformabilité, et de la géométrie du problème, définie par les conditions aux limites et le drainage du milieu.

L'équation de consolidation monodimensionnelle est,

$$\frac{\partial p}{\partial t} = C_v \frac{\partial^2 p}{\partial z^2} \tag{6.72}$$

où p est la pression du fluide, z la hauteur de l'échantillon, C_v le coefficient de consolidation, définit comme:

$$C_v = \frac{K_d E_{oed}}{\rho_f g} \quad \left[\frac{L^2}{T}\right] \tag{6.73}$$

avec K_d le coefficient de conductivité hydraulique du sol, $E_{oed} = \Delta\sigma_v^{'}/\Delta\varepsilon_v$ le module oedomètrique, g la gravité et ρ_f la densité du fluide. Un paramètre temporel adimensionnel est introduit, T_v, défini comme:

$$T_v = \frac{C_v t}{L^2} \tag{6.74}$$

où t représente le temps effectif et L la longueur du chemin le plus long parcouru par une particule de fluide.

Résultat numérique

La modèle DEM-PFV est cohérent avec les hypothèses de Terzaghi dans les conditions suivantes:

- c1) La déformation est petite est la relation contrainte-déformation est linéaire;
- c2) Le coefficient de Biot est $\alpha_B = 1$ (phases fluide et solide incompressibles);
- c3) Le déplacement est unidirectionnel;
- c4) La perméabilité et le module oedomètrique sont constants dans l'espace et le temps.

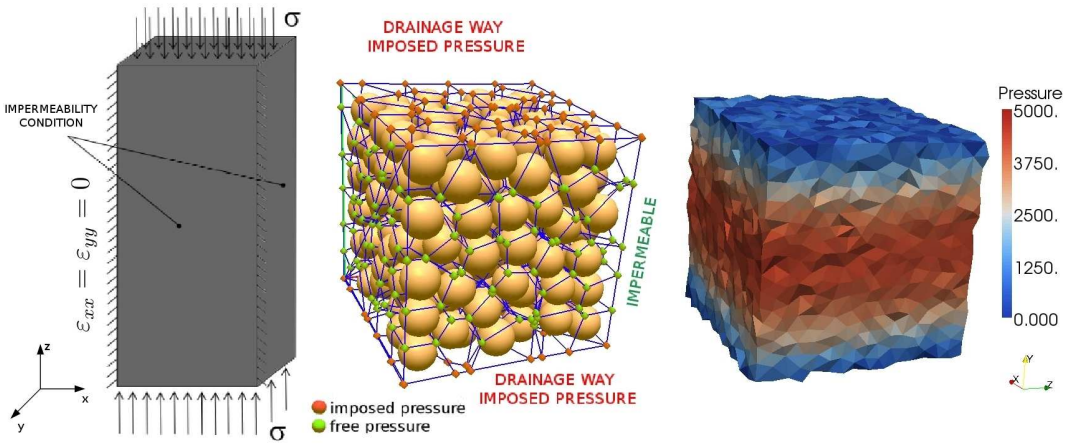

Figure 6.47: Conditions aux limites (gauche). Champ de pression à $T_v = 0.1$ (10% de consolidation) (droite).

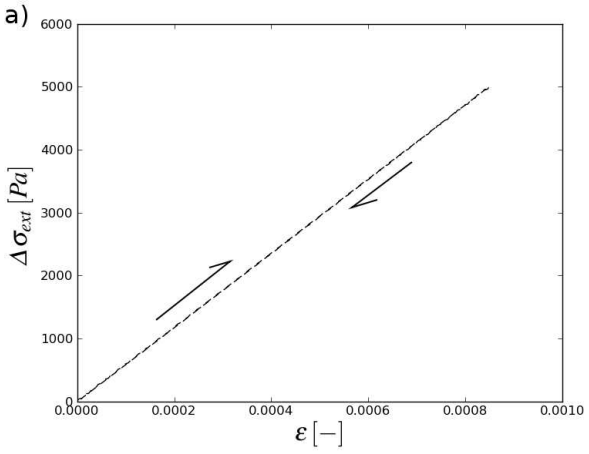

Figure 6.48: Essai de compression (conditions oedomètriques) pour l'évaluation du module oedomètrique. $\Delta\sigma_{ext} = 5\,kPa$.

La condition c1) peut être obtenu en assurant des petites déformations. La condition c2) vaut dans le modèle DEM-PFV et les conditions aux limites peuvent être spécifiées pour respecter la condition c3), même si les déplacements à l'échelle locale ne seront pas tout à fait unidirectionnels. Par définition, la condition c4) n'est pas satisfaite, mais si les déformations sont petites, on peut assumer que la perméabilité et le module de compressibilité restent constantes au cours de la simulation.

Les conditions aux limites sont représentées en fig.6.47. Les déplacements latérales sont empêchés ($\varepsilon_{xx} = \varepsilon_{yy} = 0$). Le drainage s'effectue par la frontière en haut et en bas de l'échantillon. Un échantillon dense a été utilisé, pour minimiser la dispersion de la dimension des pores. 5000 particules sont employées pour la construction d'un échantillon cubique ($l = 0.1m$) soumis à une charge externe $\Delta\sigma_{ext} = 5\,kPa$. Un test de compression sur un échantillon de la même dimension et granulométrie a été préparé pour l'estimation du module de compressibilité.

Le tableau 6.4 résume les paramètres de la simulation.

INPUT DATA		
Number of grains	[-]	5000
Sample dimensions	[m]	0.1 x 0.1 x 0.1
μ	[kPa · s]	0.25
$\Delta\sigma_{ext}$	[kPa]	5
σ_0	[kPa]	0
p_0	[kPa]	0
E	[kPa]	15000
a	[-]	0.5

Table 6.4: Essai oédomètrique - Données de la simulation pour les fig.s 6.49,6.50.

RESULTS		
ε_{final}	[-]	0.08%
E_{oed}	[kPa]	5895
K_d	[m/s]	$7.07623 \cdot 10^{-9}$

Table 6.5: Essai oédomètrique - Résultats numériques (fig.s 6.49,6.50).

Le résultat numérique est résume par le tableau 6.5. La fig.6.49 montre l'évolution de la pression de fluide moyennée sur la section à $z = H/2$. La fig.6.50 (gauche) montre l'évolution de la pression le long de la hauteur de l'échantillon dans le temps. Fig.6.50 (droite) montre l'évolution de la déformation ε, normalisée à la valeur finale ε_{final}.

L'évolution dans l'espace et le temps de la pression de fluide, ainsi que l'évolution de la déformation, sont en accord avec la solution analytique de Terzaghi, comme présentée par la fig.6.50.

Déposition gravitaire immergée

Dans cette section l'évolution de la pression du fluide sera observé sur un problème de déposition gravitaire. Un nuage de sphères, ne se touchant pas (n=0.61), est créée dans une boite rempli de fluide (fig.6.51). La gravité est ensuite appliquée et les sphères commencent ainsi à sédimenter. La pression du fluide est mesurée pendant cette phase par six capteurs équidistants placés selon le schéma de la fig.6.51. Le tableau 6.6 résume les paramètres de la simulation.

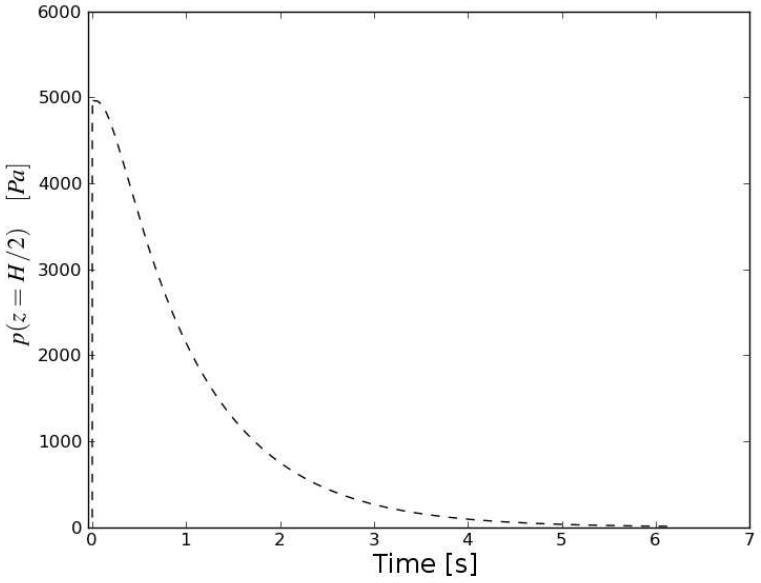

Figure 6.49: Essai oédomètrique - Pression fluide mesurée à $z = H/2$ pendant le procès de consolidation.

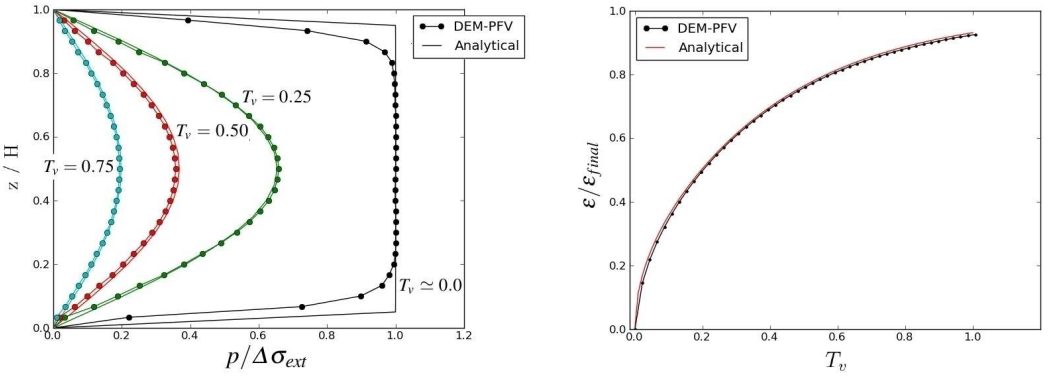

Figure 6.50: Essai oédomètrique - Évolution de la pression de fluide ($\Delta\sigma_{ext} = 5\,kPa$) (gauche) et de la déformation (droite)

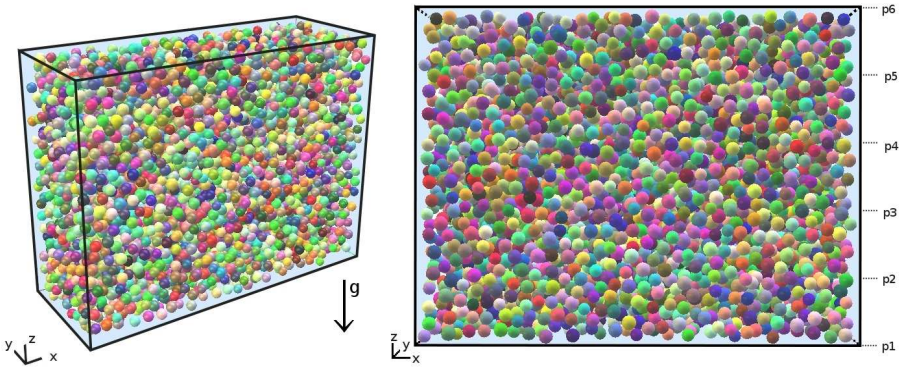

Figure 6.51: Simulation d'une déposition gravitaire immergée (a). Positions des capteurs de pression de fluide p_i (b).

INPUT DATA		
Number of grains	[-]	5000
Sample dimensions	[m]	2.00 x 1.50 x 0.75
μ	[kPa · s]	0.10
d_{50}	[m]	0.06
ρ_s	[kg/m^3]	2600
ρ_f	[kg/m^3]	1000
p_{ext}	[kPa]	0
E	[kPa]	15000
a	[-]	0.5

Table 6.6: Déposition granulaire immergée - Données de la simulation.

Gradient critique de liquéfaction

Par définition, la condition de liquéfaction d'un sol consiste dans le transfert complet du poids des particules du squelette solide (forces intergranulaires) au fluide interstitiel. Dans ce cas, la contrainte effective s'annule et le mélange fluide-solide se comporte comme un matériau visqueux. Le gradient critique de liquéfaction est ainsi défini:

$$i_c = \frac{\gamma'}{\gamma_f} = \frac{\gamma_{sat} - \gamma_f}{\gamma_f} = \frac{\nabla p}{\gamma_f} \tag{6.75}$$

où γ_{sat} est le poids spécifique du sol saturé, $\gamma_{sat} = \gamma_{soil}(1-n) + \gamma_f(n)$. On peut évaluer directement le gradient de pression ∇p, pour la valeur initiale de porosité $n = 0.61$:

$$\nabla p = \gamma_{sat} - \gamma_f = \gamma_{soil}(1-n) + \gamma_f(n) - \gamma_f = 6120 kN/m^3 \tag{6.76}$$

Le gradient critique de liquéfaction est donc:

$$\frac{\nabla p}{\gamma_f} = \nabla H_c = \frac{6120 kN/m^3}{9806,65 KN/m^3} = 0.624[-] \tag{6.77}$$

Le résultat en terme de pression de fluide moyennée sur la section à $z = H/2$ est représenté en fig.6.52(a). Le gradient de pression, évalué pour chaque couple de capteurs consecutives, est également représenté (b).

En fig.6.52a, quand la pression mesurée au niveau d'une certaine couche égalise celle d'une couche adjacente, cela signifie que les sphères sont en contact et que la couche est stable. Il peut être observé, en fig.6.52b, que les valeurs initiales de gradient hydraulique sont proches du gradient critique calculé avec l'expression (6.77), pour s'annuler au fur et à mesure que l'assemblage se stabilise.

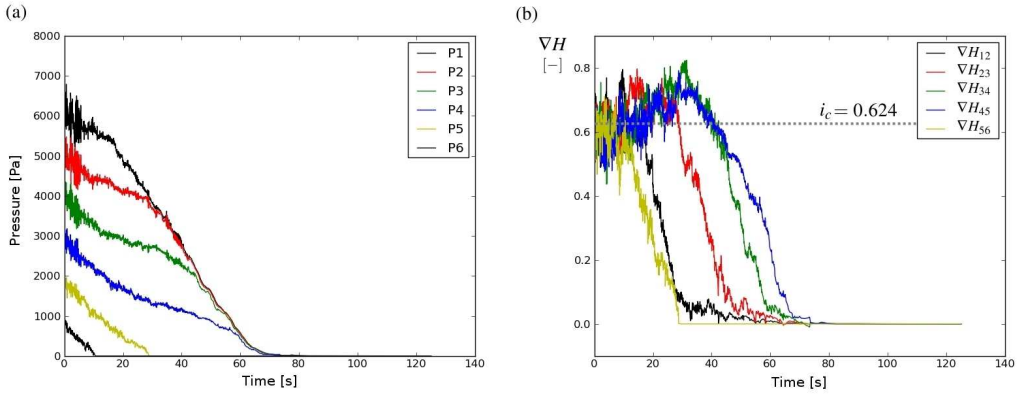

Figure 6.52: Déposition granulaire immergée, cas du tableau 6.6. Mesures de pression de fluide (a). Gradient hydraulique (b).

Hydrodynamique d'un sédiment granulaire

L'interaction entre la phase liquide et la phase fluide influence fortement le comportement des matériaux granulaires et devient fondamentale dans l'interprétation des phénomènes comme l'érosion interne ou de surface, la transport de sédiment, ou dans des problèmes d'instabilité de structures et de fondations induite par l'action des vagues ou de séismes, etc.

La modélisation à l'échelle des pores permet d'obtenir des informations sur le comportement macroscopique à partir des propriétés locales qui caractérisent la microstructure des milieux poreux (fraction solide, taille des particules), et peut aider à l'interprétation des mécanismes complexes mentionnés ci-dessus, sur la base de considérations micromécaniques. On présentera dans cette section l'application du modèle DEM-PFV au problème poro-visco-élastoplastique qui caractérise l'interaction entre l'écoulement et la déformation interne des sédiments côtiers. Cet étude fait partie du projet Hydro-Fond[2] ("Hydromécanique des Géomatériaux de Fondation Immergés"). L'objectif est la caractérisation de l'instabilité induite par le chargement cyclique associé à l'action des vagues marines, l'influence de l'état initial en terme de porosité, et l'analyse de la relation entre la période d'oscillation de la vague et le temps caractéristique de consolidation de l'assemblage.

Liquéfaction des sols

La liquéfaction des sols est un phénomène dans lequel le sol perd sa résistance au cisaillement ou sa raideur pendant un temps plus ou moins long. Cela peut arriver en cas de chargement cyclique (séisme) ou statique. La liquéfaction se produit rapidement, fréquemment sans aucun avertissement préalable, et peut causer des grosses pertes financières, voir humaines.

Tant que les grains restent en contact, la pression de fluide est celle qui correspond aux conditions hydrostatiques. Quand il est soumis à une perturbation mécanique, le sol tend à se compacter, les contacts intergranulaires se cassent et la charge extérieure est portée

[2]Réalisé avec le soutient du ministère de l'écologie, du développement durable, des transports et du logement, direction générale des infrastructures, des transports, et de la mer, dans le cadre du programme C2D2 du RGCU.

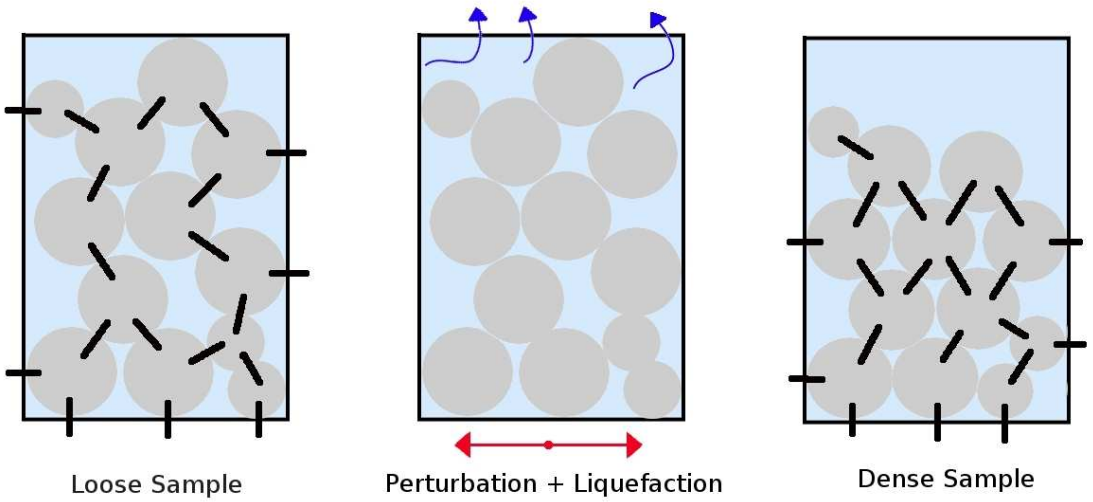

Figure 6.53: Liquéfaction des sols: schéma du mécanisme.

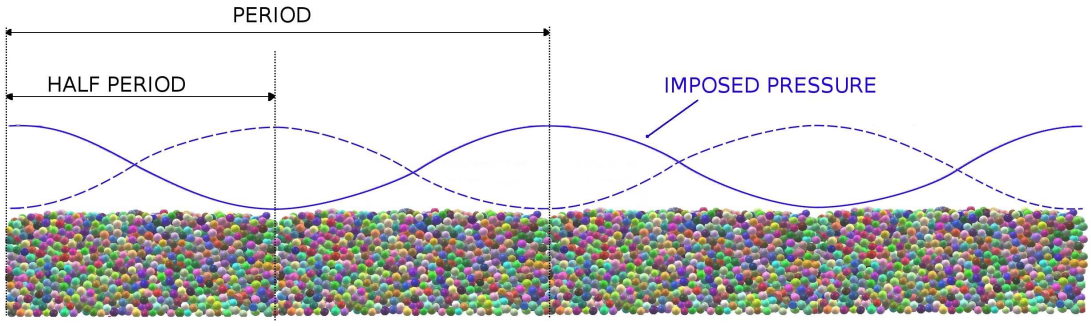

Figure 6.54: Action simplifiée de la vague: condition au limite sinusoïdale en pression.

par le fluide, provoquant une augmentation de la pression p. La liquéfaction est donc généralement associée à une augmentation de pression de fluide p, tel que la contrainte effective s'annule. Un exemple du mécanisme qui se produit en cas de liquéfaction du sol est représenté en fig.6.53, où un sol lâche saturé se liquéfie suite à un perturbation (cas typique de liquéfaction induite par séisme).

Simulation de l'action de la vague

L'action de la vague a été modélisé en spécifiant une condition en pression à la surface du sédiment suivant un profil sinusoïdale. La périodicité d'une telle représentation peut être observé en fig.6.54. Les simulations qu'on présentera dans la suite seront basées sur une démi-periode. Une condition de symétrie est donc imposée sur les parois latérales (fig.6.55), tandis que une condition d'étanchéité est imposée sur la frontière du bas.

La fig.6.56 montre le champ de pression obtenu par calcul numérique sur un échantillon de sédiment granulaire en trois dimensions. Une visualisation 2D (profondeur/hauteur=2.0) des équipotentielles et du champ de vitesse est également représentée. La fig.6.57 compare directement la solution numérique avec la solution analytique (champ de vitesse

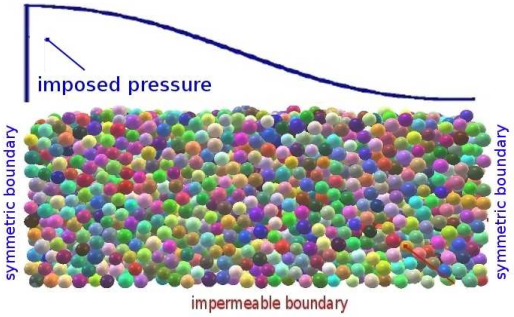

Figure 6.55: Représentation d'un lit granulaire pour l'étude de l'hydrodynamique du sédiment (demi-période en fig.6.2) - Conditions symétriques spécifiées aux parois latérales.

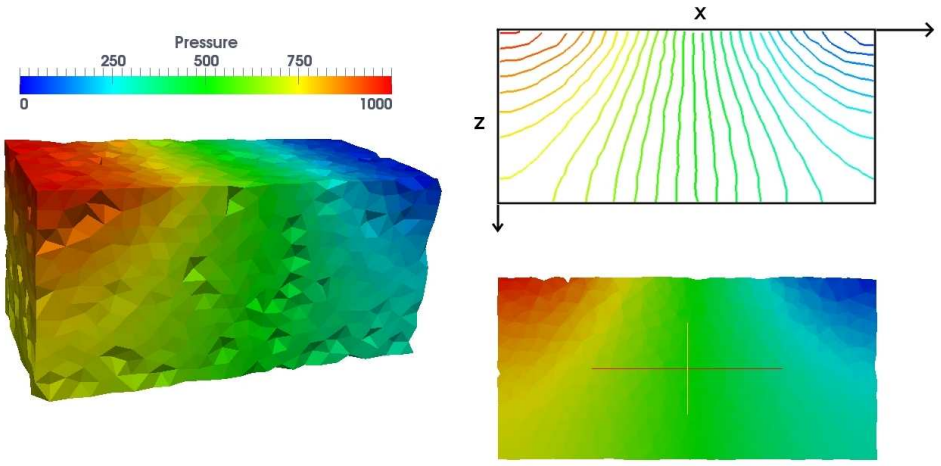

Figure 6.56: Solution numérique. Équipotentielles et champ de pression de fluide (profondeur / hauteur = 2.0).

fluide de Darcy). La comparaison est très satisfaisante.

Les effets de l'action d'une vague seront ainsi présentés de suite. L'amplitude A (en Pascal) (fig.6.58), de la vague est augmentée linéairement au cours du temps. Chaque incrément de l'amplitude correspondant à un plus fort gradient de pression imposé au sédiment, l'analyse consistera dans l'observation et l'interprétation de sa réponse. Deux scénarios seront proposés, qui différeront dans la valeur de porosité initiale de l'assemblage. On fera donc référence aux cas *lâche* ($n \simeq 0.436$) et au cas *dense* ($n \simeq 0.368$).

Pendant la simulation, la mesure de la pression de fluide est effectuée en six points verticalement équidistants (p1, p2, .. p6 en fig.6.59) le long de cinq verticales (v1, v2, .. v5 on fig.6.59).

Simulation sur échantillon dense

On présente dans cette section les résultats obtenus sur l'échantillon dense, qui a été créé en spécifiant un faible angle de frottement aux contacts entre particules pendant la phase de préparation de l'échantillon (pluviation), en favorisant donc le rearrangement mutuel

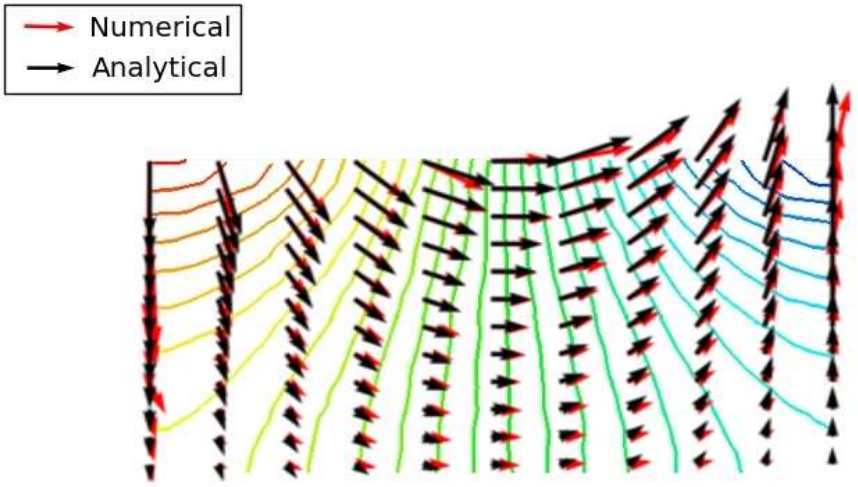

Figure 6.57: Champ de vitesse fluide - Solution numérique et analytique.

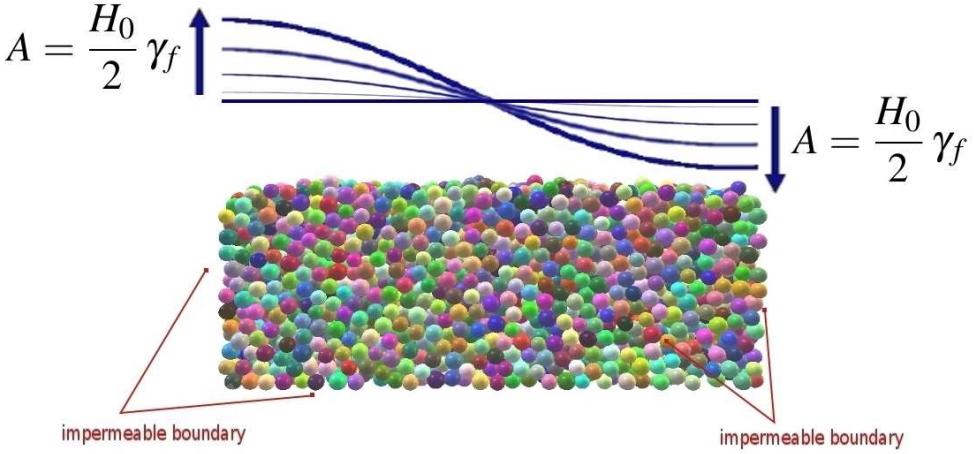

Figure 6.58: Simulation d'une vague d'amplitude croissante.

des grains vers des configurations denses.
Le tableau 6.7 présente les données de la simulation.

Paramètres d'état et cinétiques

L'évolution de certains paramètres, utiles pour l'analyse de l'état et de la cinétique du système pendant la simulation, est représentée en fig.6.60. L'amplitude A varie linéairement dans le temps. L'évolution de l'énergie cinétique KE et du paramètre λ (indicateur de stabilité, =0 en cas d'équilibre statique) sont également représentés. L'évolution de KE indique une stabilité globale qui est maintenue jusqu'à une amplitude de $1500\,Pa$. Ensuite, une instabilité apparaît, avec les particules qui accélèrent soudainement. L'évolution du λ confirme ces indications. Les deux diagrammes du bas représentent respectivement la coordonnée y maximale de l'assemblage (y_{max}) et la porosité n. Ces deux paramètres

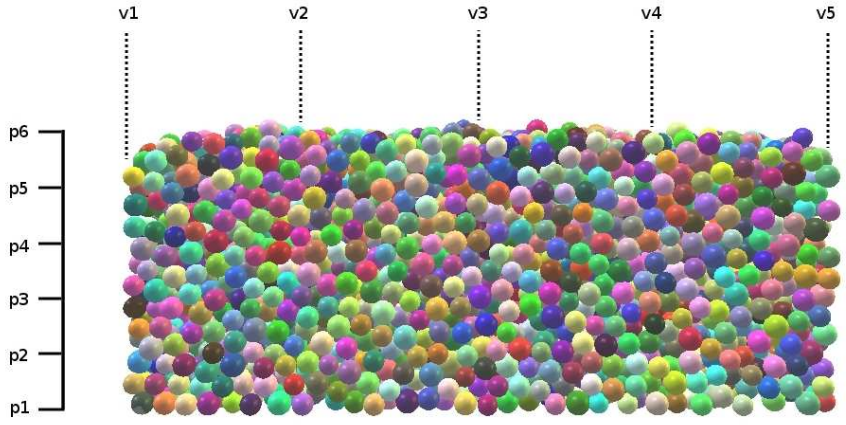

Figure 6.59: Schéma des mesures de pression de fluide.

INPUT DATA		
N	$[-]$	5000
ϕ_{c1}	$[deg]$	1
ϕ_{c2}	$[deg]$	30
E	$[kPa]$	15000
a	$[-]$	0.5
d_{50}	$[m]$	0.066
d_{max}/d_{min}	$[m]$	1.22
μ	$[kPa \cdot s]$	0.1

Table 6.7: Action de la vague sur sédiment dense - Paramètres de la simulation.

ne montrent pas de différence significative, exception faite pour la dernière partie de la simulation.

Il parait claire que l'assemblage reste globalement stable jusqu'à une amplitude $A = 1500\,Pa$. Au delà de cette valeur, la force de trainée associée au gradient imposé induit une instabilité. Aucune localisation de la déformation est remarquée. En fig. 6.61 quatre instantanées de la pression de fluide et le champ de vitesse des grains sont représentées, relatives aux temps $t = 5\,s$, $t = 10\,s$, $t = 15\,s$, $t = 19.3\,s$. Il peut être observé que le profil de pression reste similaire à l'hydrostatique le long de toute la simulation, ce qui signifie que dans la résolution du système d'éq.(6.68),

$$[\mathbf{G}]\{\mathbf{P}\} = [\mathbf{E}]\{\dot{\mathbf{X}}\} + \{\mathbf{Q_p}\} \tag{6.78}$$

avec $\{\mathbf{Q_q}\} = 0$, le terme (de droite) qui influence le plus la solution de l'équation 6.68 est $\mathbf{Q_p}$, le vecteur des pressions imposées, tandis que 'le vecteur exprimant la déformation volumique des pores, $\mathbf{E\dot{x}}$, a des effets négligeables dans la solution.

Mesures de pression de fluide

Les valeurs de pression mesurées au cours de la simulation sont représentées sur le diagramme de la fig.6.62(gauche). Leur évolution indique clairement que le profil de pression ne dévie pas des conditions hydrostatiques, sauf dans la dernière partie de la simulation ($t > 15s$), quand un mécanisme d'instabilité est observé. Sur la même figure, le rapport entre le gradient de charge hydraulique mesuré et le gradient critique de liquéfaction, i_c, calculé avec l'éq.(6.75), est représenté. L'évolution de ce rapport est linéaire tant que le sédiment reste stable, tandis qu'une évolution chaotique est observée quand l'instabilité se produit.

Interprétation du résultat

Une interprétation de ce qui se passe dans la dernière partie de la simulation est suggérée par l'instantanée de la fig.6.63, où le mouvement des particules est représenté par des flèches dont la couleur et la longueur représente respectivement leur vitesse et leur accélération. On peut observer comme le mouvement concerne principalement les grains qui se trouve en surface du sédiment. Ceux-ci ont tendance à être transportés par l'écoulement, et à s'accumuler sur la section de droite de l'échantillon. En considérant la condition de symétrie spécifiée sur les parois latérales (fig.s 6.54,6.55), ce résultat peut s'interpréter comme la formation d'une bosse. Le déviateur de la déformation, représenté en fig.6.64, confirme cette interprétation.

Simulation sur échantillon lâche

Similairement à ce qui a été fait pour le cas dense, on défini cette fois un angle de frottement intergranulaire aux contact qui préviendra le réarrangement entre les grains lors de sa mise en place, de façon à obtenir un échantillon lâche. Sur cet échantillon, on simulera l'action de la vague et on commentera les résultat, en relation aussi avec ce qui a été observé et décrit dans la section précédente. Le tableau 6.8 donne les paramètres pour cette nouvelle simulation.

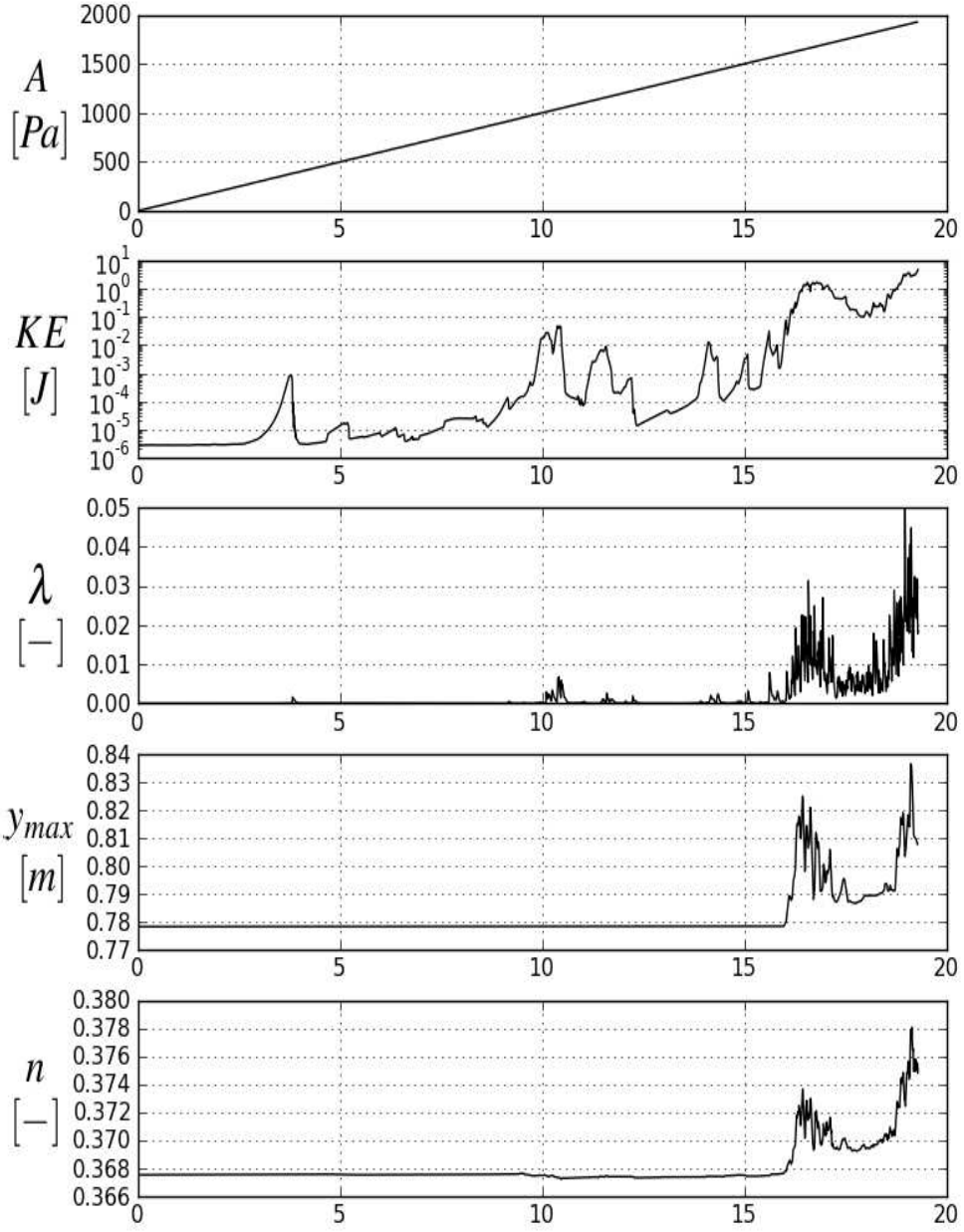

Figure 6.60: Action de la vague sur sédiment dense - Évolution des paramètres d'état et cinétiques 6.7.

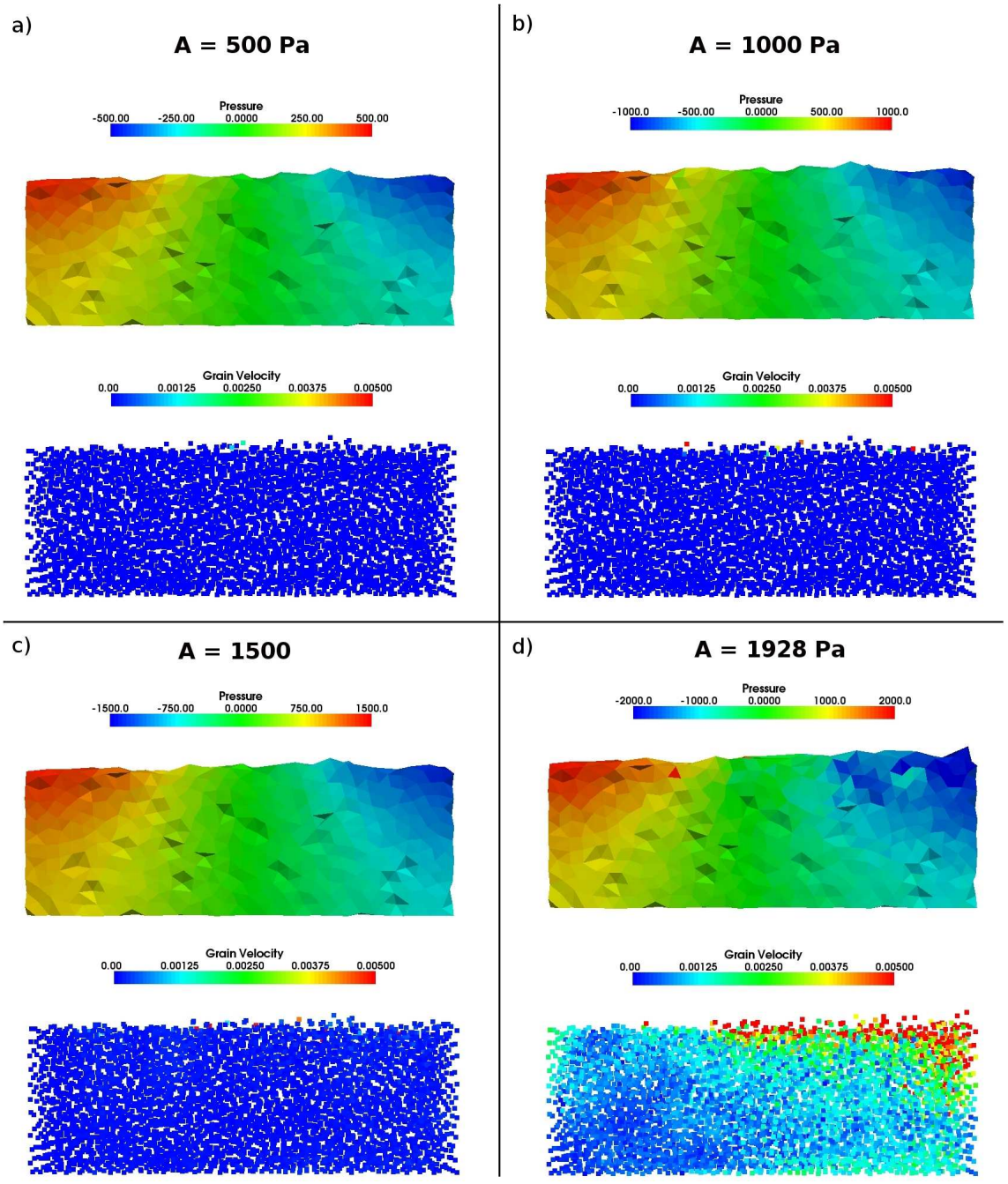

Figure 6.61: Action de la vague sur sédiment dense - Instantanée de la simulation aux temps $t = 5s$ (a), $10s$ (b), $15s$ (c), $19.3s$ (d). Pression fluide [Pa], vitesse des grains [m/s].

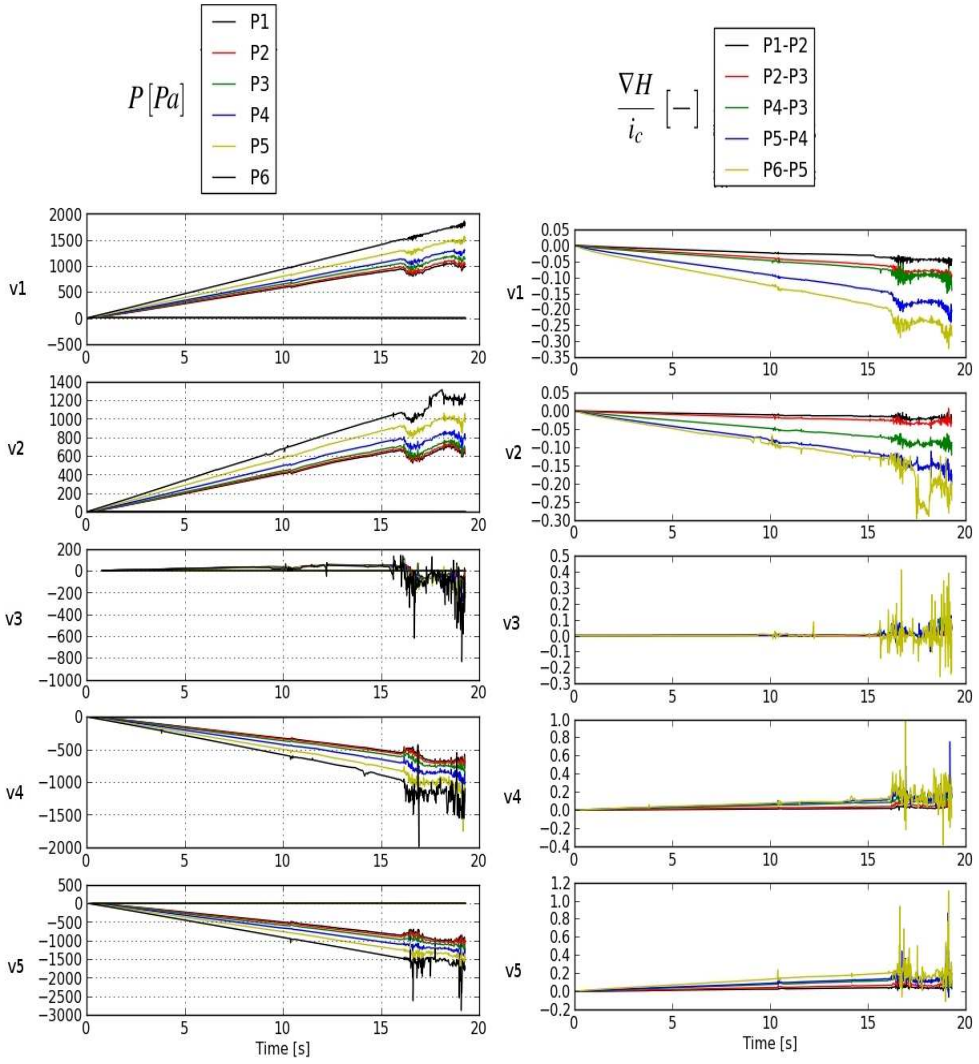

Figure 6.62: Action de la vague sur sédiment dense - Mesures de pression de fluide.

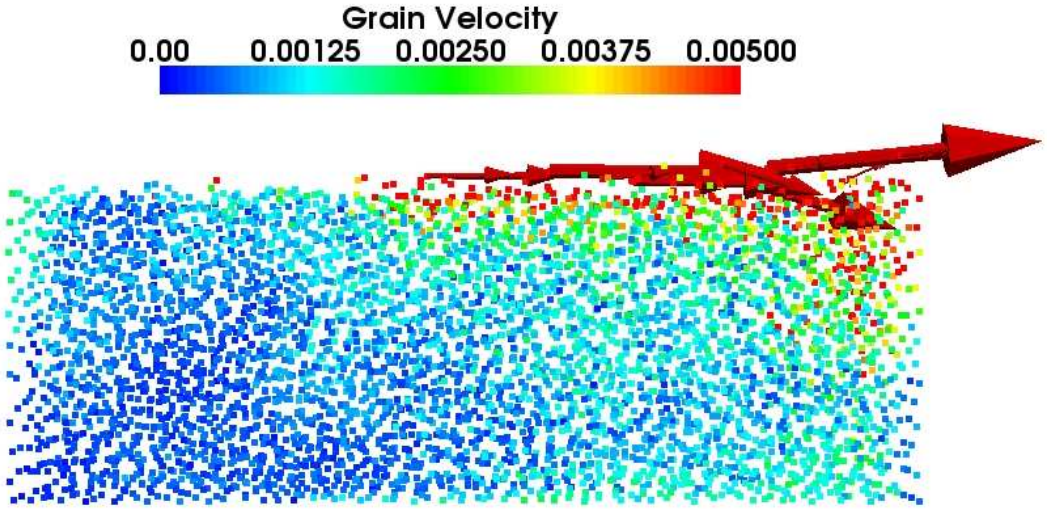

Figure 6.63: Action de la vague sur sédiment dense - Vitesses des grains (couleur flèche) et accélérations (longueur flèches).

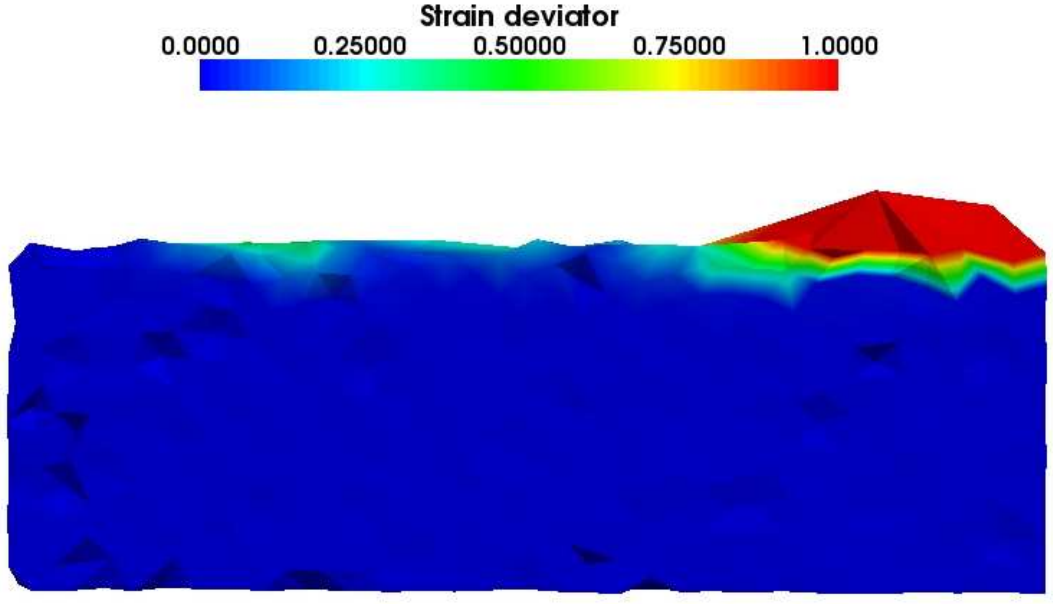

Figure 6.64: Action de la vague sur sédiment dense - Champ de déformation déviatorique.

INPUT DATA		
N	$[-]$	5000
ϕ_{c1}	$[deg]$	30
ϕ_{c2}	$[deg]$	30
E	$[kPa]$	15000
a	$[-]$	0.5
d_{50}	$[m]$	0.06
d_{max}/d_{min}	$[m]$	1.22
μ	$[kPa \cdot s]$	0.1

Table 6.8: Action de la vague sur sédiment lâche - Paramètres de la simulation.

Paramètre d'état et cinétiques

D'après les résultats représentés en fig.6.65, des différences peuvent être facilement remarquées par rapport au cas dense. L'amplitude A pour laquelle on observe une instabilité du sédiment est plus faible: l'énergie cinétique indique la présence d'un mouvement dès les premières itérations. Un mouvement plus important intervient à partir du temps $t \simeq 5\,s$: les paramètres KE et λ augmentent soudainement, cet événement est suivi par une réduction, légèrement décalée dans le temps, de la coordonnée maximale y_{max} et de la porosité n. L'échantillon est en train de se consolider.

L'interprétation de ce qui suit se complique, sur la base des données de la fig.6.65. L'échantillon est en mouvement, à une vitesse presque constante. La même chose peut se dire de la porosité. Cette phase se termine au temps $t \simeq 7.5\,s$, suivi par un état d'instabilité.

En fig.6.66 quatre instantanées de la simulation sont représentées. relatives aux temps $t \simeq 1s$, $t \simeq 4\,s$, $t \simeq 6\,s$, $t \simeq 8.5$. Le profile de pression de fluide, initialement hydrostatique (a), dévie en conséquence de la contraction des pores qui concerne une partie de l'échantillon (b), résultant finalement en une surpression (c) due au fait que l'échantillon est en train de consolider, son poids étant porté initialement par le fluide. La résistance aux cisaillement s'annule presque dans ces conditions, en conséquence de la réduction de la contrainte effective. L'instantanée (d) montre l'échantillon déformé qui persiste dans un état liquéfié. Les déformation les plus importantes sont observées à la surface du sédiment. Des mécanismes de roulement et de mise en suspension des particules concerne cette zone, dont l'analyse est toutefois hors du but de notre étude. Une dernière comparaison avec le cas *dense* nous informe que l'amplitude de la vague qui détermine l'instabilité du sédiment est quatre fois plus petite dans le cas *lâche* qu'on vient de présenter.

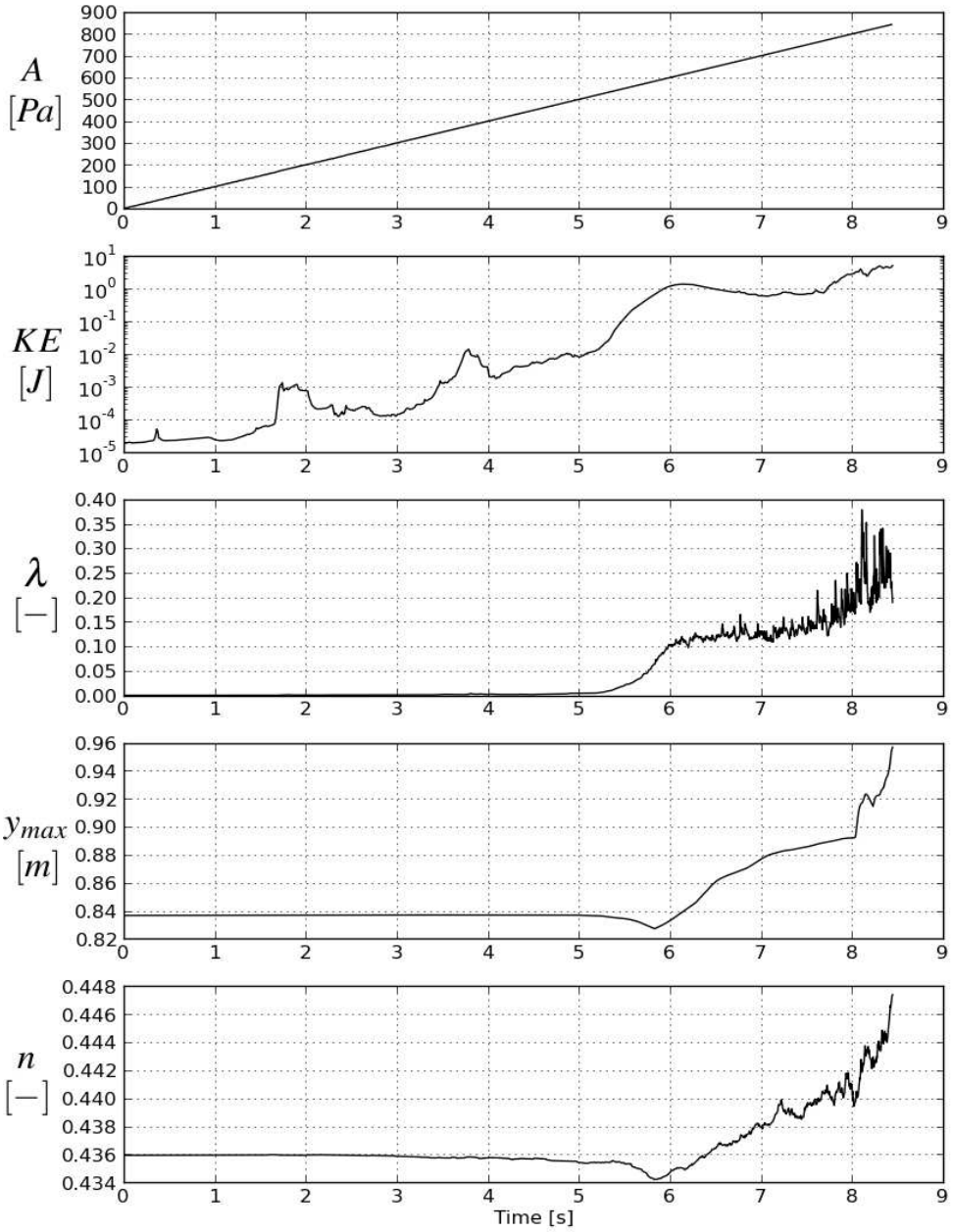

Figure 6.65: Action de la vague sur sédiment dense - Évolution des paramètres d'état et cinétiques 6.8.

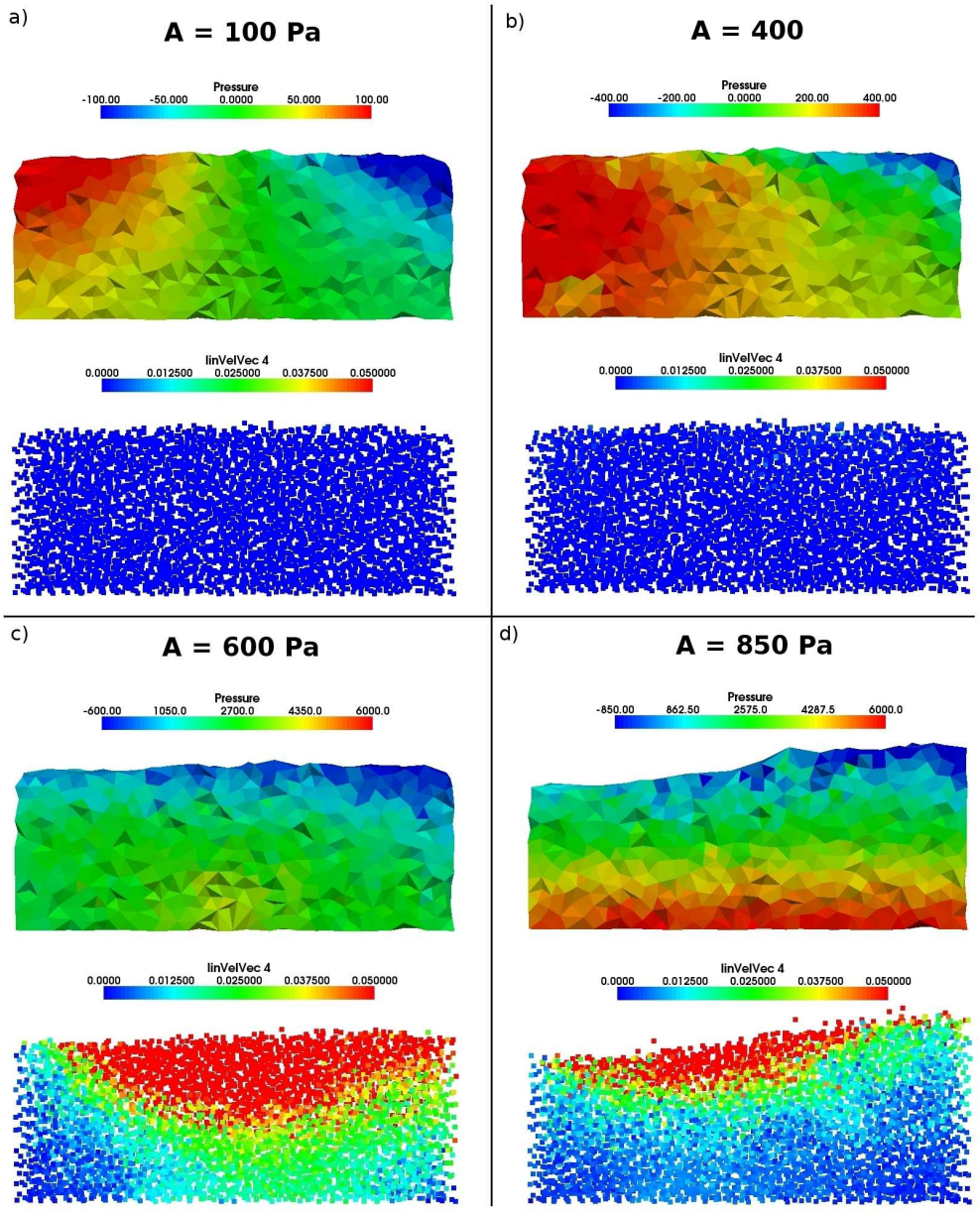

Figure 6.66: Action de la vague sur sédiment lâche - Instantanée de la simulation aux temps $t \simeq 1s$ (a), $t \simeq 4s$ (b), $t \simeq 6s$ (c), $t \simeq 8.5s$ (d). Pression fluide [Pa], vitesse des grains [m/s].

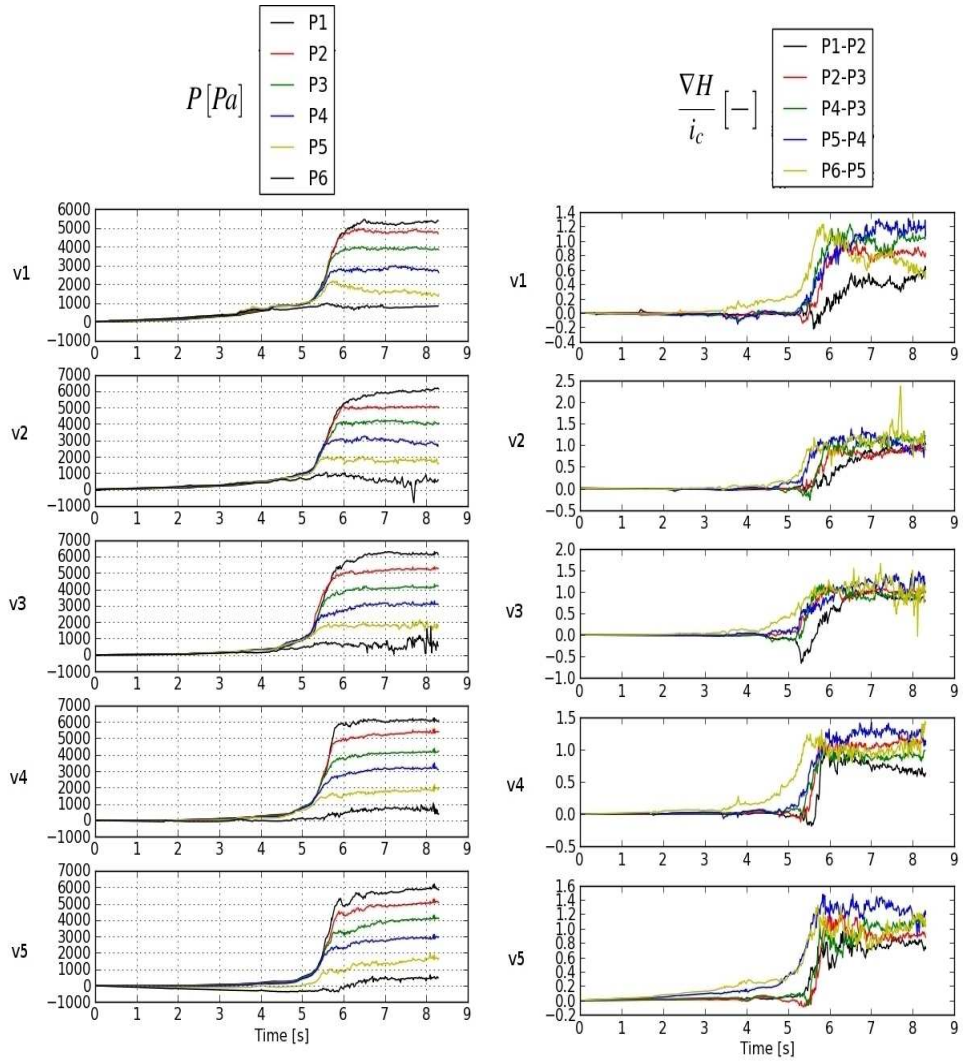

Figure 6.67: Action de la vague sur sédiment lâche - Mesures de pression de fluide.

Mesures de pression de fluide

Deux phases peuvent être distinguées en observant des mesures de pression de fluide. Une première, stable, de $t = 0$s à $t = 3$s, pendant laquelle les conditions hydrostatiques dominent. Le terme de droite de l'éq.(6.68) qui influence le plus le champ de pression est le vecteur des pression imposées $\mathbf{Q_p}$. Une deuxième, caractérisée par la liquéfaction de l'échantillon, avec une surpression interstitielle qui concerne tout l'échantillon. Le rapport $\frac{\nabla H}{i_c}$ approche et occasionnellement dépasse l'unité, dès que la liquéfaction se produit. Le terme $\mathbf{E\dot{x}}$ de l'éq.(6.68) influence donc majoritairement le champ de pression calculé dans cette phase.

Interprétation du résultat

La fig.6.19 montre la déformation déviatorique, qui fournit d'autres informations sur le mécanisme induit par la liquéfaction du sédiment, avec localisation de la déformation le long d'une bande de cisaillement.

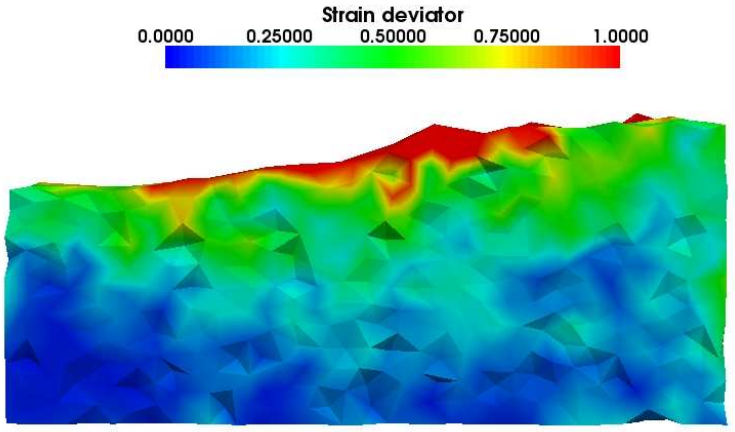

Figure 6.68: Action de la vague sur sédiment lâche - Champ de déformation déviatorique.

La vitesse (couleur flèche) et l'accélération (longueur) des grains, visualisées en fig.6.69, confirment nos conclusions.

Simulation de vague stationnaire

Dans cette dernière section on présente les résultats numériques obtenus en définissant un profil de pression de fluide, à la surface du sédiment, qui simule une action de vague plus réaliste que le cas précédent. Une vague stationnaire est en fait simulée, oscillante avec un certain période parmi un maximum et un minimum d'amplitude A, comme représenté en fig.6.70.

Notamment, l'échantillon lâche sera soumis à ce nouveau type de chargement hydraulique. L'objectif sera d'analyser la relation entre la période d'oscillation de la vague et le temps caractéristique de consolidation associé à l'assemblage granulaire. La relation entre ces deux quantités est supposée déterminer la réponse mécanique de l'échantillon. Quand la période est plus longue que ce temps caractéristique, l'échantillon, lors de la perturbation, est censé avoir le temps de se consolider et d'atteindre une configuration stable sans subir de déformation déviatorique. Dans le cas contraire, l'échantillon n'a pas le temps de se consolider, et la liquéfaction du sol peut se produire.

Une analyse paramétrique sera présentée, en faisant varier la valeur d'amplitude A et la période d'oscillation de la vague.

Réponse de l'échantillon lâche

On présentera dans une première partie le résultat qui a été obtenu en faisant osciller une vague avec une période de 1 s avec $A \pm 150$ Pa. Le tableau 6.8 résume les paramètres pour cette simulation.

Paramètre d'état et cinétiques

En fig.6.71 on peut observer l'évolution des paramètres nous renseignant sur l'état et la cinétique au cours de la simulation. Les paramètres cinétiques, KE et λ, indiquent la

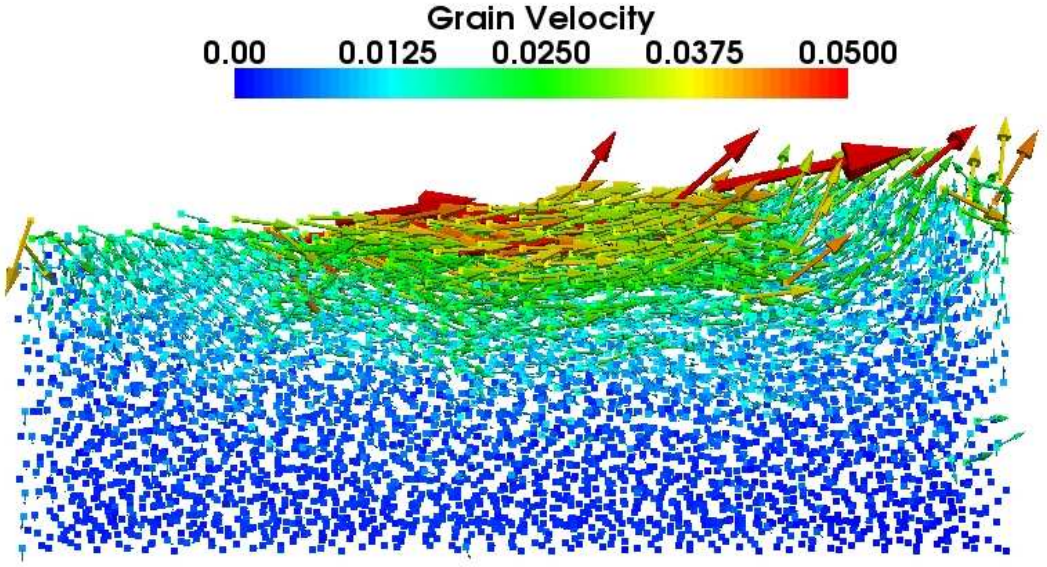

Figure 6.69: Action de la vague sur sédiment lâche - Vitesses des grains (couleur flèche) et accélérations (longueur flèches).

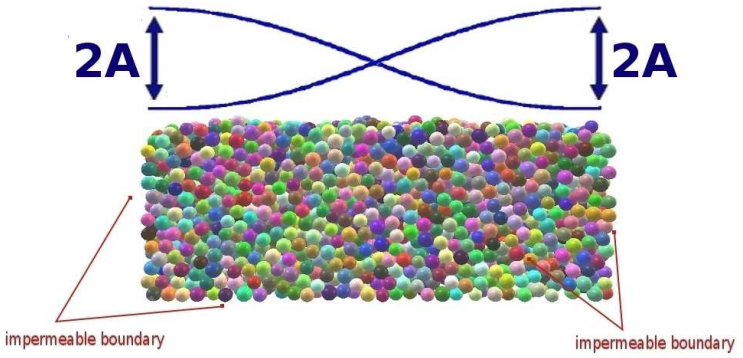

Figure 6.70: Schéma de l'échantillon (profondeur/hauteur=2.0) pour la simulation de l'action d'une vague stationnaire sur un échantillon lâche.

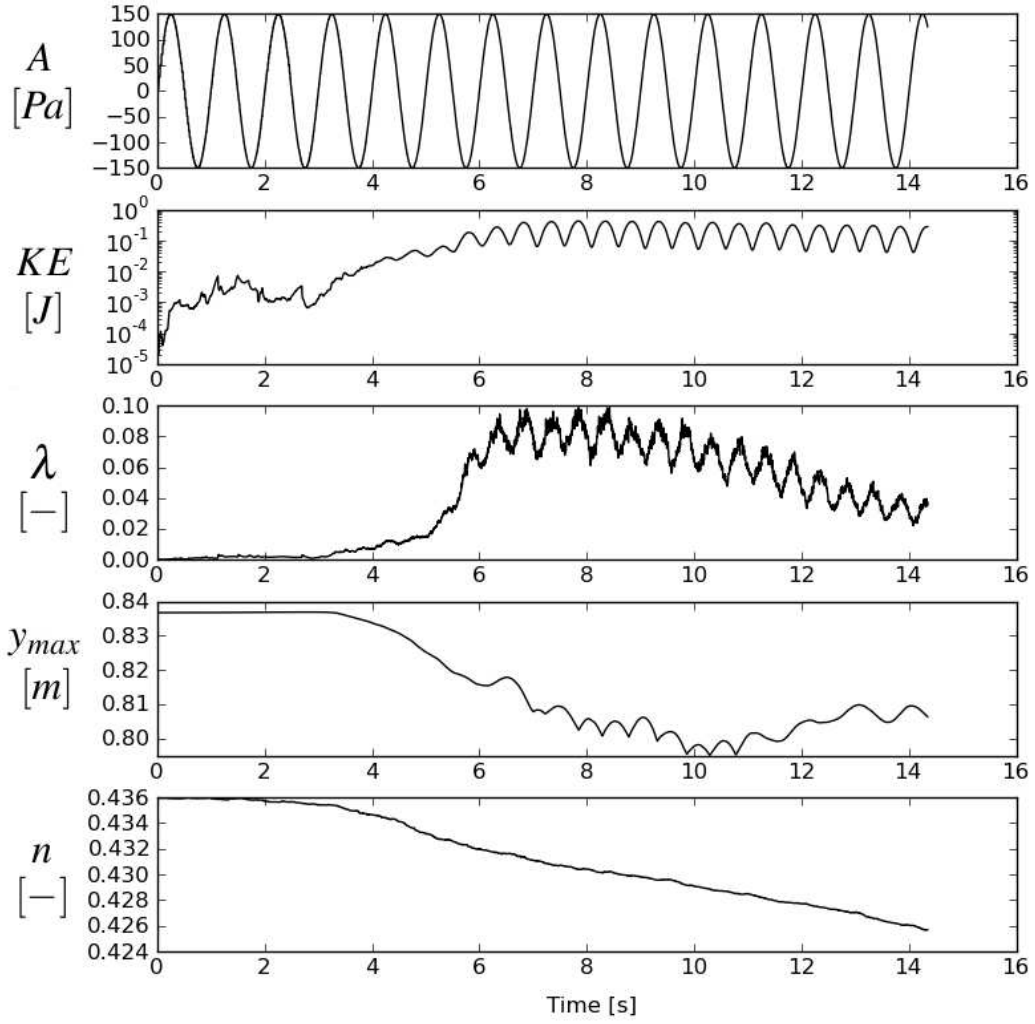

Figure 6.71: Vague stationnaire (période = 1s) sur échantillon lâche ($n \simeq 0.436$) - Évolution des paramètres d'état et cinétiques.

présence de mouvement dès les premières itérations, jusqu'au temps $t \simeq 3$s. Après cette première partie, l'échantillon commence à se tasser, comme en témoigne la réduction de la porosité n et de la coordonnée maximale y_{max}. A partir de $t \simeq 6s$, l'évolution de λ et KE suggère la présence d'un mécanisme de déformation complexe, dont l'interprétation sera donnée dans la prochaine section.

Mesures de pression de fluide

Les profils de pression de fig.6.72 indiquent que le sédiment liquéfie sous l'action de la vague. L'évolution du rapport adimensionnel $\frac{\nabla H}{i_c}$ nous informe de l'état liquéfié qui concerne le sédiment, à partir de $t \simeq 6$ s jusqu'à la fin de la simulation. Cela explique l'allure oscillante des paramètres λ et KE de 6.71: l'échantillon n'ayant presque plus de résistance au cisaillement, sa réponse ressemble fortement à l'action qui lui est appliquée.

Temps caractéristique de consolidation

Pour estimer l'ordre de magnitude du temps de consolidation associé à l'échantillon qu'on utilise, on peut utiliser la définition de l'éq.6.74

$$T_v = \frac{t}{t_c} \quad \rightarrow \quad t_c = \frac{L^2 \gamma_w \varepsilon_c}{K_d \sigma_c} \tag{6.79}$$

en l'adaptant au cas que l'on veut étudier. L, la longueur du chemin le plus long parcouru par une particule de fluide, correspond maintenant à la hauteur de l'échantillon. Le terme de contrainte σ_c est associé au poids des particules, $\rho' H$, tandis que ε_c peut être estimé au tour de 0.01. On obtient:

$$t_c \simeq 10\,s \tag{6.80}$$

Cet estimation permet l'interprétation du résultat qui est obtenu par comparaison au période d'oscillation de la vague. Dans le cas que l'on vient de présenter, la période était de 1s. L'échantillon n'a pas le temps de se consolider et d'atteindre une configuration stable. Les effets du gradient de pression domine la réponse globale du milieu, un effet amplifié par la liquéfaction du sol.

D'autres mécanismes de déformation devraient se produire en faisant varier la période d'oscillation de la vague. Cela est l'objectif de l'analyse présentée dans la suite.

Autres combinaisons Amplitude - Période

Pour mieux caractériser le comportement de l'assemblage sous l'action d'une vague stationnaire, plusieurs combinaisons A - période d'oscillation ont été testées. La liquéfaction étant un aspect qui influence fortement la réponse du sédiment, on a choisi de bien définir une limite des valeurs amplitude/période pour lesquelles ça se produit (fig.6.73). Le critère se base sur le rapport adimensionnel $\nabla H / i_c$, qui approche l'unité quand le gradient hydraulique égalise le gradient de liquéfaction. Les événement de liquéfaction partielle ($\nabla H / i_c > 0.80$), ont été aussi marqué en rouge (état liquéfié) sur le diagramme. On remarque qu'il y a jamais de la liquéfaction pour des faibles amplitudes. Pour les amplitudes les plus grandes ($A = 200\,/400\,\mathrm{Pa}$) l'échantillon liquéfie pour toutes les periodes testées. Pour des amplitudes intermédiaires, il est intéressant de voir comme la liquéfaction ne se produit que pour les plus hautes fréquences. Notre intérêt n'étant pas limité à savoir si l'échantillon liquéfie ou pas, on s'intéresse à évaluer les déplacements horizontaux qui concernent les particules qui se trouvent le long de l'axe de symétrie de l'échantillon (fig.6.74).

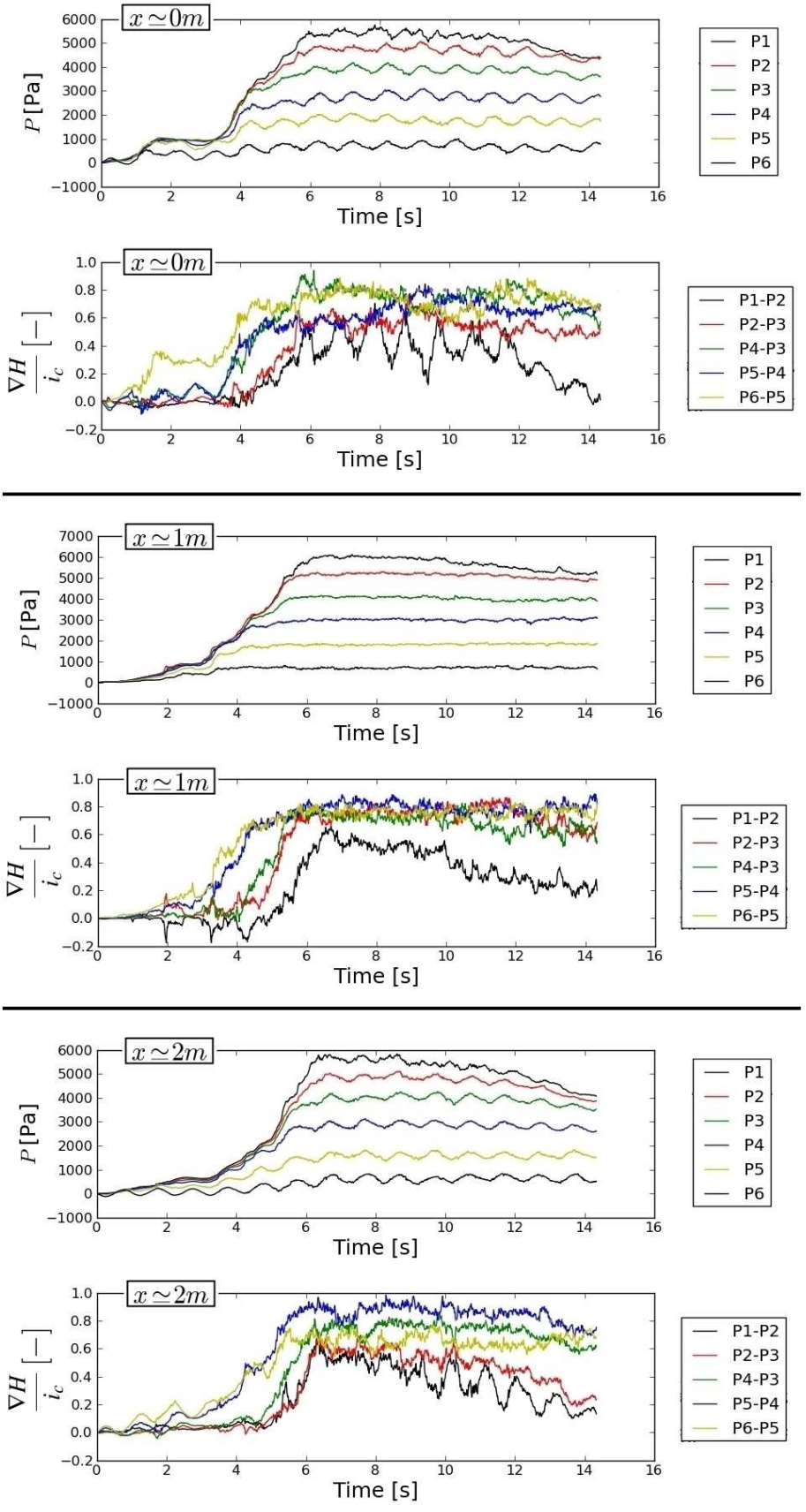

Figure 6.72: Vague stationnaire (période = 1s) sur échantillon lâche ($n \simeq 0.436$) - Mesures de pression de fluide.

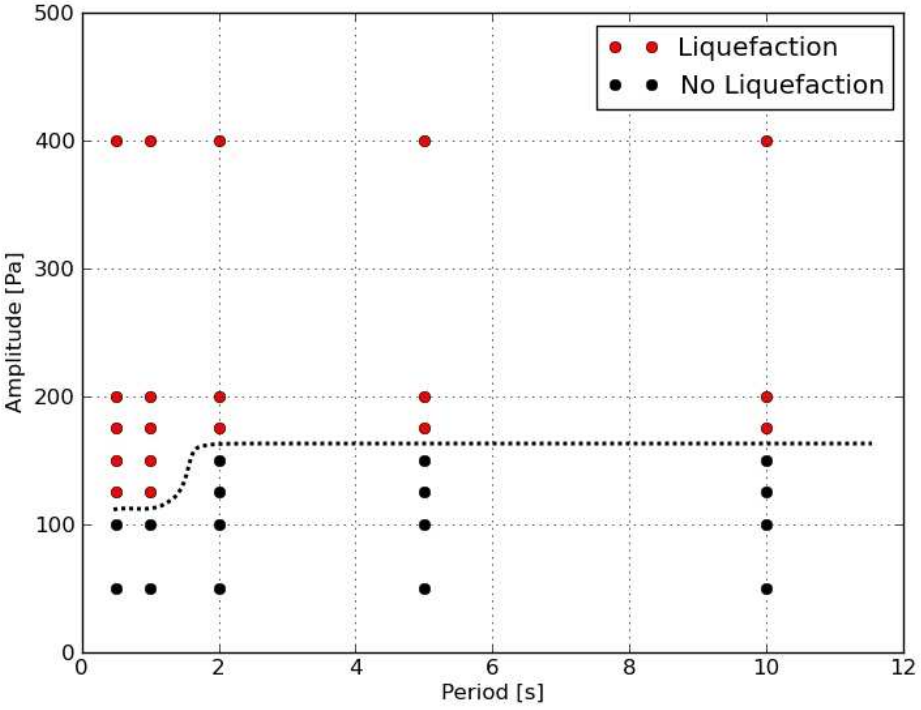

Figure 6.73: Événements de liquéfaction pour différentes combinaisons amplitude / fréquence.

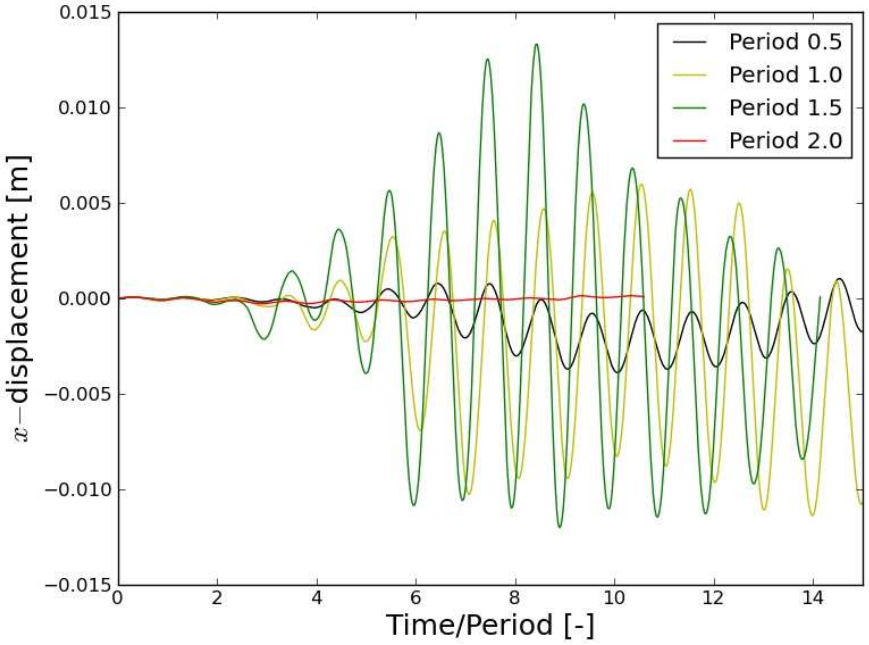

Figure 6.74: Déplacement horizontal des particules sur l'axe de symétrie en fonction de la fréquence d'oscillation de la vague.

Quand la liquéfaction ne se produit pas (période = 2.0s, voir fig. 6.78) le déplacement horizontal est quasiment nul. Pour les périodes les plus courtes, le sédiment liquéfie (fig.s 6.76, 6.77) et les déplacements deviennent plus importants. Dans ces conditions, c'est la relation entre la période d'oscillation de la vague et le temps associé à l'inertie des particules qui gouverne l'évolution du système fluide-particules. Pour une période de 0.5s, les particules n'ont pas le temps d'accélérer mais juste d'osciller au tour de leur position initiale (fig. 6.74). Le déplacement horizontal mesuré est très bas mais favorise le réarrangement des grains vers des configurations plus compactes (fig. 6.76). Au contraire, pour les périodes les plus longues, 1.0s/1.5s, les déplacements horizontaux deviennent plus importants (fig.s 6.74, 6.77). Fig.6.75 résume les valeurs de déplacement horizontal qui ont été mesurées dans cette simulations.

Conclusions et perspectives

La méthode des élément discrets (DEM) a été utilisé pour la description de l'interaction mécanique entre particules solides. Ce modèle numérique permet la représentation des matériaux granulaires à l'aide de corps indépendants qui interagissent entre eux, suivant une loi d'interaction défini par l'utilisateur. Les particules solides ont été modélisée par des éléments sphériques. Cette choix nous permet de simplifier fortement le traitement de la géométrie locale tout en assurant l'obtention de résultats intéressants d'un point de vue physique et mécanique. Il n'y a pas besoin d'augmenter la complexité de la forme des particules, tant que un comportement spécifique macroscopique, dont les origines micromécaniques résident dans cet aspect, n'est pas à reproduire. L'idée de base qui a été suivie en définissant le modèle d'écoulement a été la préservation de la nature discrete

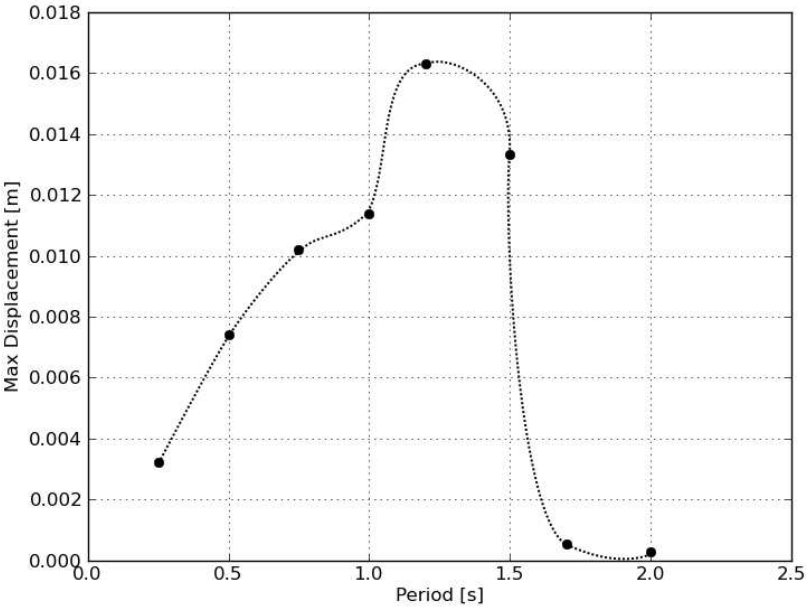

Figure 6.75: Déplacement horizontal maximal en fonction de la fréquence d'oscillation.

de la DEM, de façon de pouvoir accéder aux informations nécessaires pour définir une force fluide à appliquer à chaque particule. Les modèles existants arrivant normalement à ce niveau de détail dans la description de l'interaction particule-fluide impliquent un excessif coût de calcul. L'objectif du modèle aux volume finis (PFV) qu'on a proposé était d'atteindre un niveau détaillé dans la description de l'hydrodynamique des milieux granulaires saturés tout en assurant des temps de calculs avantageux et la possibilité d'utiliser de milliers de particules en trois dimensions. Des hypothèse ont été introduites pour simplifier les équations de Navier-Stokes et formuler un problème tractable. Un écoulement stationnaire d'un fluide incompressible est considéré avoir lieu dans le régime laminaire. Ceci est une hypothèse cohérente en considérant qu'on traite des problèmes caractérisés par une vitesse de fluide très faible, et des nombre de Reynolds et de Mach petits. Dans ces conditions, le terme inertiel des équations de Navier-Stokes peut être négligé si comparé au terme visqueux. Les équations deviennent ainsi linéaires.

La résolution du problème d'écoulement a été basée sur un algorithme utilisant un schéma implicite aux différences finies. Le couplage avec la DEM résulte naturellement adapté dans ces conditions. Un critère pour assurer la stabilité du schéma numérique couplé a été formulé par un étude paramétrique. En introduisant d'autres simplifications, dont l'hypothèse de pression constante par morceaux, le nombre d'inconnues pour la résolution du problème de l'écoulement devient comparable au cas du problème solide. L'analogie du problème couplé ainsi obtenu avec la théorie de la poroélasticité de Biot nous a suggéré que le modèle pouvait être capable de reproduire des problèmes classiques hydromécaniques, tels que la consolidation des sols, dont la simulation et comparaison avec la solution de Terzaghi a constitué la validation du modèle.

L'application à l'analyse de l'hydrodynamique d'un sédiment granulaire soumis à l'action d'une vague a été finalement présentée. Deux scénarios ont été évalués, car-

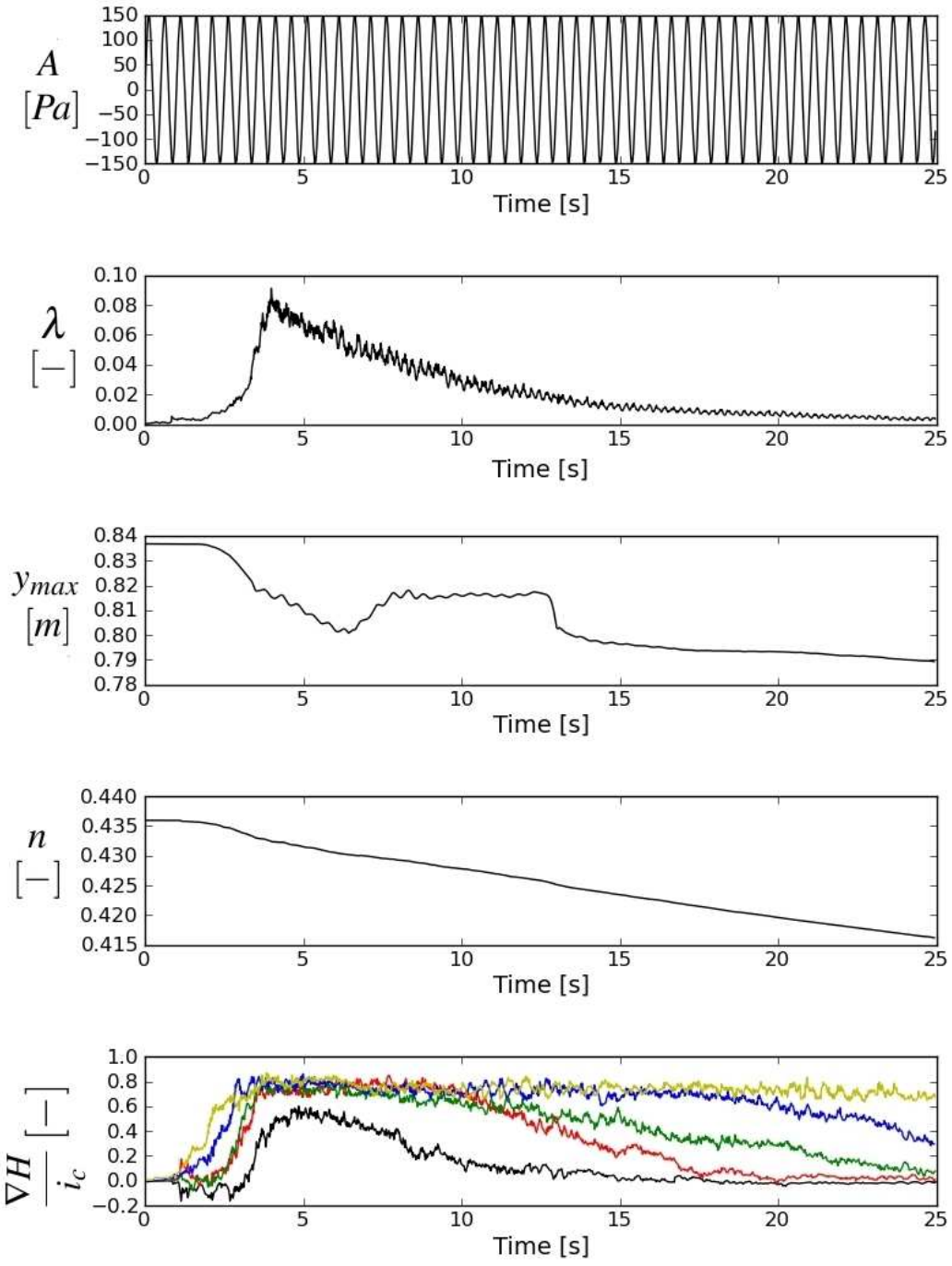

Figure 6.76: Vague stationnaire (période = 1s) sur échantillon lâche ($n \simeq 0.436$) - Période = 0.5s.

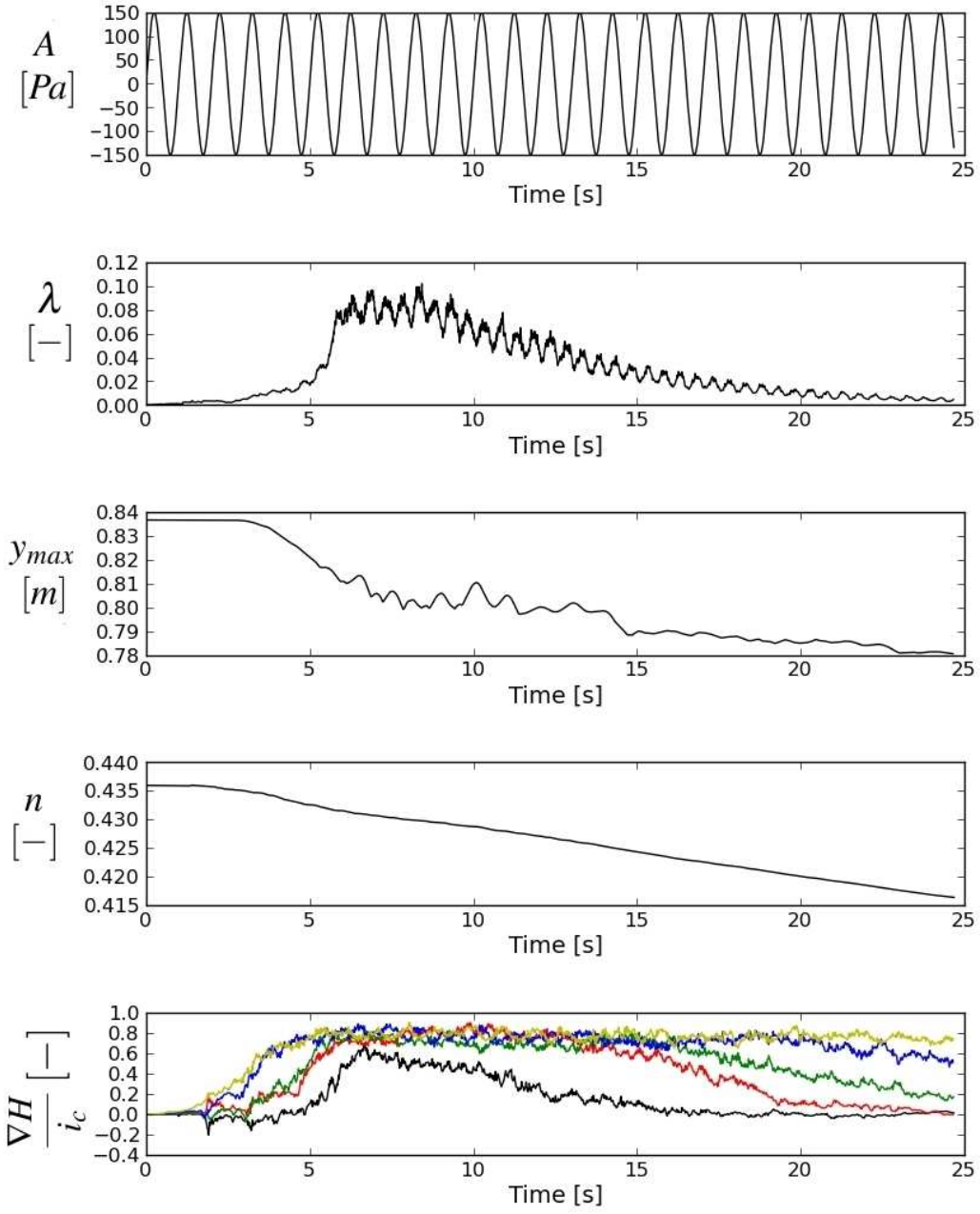

Figure 6.77: Vague stationnaire (période = 1s) sur échantillon lâche ($n \simeq 0.436$) - Période = 1.0s.

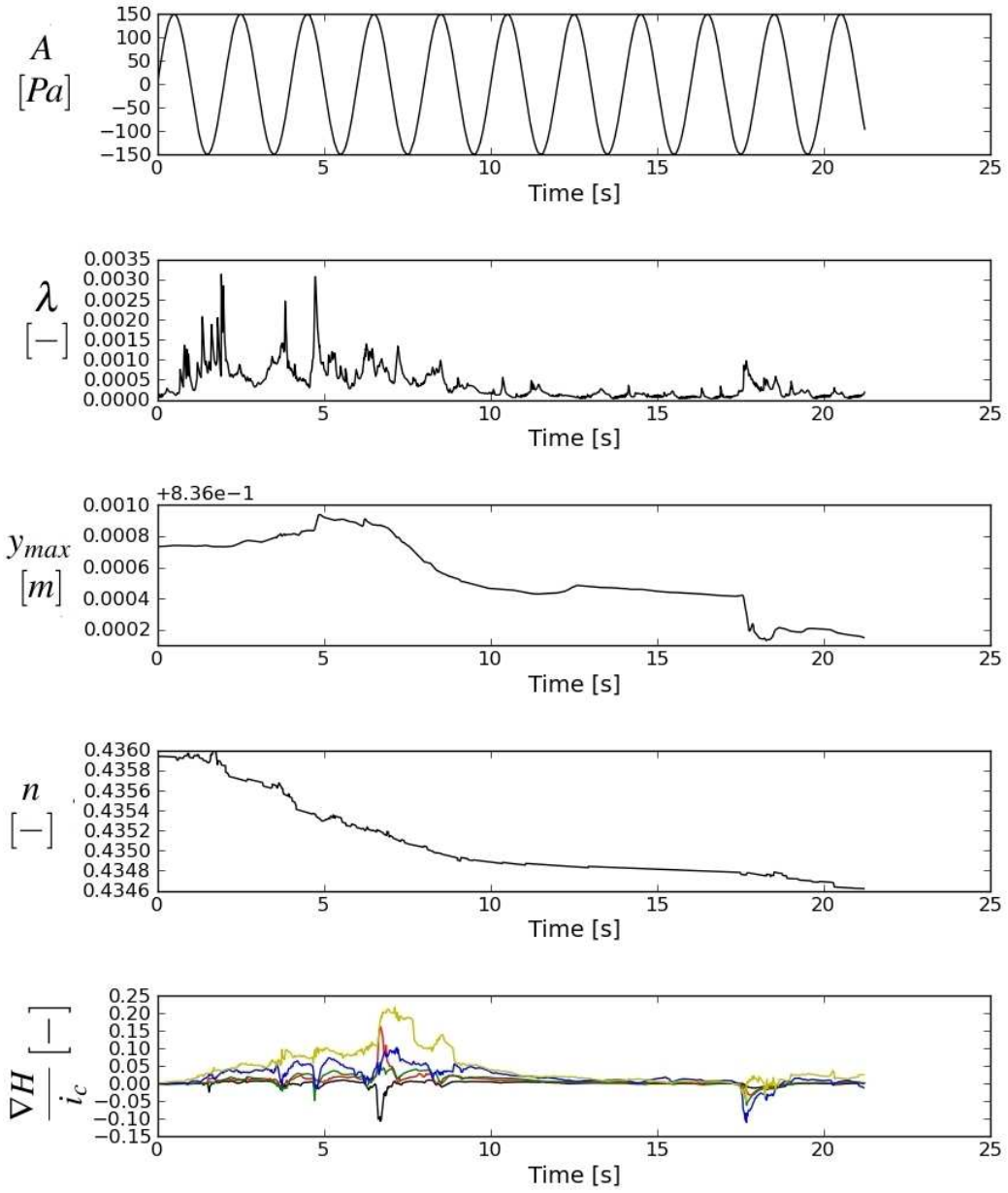

Figure 6.78: Vague stationnaire (période = 1s) sur échantillon lâche ($n \simeq 0.436$) - Période = 2.0s.

actérisés par deux échantillon qui différaient dans la valeur initiale de porosité. Les résultats obtenus nous ont permis d'en tirer des conclusions intéressantes d'un point de vue mécanique. Dans le cas *dense* le problème était dominé par la condition en pression imposée aux limites, tandis que la dynamique de l'échantillon initialement lâche était fortement influencé par la déformation des pores. L'amplitude à laquelle on a pu assister au début de l'instabilité était quatre fois plus petite dans ce dernier cas que dans le précédent. La deuxième partie de l'analyse a été consacrée aux effets sur un sédiment lâche d'une onde stationnaire, oscillante avec une certaine fréquence entre deux valeurs limites d'amplitude. La relation entre le temps caractéristique de consolidation, la période d'oscillation de la vague et le temps associé à l'inertie des particules a été invoquée pour interpréter le comportement du sédiment et sa tendance à se liquéfier. Par cette analyse, il en résulte une formulation d'un critère pour la liquéfaction.

Concernant les possibles extensions du modèle, ceux-ci concernent des aspects physiques et numériques. D'un point de vue physique, la description de la contrainte et déformation du fluide, limité aux composantes sphérique dans le modèle actuel, pourra inclure la composante déviatorique, comme d'ailleurs c'est déjà le cas dans les récents travaux de Marzougui [63]. L'introduction d'un module de compressibilité pour le fluide est aussi une extension qui est en cours de développement (post-doc de Luc Scholtès au Laboratoire 3SR). D'un point de vue numérique, la parallélisation du code est concevable et constitue une perspective pour les prochain développements. La structure de l'algorithme suggère une parallélisation pour l'utilisation de plusieurs processeurs simultanément. En termes d'application du modèle, l'analyse de problèmes d'érosion interne, avec l'analyse du phénomène de migration de particules fines dans le milieux poreux, dont des résultats préliminaires peuvent être trouvés en [84], peut être approfondi, comme le transport de particules à la surface du sédiment. L'implémentation des conditions aux limites périodiques est en développement (PhD de Donia Marzougui) et pourra ouvrir à des analyses plus complexes de l'hydrodynamique du sédiment granulaire ou d'autres problèmes dans le domaine de la stabilité des pentes (e.g. debris flow).